

(Model ID = 454988)

Ineris -229431-2829642- 2.0

25/06/2026

Modisafe - Studies of vapour and droplet evaporation

FOI

TOTALFORSVARETS FORSKNINGSINSTITUT, FOI

INERIS
controlling risks
for sustainable development

PREAMBLE

This document has been prepared on the basis of information provided to INERIS. INERIS cannot be held liable, directly or indirectly, for any inaccuracies, omissions, errors or similar issues relating to the information provided.

The accuracy of this document must be assessed on the basis of available and objective knowledge and, where applicable, the regulations in force on the date of preparation of this document. Consequently, INERIS cannot be held liable for any changes to these elements after that date. The service does not include any obligation on the part of INERIS to update the document after that date.

The preparation of this document and the associated service are provided under an obligation of means.

In view of the mission incumbent upon INERIS under Article R131-36 of the French Environmental Code, INERIS is not a decision-maker. Thus, any opinions, recommendations, suggestions or equivalent proposed by INERIS in the context of this service are intended solely to advise the decision-maker. Consequently, INERIS cannot be held liable in place of the decision-maker, who is therefore solely responsible for any interpretations they may make on the basis of this document. Any recipient of the document shall use the results contained therein in their entirety or otherwise objectively. The use of this document in the form of extracts or summary notes shall also be the sole and entire responsibility of the recipient. The same applies to any other modifications made to it. INERIS also disclaims all liability for any use of the document outside its intended purpose.

In the event of any contradiction between the general terms and conditions of sale and the provisions of this preamble, the provisions of this preamble shall prevail over the provisions of the general terms and conditions of sale.

Division responsible for the report: Fire, Dispersion and Explosion Department

Author: LEROY Guillaume

Review: GENTILHOMME OLIVIER

Approval: Document approuvé le 25/06/2026 par BOUET REMY

Table of contents

1 Introduction 7
1.1 Background and objectives 7
1.2 Contractual elements 7
2 Experimental setup 8
2.1 Facilities 8
2.2 Test bench 9
2.2.1 Description 10
2.2.2 Substrates 12
2.2.3 The liquids tested 16
2.2.4 Measurements and instrumentation 19
2.3 Test matrix 26
2.3.1 Matrix 26
2.3.2 Reference test – Test N°1 26
2.3.3 Summary of instrumentation 27
3 Atmospheric boundary layer analysis 29
3.1 Scale 29
3.2 Law of similarity 29
3.3 Calculation of wind and turbulence profile at scale 1 30
3.4 Measurement of wind velocity and turbulence profiles in the gallery 30
3.4.1 Generation of turbulence 30
3.4.2 Instrumentation 31
3.4.3 Results 33
4 Measurement of evaporation rate 37
4.1 Pool evaporation tests 37
4.1.1 Based on the overall concentration 37
4.1.2 Based on mass 38
4.1.3 Discussion specific to TEP 38
4.2 Droplet evaporation tests 38
4.2.1 General method 38
4.2.2 Discussion specific to TEP 39
4.2.3 Accumulation chamber 41
5 Experimental results – Pool evaporation tests 44
5.1 Description of the test procedure 44
5.2 Observations 46
5.3 Analysis of different parameters 47
5.3.1 Wind velocity at 1 m high 47
5.3.2 Temperature 48
5.3.3 Product mass 49
5.3.4 Near-field concentration 52
5.3.5 Evaporation rate 52

6 Experimental results – Droplet evaporation tests 61
6.1 Description of the test procedure 61
6.2 Analysis of the different parameters 63
6.2.1 Reference velocity at a height of 1 m 63
6.2.2 Temperature 63
6.2.3 Product mass 63
6.2.4 Evaporation rate 64
7 Conclusion 68
7.1 Pool evaporation 68
7.2 Evaporation of droplets 69
8 References 70
9 Appendices 71

List of illustrations

Figure 1: Ineris fire platform....8
Figure 2: Plan of the gallery....8
Figure 3: Cross-section of the gallery....9
Figure 4: End of the gallery – exterior view (left) – interior view looking upwards (right) 9
Figure 5: Arrangement of cardboard blocks to generate turbulence 10
Figure 6 : Photos of the cardboard blocks....10
Figure 7: Representation of the platform....11
Figure 8: Photo of the platform 11
Figure 9: Glass plate 12
Figure 10: Concrete block 13
Figure 11: Edges of blocks a1, a2, a3 and c (left) – edge of block b (right) 13
Figure 12: Reinforcement of the blocks....14
Figure 13: Concrete mixer truck 14
Figure 14: Concrete mixer 15
Figure 15: Saturation vapour pressure of tested liquids 17
Figure 16: Latent heat of vaporisation 18
Figure 17: Position of temperature measurement points....19
Figure 18: Position of sampling points located behind the substrate 20
Figure 19 : Sampling system in the vapour cloud....20
Figure 20 : Numbering of points 21
Figure 21 : Position of the sampling point in the extraction duct 21
Figure 22: Position of the sampling point located at the rear of the substrate....22
Figure 23: FTIR 23
Figure 24: PID 24
Figure 25: AP4C 24
Figure 26: Camera....25
Figure 27: Instrumentation pour les essais d'évaporation de nappe 27
Figure 28: Instrumentation for droplet evaporation tests 28
Figure 29: Theoretical wind and turbulence profiles at a scale of 1:1 30
Figure 30 : Arrangement of blocks used to generate turbulence....30
Figure 31: McCaffrey probe on the left and ultrasonic anemometer on the right. 31
Figure 32 : Probe positions....31
Figure 33: Mean velocity profile....34
Figure 34: Reynolds stress....34
Figure 35: Integral length scale 35
Figure 36: Turbulent kinetic energy 35
Figure 37: Friction velocity....36
Figure 38 : Position of the concentration measurement point 37
Figure 39 : heated vapour generation system 38
Figure 40 : Setup for the preliminary AP4C droplet evaporation test on glass....40
Figure 41 : Setup for the AP4C droplet evaporation test on concrete 40
Figure 42 : Glass slides onto which AP4C droplets were applied 41
Figure 43 : TEP evaporation tests on concrete – left: position of droplets – right: zoom on the position of the AP4C 41
Figure 44 : Example of a curve showing the evolution of vapour concentration in the AC 42
Figure 45 : Schematic diagram of how a circular AC works 42
Figure 46 : Photo of an AAC positioned on the substrate 43
Figure 47 : Illustration of the setup of concrete plate....44
Figure 48 : Illustration of liquid spillage 45
Figure 49 : toothed funnel....45
Figure 50 : Illustration of n-heptane leaking beneath the glass plate 47
Figure 51 : Average velocity 47
Figure 52 : $u'u'$ component of the Reynolds stresses 48
Figure 53 : Mass balances 51
Figure 54 : Evaporation rate – test 2 53

Figure 55 : Evaporation rate – test 6 53
Figure 56 : Evaporation rate decay phase associated with the reduction in liquid layer size....54
Figure 57 : Evaporation rate measured from pool receding time – test 4....55
Figure 58 : Global concentration measured from pool receding time – test 4 55
Figure 59 : Repeatability - n-heptane on glass....57
Figure 60 : Repeatability - n-heptane on concrete 57
Figure 61 : Impact of initial quantity of liquid on evaporation rate 58
Figure 62 : Average evaporation rate for tests involving n-heptane....59
Figure 63 : Average evaporation rate for tests involving acetone 60
Figure 64 : Average evaporation rate for tests involving the four products at reference conditions....60
Figure 65: Illustration of droplet deposition on the substrate....62
Figure 66 : Position of droplets deposited on the substrate depending on the substance 62
Figure 67: Evaporation rate – n-octane droplets 65
Figure 68: Evaporation rate – n-heptane droplets....66
Figure 69: Evaporation rate – TEP droplets 67

List of tables

Table 1: Concrete quality for the two porosities 15
Table 2: Thermomechanical characteristics of substrates 16
Table 3: Main characteristics of products (DIPPR database)....17
Table 4: DIPPR coefficients for the saturated vapour pressure of products....18
Table 5: DIPPR coefficients for latent heat of vaporisation 18
Table 6: Detection thresholds for concentration measurement devices....25
Table 7: Test matrix....26
Table 8: Apparatus used for soil vapour testing 28
Table 9: Apparatus used for droplet evaporation tests....28
Table 10: Scale factors....29
Table 11: Probe positions....32
Table 12 : Steps for tests on glass 44
Table 13 : Steps for tests on concrete....44
Table 14 : Main observations 46
Table 15 : Initial temperatures....48
Table 16 : Initial inventories....49
Table 17 : Mass balances....50
Table 18 : Start and end of the stationary phase....58
Table 19 : Steps for tests on glass 61
Table 20 : Steps for concrete tests....61
Table 21: Initial temperatures....63
Table 22: Initial inventories....63
Table 23: Mass balances....64
Table 24: Dilution Factors....64

1 Introduction

1.1 Background and objectives

MODISAFE (Modelling of Sources and Agent Fate) is an international collaborative project conducting research on three technical topics related to the atmospheric dispersion of hazardous substances: evaporation from porous and non-porous substrates, deposition and resuspension, and the dispersion of buoyant plumes in urban environments.

MODISAFE is a collaboration between FOI (Swedish Defence Research Agency, Sweden), FFI (Norwegian Defence Research Establishment, Norway), DGA (Direction générale de l'armement, France), the HSE (Health and Safety Executive, United Kingdom), INERIS (Institut national de l'environnement industriel et des risques, France) and the University of Surrey (United Kingdom).

The overall objective of the project is to improve understanding of the characteristics of sources, loss processes and the fate of agents. In each research area, new experimental data has been produced and will be made available to the public.

Research on deposition and resuspension aims to improve understanding of the fate of biological aerosols or radioactive particles dispersed in an urban environment. A preliminary study on particle deposition on horizontal and vertical building surfaces was conducted in the HSE dust wind tunnel in Buxton, UK. This study focused on developing methodologies and evaluating sampling methods.

The final area of research aims to improve understanding of the transport of positively and negatively buoyant gases in an urban environment. This study was carried out in the EnFlo wind tunnel at the University of Surrey in the United Kingdom, using a scale model of a 2 km² area of Oslo city centre. It is a continuation of the work carried out as part of the MODITIC (Modelling the dispersion of toxic industrial chemicals in urban environments) project.

The experimental results have deepened our understanding of the underlying physical processes and improved modelling capabilities. In particular, they have contributed to the development of computational fluid dynamics (CFD) models and provided a basis for model comparison and validation exercises.

Finally, the amount of substance that evaporates from a surface depends on the absorption properties of that surface. An experimental programme to study the evaporation of poll and droplets deposited on substrates with varying degrees of porosity was conducted in the INERIS fire gallery in Verneuil-en-Halatte, France.

This document is the report on this test campaign. The objective of this campaign was to measure the evaporation rate of a liquid in the form of:

- a 1 m² pool poured onto a glass plate (non-porous substrate) or a concrete plate (porous substrate) more or less saturated with liquid,
- droplets deposited on the same substrates.

The different liquids tested were as follows:

- Acetone,
- n-heptane,
- n-octane,
- TEP.

Two concrete porosities were tested, as well as two wind velocities. Similarly, several quantities of spilled liquid were tested.

1.2 Contractual elements

This service follows:

- our offer, referenced Ineris - 229431 - 2796169 - v1.0, sent on the 21st of May 2024;
- your order, received on the 2nd of July 2024.

2 Experimental setup

2.1 Facilities

The tests were carried out on the Ineris fire platform, specifically in the fire gallery.

Figure 1 shows a photo of the fire platform with the gallery in the foreground.



Figure 1: Ineris fire platform

The gallery has internal dimensions of 50 x 3 x 3.75 m^3. A detailed plan is presented in Figure 2 .

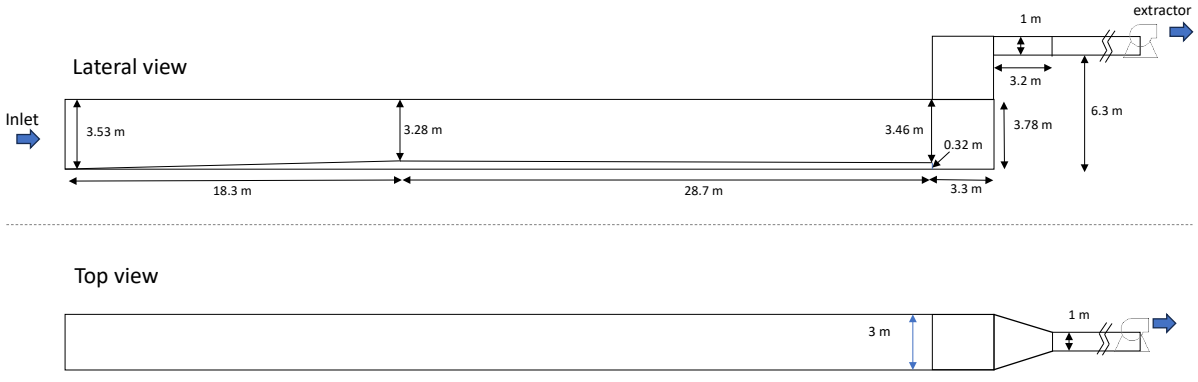


Figure 2: Plan of the gallery

The floor of the gallery slopes slightly. There is a 0.32 m step at the end of the gallery. A cross-section of the gallery is shown on the Figure 3 . The dimensions are internal dimensions. The wall thickness is 26 cm. The cross-sectional area of the gallery is close to 10 m².

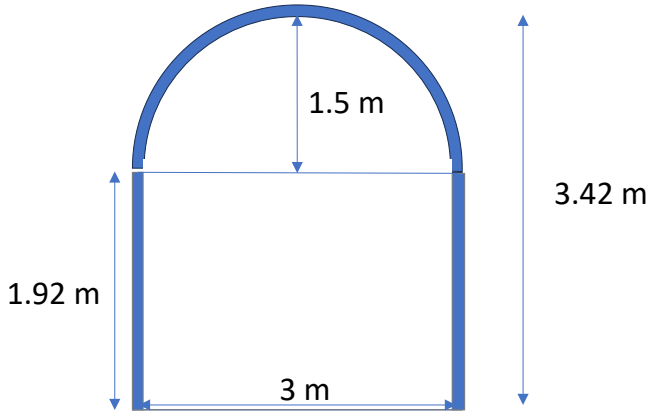


Figure 3: Cross-section of the gallery

The gallery is connected to a fan capable of extracting a maximum flow rate of 70,000 Nm³/h. The air flow then flows from the inlet to the extraction duct. The target flow velocities for the tests are 1 m/s and 2 m/s at a height of 1 m. Given that the velocity is not uniform across the gallery section, the required flow rates are 20,000 Nm³/h and 43,000 Nm³/h respectively.

Figure 4 shows the end of the gallery connected to the extraction duct via a steel chamber. The extraction duct has a diameter of 1 m.



Figure 4: End of the gallery – exterior view (left) – interior view looking upwards (right)

In order to homogenise the gases at the fire gallery outlet, steel plate deflectors (Figure 4 - right) have been installed in the funnel-shaped chamber.

2.2 Test bench

The test bench consists of two distinct areas:

- An area for generating turbulence,
- A wooden platform on which the substrate is installed.

2.2.1 Description

2.2.1.1 Generation of turbulence

Turbulence is generated using 60 cm square cardboard blocks placed upstream of the substrate.

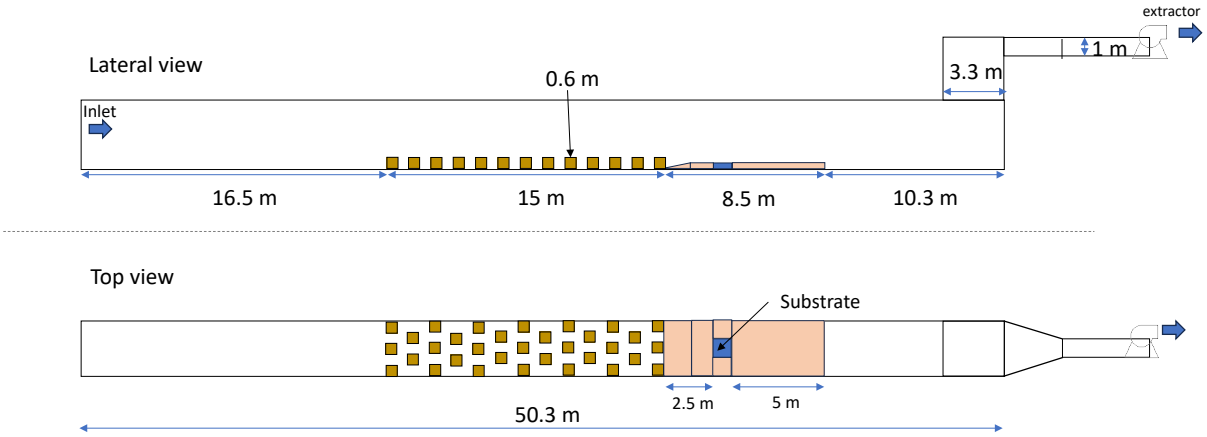


Figure 5: Arrangement of cardboard blocks to generate turbulence

Thirteen rows of cardboard boxes (Figure 6) are arranged in a staggered pattern 16.5 metres from the inlet of the gallery over 15 metres. The boxes are spaced 60 cm apart. The last boxes are attached to the platform.

The cardboard blocks are shown in Figure 6 .



Figure 6 : Photos of the cardboard blocks

The method used to measure turbulence is described in the chapter 4.

2.2.1.2 The platform

The platform is positioned 31.5 m from the inlet. It is 8.5 m long and has a 1.25 m long ramp. Its height is 0.27 m. The Figure 7 shows its precise dimensions.

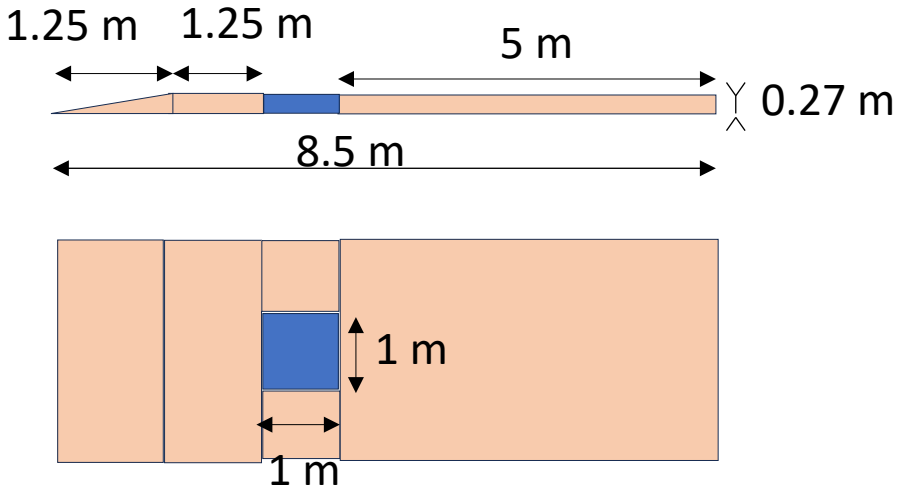


Figure 7: Representation of the platform

The platform is attached to the side walls. Figure 8 presents the platform. The photo is taken in the direction of flow.



Figure 8: Photo of the platform

2.2.2 Substrates

2.2.2.1 General description

The substrate onto which the liquid was poured or the droplets were deposited measures 1 x 1 m². It is placed 2.5 m from the upstream edge of the platform and 1 m from the side edges. Six different substrates were used in this test campaign:

- A non-porous substrate. This is a 6 mm thick glass plate positioned in a steel tray with 10 mm edges (Figure 9). The edges are sealed with aluminium adhesive tape.



Figure 9: Glass plate

- Porous substrates: these are five 60 mm thick concrete blocks surrounded by a metal frame:
    - 3 identical blocks a1, a2, a3 with porosity p1, for which the frame is raised 20 mm above the block. Block a2 was initially used untreated and then painted ;
    - 1 block b with porosity p1, for which the frame is raised 40 mm above the block;
    - A block c with porosity p2 greater than p1, for which the frame is raised 20 mm above the block.

Figure 10 shows an example of concrete blocks used in the tests.

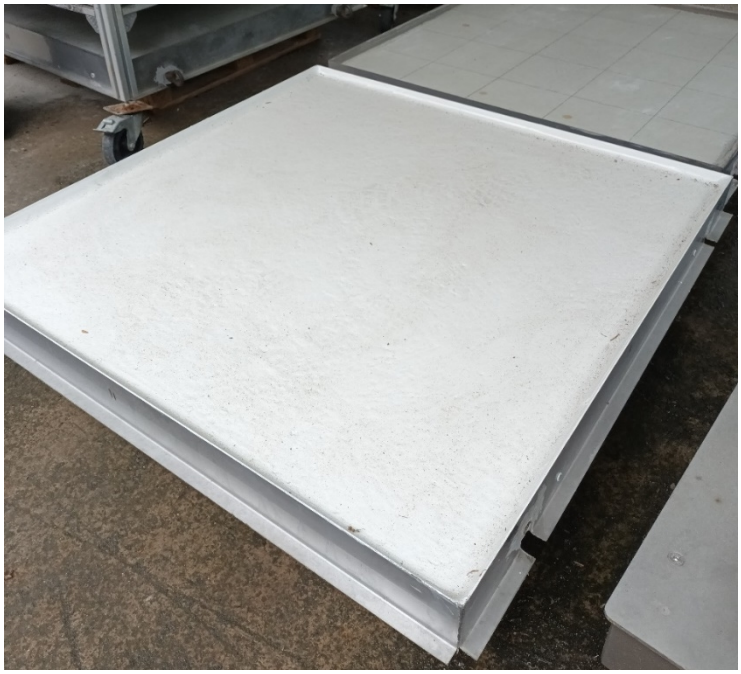


Figure 10: Concrete block

Figure 10 shows the edges of blocks a1, a2, a3 and c on the left and the larger edge of block b on the right.



Figure 11: Edges of blocks a1, a2, a3 and c (left) – edge of block b (right)

The substrate with its frame for concrete blocks or with its steel tray for glass is placed in the centre of the wooden platform on a 300 kg scale.

In order to limit liquid leakage under the plate, a vinyl ester resin-based sealant was applied between the frame and the concrete block or between the tray and the glass plate to make the interface as airtight as possible. It should be noted that during some tests, partial dissolution of the resin was observed due to the corrosive nature of the products tested (n-heptane and especially acetone), which led to product leakage under the glass or concrete plate.

The concrete blocks were insulated underneath and on the sides with 20 mm thick uncoated rock wool with a thermal resistance of 0.55 m².K/W.

The paint used for block a2 is highly resistant to grease and oil, acids, thinners, and alkaline and saline solutions. Its characteristics are presented at APPENDIX 3.

2.2.2.2 Details on the manufacture of concrete blocks

The concrete blocks were cast at Ineris. Five formworks were constructed in advance with reinforcement to prevent any cracks from appearing when handling the blocks (Figure 12).



Figure 12: Reinforcement of the blocks

Four anchor rings were cast into the concrete for handling the blocks. Blocks a1, a2, a3 and b were cast directly with the raw concrete coming out of the concrete mixer truck.



Figure 13: Concrete mixer truck

For block c, an additional operation was carried out to increase its porosity. Approximately 3 litres of water per 50 litres of concrete were added to a concrete mixer (Figure 14) and then mixed, corresponding to adding 60 litres to 1 m³ of concrete.



Figure 14: Concrete mixer

Details of the concrete quality for the two porosities are presented in Table 1.

Substrate name	a1, a2, a3, b	c	Unit
Porosity	P1	P2	
Granulat (4 types différents)	635	635	kg/m3
	165	165	
	520	520	
	415	415	
cement	396	396	
water	122	182	
Adjuvant	1.72	1.72	
	0.79	0.79	
total	2255.51	2315.51	
w/c	0.31	0.46	

Table 1: Concrete quality for the two porosities

The water-to-cement ratio was increased by 15% according to theory. The resulting porosities are presented in the section 2.2.2.3 .

2.2.2.3 Thermomechanical characteristics of substrates

The characteristics of the substrates are presented in the Table 2.

These data were measured by INERIS or taken from the literature. The data highlighted in grey are taken from the literature, as the relevant measurements could not be completed.

APPENDIX 1 describes the different characteristics of concrete and the associated measurement methods used to determine them, in particular effective porosity, density, roughness length, surface energy and contact angle. APPENDIX 2 provides some characteristics of glass.

The surface area of droplets cannot be measured on concrete because the liquid is immediately absorbed by the substrate.

Characteristics	unit	a1, a2 (no painted), a3, b	a2 painted	c	glass	Rererence
Mass (dry)	kg	144.60	144.60	141.90	13.89	Measured by Ineris
Volume	m3	0.06	0.06	0.06	0.0058	Measured by Ineris
Density (dry)	kg/m3	2312.00	2312.00	2178.00	2500.00	Annex 1 for concrete and Annex 2 for glass
W/C ratio	-	0.31	0.31	Not well established	Not applicable	Given by the concrete supplier
Effective porosity	%	8.76	8.76	11.89	0.00	Annex 1 for concrete
Heat capacity (dry)	J/kg/K	800 - 1000	800 - 1000	800 - 1000	858	Given by littérature for concrete - Annex 2 for glass
Dry thermal conductivity	W/m/K	0.6 to 3.3	0.6 to 3.3	0.6 to 3.3	0.937	Given by littérature for concrete - Annex 2 for glass
Surface roughness	nm	5793	Not measured	4774	16	Annex 1 for concrete [6] for glass
Contact angle (Diiodomethane)	°	22	Not measured	19	Not determined	Annex 1 for concrete
Contact angle (Formamide)	°	18	Not measured	15	Not determined	Annex 1 for concrete
Contact angle (Water)	°	11	Not measured	11	12	Annex 1 for concrete [5] for glass
Total Surface Energy	mN/m	53	Not measured	54	Not determined	Annex 1 for concrete
Average Pore diameter	µm	0.03	0.03	0.03	Not applicable	Annex 1 for concrete
n-octane droplet surface	mm	absorbed	absorbed	absorbed	10	Measured by Ineris
TEP droplet surface	mm	absorbed	absorbed	absorbed	6	Measured by Ineris
n-heptane droplet surface	mm	absorbed	absorbed	absorbed	10.5	Measured by Ineris

Table 2: Thermomechanical characteristics of substrates

2.2.3 The liquids tested

The four liquids tested as part of this trial campaign are:

- Acetone,
- n-heptane,
- n-octane,
- TEP.

These liquids were chosen for the following reasons:

- These four products are low in toxicity, meaning they can be handled safely provided basic safety rules are followed (wearing a mask, no sources of ignition, etc.) ;
- This list covers a wide range of saturated vapour pressures at room temperature (10°C), from 15,423 Pa for acetone to 15.4 Pa for TEP, i.e. a factor of 1,000 ;
- Acetone and n-heptane are sufficiently volatile to be detected in the gallery by FTIR, a measuring device described in the paragraph 2.2.4.3.1;
- n-octane is difficult to detect by FTIR but can be detected by PID, a device also described in the paragraph 2.2.4.3.1;
- TEP is less volatile than the other products, but as it contains a phosphorus atom, it can be detected at very low concentrations by the AP4C measuring device, also described in the paragraph 2.2.4.3.1 .

The main characteristics of these products are presented in the Table 3 .

		unit	Product			
			Acetone	n-heptane	n-octane	TEP
Characteristics	molar mass	g/mol	58.08	100.204	114.231	182.156
	Boiling point	K	329.44	371.58	398.83	484.15
	Critical temperature	K	508.2	540.2	568.7	750
	Critical Pressure	Pa	4701004	2740000	2490001	4600003
	Vapour pressure (283 K)	Pa	15423	2713	754	15.4
	Liquide density (283 K)	kg/m3	803.6	694.2	711.0	1081.4

Table 3: Main characteristics of products (DIPPR database)

The concentration of the products is presented in the following table.

Product	Purity (%)
Acetone	99%
n-heptane	95%
n-octane	95%
TEP	99%

Figure 15 shows the saturated vapour pressures of liquids as a function of temperature.

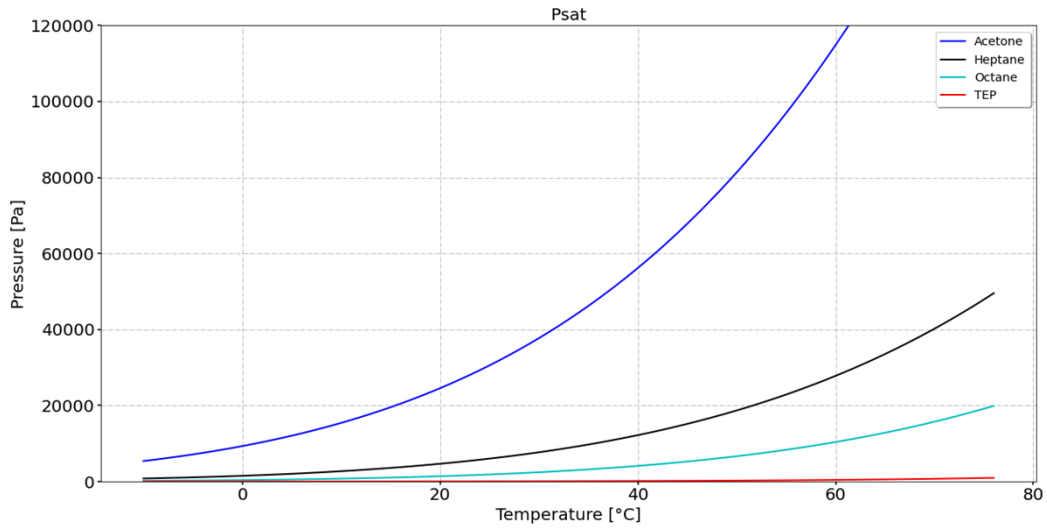


Figure 15: Saturation vapour pressure of tested liquids

The equation used is formula No. 101 from the DIPPR database [1] with the coefficients presented in Table 4 .

Product	DIPPR equation n°101				
	A	B	C	D	E
Acetone	69.006	-5599.6	-7.0985	6.22E-06	2
n-heptane	87.829	-6996.4	-9.8802	7.21E-06	2
n-octane	96.084	-7900.2	-11.003	7.18E-06	2
TEP	51.99	-7457.3	-4.0571	8.96E-19	6

Table 4: DIPPR coefficients for the saturated vapour pressure of products

Figure 16 shows the latent heat of saturated vaporisation of liquids as a function of temperature.

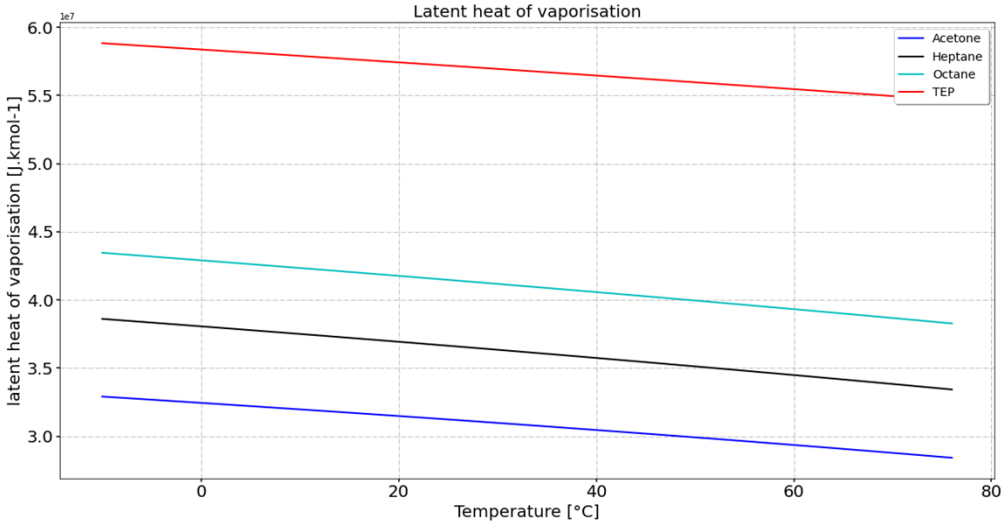


Figure 16: Latent heat of vaporisation

The equation used is formula No. 106 from the DIPPR database [1] with the coefficients presented in Table 5 .

Product	DIPPR equation n°106				
	A	B	C	D	E
Acetone	42150000	0.3397	0	0	0
n-heptane	50014000	0.38795	0	0	0
n-octane	55180000	0.38467	0	0	0
TEP	69335000	0.38022	-0.00042768	2.24E-04	0

Table 5: DIPPR coefficients for latent heat of vaporisation

2.2.4 Measurements and instrumentation

2.2.4.1 Measurements associated with pool evaporation tests

During each test, the following continuous measurements were taken:

- Wind velocity at a height of 1 metre,
- The mass of the substrate,
- 12 concentration measurement points located behind the substrate to map the vapour cloud. These measurements were not taken for TEP and n-octane because the evaporation rate was very low,
- 1 concentration measurement point located under the substrate for cases involving concrete substrates to assess the possible presence of product vapours under the substrate,
- 1 concentration measurement point in the duct for a mass balance,
- Three temperature measurement points on the substrate (in the liquid, on the skin of the upper wall of the substrate and on the skin of the lower wall). The temperature measurement points in the liquid and on the skin of the upper wall of the substrate are located more or less in the centre of the pool, depending on the tests (Figure 17). For some tests, the position of these two points is rather located towards the centre of the pool. The test videos allow the exact position of the thermocouples to be verified.
- Measurement of ambient temperature, ambiant pressure relative humidity.

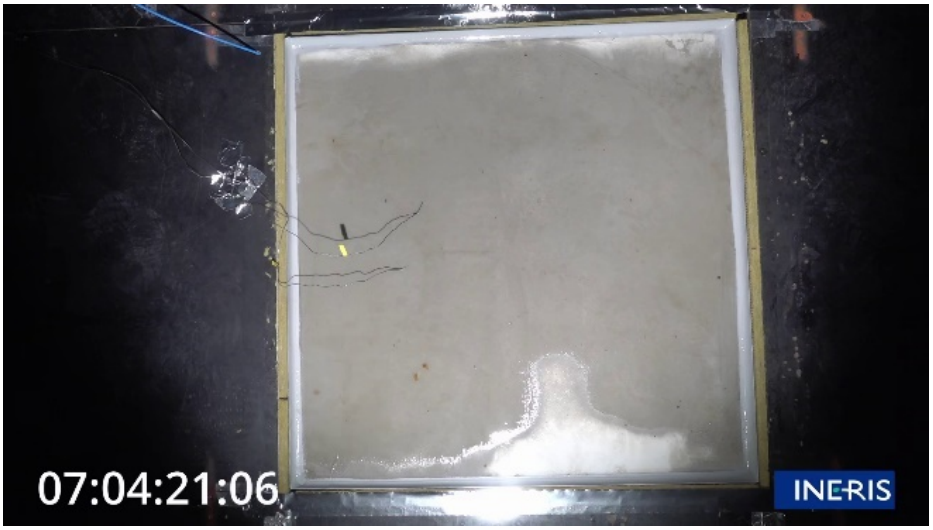


Figure 17: Position of temperature measurement points

A distinction is made between the overall concentration, which is measured in the extraction duct in an area where the gases are completely homogeneous, and the local concentration, which is measured in the near field in the vapour cloud.

The instrumentation is illustrated in the paragraph 2.2.4.3.

2.2.4.1.1 Wind velocity measurement

Measuring wind velocity at a height of 1 m (above the platform) allows turbulence to be assessed during the evaporation test. A detailed study of turbulence in the gallery was carried out during a preliminary campaign. This study is presented in the chapter 2.3.3 .

2.2.4.1.2 Measuring substrate mass

The substrate mass is measured continuously using a 300 kg balance.

2.2.4.1.3 Local vapour cloud concentration measurements

For the vapour plume tests, 12 sampling points were placed downstream of the substrate in order to map the vapour cloud. The exact position of the sampling points is shown in Figure 18.

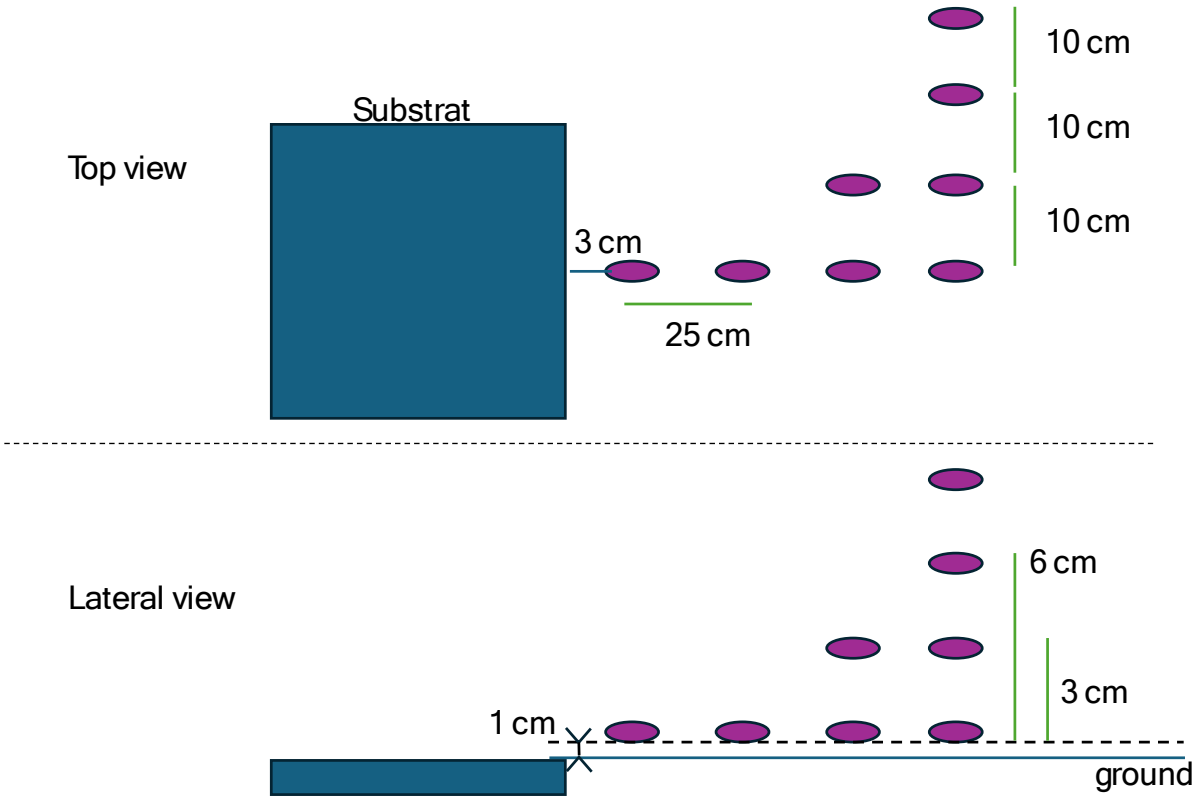


Figure 18: Position of sampling points located behind the substrate

The sampling points were small tubes connected to a pump (Figure 19), which was itself connected to the FTIR. The FTIR is described in the paragraph 2.2.4.3.1.The stiffness of the steel custom-shaped sampling tubes is sufficiently high to consider that the sampling point is at the exact location with an uncertainty of +/- 2 mm.

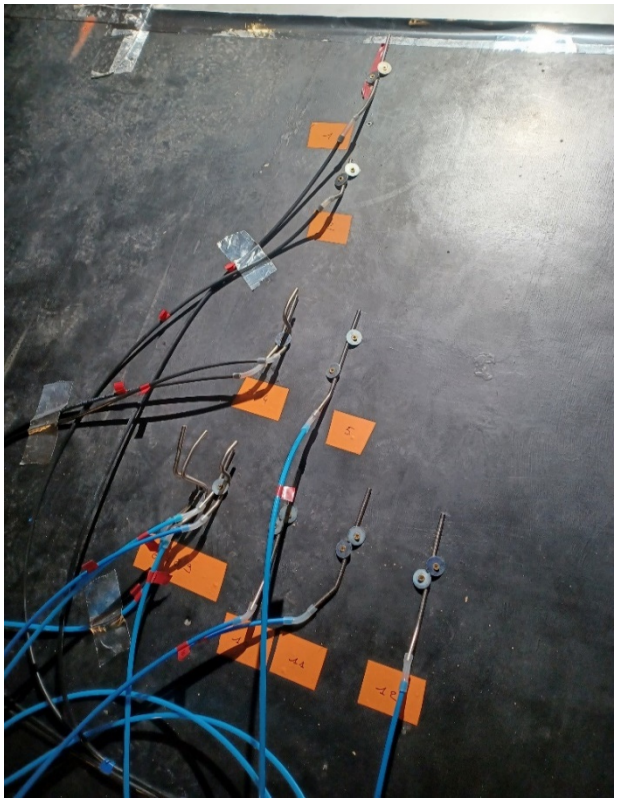


Figure 19 : Sampling system in the vapour cloud

A scanner was used to sequentially switch the measurement point for sequential concentration measurement. The sampling points are referenced in Figure 20.

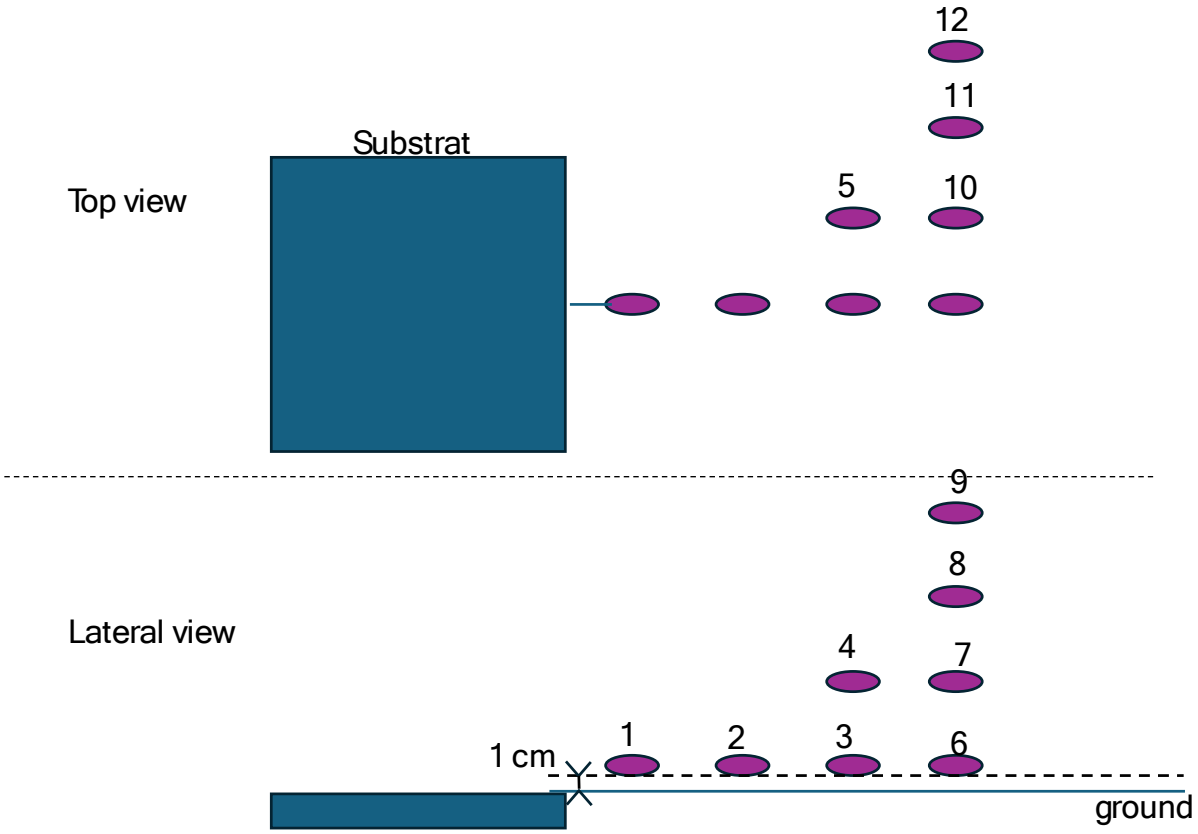


Figure 20 : Numbering of points

2.2.4.1.4 Measurement of the overall vapour concentration

Sampling points were placed in the extraction duct at the fire gallery exit (Figure 21).

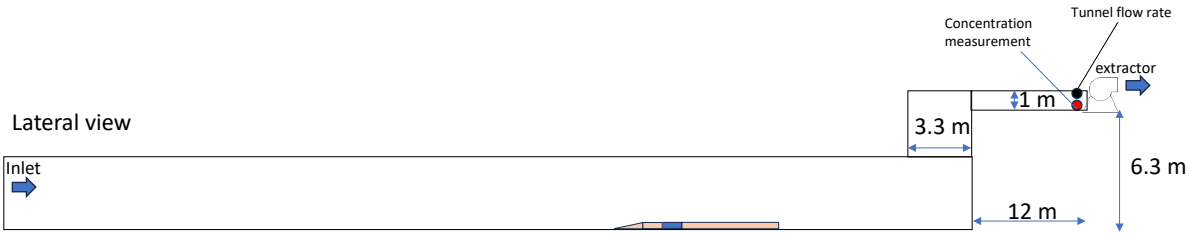


Figure 21 : Position of the sampling point in the extraction duct

Depending on the type of product studied, one or more analysers were used, namely FTIR, PID or AP4C. These devices are described in the section entitled 2.2.4.3.1.

The sampling points for these analysers were located 12 m from the end of the gallery, in the centre of the shaft.

A pressure sensor was also present to measure the velocity and therefore the flow rate in the duct (fire gallery flow rate).

The measurement uncertainty is estimated by the manufacturer at 0.25% of the pressure difference value.

2.2.4.2 Measurements associated with droplet evaporation tests

The following measurements were taken during each test:

- Wind velocity at a height of 1 m, as described in the previous paragraph,
- One concentration measurement point located downstream of the substrate at a height of 1 cm,
- In some cases, measurement of overall concentration in the duct,
- Measurement of ambient temperature and pressure and measurement of relative humidity.

The measurement systems are described in the following paragraph.

The measurement point in the duct was not always used because in some cases, particularly for droplet evaporation tests, the concentrations in the duct were too low in relation to the detection threshold of the measuring device.

2.2.4.2.1 Wind velocity measurement

The measurement system is identical to that used for pool evaporation tests.

2.2.4.2.2 Measurement of local concentration downstream of the substrate

A single point was placed downstream of the substrate, at a height of 1 cm. The exact position is shown in Figure 22.

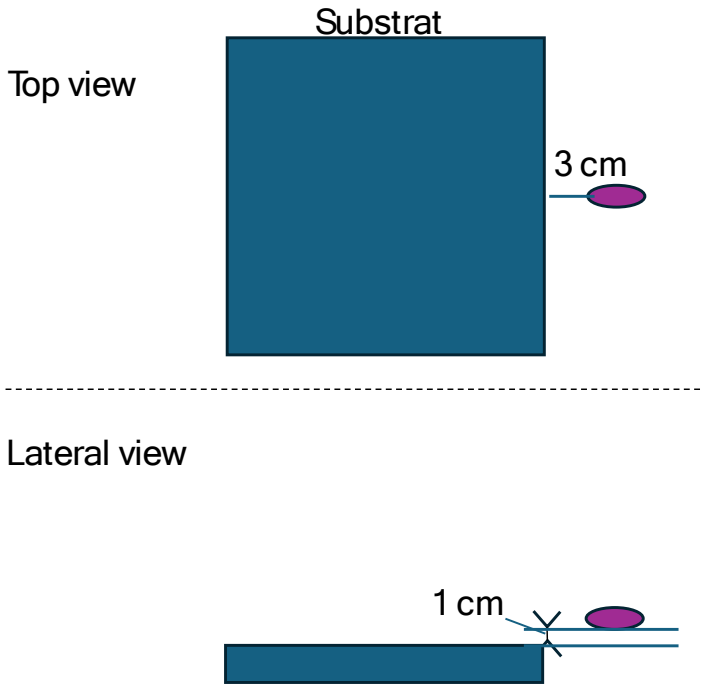


Figure 22: Position of the sampling point located at the rear of the substrate

The use of this measurement point is described in the paragraph 4.2.

Depending on the product being tested, the measuring device used is FTIR, PID or AP4C. These are described in the following paragraph.

2.2.4.3 Instrumentation

2.2.4.3.1 Product concentration measuring devices

The various measuring devices used in this campaign are:

- FTIR,
- PID
- AP4C.

The following paragraphs describe the devices.

FTIR

Fourier transform infrared spectroscopy (FTIR) is an analytical technique used to identify the molecular composition of a sample by measuring the absorption of infrared radiation by chemical bonds (Figure 23). The core of this method is based on a Michelson interferometer, which modulates broadband infrared radiation using a moving mirror, generating an interferogram. This signal, once transmitted or reflected by the sample, is captured by a detector. It contains all the spectral information in the time domain. A Fourier transform is then applied to convert this signal into an IR spectrum, expressed in frequency, where each absorption peak corresponds to a characteristic vibration of a chemical bond (stretching, bending, etc.). This technique is fast, non-destructive, and suitable for many types of samples, including the vapours studied in this study.



Figure 23: FTIR

PID

A photoionisation detector (PID) works by using an ultraviolet (UV) lamp to ionise molecules of volatile organic compounds (VOCs) or other gases present in the air. When UV photons strike these molecules, they transfer enough energy to eject an electron, creating positive ions and free electrons. These charged particles are then attracted to opposing electrodes in a detection chamber, generating an electrical current proportional to the concentration of ionisable gases. This signal is measured and converted into a concentration reading, allowing rapid detection of trace gases at low concentrations, often in ppm or ppb. The PID used in these tests is shown on Figure 24 .



Figure 24: PID

AP4C

The AP4C is a portable chemical contamination detector that uses plasma atomic emission spectrometry to quickly identify the presence of toxic substances (chemical warfare agents, industrial toxins, etc.) in the air. It draws in ambient air and heats it to a very high temperature in a dihydrogen flame, which breaks down the molecules into excited atoms.

These atoms then emit light at specific wavelengths depending on their nature (e.g. phosphorus, sulphur, arsenic, etc.). An optical system analyses this light and transcribes it into an electrical signal. The AP4C used in these tests is used solely to detect phosphorus present in PET molecules. It is presented on the Figure 25 .



Figure 25: AP4C

The detection thresholds for the various devices are shown in Table 6 .

Measuring device	Detected product	Limite of detection (ppm)
FTIR	Acetone	0.15
	n-heptane	0.15
	n-octane	0.15
	TEP	0.3
PID	Acetone	0.01
	n-heptane	0.01
	n-octane	0.01
AP4C	TEP	0.005

Table 6: Detection thresholds for concentration measurement devices

The quantification thresholds are 3.3 times higher. It should be noted that the quantification limit corresponds to a signal-to-noise ratio of 10 and the detection limit to a signal-to-noise ratio of 3.

2.2.4.3.2 Mass

The mass was measured using a 300 kg balance with a verification scale of a few dozen grams.

2.2.4.3.3 Thermocouple

The thermocouples are type K, stainless steel sheathed, class I, with a hot junction insulated from the mass, 1.5 mm in diameter and 10 m long. Class I guarantees ± 1.5°C for a measured temperature between -40°C and 375°C.

2.2.4.3.4 Camera

The camera used is a SONY FDR AX700 with a resolution of approximately 12 megapixels. It is paired with a Nanlite FS-60B LED projector to avoid any unwanted shadows on the area being filmed and to accurately monitor the evolution of the pool and droplets. It was attached to a structure above the substrate.

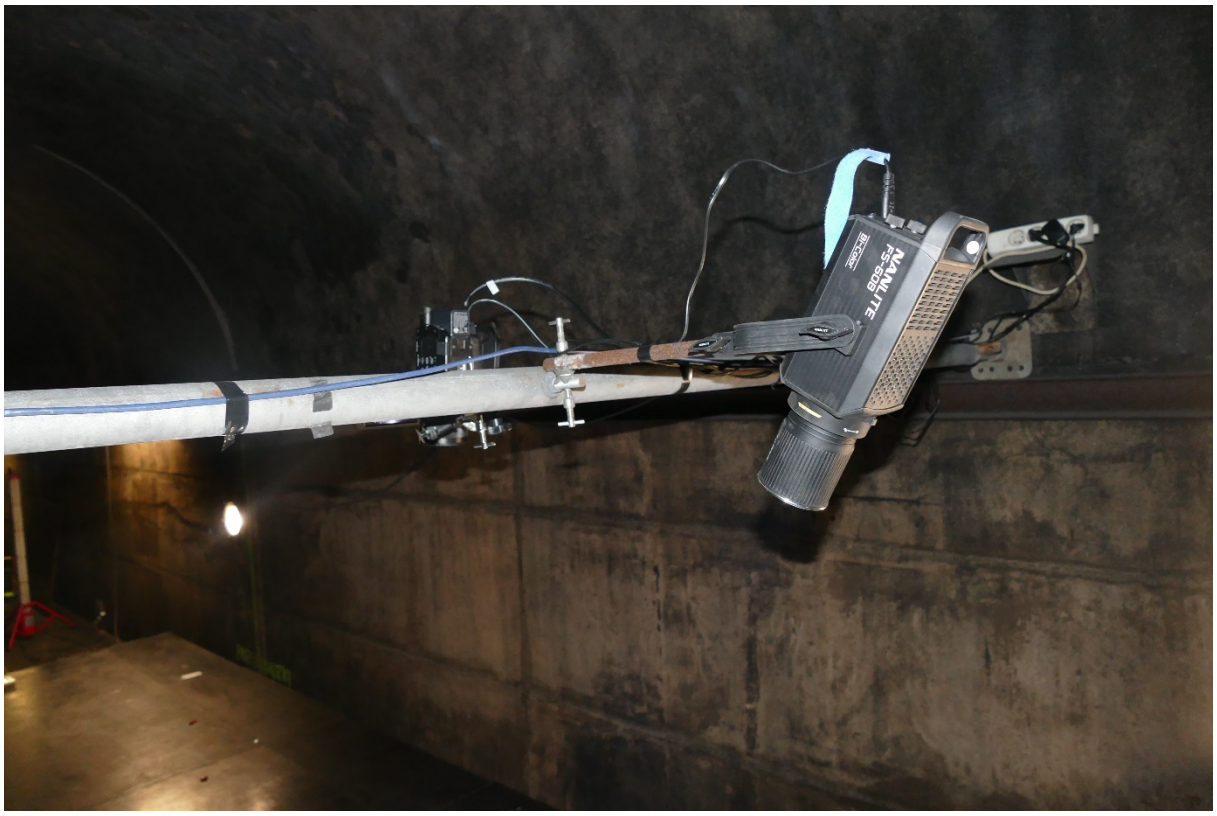


Figure 26: Camera

2.3 Test matrix

2.3.1 Matrix

The test matrix is shown in Table 7.

Week	Day	Test N°		Product	Target height (mm) = quantity (L)	Velocity at refence point (m/s)	Substrate
7	13/02	1	Pool	Heptane	5	1	glass
	14/02	2		Heptane	5	1	glass
8	17/02	3		Heptane	10	1	a1
	18/02	4		Heptane	10	1	a1
	19/02	5		Heptane	20	1	b
	20/02	6		Acetone	10	1	a2
	21/02	7		Acetone	10	2	a2
9	26/02	8		Heptane	10	1	c
	27/02	9		TEP	2	1	a3
	28/02	10		Heptane	10	1	a1
10	03/03	11		Heptane	10	2	a2 painted
	07/03	14a	Droplet	Octane (FTIR)	-	1	glass
		14b		Octane (PID)	-	1	glass
		15a		Heptane (FTIR)	-	1	glass
		15b		Heptane (PID)	-	1	glass
11	10/03	16		Octane (PID)	-	1	a3
	11/03	17		Octane (PID)	-	1	a3
	12/03	18a		Octane (FTIR)	-	1	a3
		18b		Octane (FTIR)	-	1	a3
		19a		Heptane (FTIR)	-	1	a3
		19b		Heptane (FTIR)	-	1	a3
		19c		Heptane (PID)	-	1	a3
	13/03	20	Pool	Octane	5	1	b
	14/03	21		Heptane	10	1	a2 painted
12	17/03	22		Acetone	10	1	a1
	17/03	23	Droplet	TEP	-	1	a1
	18/03	24		TEP	-	1	glass

a1, a2, a3: reference susbtrates (20 mm, porosity N°1)
b: substrate 40 mm
c: substrate 20 mm, porosity n°2

Table 7: Test matrix

The heights targeted for the groundwater evaporation tests presented in the Table 7 are those decided upon when the protocol was implemented. Some of the heights have been revised downwards. The chapter 5 presents the actual heights used.

2.3.2 Reference test – Test N°1

The selection of the reference test was based on the need to define a simple, well-controlled, and reproducible configuration that could serve as a baseline for comparison across all parametric studies. The chosen configuration, consisting of a 1 m² pool of n-heptane with a height of 5 mm spread over a non-porous glass substrate, was intended to eliminate any interaction between the liquid and the supporting surface. This choice ensures that the observed phenomena are primarily governed by evaporation and mass transfer mechanisms at the liquid–air interface, without the influence of absorption or retention processes within the substrate.

The product n-heptane was selected due to its well-documented physicochemical properties and its intermediate volatility, making it a commonly used reference compound in evaporation studies. The 1 m² surface area and the 5 mm pool depth provide a sufficient liquid thickness to limit rapid depletion effects while remaining representative of realistic experimental scenarios.

The wind speed in the test chamber was set to 1 m/s at the reference height, corresponding to a moderate flow regime that ensures adequate air renewal above the liquid pool without inducing excessive aerodynamic disturbances.

Based on this reference case, additional experiments were conducted by varying a single parameter at a time—namely substrate porosity, liquid volume (1, 10, and 20 L), chemical nature of the product (less volatile and more volatile compounds), and wind speed (2 m/s)—in order to isolate and accurately assess the influence of each parameter on the evaporation kinetics.

2.3.3 Summary of instrumentation

2.3.3.1 Pool evaporation tests

Figure 27 summarises the various measurements taken during the pool evaporation tests.

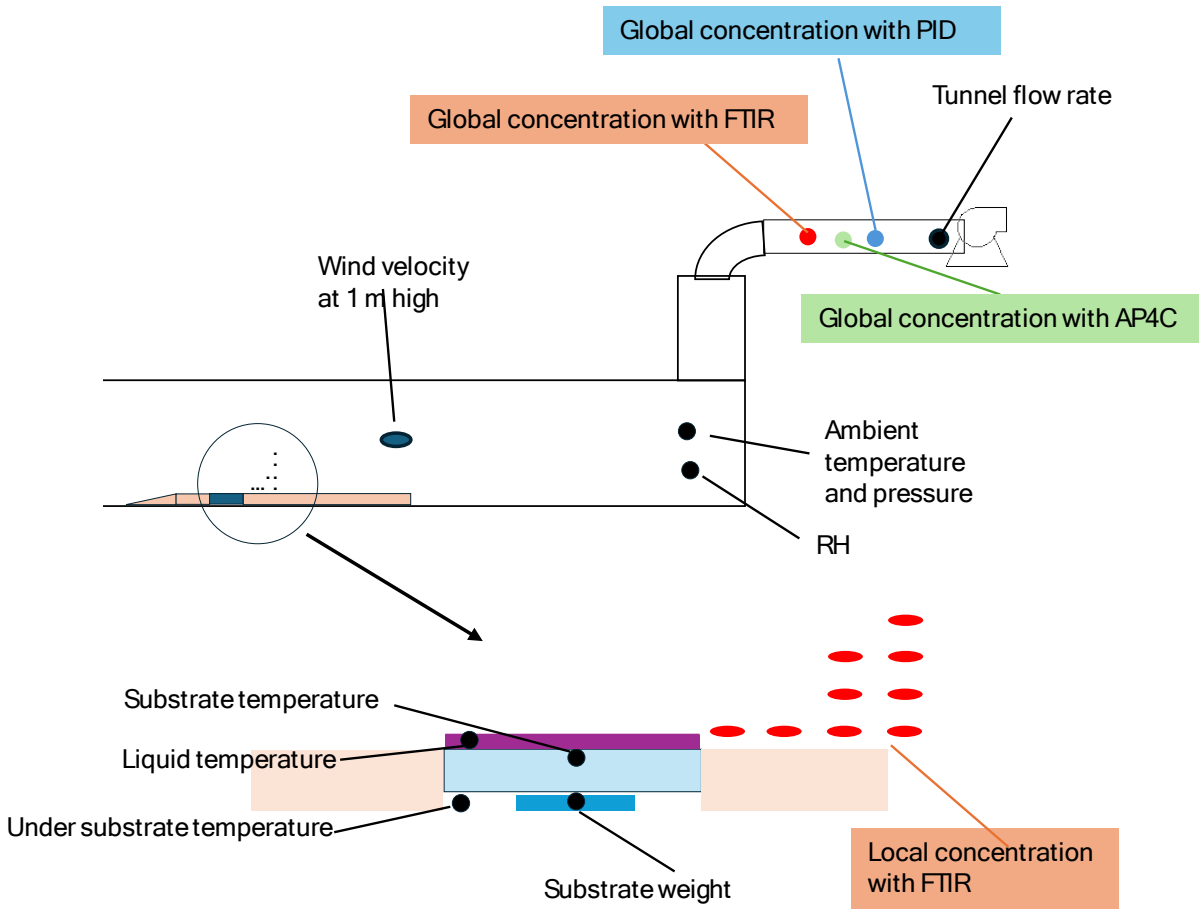


Figure 27: Instrumentation pour les essais d'évaporation de nappe

For overall concentration, the devices used are presented in Table 7.

Test	Device
01/02	FTIR
03/04/05/06/07/08/10/11/21/22	FTIR/PID
09	AP4C
20	PID

Table 8: Apparatus used for soil vapour testing

For local concentration, a second FTIR is used with a scanner.

2.3.3.2 Droplet evaporation tests

Figure 28 summarises the various measurements taken during the droplet evaporation tests.

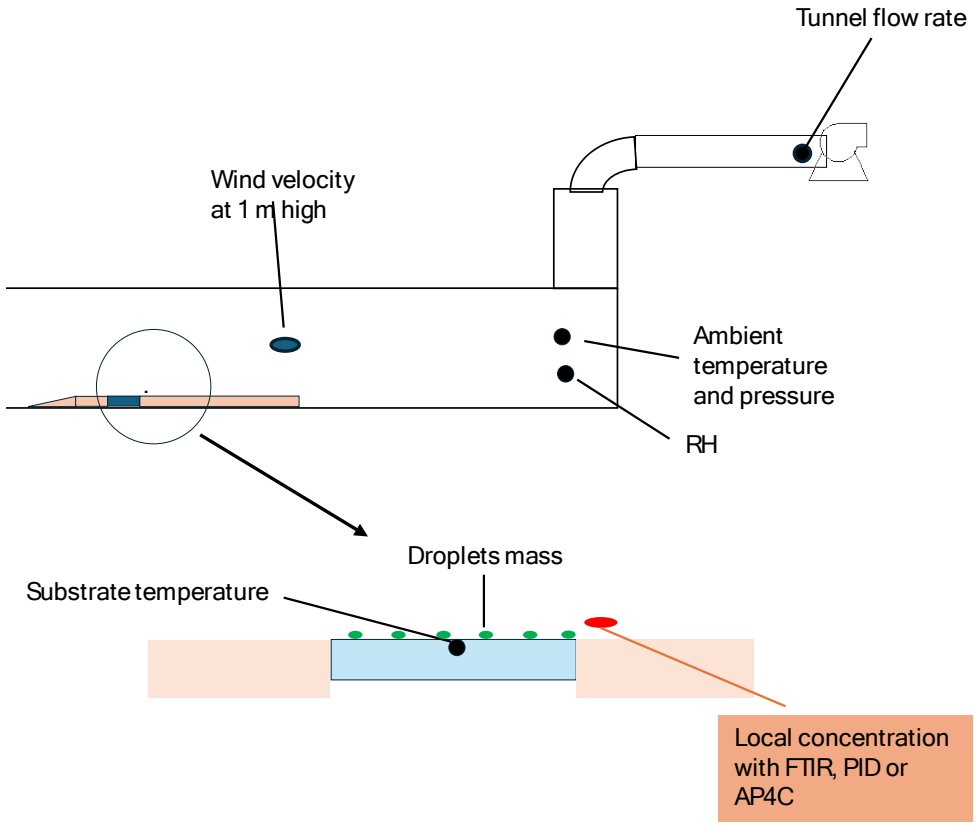


Figure 28: Instrumentation for droplet evaporation tests

For local concentration, the devices used are shown in Table 8.

Test	Device
14a, 15a, 18a, 18b, 19a, 19b	FTIR
14b, 15b, 16, 17, 19c	PID
23, 24	AP4C

Table 9: Apparatus used for droplet evaporation tests

3 Atmospheric boundary layer analysis

3.1 Scale

The scale of the gallery is approximately 1/10. Studying a 1 square meter pool is therefore equivalent to studying a 10 square meter pool. The scale factor, referred to as s, is equal to 10.

3.2 Law of similarity

In order to carry out tests under conditions representative of a scale of 1:1, the dimensionless number retained in our case is the Froude number, which is written as:

$$Fr = \frac{U}{\sqrt{gL}} \qquad \textit{Equation 1}$$

With

U : velocity (m/s)

g : gravitational acceleration (m²/s)

L : characteristic length (m)

Conservation of the Froude number implies:

$$Fr_{reel} = Fr_{galerie} \qquad \text{Equation 2}$$

Or

$$\frac{U_{reel}}{\sqrt{gL_{reel}}} = \frac{U_{galerie}}{\sqrt{gL_{galerie}}} \qquad \text{Equation 3}$$

Or $L_{reel} = 10L_{galerie}$

So we obtain :

$$\frac{U_{reel}}{\sqrt{g10L_{galerie}}} = \frac{U_{galerie}}{\sqrt{gL_{galerie}}} \qquad \text{Equation 4}$$

$$\frac{U_{reel}}{U_{galerie}} = \sqrt{10} \qquad \text{Equation 5}$$

The Table 10 shows the different scale factors that result from the conservation of the Froude number for the different characteristic quantities of atmospheric turbulence:

Greatness	Ratio	Scale factor
Length	$\frac{L_{reel}}{L_{galerie}}$	s = 10
Velocity	$\frac{U_{reel}}{U_{galerie}}$	$\sqrt{s} = \sqrt{10}$
Kinetic energy of turbulence	$\frac{k_{reel}}{k_{galerie}} = \frac{U_{reel}^2}{U_{galerie}^2}$	s = 10

Table 10: Scale factors

3.3 Calculation of wind and turbulence profile at scale 1

We are seeking to reproduce a stable wind profile between stable and neutral conditions for a velocity of approximately 3.16 m/s at an altitude of 10 m. The velocity of 3.16 m/s was chosen to obtain a velocity of 1 m/s at a height of 1 m at the gallery scale. The roughness length is 0.183 m, representative of the roughness of ground in an industrial area according to the INERIS Omega 12 reference document [2].

The methodology used to define wind and turbulence profiles is taken from Appendix 1 of the Guide to Good Practice for 3D Modelling of Atmospheric Dispersion Scenarios in Accident Situations [3].

The curves obtained by applying this methodology with the previously established assumptions are presented in Figure 29.

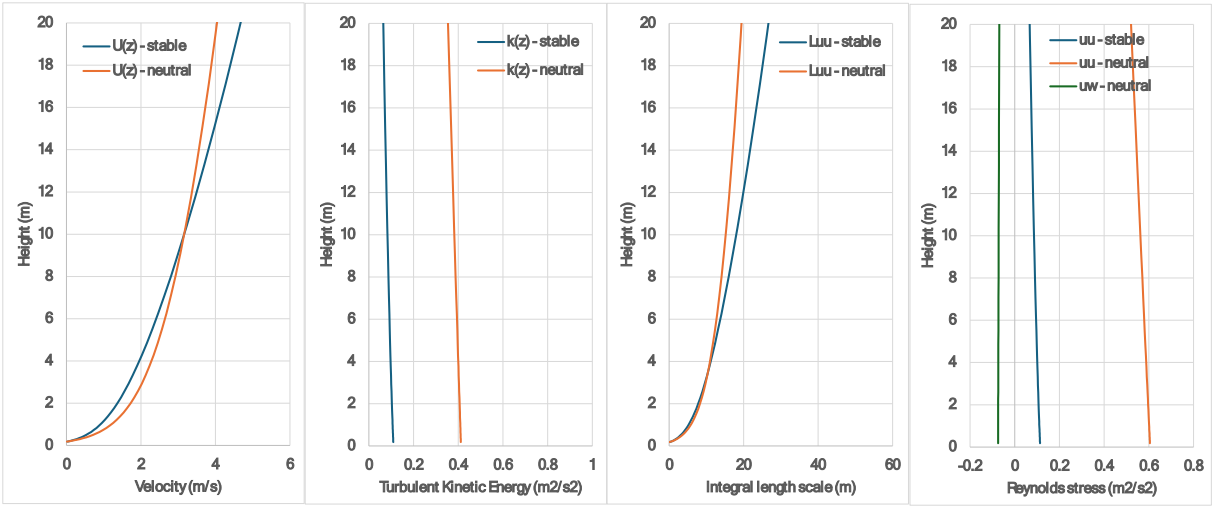


Figure 29: Theoretical wind and turbulence profiles at a scale of 1:1

3.4 Measurement of wind velocity and turbulence profiles in the gallery

3.4.1 Generation of turbulence

Turbulence is generated using 60 cm square cardboard blocks placed upstream of the wooden platform on which the substrate is positioned.

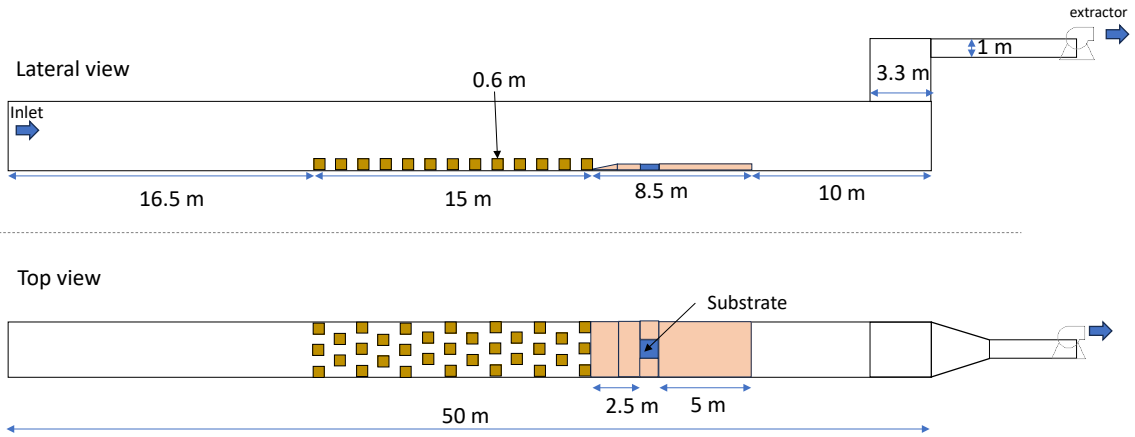


Figure 30 : Arrangement of blocks used to generate turbulence

Thirteen rows of cardboard boxes are arranged 16.5 m from the fire gallery entrance over a distance of 15 m. The boxes are spaced 60 cm apart. They are attached to the platform.

3.4.2 Instrumentation

The instrumentation used consists of McCaffrey probes and an ultrasonic anemometer. Both sensors are shown in Figure 31.



Figure 31: McCaffrey probe on the left and ultrasonic anemometer on the right.

The McCaffrey probe is a device used to measure the velocity of a gas flow. It consists of a vertical tube open at both ends, placed in the centre of the air flow, with a side port connected to a differential pressure sensor. The principle is based on measuring the dynamic pressure induced by the upward air flow, compared to the pressure inside the tube, which allows the longitudinal velocity to be deduced from Bernoulli's equation. This simple and robust method requires experimental calibration to be accurate. The probe is connected to a pressure sensor, which is itself connected to a data acquisition unit. The pressure sensor's acquisition frequency is 50 Hz. The disadvantage of this sensor is its unidirectional nature, which means it can only measure the axial component of velocity.

The ultrasonic anemometer measures wind velocity and direction using the transit time of ultrasonic waves between several sensors arranged in 3D. The principle is based on the difference in time it takes for sound waves to travel the same distance depending on whether they propagate in the direction of the wind or against the wind. By comparing these transit times between each pair of transmitters and receivers, the device calculates the components of wind velocity. The anemometer is directly connected to an acquisition unit with an acquisition frequency set at 50 Hz to be in phase with the McCaffrey probe.

Two probes are used for each measurement. A first reference probe is placed at point A and a second probe is moved to each measurement point. The measurement time at each point is maintained for 3 minutes.

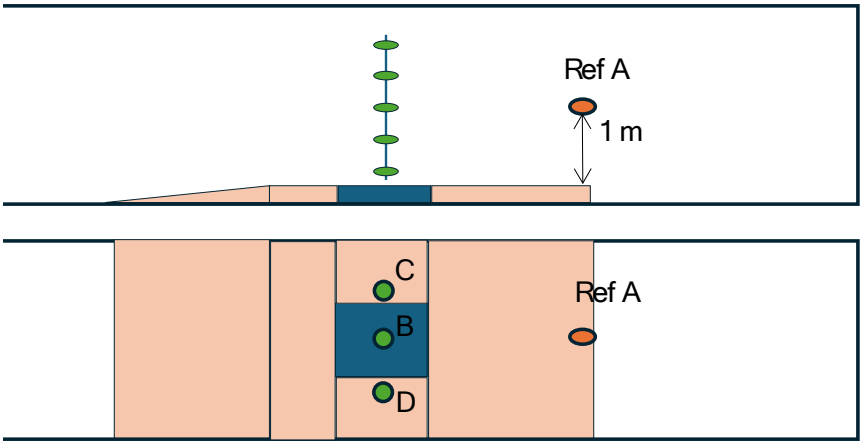


Figure 32 : Probe positions

The different positions and heights of the measurement points are summarised in Table 11 .

Technology	McCafrey				Ultrasonic
Aquisition frequency (Hz)	50				50
Position	A	B	C	D	B
Sensor height (cm)	-	2	-	-	-
	-	5	-	5	-
	-	10	-	10	-
	-	20	-	20	-
					25
	-	30	-	30	
	-	50	-	50	50
	-	75	-	75	75
	100	100	100	100	100
	-	125	-	125	-
	-	150	-	150	150

Table 11: Probe positions

The velocity measurements were repeated several times, particularly at point B, to ensure their repeatability.

As the velocity measurements at each height were not taken at the same time, the reference velocity varied from one test to another because atmospheric conditions changed over time. In order to bring all the information to the same level and compare comparable values, the velocity values measured at each height were corrected using the reference velocity. The specific methodology adapted to the Ineris facility is as follows:

At each stage, the velocity was measured for 3 minutes at two points:

- Reference velocity at 1 m ($U_{ref}(t)$),
- Velocity at height h ($U(h,t)$

Then we moved the velocity measurement to a higher position while keeping the measurement at reference point A.



At the end of the measurement campaign, each velocity value at height h was corrected using the following formula:

$$U_{corr}(h,t) = U(h,t)\left(\frac{\overline{U_{ref}}}{\overline{U_{ref}^{h}}}\right) \quad \text{Equation 6}$$

Where:

$U(h,t)$	Gross velocity as a function of time measured by the main sensor at height h	m/s
$\overline{U_{ref}^{h}}$	Average reference velocity measured when the main sensor is positioned at height h	m/s
$\overline{U_{ref}}$	Average of the averages of the reference velocities calculated when all measurements were taken at the same column.	m/s

This equation allows for the correction of discrepancies obtained when the average velocity deviates slightly due to changes in atmospheric conditions between different altitudes. Note that the velocities $\overline{U_{ref}(h)}$ and $\overline{U_{ref}}$ deviate slightly and remain close to 1 m/s ($\overline{U_{ref}(h)}$ is between 0.8 and 1.2). It is assumed that atmospheric conditions remain stable during the 3 minutes of measurement.

This methodology assumes that the scaling is independent of the distance between column B and point A, and the time the wind takes to travel this distance.

3.4.3 Results

The quantities measured or deduced from the measurements are as follows:

- The average velocity in the main direction,
- The three components u'u', w'w' and u'w' of the Reynolds tensor,
- The integral length in the main direction,
- The kinetic energy of turbulence,
- The friction velocity,
- Simulated ground roughness length.

In the atmospheric boundary layer, turbulent motions are described statistically using the Reynolds tensor, which represents the correlations between the velocity fluctuations of the different wind components. This tensor, generally denoted by $\overline{u_i' u_j'}$, is an average of the products of the velocity fluctuations u_i' and u_j' in the i and j directions. It is essential for describing the turbulent transport of momentum. In the case of atmospheric flow near the ground, it is mainly the component $\overline{u'w'}$ correlating the horizontal fluctuation u' and vertical fluctuation w' that dominates, as it reflects the turbulent shear responsible for exchanges between the surface and the atmosphere. This component is directly related to the friction velocity u*, a key quantity in meteorology and atmospheric dynamics, defined by:

$$u^* = \sqrt{-\overline{u'w'}} \quad \text{Equation 7}$$

Friction velocity represents the intensity of momentum transfer between the ground and the air, and plays a central role in the logarithmic wind velocity profile in the boundary layer.

The kinetic energy of turbulence is expressed as follows:

$$k = \frac{1}{2}\left(\overline{u'u'} + \overline{v'v'} + \overline{w'w'}\right) \quad \text{Equation 8}$$

In our case, turbulent kinetic energy is mainly governed by longitudinal fluctuations, i.e. by the term u'u', as its value is greater than the other two terms by a factor of 3 to 10 according to MODITIC campaign [9]. In an acceptable approach, TKE is calculated solely with the u'u' component.

3.4.3.1 Measured quantities

The main measured or deduced quantities are shown in the following figures. The scaling factors detailed above were applied for theoretical atmospheric conditions, namely $\frac{1}{10}$ for distances and kinetic energies and $\frac{1}{\sqrt{10}}$ for velocities. The ultrasonic probe has been used only for the test n°07.

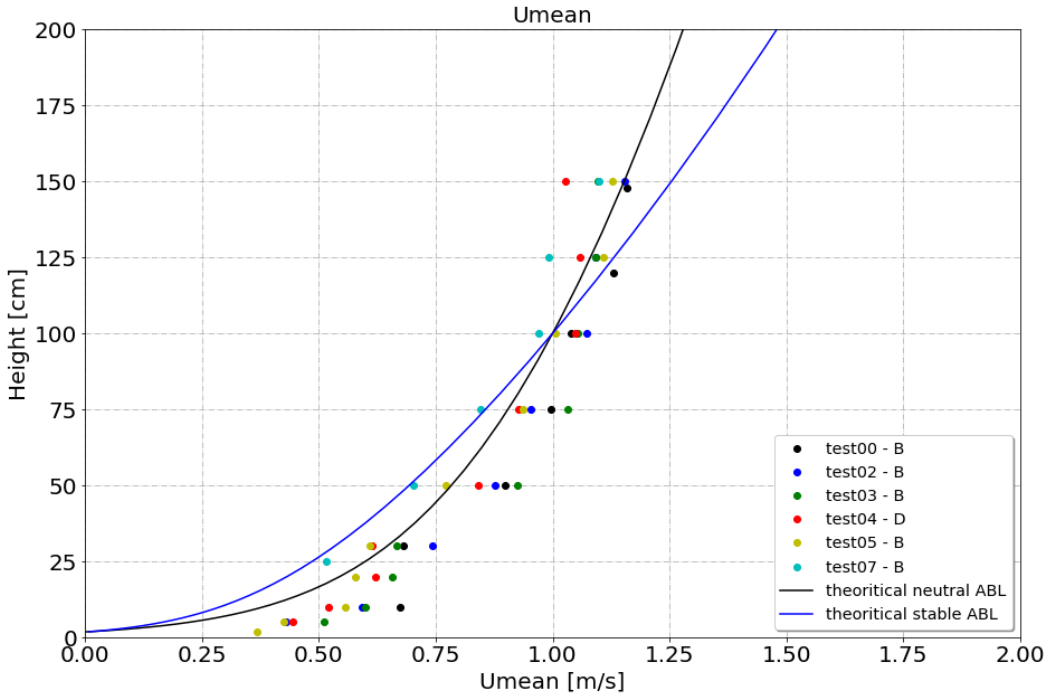


Figure 33: Mean velocity profile

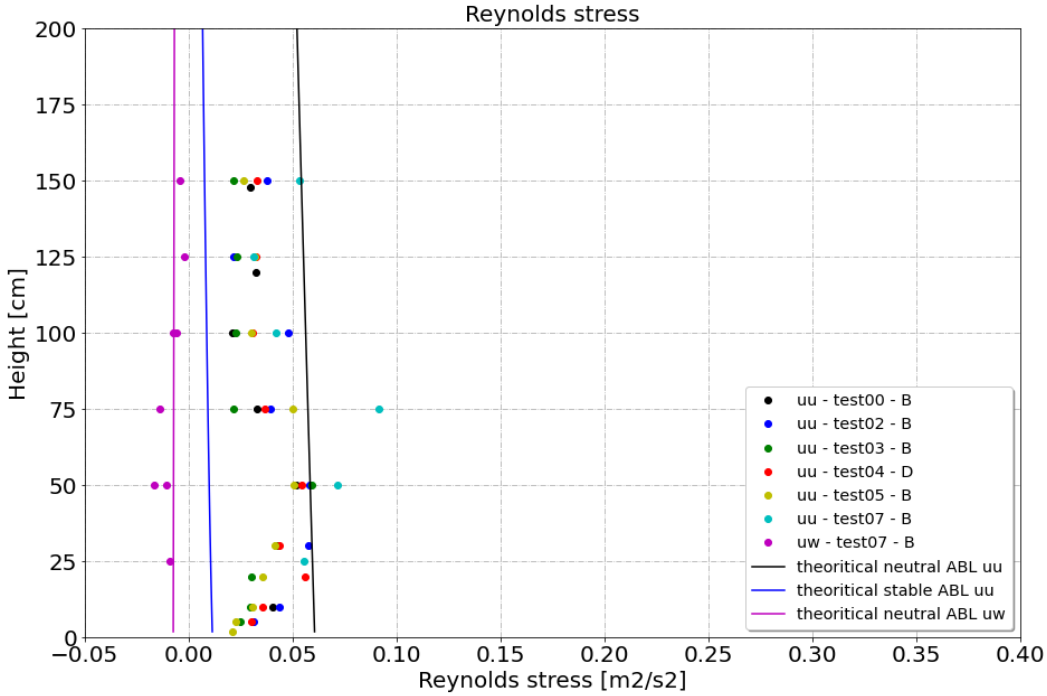


Figure 34: Reynolds stress

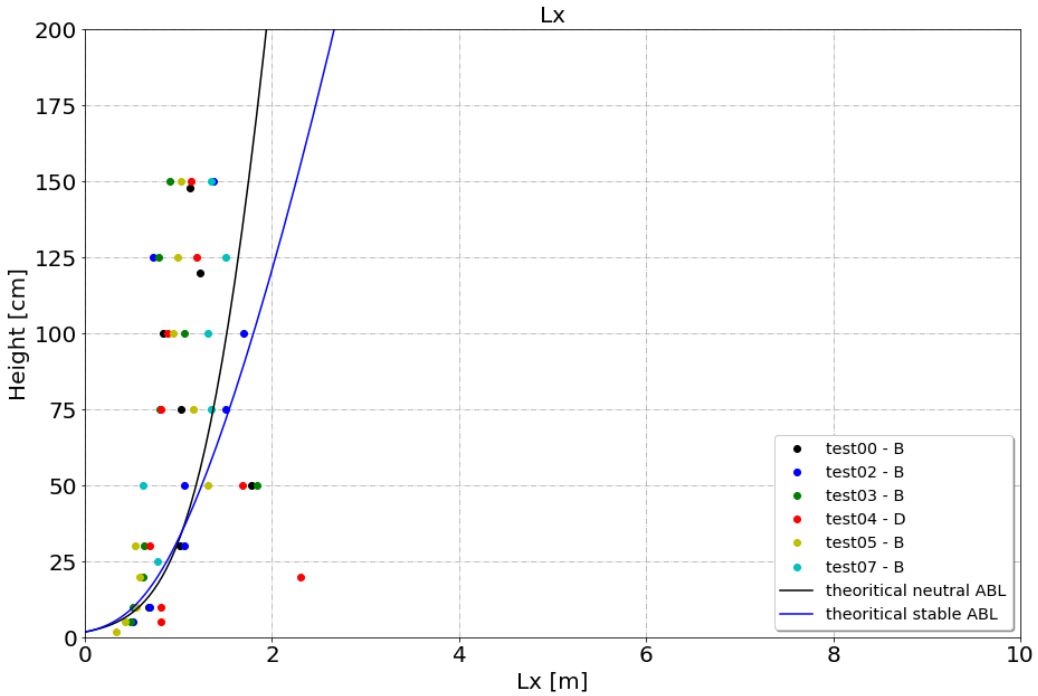


Figure 35: Integral length scale

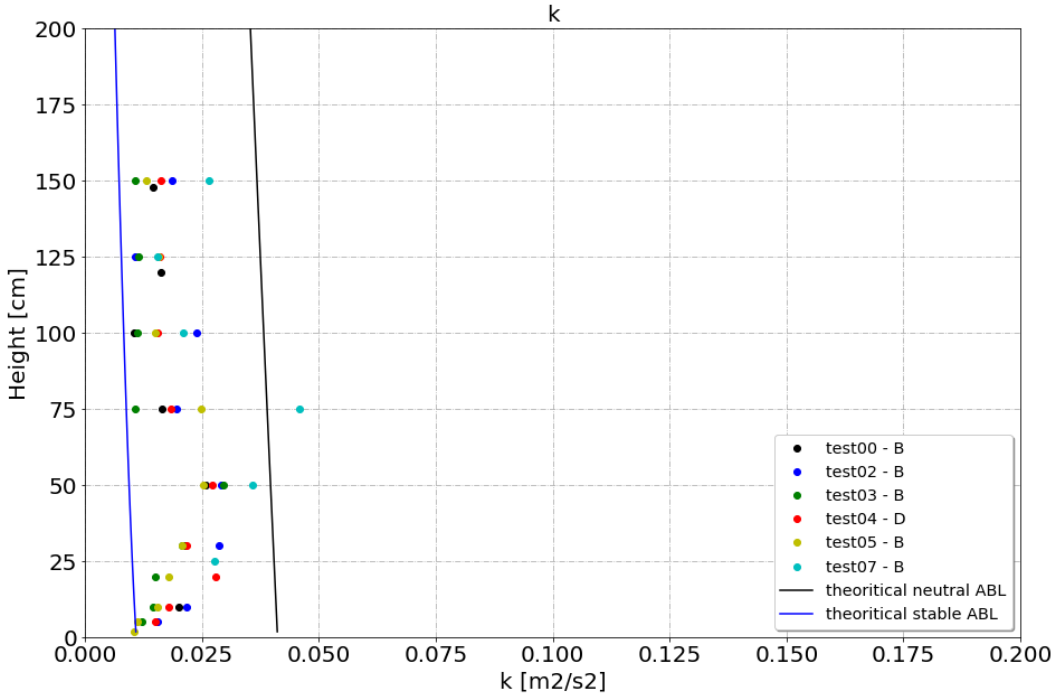


Figure 36: Turbulent kinetic energy

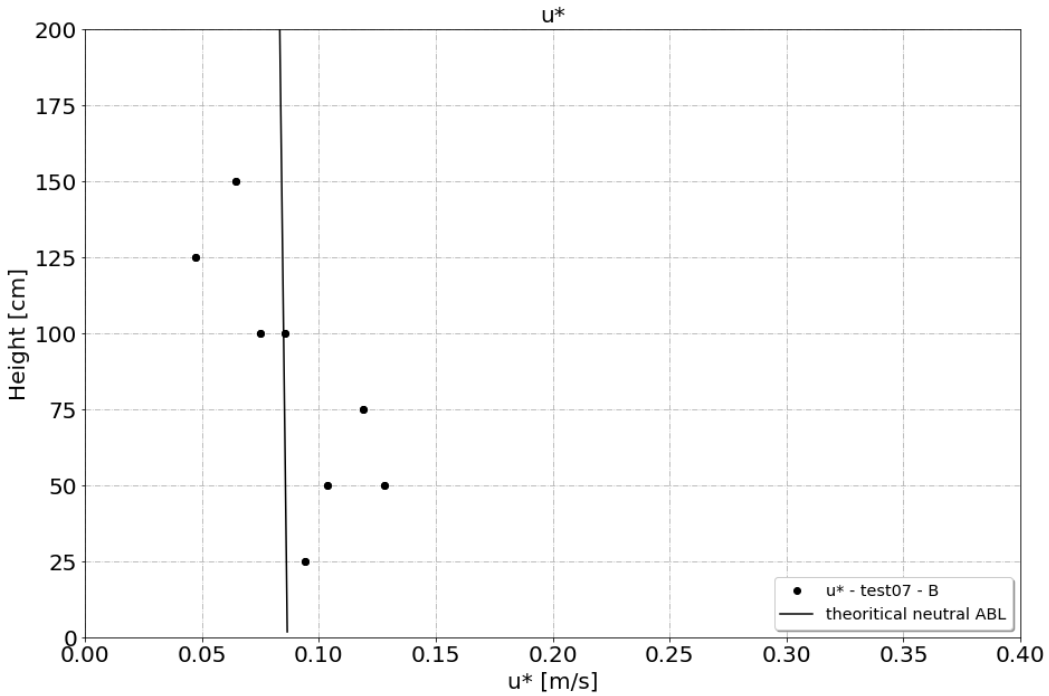


Figure 37: Friction velocity

The ramp has a significant influence on the wind profile, particularly on speeds measured at heights below 50 cm. This impact could not be thoroughly analysed in, but the profiles obtained with this configuration were nevertheless deemed satisfactory.

3.4.3.2 Wind velocity: 2 m/s

The turbulence analysis for a reference wind velocity of 2 m/s was not conducted in the same depth as that performed for a wind velocity of 1 m/s.

3.4.3.3 Roughness length

Roughness length is assessed for neutral conditions using the following formula:

$$z_0 = z.e^{\left(-\frac{kU(z)}{u*}\right)} \quad \text{Equation 9}$$

With

z_0	Roughness length	[m]
z	Altitude	[m]
U(z)	Wind velocity	[m/s]
u*	Friction velocity	[m/s]
k	Von Karman constant = 0.4	[-]

The numerical application performed at 0.25 m above the ground for an average wind velocity of 0.6 m/s and a friction velocity of 0.09 m/s gives a simulated surface roughness of 0.017 m in the fire gallery.

4 Measurement of evaporation rate

4.1 Pool evaporation tests

For pool evaporation tests, two methods were used to measure evaporation rate.

- One method based on the overall concentration measured in the extraction duct,
- A more direct method based on measuring the mass of liquid over time.

4.1.1 Based on the overall concentration

The general method for estimating the evaporation rate is obtained using the following formula:

$$\dot{m} = \frac{PM_{mol}}{RT} * 1000 * D_{extraction} * \frac{1}{3600} * C_{gloabl} * 10^{-6} \qquad \text{Equation 10}$$

With

$\dot{m}$	Product evaporation rate	[g.s^{-1}]
M_{mol}	Product molar mass	[kg.mol^{-1}]
P	Atmospheric pressure	[Pa]
R	Gas constant	[J.K^{-1}.mol^{-1}]
T	Atmospheric temperature	[K]
$D_{extraction}$	Extraction flow rate	[m³/h]
C_{global}	Product concentration measured in the duct	[ppm]

As the extraction flow rate is provided directly in Nm³/h by the analyser permanently installed in the extraction duct, the following formula is used instead:

$$\dot{m} = \frac{M_{mol}}{V_{mol}} * 1000 * D_{extraction} * \frac{1}{3600} * C_{global} * 1e^{-6} \qquad \text{Equation 11}$$

With

V_{mol}	Molar volume	= 0.0224 [Nm^3.mol-1]

Figure 38 shows the position of the concentration measurement point (PID, AP4C or FTIR depending on the product).

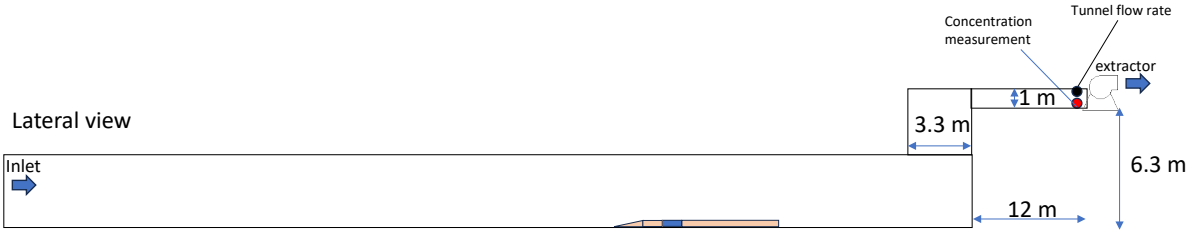


Figure 38 : Position of the concentration measurement point

4.1.2 Based on mass

The evaporation flow rate is obtained using the following formula:

$$\dot{m} = -\frac{dM}{dt}$$ Equation 12

With

M	Mass measured at each time step	[kg]

4.1.3 Discussion specific to TEP

The AP4C has been specifically calibrated to measure TEP concentration in the duct. A preliminary test was carried out with a known quantity of TEP. To do this, a known concentration of TEP vapours was generated in the gallery at the bench level and under the desired turbulence conditions using a heated vapour generation system (Figure 39).

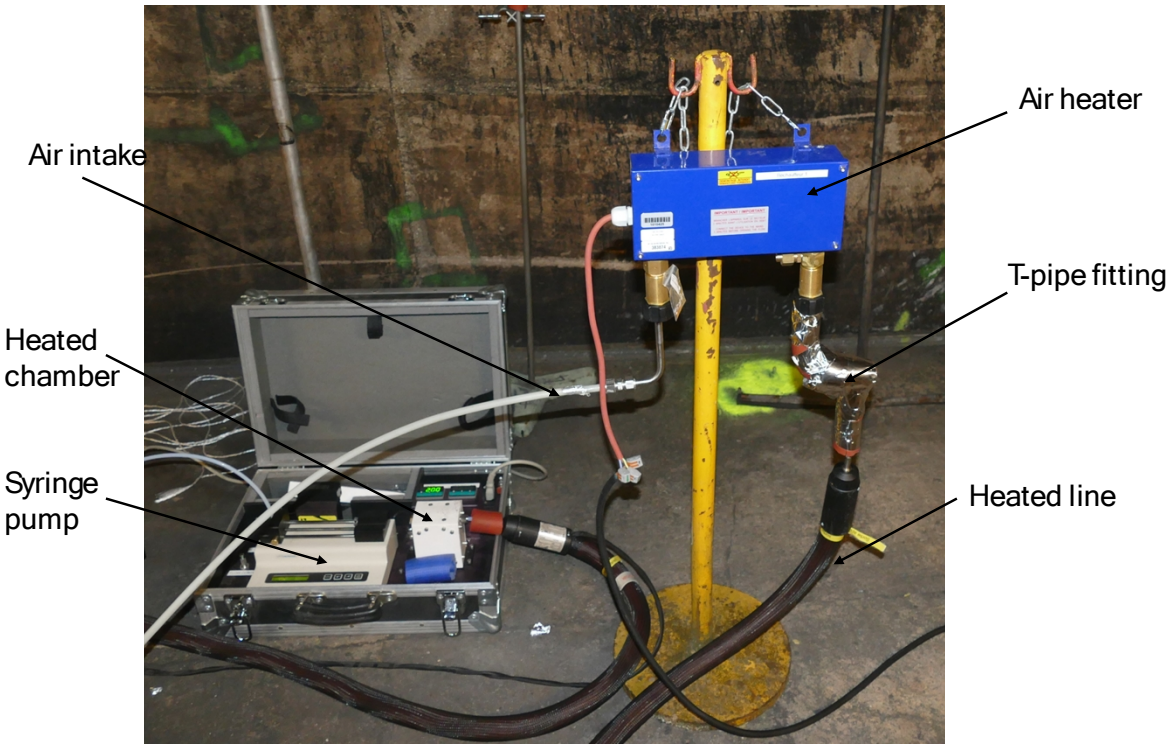


Figure 39 : heated vapour generation system

This system consists of transferring a known quantity of TEP using a mechanical syringe pump into a chamber heated to 200°C. The vapours produced are then channelled through a line heated to 180°C to a dilution point with a pre-set hot air flow rate. The concentration obtained at the outlet of the line is close to that expected during the slurry evaporation test. The concentration of TEP vapours is measured in the gallery extraction duct using the AP4C. The concentration integration is compared to the total amount of TEP previously injected by the syringe pump. A correction factor of 1,5 is applied and used during the pool evaporation tests to compensate the drift of the AP4C.

4.2 Droplet evaporation tests

4.2.1 General method

As the overall concentration is difficult to detect using measuring devices, the method used to determine the droplet evaporation rate consisted of measuring the local concentration in an area just behind the substrate (Figure 22) as part of a test on a glass substrate.

The mass obtained by integrating this concentration was then compared to the actual mass deposited on the substrate. The ratio of the two values gave us a factor to be applied subsequently for tests on concrete substrates. A factor was determined for each product in the order of approximately 1000. It should be noted that this method suggests that the vapour cloud behaves in the same way for a test on glass as for a test on concrete. The methodology is described below.

The total mass evaporated from a non-porous substrate is estimated using the following equation:

$$m_{evap} = m_{initial} - m_{final} \qquad \text{Equation 13}$$

Furthermore, the total mass evaporated is determined using the following second equation.

$$m_{evap} = \int_0^{tf} \frac{\mathrm{M_{mol}}}{\mathrm{V_{mol}}} * 1000 * \mathrm{D_{extraction}} * \frac{1}{3600} * \mathrm{C}_{global}(\mathrm{t}) * 1\mathrm{e}^{-6} dt \qquad \text{Equation 14}$$

$$m_{evap} = \int_0^{tf} \frac{\mathrm{M_{mol}}}{\mathrm{V_{mol}}} * 1000 * \mathrm{D_{extraction}} * \frac{1}{3600} * \frac{1}{F_{dilution}} * \mathrm{C}_{local}(\mathrm{t}) * 1\mathrm{e}^{-6} dt \qquad \text{Equation 15}$$

With

m_{evap}	Evaporation rate	[g.s^{-1}]
$\mathrm{M_{mol}}$	Product molar mass	[kg.mol^{-1}]
$\mathrm{V_{mol}}$	Molar volume	= 0.0224 [Nm^3.mol^{-1}]
$\mathrm{D_{extraction}}$	Extraction flow rate	[Nm^3.h^{-1}]
$\mathrm{C}_{local}(\mathrm{t})$	Product local concentration	[ppm]
$F_{dilution}$	Dilution factor	[-]
tf	Final time	[s]

The value of F_{corr} is then obtained by equating the two previous equations.

$$m_{initial} - m_{final} = \frac{1}{F_{dilution}} \int_0^{tf} \frac{\mathrm{M_{mol}}}{\mathrm{V_{mol}}} * 1000 * \mathrm{D_{extraction}} * \frac{1}{3600} * \mathrm{C}_{local}(\mathrm{t}) * 10^{-6} dt \qquad \text{Equation 16}$$

The evolution of the evaporation rate can then be estimated using the following formula:

$$\dot{m}_{evap} = \frac{1}{F_{dilution}} \frac{\mathrm{M_{mol}}}{\mathrm{V_{mol}}} * 1000 * \mathrm{D_{extraction}} * \frac{1}{3600} * \mathrm{C}_{local}(\mathrm{t}) * 1\mathrm{e}^{-6} \qquad \text{Equation 17}$$

$\frac{1}{F_{dilution}}$ can then be used for measurements on a porous substrate.

4.2.2 Discussion specific to TEP

As with the pool evaporation tests, the AP4C was calibrated in advance for TEP droplet evaporation tests. The preliminary test consisted of depositing a known quantity of TEP on glass strips placed on the glass plate. The AP4C was installed downstream of the glass plate (Figure 40).

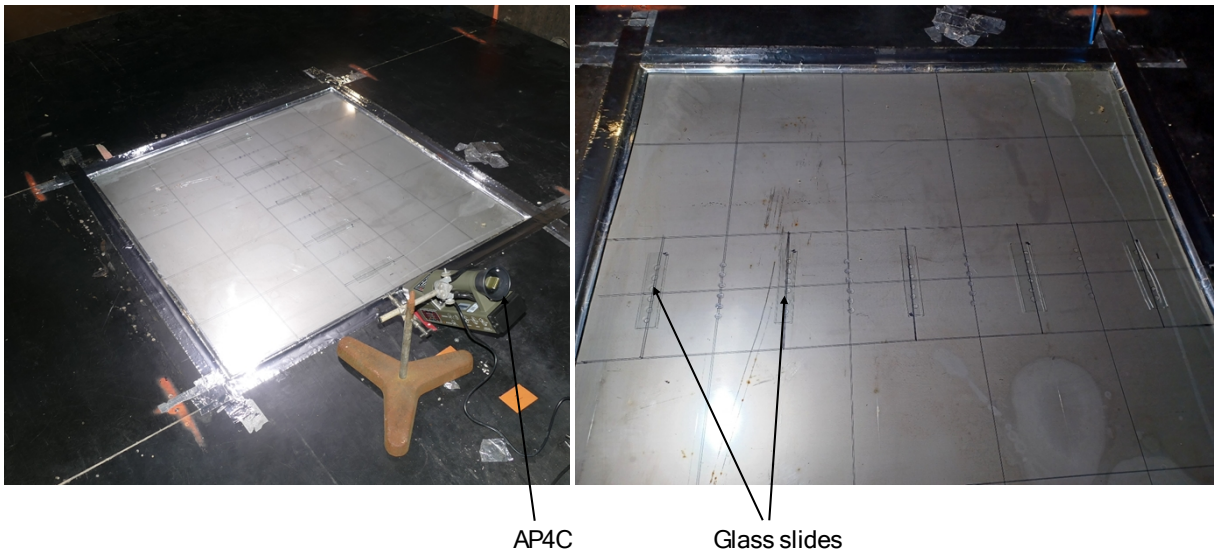


Figure 40 : Setup for the preliminary AP4C droplet evaporation test on glass

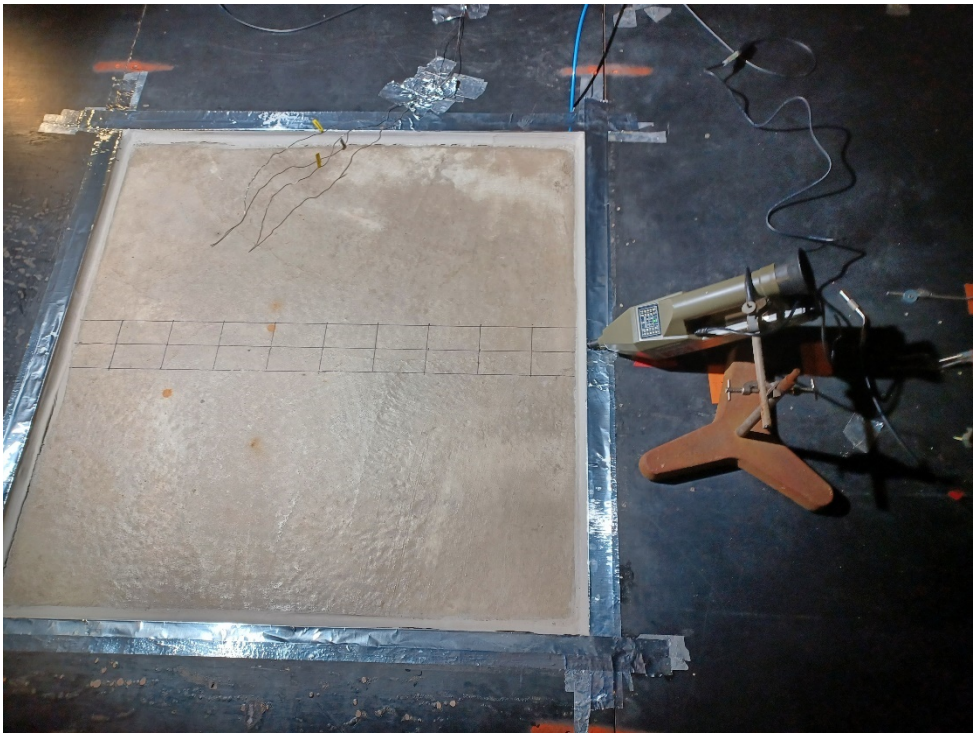


Figure 41 : Setup for the AP4C droplet evaporation test on concrete

The preliminary test was conducted under the same ventilation conditions as the tests planned in the matrix. The test lasted approximately 20 hours. At the end of the test, the strips with droplets still partially present were immersed in a known quantity of water (Figure 42).



Figure 42 : Glass slides onto which AP4C droplets were applied

The whole thing was analysed to deduce, on the one hand, the mass of TEP evaporated at the level of a droplet and, on the other hand, the mass of water absorbed by a droplet, as TEP is highly hygroscopic. The total mass of TEP evaporated from all the droplets deposited on the glass plate was then compared with the concentration measured at the same time with AP4C. The quantity measured with the AP4C by concentration divided by the quantity measured by mass gave a correction factor to be applied for the test of the matrix on concrete substrate (Figure 43).

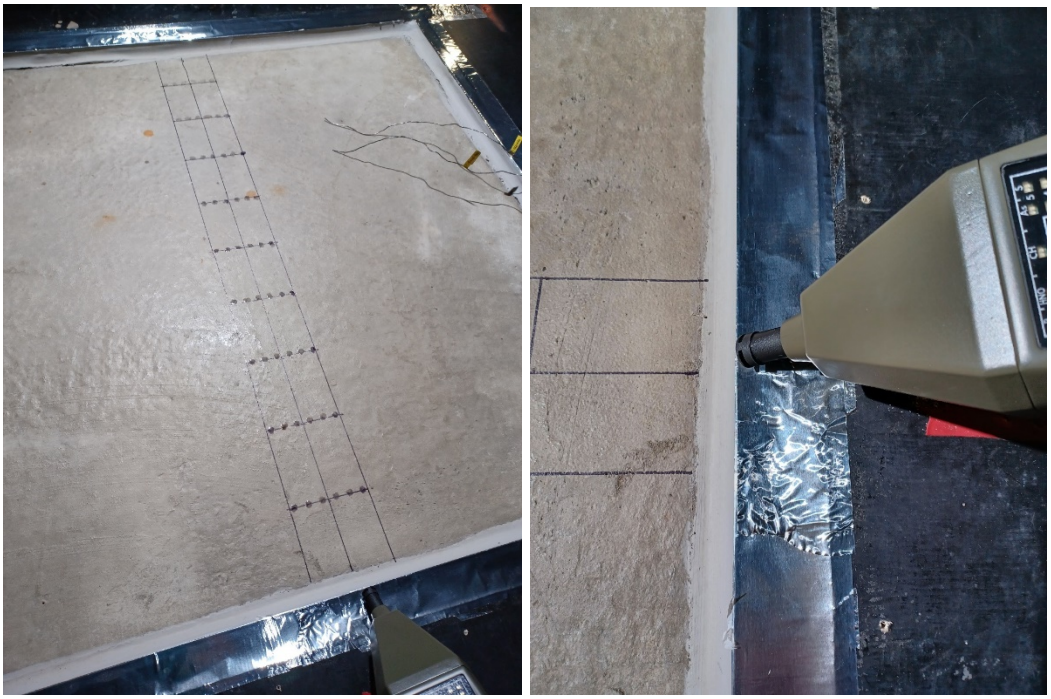


Figure 43 : TEP evaporation tests on concrete – left: position of droplets – right: zoom on the position of the AP4C

4.2.3 Accumulation chamber

The concept of the accumulation chamber was developed by Zbigniew POKRYSZKA [7][8], an engineer at Ineris. The method consists of covering a certain surface area of the substrate with a cylindrical Accumulation Chamber (AC) in a virtually airtight manner without significantly altering the environmental conditions. This operation creates an "accumulation effect" which is a basic mechanism for measuring the local gas flow.
The gases emitted by the covered surface accumulate in the confined atmosphere of the package, which initially consists of air that is virtually free of or contains only a small amount of the helium to be measured.

It should be noted that in the context of these experiments, the AC were adapted based on the concept invented by Zbigniew POKRYSZKA.

The average vapour content inside the AC increases gradually. In the initial period after the AC is installed, this increase is almost proportional to time and can be assimilated to a linear function of the content as a function of time.
In the Ineris method [8], it is this period of increase that is observed and processed in order to deduce the local gas flow.

To do this, a system continuously samples a certain amount of the gas mixture inside the chamber. The sampled gas is conveyed through a pipe to an analyser and then reinjected into the chamber, creating gas recirculation. Monitoring the vapour enrichment rate of the recirculated mixture makes it possible to deduce the local vapour flow on the surface in question. A vent allows vapours to be evacuated in the event of excessive pressure in the AC in order to limit the system's impact on evaporation through the pores of the substrate.

The vapour concentration curve is shown in Figure 44. The inflection in the curve, which appears about ten minutes after the start of the measurement and leads to a steady state, is related to vapour leaks through the vent on the AC and through the contact areas between the CAA and the package.

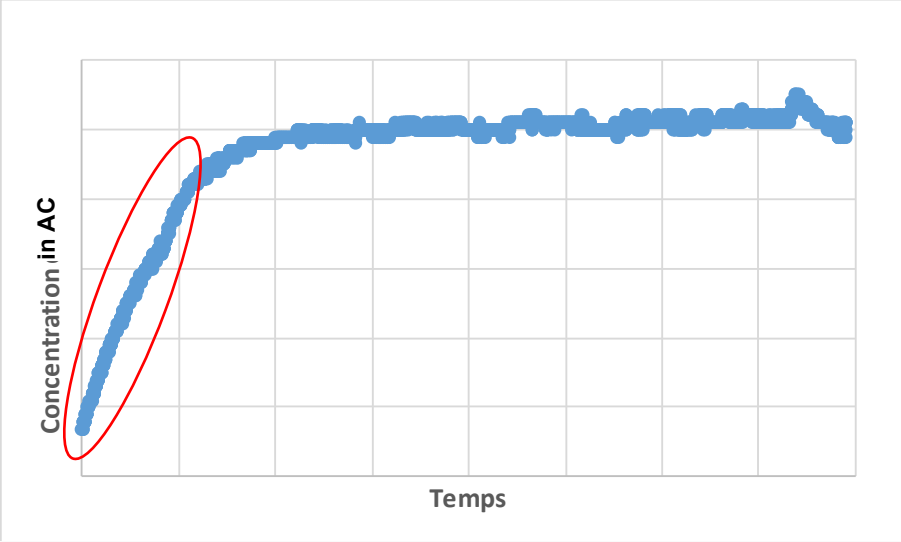


Figure 44 : Example of a curve showing the evolution of vapour concentration in the AC

The AC used is shown in Figure 45 and Figure 46..

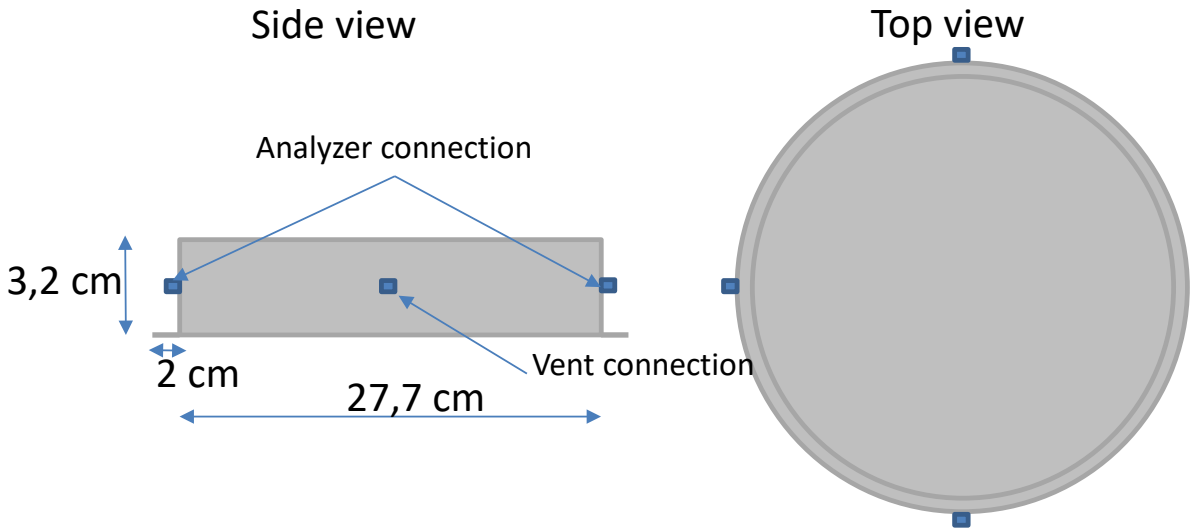


Figure 45 : Schematic diagram of how a circular AC works

The CAA is open at the base and closed at the top (same principle as a hat). A 2 cm wide collar is welded to the base of the CAA for better adhesion between it and the package. The CAA is attached to the package using high-strength aluminium foil.



Figure 46 : Photo of an AAC positioned on the substrate

This method has only been applied in a few cases. It should be noted that it would be appropriate to fully exploit the advantages of this promising method for a future campaign.

5 Experimental results – Pool evaporation tests

5.1 Description of the test procedure

For tests on glass, the following steps were carried out :

Step	Operation
1	Positioning of the glass with its steel frame on the balance, in the middle of the platform.
2	Start ventilation and adjust the flow rate to reach a velocity of 1 m/s (or 2 m/s) at the reference point.
3	Start data acquisition (concentrations and temperatures).
4	Spill of the liquid on the glass
5	Waiting time between 5 and 10 hours
6	End of test

Table 12 : Steps for tests on glass

For tests on concrete substrates, the following steps were carried out :

Step	Operation
1	Soak the concrete block in water for 24 hours to clean it and saturate it with 100% water.
2	Dry the concrete block in an oven for 8 hours or even 24 hours in some cases.
3	Position the concrete block on the scale, in the middle of the platform (Figure 47).
4	Start ventilation and adjust the flow rate to reach a velocity of 1 m/s (or 2 m/s) at the reference point
5	Start data acquisition (concentrations and temperatures).
6	Spill of the liquid on the substrate
7	Waiting time between 8 and 24 hours
6	End of test

Table 13 : Steps for tests on concrete



Figure 47 : Illustration of the setup of concrete plate

The spillage of the liquid was consistently carried out under identical conditions, namely by using a toothed funnel placed on the substrate and spilling the liquid through the funnel as close as possible to the center of the pool (Figure 48). The teeth make it possible to limit turbulence during the spillage process.

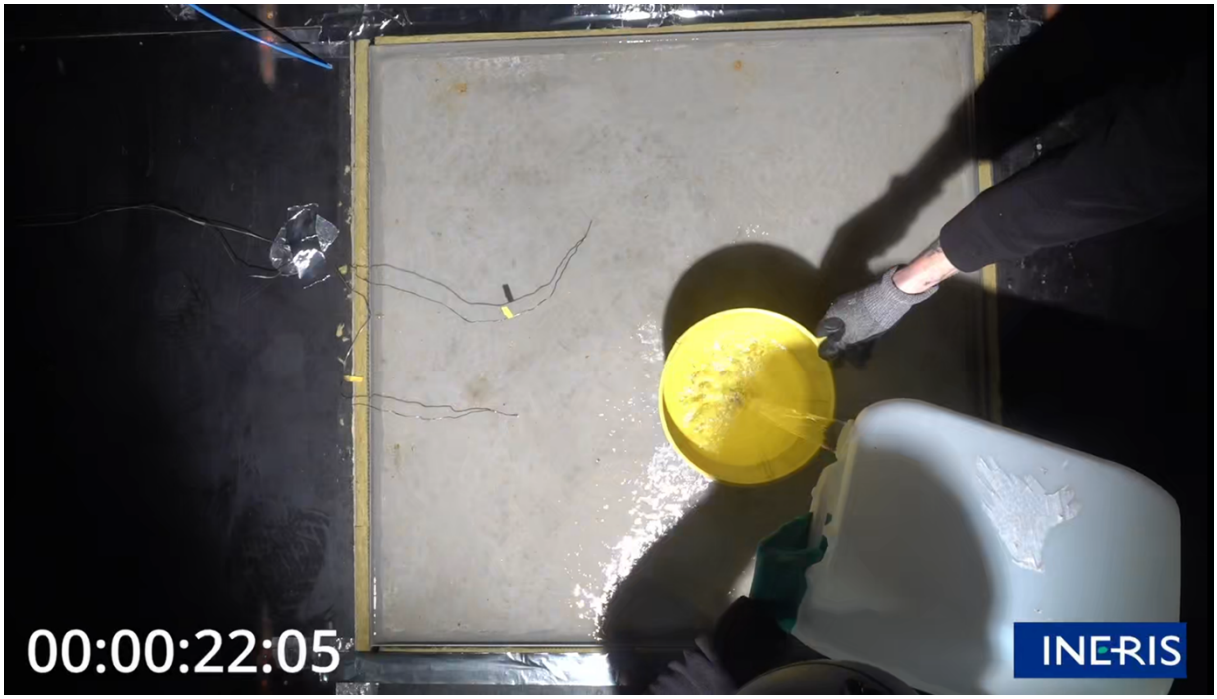


Figure 48 : Illustration of liquid spillage

Figure 49 gives a lateral view of the toothed funnel.



Figure 49 : toothed funnel

5.2 Observations

The notable observations made during the experiments are presented in Table 14.

Test	Observation
1	During this test, a small amount of n-heptane leaked beneath the glass due to a defective seal (Figure 50). The leaked quantity did not exceed 0.06 kg. The presence of the small amount of heptane from Test No. 1, which seeped beneath the plate, may have introduced a minor degree of uncertainty into Test No. 2. However, given the limited quantity involved and the fact that the heptane from Test No. 1 was trapped beneath the plate, its contribution to the vapours generated during Test No. 2 should be negligible.
2	The n-heptane that leaked during Test 1 remained beneath the glass. Presumably, in Test 2, all the poured n-heptane evaporated.
3	At the beginning of the test, the concrete block was warmer than ambient temperature as it was removed from the oven. The FTIR experienced a malfunction for approximately 2 hours starting at t0 + 45 min. Around 1.35 kg of n-heptane leaked at the edges due to defective seals. The insulating material placed at the edges absorbed the n-heptane. It is possible that n-heptane contained in the insulation evaporated during the test, likely at a very low rate compared to the puddle, though it may have influenced the final stage when n-heptane vapors evaporated through the concrete pores. Therefore, it is difficult to draw conclusions regarding the evaporation rate through the concrete pores.
4	During this test, approximately 1.65 kg of n-heptane was also absorbed by the insulation. The effect is similar to Test 3 regarding the final stage. It remains difficult to conclude on the evaporation rate through the concrete pores.
5	The substrate and the liquid were warmer than ambient temperature. Sealing issues were also noted during this test. It is difficult to conclude on the evaporation rate through the concrete pores. The test was interrupted before complete evaporation of the puddle.
6	Sealing issues were again observed during this test. It is difficult to conclude on the evaporation rate through the concrete pores.
7	Sealing issues were once more observed during this test. It is difficult to conclude on the evaporation rate through the concrete pores.
8	No noticeable comment
9	The test was interrupted before completion. Note that the TEP is highly hygroscopic and gradually absorbs water during the test. Analyses were conducted to determine the TEP evaporation rate by measuring the water content in the mixture at the end of the test.
10	No noticeable comment
11	After 890 minutes, local concentration measurement data are no longer relevant due to a technical failure of the FTIR.
20	The concrete block did not undergo the usual preparation protocol (neither washed nor oven-dried). The PID stopped after 2 h 15 min due to depleted batteries.
21	No noticeable comment
22	The substrate and liquid temperatures were below the water dew point; acetone trapped water during the test, explaining the presence of liquid (100% water) on the substrate at the end. During the test, pieces of the seal detached due to acetone degradation. Small seal fragments floated in several locations throughout the test.

Table 14 : Main observations

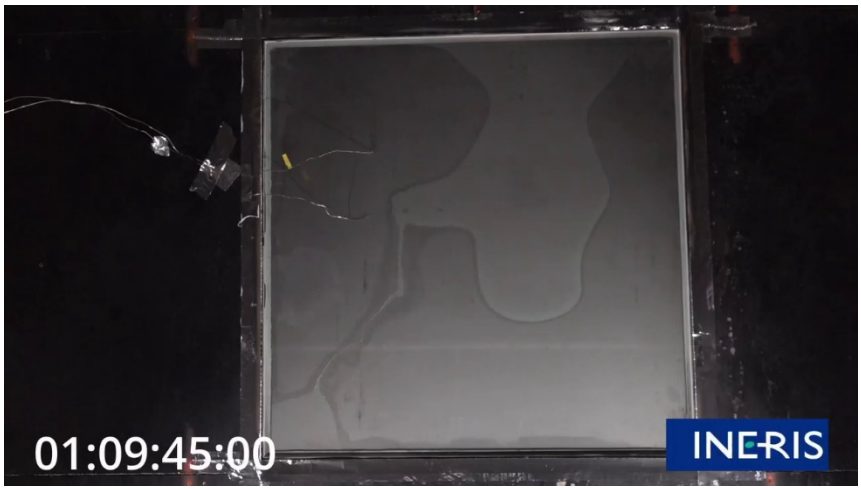


Figure 50 : Illustration of n-heptane leaking beneath the glass plate

5.3 Analysis of different parameters

5.3.1 Wind velocity at 1 m high

For each test, the velocity in the fire gallery was measured at the reference point located at the center of the fire gallery, 1 m above the floor. The values for all tests are presented in Figure 51.

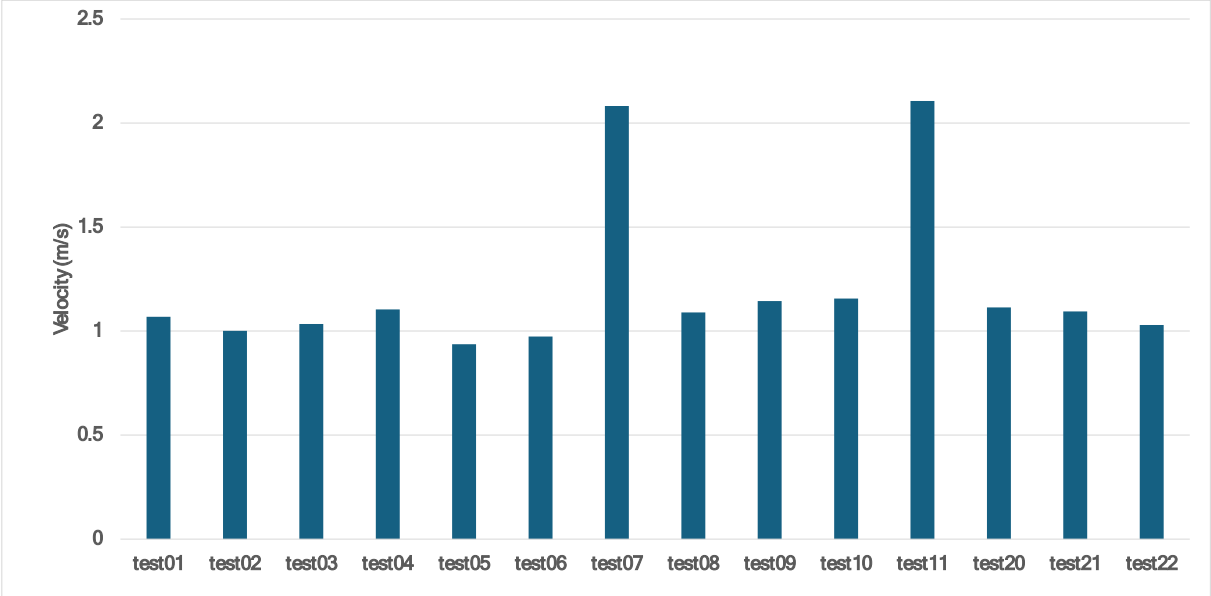


Figure 51 : Average velocity

The average was calculated from the beginning to the end of the test. The average values of 1 m/s and 2 m/s were consistently maintained from one test to another. Figure 52 presents the $\overline{u'u'}$ component of the Reynolds stresses measured for each test.

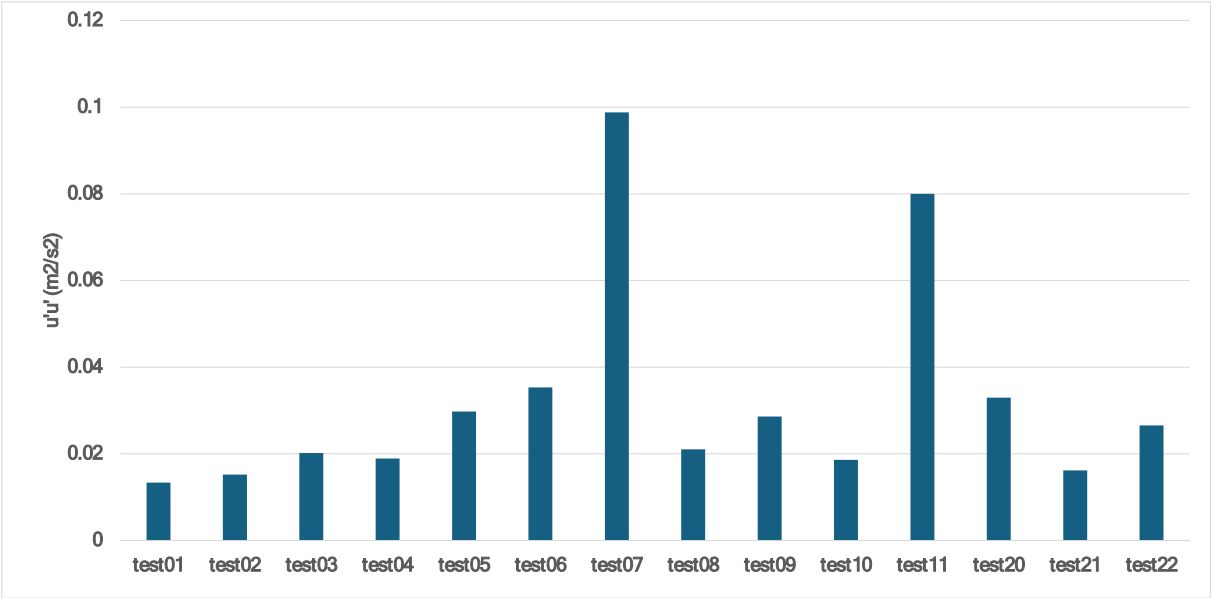


Figure 52 : $\overline{u'u'}$ component of the Reynolds stresses

For the tests involving a wind velocity of 1 m/s, the $\overline{u'u'}$ term ranges between 0.013 and 0.035 m²/s², which corroborates the values obtained during the preliminary phase (see Figure 34) at a height of 1 m. The results indicate that the turbulence generated for an average wind velocity of 2 m/s is approximately 2 to 3 times higher than that generated with an average wind velocity of 1 m/s. This discrepancy must be taken into account when reproducing the velocity field at 2 m/s in modeling studies.

5.3.2 Temperature

Initial temperatures for each case are presented in Table 15

Test N°		Product	Velocity at refence point (m/s)	Substrate	Initial ambient temperature at t0 (°C)	Initial substrate temperature at t0 (°C)	Initial liquid temperature at t0 (°C)
1		Heptane	1	glass	5.3	6.2	6
2		Heptane	1	glass	0.4	0.8	9.4
3		Heptane	1	a1	1.6	15.5	unknown
4		Heptane	1	a1	3.5	3.1	9.8
5		Heptane	1	b	2.9	13.1	unknown
6	Pool	Acetone	1	a2	7.9	18.5	unknown
7		Acetone	2	a2	12	10.6	12.6
8		Heptane	1	c	7.1	14.5	unknown
9		TEP	1	a3	7	29.5	unknown
10		Heptane	1	a1	6.8	8	7.6
11		Heptane	2	a2 painted	8	8.5	14.5
20		Octane	1	b	6.2	7.6	16
21	Pool	Heptane	1	a2 painted	5.9	8	12.5
22		Acetone	1	a1	5	4	9

a1, a2, a3: reference susbtrates (20 mm, porosity N°1)
b: substrate 40 mm
c: substrate 20 mm, porosity n°2

Table 15 : Initial temperatures

For all cases, the temperature evolution is presented over the entire duration of the test in APPENDIX 4 and for the first 20 minutes in APPENDIX 5.

Upon spilling the liquid, three distinct behaviors were observed:

- In some cases, the liquid poured onto the substrate was warmer than the ambient temperature (up to 10 °C higher during the initial moments in certain tests), which could cause a slight increase of the substrate temperature. This was due to the conditioning of the product in a heated hall. This temperature rise was observed in Tests 2, 4, 11, 20, 21, and 22. However, in these cases, both the liquid and the substrate reached ambient temperature within approximately 10 minutes.
- In other cases, the substrate temperature was higher than the ambient temperature due to its prior oven treatment. These correspond to Tests 3, 5, 6, 8, and 9. The substrate then transferred heat to the liquid during the initial moments. In these cases, it is difficult to define the initial temperature of the liquid, as it is immediately heated upon contact with the substrate. Nevertheless, since concrete transfers its heat to the liquid, considering the initial liquid temperature as equal to that of the concrete remains acceptable.
- Finally, in some cases, both the substrate and the liquid were at ambient temperature (Tests 1, 7, and 10).

It should be noted that in Test 1, the two temperature spikes of the liquid are due to operator manipulation of the thermocouple and should not be considered in the analysis.

These represent three initial conditions that must be taken into account in the modeling. In all cases, a subsequent temperature drop is observed, which is more or less pronounced depending on the initial liquid temperature, and is associated with the liquid's evaporation and/or substrate cooling (only for Tests 3, 5, 6, 8, and 9).

5.3.3 Product mass

Table 16 presents initial inventories for each test.

Week	Day	Test N°		Product	Substrate	Velocity at refence point (m/s)	Height (mm) = quantity (L)	Measured initial mass (kg)	density (kmol/m3)	molar mass (g/mol)	Density (kg/m3)	Deduced initial volume (L)
7	13/02	1		Heptane	glass	1	5	3.33	6.96081	100.2	697.5	4.8
	14/02	2		Heptane	glass	1	5	3.37	7.00888	100.2	702.3	4.8
8	17/02	3		Heptane	a1	1	10	6.74	6.9362	100.2	695.0	9.7
	18/02	4		Heptane	a1	1	10	6.73	6.97634	100.2	699.0	9.6
	19/02	5		Heptane	b	1	20	13.50	6.9575	100.2	697.1	19.4
	20/02	6	Pool	Acetone	a2	1	10	7.80	13.725	58.08	797.1	9.8
	21/02	7		Acetone	a2	2	10	7.85	13.78	58.08	800.3	9.8
9	26/02	8		Heptane	c	1	10	6.87	6.986	100.2	700.0	9.8
	27/02	9		TEP	a3	1	2	2.07	5.885	182.15	1072.0	1.9
	28/02	10		Heptane	a1	1	10	6.85	6.9477	100.2	696.2	9.8
10	03/03	11		Heptane	a2 painted	2	10	6.75	6.9387	100.2	695.3	9.7
	13/03	20		Octane	b	1	5	3.23	6.243	114.23	713.1	4.5
	14/03	21	Pool	Heptane	a2 painted	1	10	6.77	6.945	100.2	695.9	9.7
12	17/03	22		Acetone	a1	1	10	7.75	13.94	58.08	809.6	9.6

a1, a2, a3: reference susbtrates (20 mm, porosity N°1)
b: substrate 40 mm
c: substrate 20 mm, porosity n°2

Table 16 : Initial inventories

Table 17 presents the mass balances, including the initial masses and the total evaporated masses, obtained either by integrating the evaporation rate curves using the method described in Chapter 4 or by measuring the final mass.

Test	Mass measured with balance (kg)			Mass based on apparatus (kg)		
	Initial mass	Final mass	Déduced evapored mass	FTIR	PID	AP4C
test01	3,33	0,06	3,27	3,31	0	0
test02	3,37	0	3,37	3,41	0	0
test03	6,74	1,47	5,27	5,05	5	0
test04	6,73	1,64	5,09	4,47	4,61	0
test05	13,5	4,22	9,28	7,03	5,7	0
test06	7,8	0,74	7,06	6,41	6,48	0
test07	7,85	0,36	7,49	7,44	7,43	0
test08	6,87	0,46	6,41	6,38	5,7	0
test09	2,07	2,04	0,03	0	0	0,03
test10	6,85	0,06	6,79	6,96	6,52	0
test11	6,75	0,06	6,69	6,84	6,78	0
test20	3,23	0,46	2,77	0	2,625	0
test21	6,77	0,15	6,62	6,75	6,75	0
test22	7,75	1,14	6,61	5,88	5,98	0

Table 17 : Mass balances

Figure 53 presents the histogram derived from Table 17.

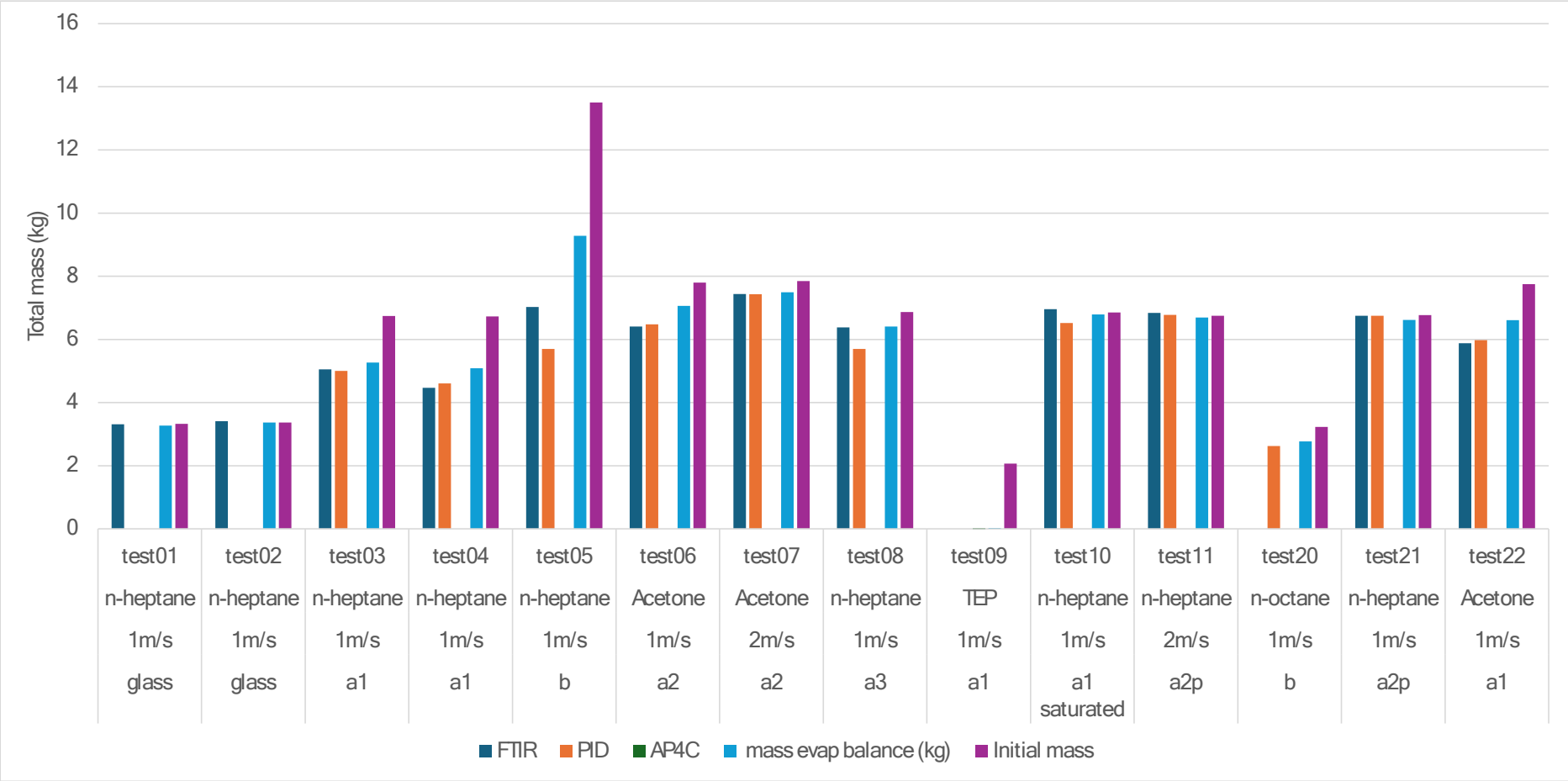


Figure 53 : Mass balances

For Tests 1, 2, 3, 7, 11, and 21, the evaporated masses deduced from the different measuring methods are in very good agreement. It should be noted that in Test 1, a small amount of n-heptane leaked beneath the glass plate due to defective seals. However, as the leaked quantity was very small, it is unlikely to have affected the study results.

Tests 4 and 6, which show good agreement between the FTIR and the PID, exhibit discrepancies of 12 % and 10 %, respectively, between measurements based on concentration and those based on weighing. Ineris recommends prioritizing concentration measurements, as part of the liquid flowed beneath the substrate due to insufficient sealing (indeed, post-test inspection of the seals revealed partial deterioration). The portion trapped beneath the balance corresponds to the initial mass minus the evaporated mass.

For Tests 3, 4, and 7, the mass balance is unsatisfactory because part of the liquid flowed beneath the substrate.

Test 5 shows a discrepancy between the PID and the FTIR because the PID was stopped before the FTIR. Additionally, the mass balance is unsatisfactory because the test was interrupted before complete evaporation.

Regarding Tests 8 and 10, the discrepancy between the FTIR and the PID is due to poor calibration of the latter.

In Test 9, the experiment was interrupted before completion because the product is not very volatile. Moreover, as the TEP is highly hygroscopic, the liquid layer absorbed approximately 10 % of its mass in water. This observation was confirmed at the end of the test through mixture analysis.

Test 20 was also interrupted before completion for the same reasons as Test 9.

Test 22 was interrupted before completion, resulting in an unsatisfactory mass balance.

5.3.4 Near-field concentration

The concentrations measured in the near field are presented in APPENDIX 6. These concentrations are not analyzed in the present report; they serve as a database for the validation of a computational code.

5.3.5 Evaporation rate

5.3.5.1 Measured data

The evaporation rates are directly deduced from the concentrations measured in the duct using different systems (FTIR, PID AP4C) and from the masses measured with the balance, as described in Chapter 4.

The evaporation rate curves obtained with the two methods are presented in APPENDIX 7. The results from the different methods are generally in good agreement. The curves derived from mass measurements are generally noisier due to the balance’s pronounced sensitivity to wind fluctuations in the fire gallery.

It should be noted that at the end of the test, the evaporation rate curve measured with the FTIR deviates from that measured with the PID, owing to the PID’s much lower quantification limit. In some cases, the PID may be unreliable due to its high sensitivity to gases originating from outside, such as vehicle exhaust gases.

Figure 54 presents the curves obtained for Test 2, and Figure 55 for Test 6.

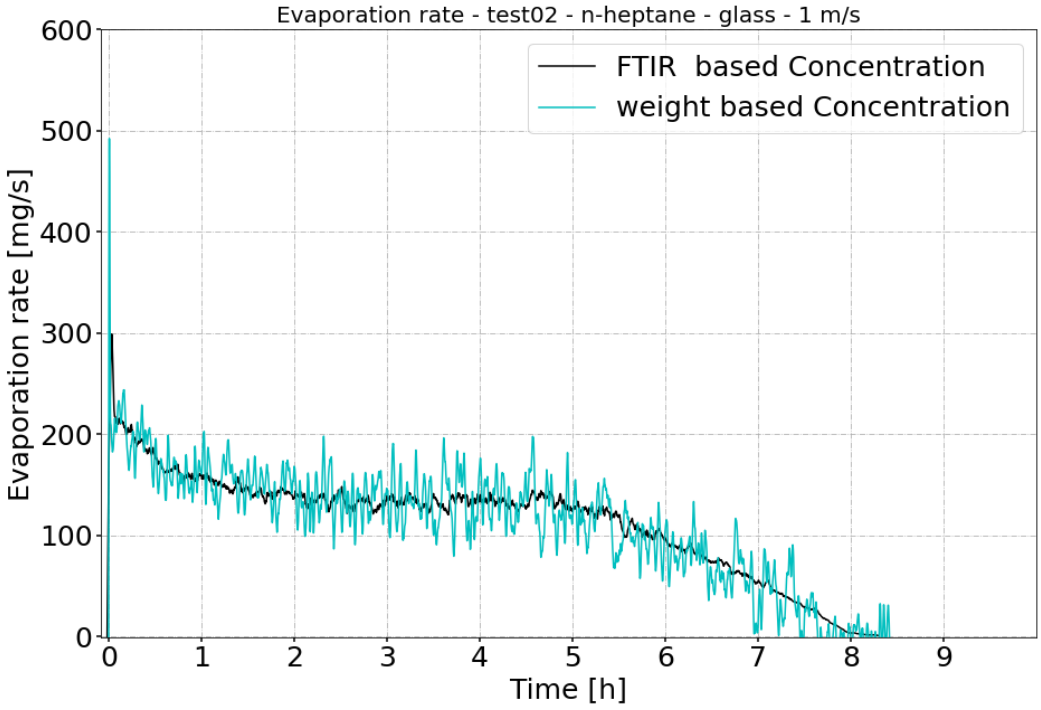


Figure 54 : Evaporation rate – test 2

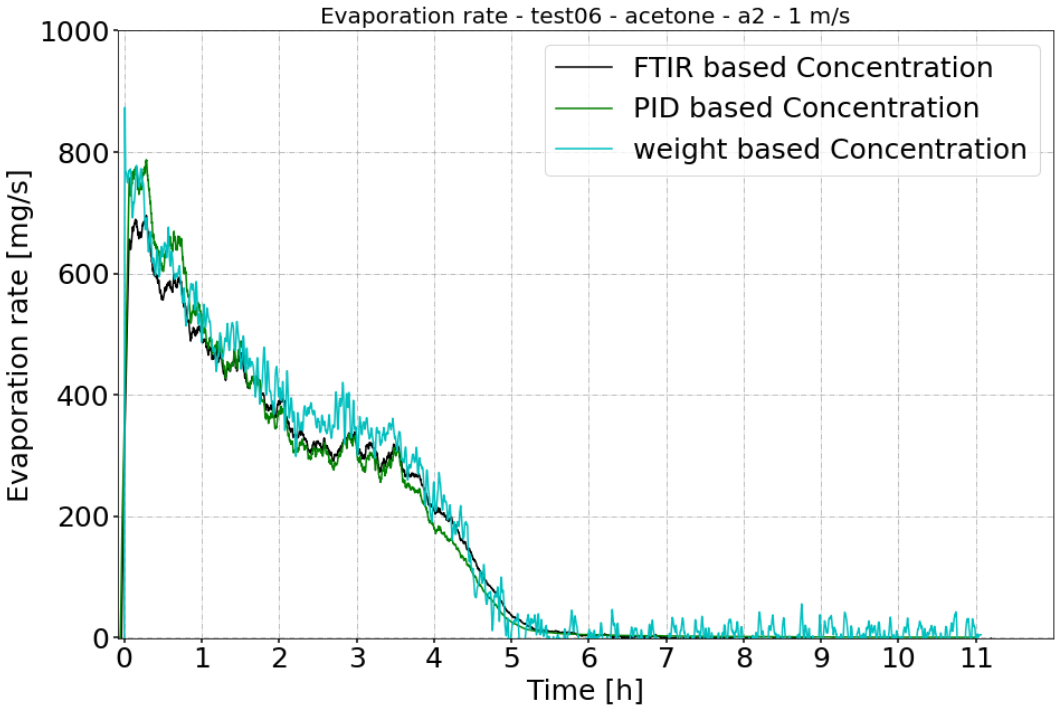


Figure 55 : Evaporation rate – test 6

In general, the following observations can be made (with the exception of Tests 5, 9, and 20, for which the liquid layer was not completely evaporated):

- An initial transient phase lasting a few minutes, during which a marked decrease occurs due to turbulence induced by spilling the liquid onto the substrate.
- A decay phase or progressive decreasing plateau (phase 1) lasting several hours, corresponding to the actual evaporation of the liquid layer, accompanied by cooling of the liquid over time. This cooling can explain the decrease in some cases, as the product's volatility decreases with temperature.
- A final decay phase (phase 2), reaching 0 mg/s for cases on glass substrates and near 0 mg/s for cases on concrete substrates, corresponding to the gradual reduction in the size of the liquid layer over time (see Figure 56).
- For cases with a concrete substrate, a very slow evaporation over several hours occurs, associated with the progressive drying of the concrete as it transports the liquid through its pores. This very slow evaporation is highlighted in Figure 57 (Test 4 – 10 L of n-heptane poured on concrete, 1 m/s wind velocity), where the scale has been adjusted to focus on the tail of the evaporation rate curves. A discrepancy appears between the two concentration measurement methods (FTIR and PID) due to measurement uncertainties and accuracies. It is likely that the PID curve is more relevant for very low evaporation rates, as its quantification limit is on the order of tens of ppb, whereas that of the FTIR is hundreds of ppb. The concentrations obtained for Test 4 are presented in Figure 58. The two lines show the limit of detection of the devices.

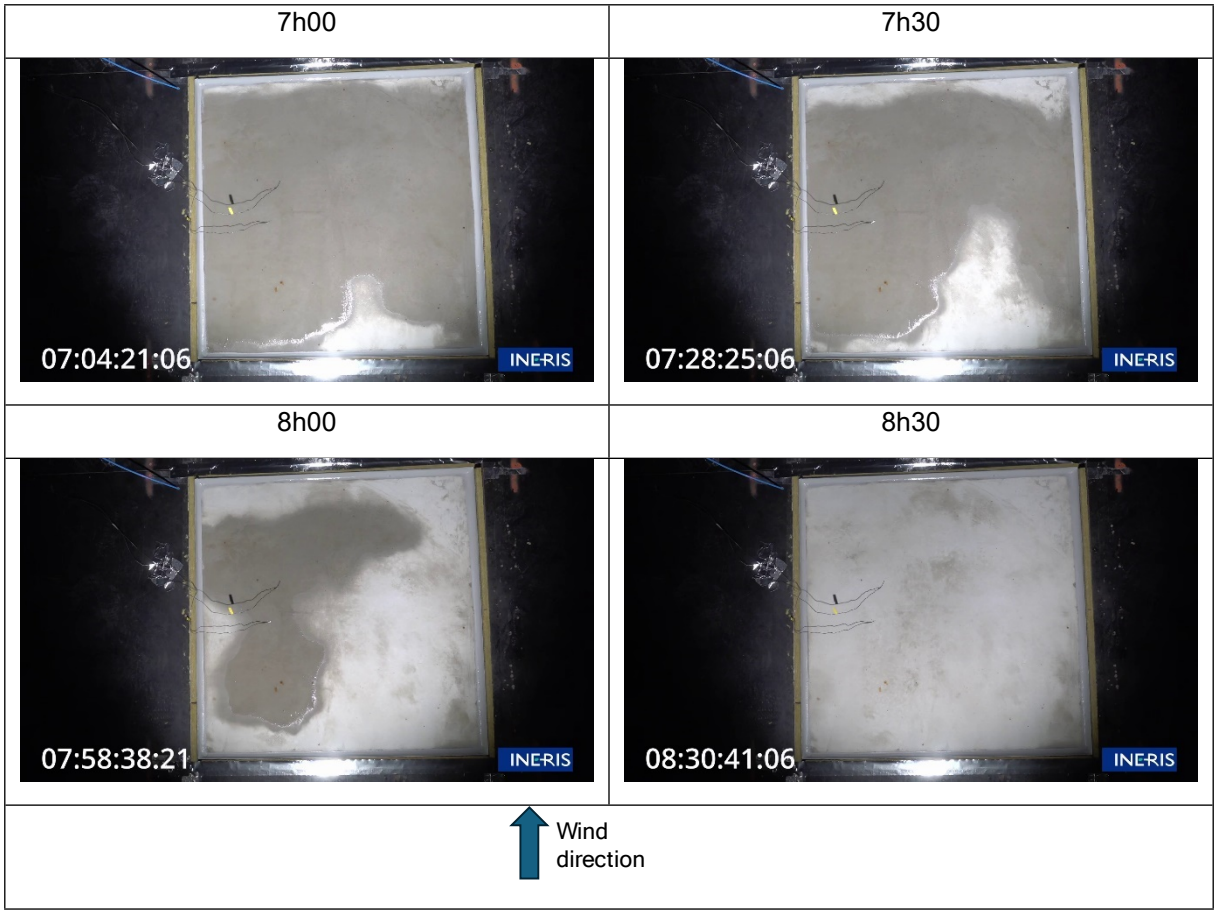


Figure 56 : Evaporation rate decay phase associated with the reduction in liquid layer size

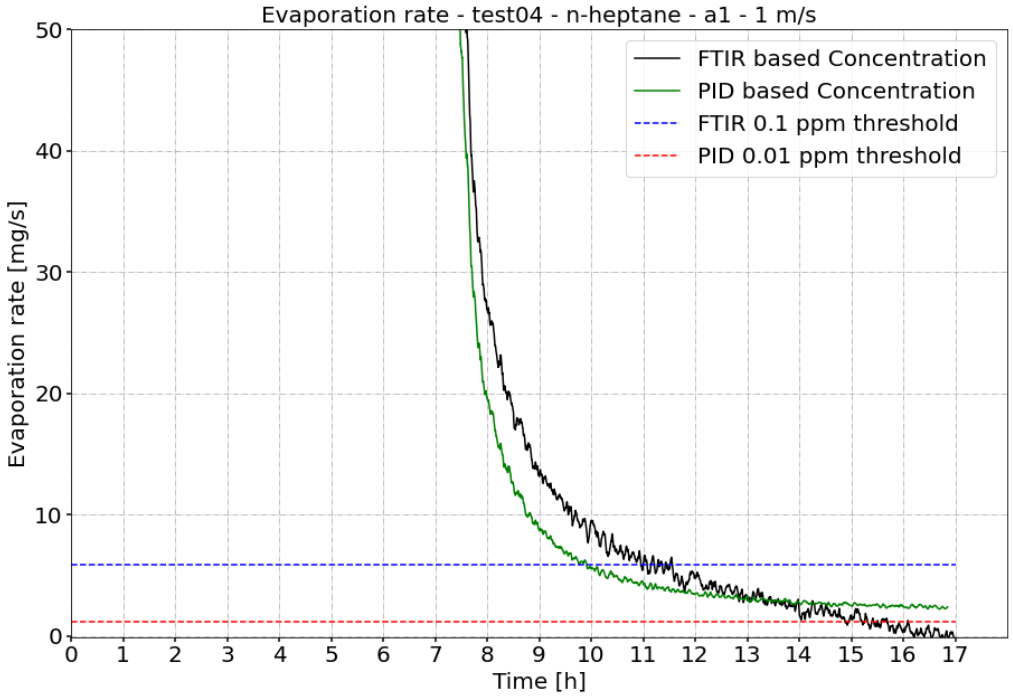


Figure 57 : Evaporation rate measured from pool receding time – test 4

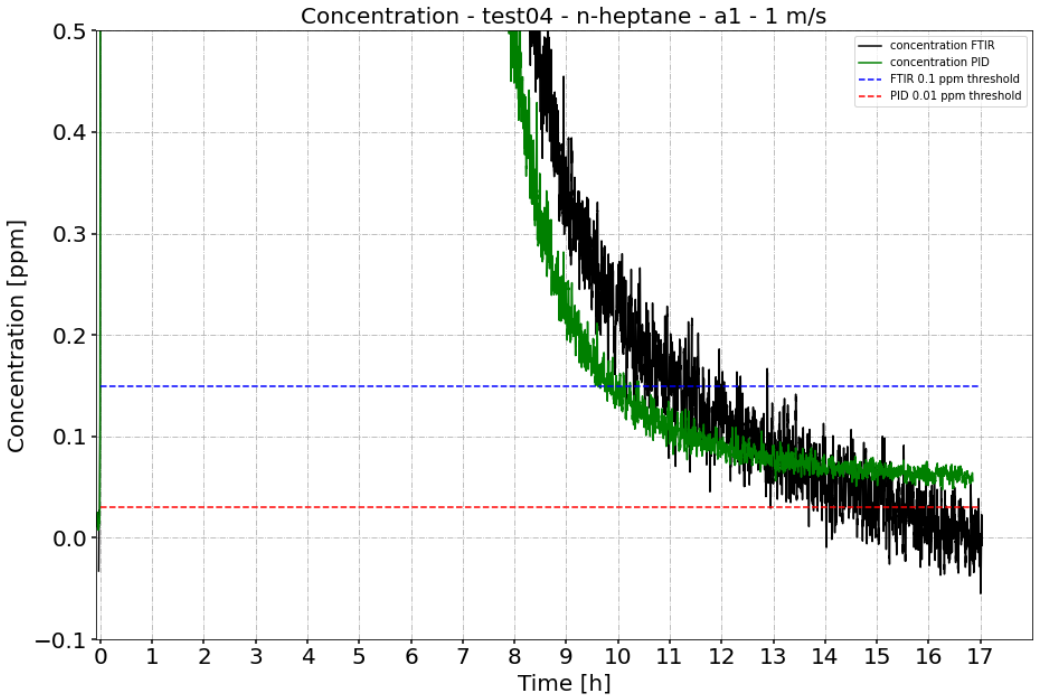


Figure 58 : Global concentration measured from pool receding time – test 4

The negative FTIR concentration observed is due to the noise. The average value of the FTIR concentration tends towards 0.

5.3.5.2 Correction of evaporation rate

It is useful to recall that the evaporation rate is generally expressed by the following semi-empirical formula. [4] :

$$\dot{m} = SKU_h^m L^n Sc^p \frac{P_{sat}(T_p)M}{RT_p} \qquad \textit{Equation 18}$$

With

S	Pool area	[m²]
K	Constant	[-]
U_h	Wind velocity at height h	[m/s]
L	Pool characteristic length	[m]
Sc	Schimdt number associated with the tested product	[-]
T_p	Liquid temperature	[K]
P_{sat}	Saturated pressure	[Pa]
M	Product molar mass	[kg/mol]
R	Ideal gas constant	[J/mol/K]

To eliminate the influence of temperature and thereby enable comparison of evaporation rates measured during two tests conducted under different conditions, the evaporation rate is normalized by neutralizing the temperature-dependent terms as follows :

$$\dot{m}_{revised} = \dot{m}_{measured} \frac{P_{sat}(T_{reference})T_{measured}}{P_{sat}(T_{measured})T_{reference}} \qquad \text{Equation 19}$$

$T_{reference}$	Reference temperature	[K]
$T_{measured}$	Liquid measured temperature	[K]
P_{sat} $(T_{reference})$	Saturated pressure at reference temperature	[Pa]
P_{sat} $(T_{measured})$	Saturated pressure at measured temperature	[Pa]

The reference temperature is fixed to 5°C. The following paragraphs compare the corrected evaporation rates.

5.3.5.3 Verification of the repeatability of the tests

Figure 59 compares the corrected evaporation rates between Tests 1 and 2, and Figure 60 between Tests 6 and 22.

With this correction, it is shown that decreasing pool evaporation phases after the first 10 min are in very good agreement. It should be noted that this correction does not account for the transient phases, which explains the discrepancies observed during the first hour and/or during the decay phase.

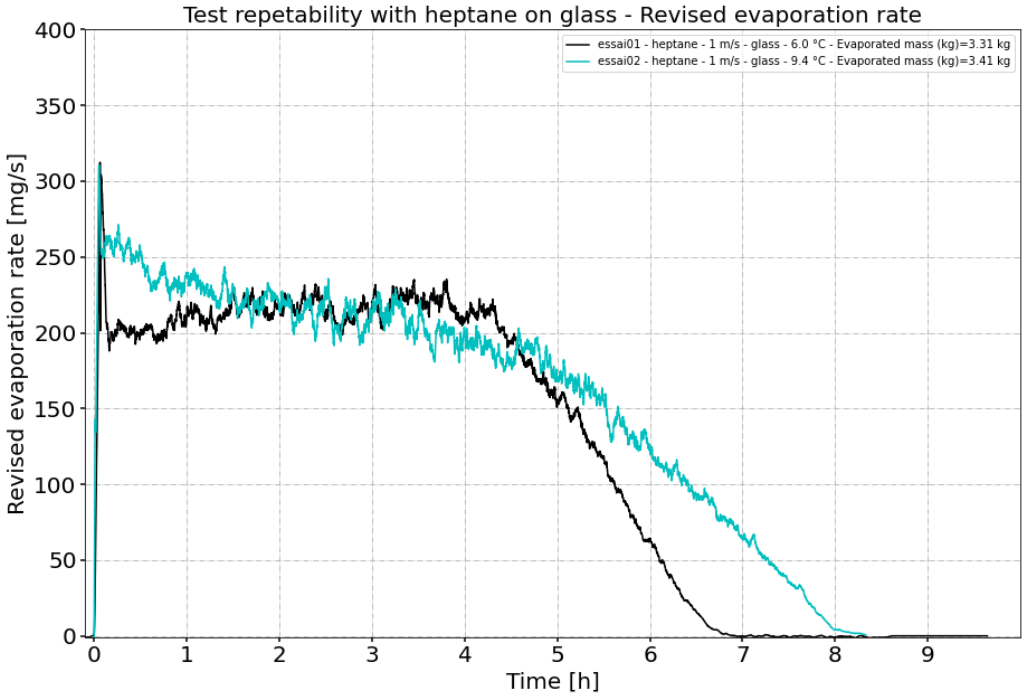


Figure 59 : Repeatability - n-heptane on glass

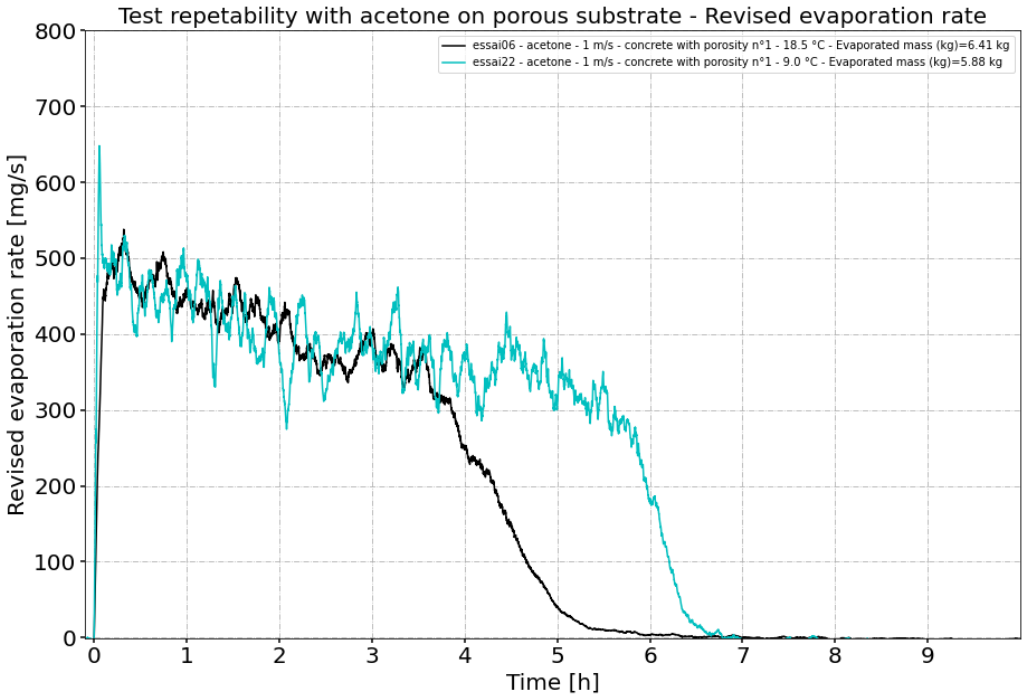


Figure 60 : Repeatability - n-heptane on concrete

5.3.5.4 Impact of initial quantity of liquid

Figure 61 compares the corrected evaporation rates between Tests 4 and 5. The only difference between the tests is the quantity of product involved.

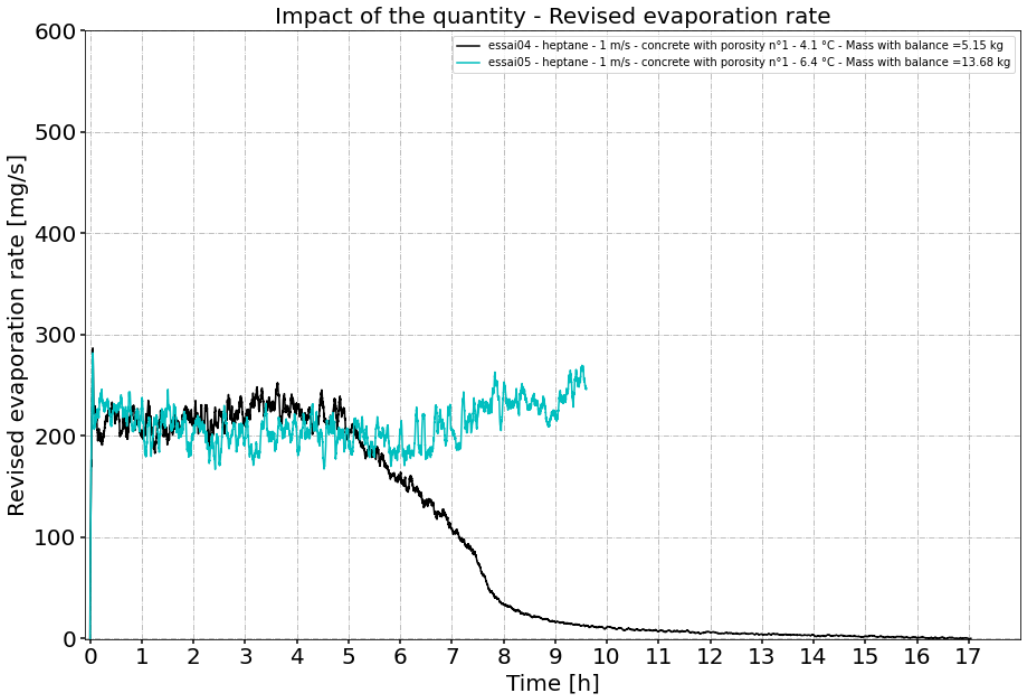


Figure 61 : Impact of initial quantity of liquid on evaporation rate

The difference observed between 3 and 6 hours could be linked to edge effects, which are more significant in test 5 since the substrate is positioned deeper in relation to the ramp level. This could explain a slight slowdown in the evaporation rate due to a weaker wind field at the liquid level when this latter is very low. This observation could be confirmed by modelling.

5.3.5.5 General comparison

Figure 62 presents the average evaporation rates during the phase 1 obtained for all tests involving n-heptane. The start and end of the stationary phase estimated are presented in Table 18.

test	Start (h)	End (h)
test01	1	4
test02	1	4
test03	1	5
test04	1	5
test05	1	9
test06	1	3
test07	0.5	2
test08	1	7
test09	1	12
test10	1	8
test11	1	4
test20	1	14
test21	1	9
test22	1	5

Table 18 : Start and end of the stationary phase

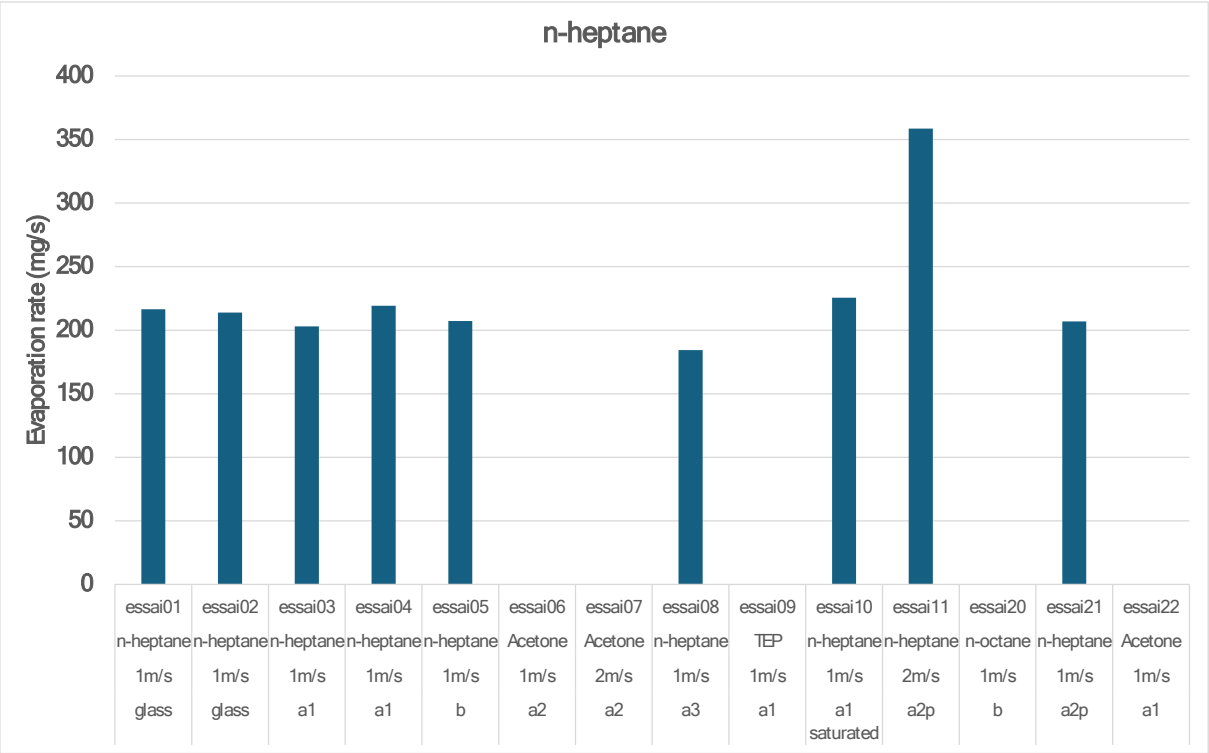


Figure 62 : Average evaporation rate for tests involving n-heptane

Overall, the values obtained with a wind velocity of 1 m/s are in good agreement. The average value is 210 mg/s. The ratio of the evaporation rate measured at 2 m/s to that measured at 1 m/s is 1.71. Considering that the experimental correlations commonly used to simulate the evaporation rate involve a term of the form ($u^{0.78}$) [4], where u is the wind velocity at the reference height, the ratio between the two evaporation rates would therefore be 1.71, which is consistent with the results of these tests.

The figure shows that other parameters, such as the quantity of product, concrete saturation, or concrete coating, have little influence on the evaporation rate during the so-called “steady-state” phase of the test.

Figure 63 presents the average evaporation rates during the steady-state phase (or slightly decreasing plateau) obtained for tests involving acetone.

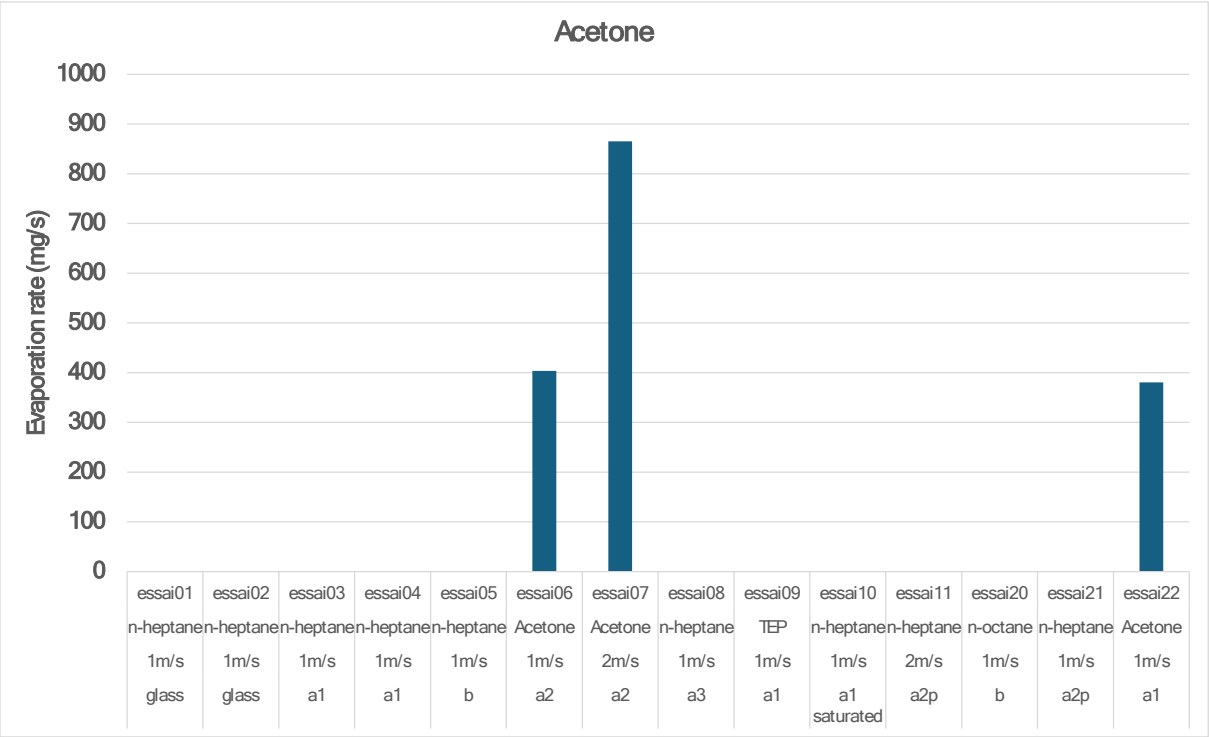


Figure 63 : Average evaporation rate for tests involving acetone

The evaporation rates obtained for a wind velocity of 1 m/s are once again in good agreement. The ratio of the evaporation rate measured at 2 m/s to that measured at 1 m/s is 2.2. This measured value deviates slightly from the theoretical value (2.2 versus 1.7).

Figure 64 presents the average evaporation rates during the phase 1 obtained for the tests involving all four types of products.

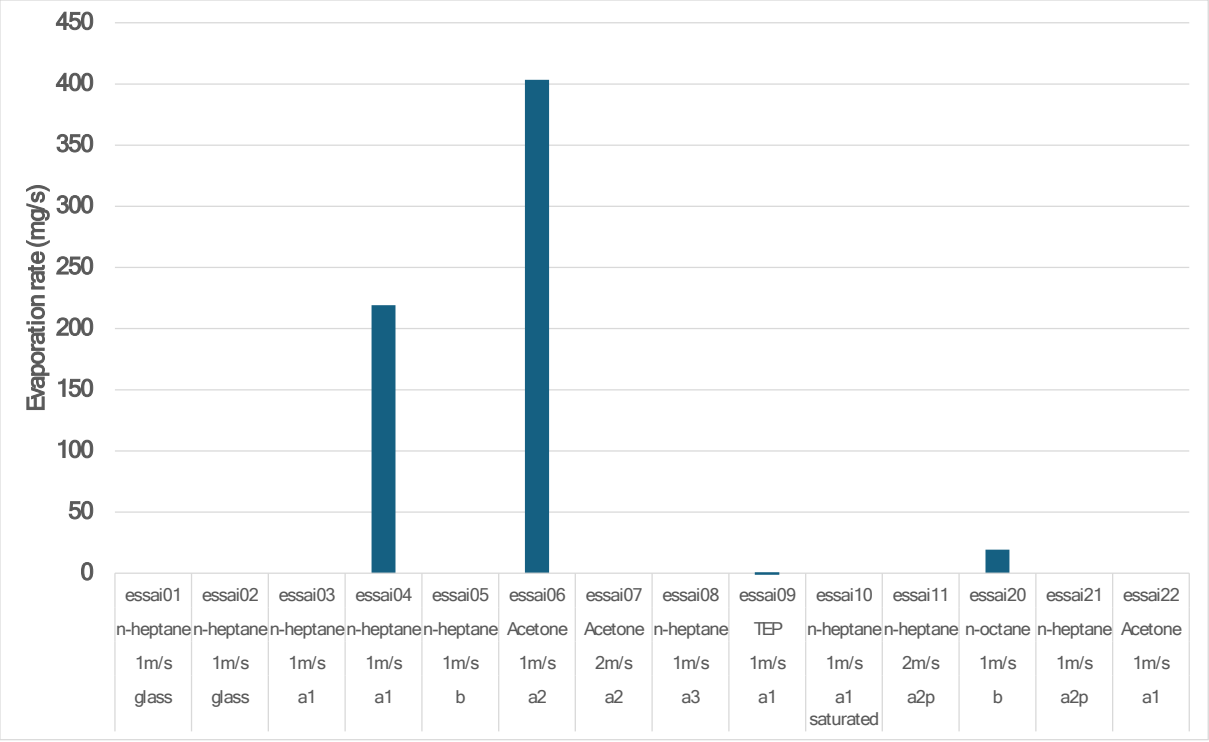


Figure 64 : Average evaporation rate for tests involving the four products at reference conditions

The significant influence of volatility is highlighted by these results. A theoretical analysis of the findings is presented in Section WP 10/WE16 of the project.

6 Experimental results – Droplet evaporation tests

6.1 Description of the test procedure

For tests on glass, the following steps were carried out:

Step	Operation
1	Positioning of the glass with its steel frame on the balance, in the middle of the platform.
2	Start ventilation and adjust the flow rate to reach a velocity of 1 m/s at the reference point.
3	Start data acquisition (concentrations, temperatures).
4	Deposition of droplets on the glass
5	Waiting time between a few minutes and 20 hours.
6	End of test

Table 19 : Steps for tests on glass

For tests on concrete substrates, the following steps were carried out:

Step	Operation
1	Soak the concrete block in water for 24 hours to clean it and saturate it with 100% water.
2	Dry the concrete block in an oven for 8 hours or even 24 hours in some cases.
3	Position the concrete block on the scale, in the middle of the platform
4	Start ventilation and adjust the flow rate to reach a velocity of 1 m/s at the reference point
5	Start data acquisition (concentrations, temperatures).
6	Deposition of droplets on the substrate
7	Waiting time between 2 and 20 hours
6	End of test

Table 20 : Steps for concrete tests

The droplets were always deposited under the same conditions, namely using a multichannel pipette (Figure 65).

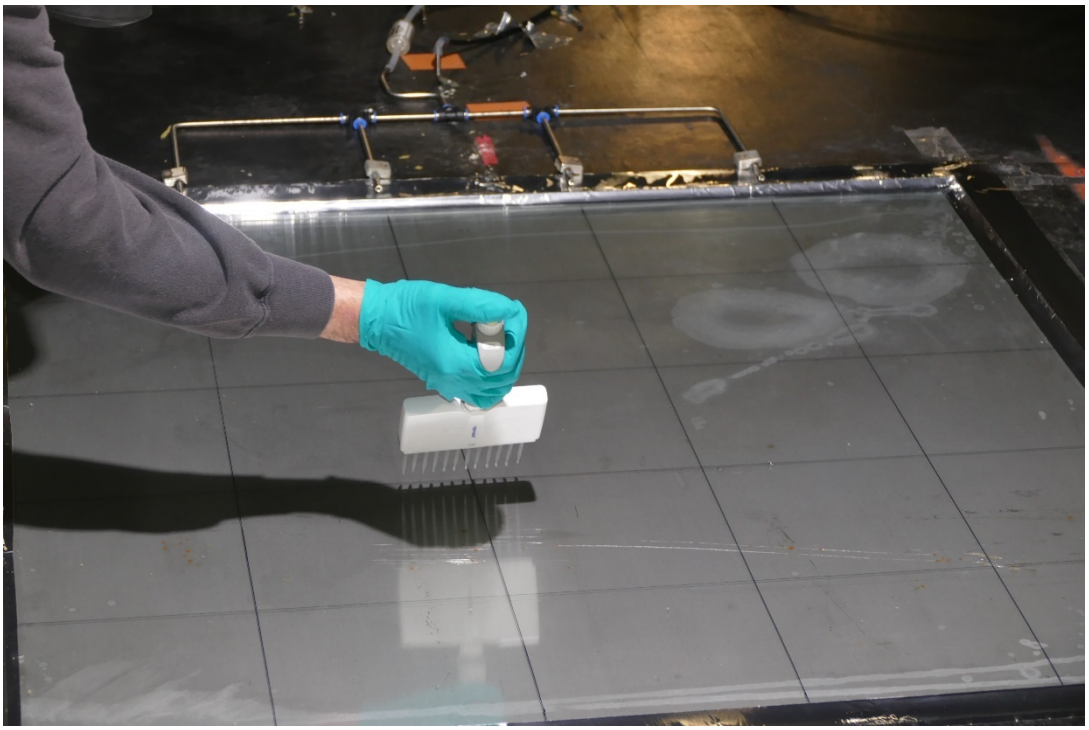


Figure 65: Illustration of droplet deposition on the substrate

For n-heptane and n-octane, 16 x 6 droplets were deposited. For TEP, 9 x 6 droplets were deposited. Figure 66 illustrates the two configurations.

The droplet size is 10 µL.

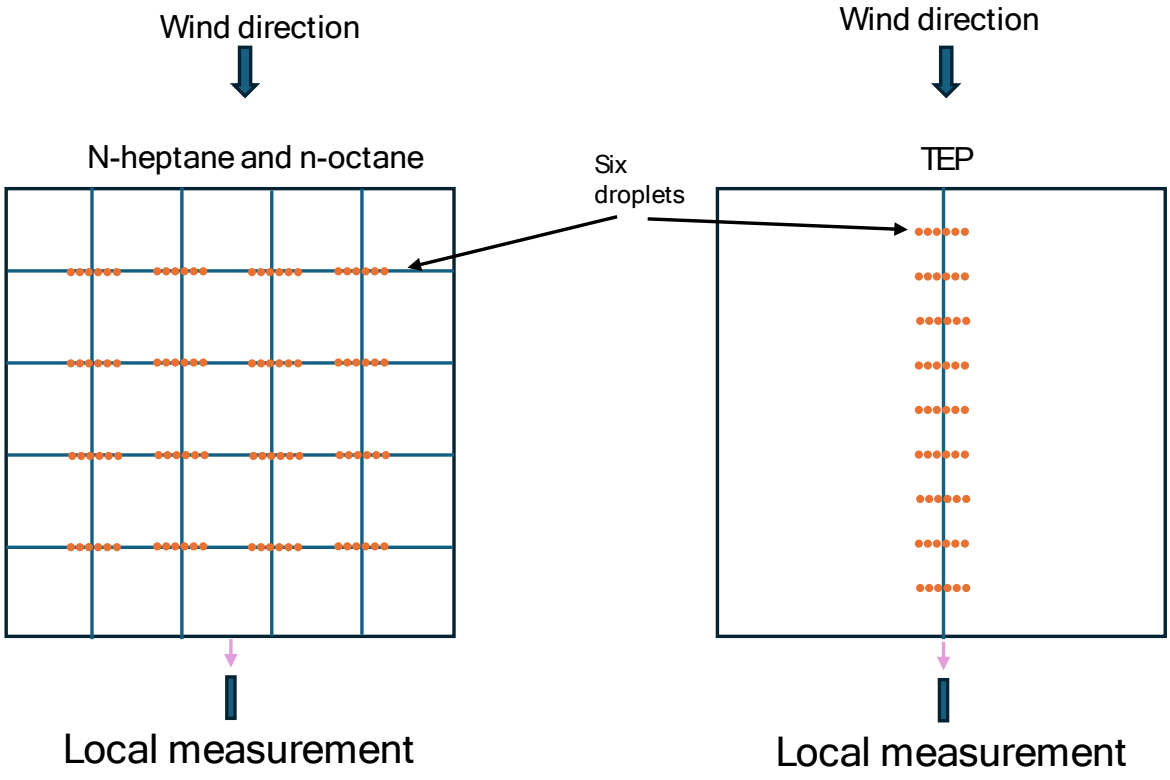


Figure 66 : Position of droplets deposited on the substrate depending on the substance

These tests are based on the assumption that evaporation is relatively similar from one droplet to another. In reality, as the turbulence above the substrate is not homogeneous, the mechanisms of droplet evaporation are certainly different. The number of droplets was chosen according to the quantification limit of the measuring device.

6.2 Analysis of the different parameters

6.2.1 Reference velocity at a height of 1 m

For each test, the velocity in the gallery is measured at the reference point located in the centre of the gallery at a height of 1 m. The average values of 1 m/s are well maintained from one test to another.

6.2.2 Temperature

The initial temperatures for each case are presented in the table 13.

Test N°		Product	Velocity at refence point (m/s)	Substrate	Initial ambient temperature at t0 (°C)	Initial substrate temperature at t0 (°C)
14a	Droplet	Octane (FTIR)	1	glass	11.2	13.1
14b		Octane (PID)	1	glass	13	15.5
15a		Heptane (FTIR)	1	glass	13.7	15.5
15b		Heptane (PID)	1	glass	13.7	15.5
16		Octane (PID)	1	a3	12.4	12.9
17		Octane (PID)	1	a3	8.8	9.3
18a		Octane (FTIR)	1	a3	5.7	6.3
18b		Octane (FTIR)	1	a3	6.3	6.8
19a		Heptane (FTIR)	1	a3	6.9	7.6
19b		Heptane (FTIR)	1	a3	7.2	7.7
19c		Heptane (PID)	1	a3	6.8	7.5
23	Droplet	TEP	1	a1	8.8	5.4
24		TEP	1	glass	5.6	5.8

a1, a2, a3: reference susbtrates (20 mm, porosity N°1)
b: substrate 40 mm
c: substrate 20 mm, porosity n°2

Table 21: Initial temperatures

6.2.3 Product mass

Table 22 shows the initial masses for each test. The volumes per droplet are also provided.

Week	Day	Test N°	Product	Substrate	Velocity at refence point (m/s)	Measured initial mass (kg)	Density (kg/m3)	Deduced total initial volume (L)	Deduced total initial volume (µL)	Deduced initial volume / droplet (µL)
10	07/03	14a	n-octane (FTIR)	glass	1	6.190E-04	709.9	8.719E-04	8.719E+02	9.082E+00
		14b	n-octane (PID)	glass	1	6.190E-04	707.1	8.753E-04	8.753E+02	9.118E+00
		15a	n-heptane (FTIR)	glass	1	5.960E-04	691.3	8.622E-04	8.622E+02	8.981E+00
		15b	n-heptane (PID)	glass	1	5.960E-04	691.3	8.622E-04	8.622E+02	8.981E+00
11	10/03	16	n-octane (PID)	a3	1	6.190E-04	708.5	8.736E-04	8.736E+02	9.100E+00
	11/03	17	n-octane (PID)	a3	1	6.190E-04	711.8	8.696E-04	8.696E+02	9.059E+00
	12/03	18a	n-octane (FTIR)	a3	1	6.190E-04	714.3	8.665E-04	8.665E+02	9.026E+00
		18b	n-octane (FTIR)	a3	1	6.190E-04	713.4	8.677E-04	8.677E+02	9.038E+00
		19a	n-heptane (FTIR)	a3	1	5.960E-04	695.9	8.564E-04	8.564E+02	8.921E+00
		19b	n-heptane (FTIR)	a3	1	5.960E-04	695.9	8.564E-04	8.564E+02	8.921E+00
		19c	n-heptane (PID)	a3	1	5.960E-04	696.2	8.561E-04	8.561E+02	8.918E+00
12	17/03	23	TEP	a1	1	5.22E-04	1086.1	4.806E-04	4.806E+02	8.901E+00
	18/03	24	TEP	glass	1	5.22E-04	1085.5	4.809E-04	4.809E+02	8.905E+00

a1, a2, a3: reference susbtrates (20 mm, porosity N°1)
b: substrate 40 mm
c: substrate 20 mm, porosity n°2

Table 22: Initial inventories

Table 23 shows the mass balances, i.e. the initial masses and total evaporated masses obtained by integrating the evaporation rate curves using the method described in the Chapter 4.

Week	Day	Test N°	Product	Substrate	Velocity at refence point (m/s)	Measured initial mass (mg)	Evaporated mass (mg)	Difference (%)
10	07/03	14a	n-octane (FTIR)	glass	1	619.00	618.82	0.03
		14b	n-octane (PID)	glass	1	619.00	619.72	-0.12
		15a	n-heptane (FTIR)	glass	1	596.00	596.07	-0.01
		15b	n-heptane (PID)	glass	1	596.00	595.88	0.02
11	10/03	16	n-octane (PID)	a3	1	619.00	2275.95	-267.68
	11/03	17	n-octane (PID)	a3	1	619.00	309.15	50.06
	12/03	18a	n-octane (FTIR)	a3	1	619.00	325.57	47.40
		18b	n-octane (FTIR)	a3	1	619.00	285.95	53.80
		19a	n-heptane (FTIR)	a3	1	596.00	330.74	44.51
		19b	n-heptane (FTIR)	a3	1	596.00	243.61	59.13
		19c	n-heptane (PID)	a3	1	596.00	230.51	61.32
12	17/03	23	TEP	a1	1	522.00	11.52	97.79
	18/03	24	TEP	glass	1	522.00	222.06	57.46

a1, a2, a3: reference susbtrates (20 mm, porosity N°1)
b: substrate 40 mm
c: substrate 20 mm, porosity n°2

Table 23: Mass balances

For the cases involving a concrete substrate, the mass balance shows discrepancies. The explanations are provided in the following paragraphs.

6.2.4 Evaporation rate

Evaporation rates are deduced directly from the concentrations measured at the measuring point located at the rear of the substrate using different systems (FTIR, PID, AP4C) as described in the paragraph 4.2. The evaporation rate curves obtained with the three measurement methods are presented in APPENDIX 8. The dilution factor applied in Equation 17 are presented in Table 24.

Week	Day	Test N°	Product	Substrate	Velocity at refence point (m/s)	Dilution factor [-]
10	07/03	14a	n-octane (FTIR)	glass	1	1060.00
		14b	n-octane (PID)	glass	1	665.00
		15a	n-heptane (FTIR)	glass	1	946.00
		15b	n-heptane (PID)	glass	1	1130.00
11	10/03	16	n-octane (PID)	a3	1	665.00
	11/03	17	n-octane (PID)	a3	1	665.00
	12/03	18a	n-octane (FTIR)	a3	1	1060.00
		18b	n-octane (FTIR)	a3	1	1060.00
		19a	n-heptane (FTIR)	a3	1	946.00
		19b	n-heptane (FTIR)	a3	1	946.00
		19c	n-heptane (PID)	a3	1	1130.00
12	17/03	23	TEP	a1	1	1351.00
	18/03	24	TEP	glass	1	1351.00

a1, a2, a3: reference susbtrates (20 mm, porosity N°1)
b: substrate 40 mm
c: substrate 20 mm, porosity n°2

Table 24: Dilution Factors

6.2.4.1 N-octane

Figure 67 presents the evaporation rate for the tests carried out on n-octane droplets.

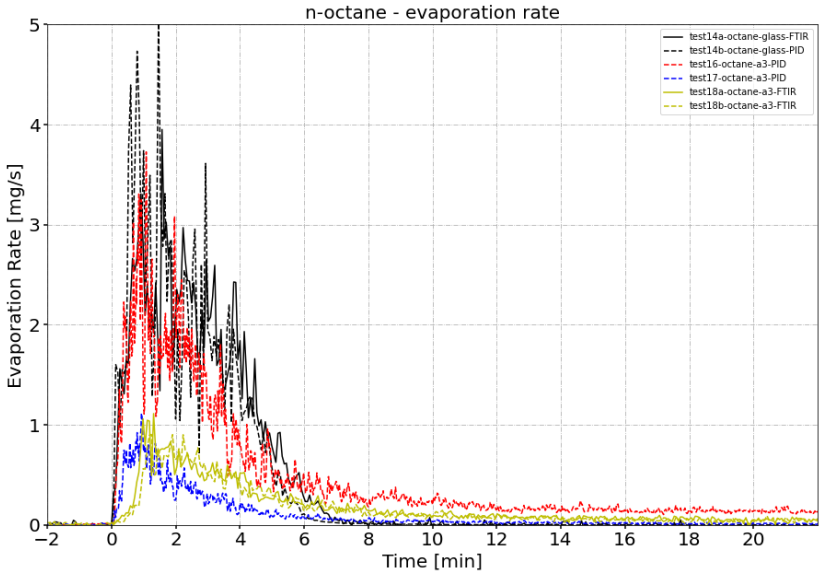


Figure 67: Evaporation rate – n-octane droplets

The mass balance obtained by integrating the curves is presented in Table 23.

The mass balance is satisfactory for the tests conducted on glass.

For Tests 17, 18a and 18b (performed on concrete), the evaporation rate curves exhibit comparable kinetics. The discrepancy between the blue curve (Test 17) and the yellow curves (Tests 18a and 18b) may be attributed to the ambient temperature, which was 3°C higher during Test 17. Furthermore, for these three tests, the measured mass is approximately 50% lower than the mass initially deposited. This deviation may result from:

- an overestimation of the dilution factor $F_{dilution}$, as the vapor cloud appears to behave differently from that observed on the glass substrate. It would therefore be possible to reassess the $F_{dilution}$ factor while preserving mass conservation,
- the migration of part of the liquid into the concrete substrate.

For Test 16, the measured mass is significantly higher than the deposited mass, which is inconsistent with the other results. While the overall shape of the curve is not called into question, its amplitude appears excessive, and the PID indicates a non-negligible concentration after 20 minutes, likely due to instrumental drift or external contamination.

6.2.4.2 N-heptane

Figure 68 presents the evaporation rate for the tests carried out on n-heptane droplets.

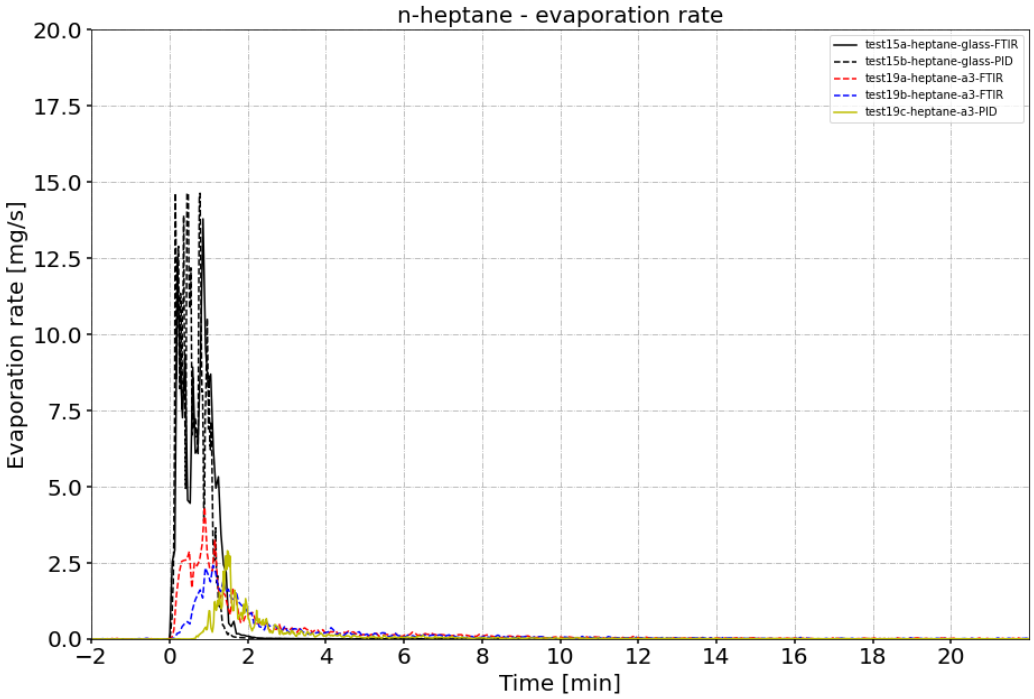


Figure 68: Evaporation rate – n-heptane droplets

The mass balance obtained by integrating the curves is presented in Table 23.

The mass balance is also satisfactory for the tests conducted on glass.

For Tests 19a, 19b and 19c, the measured mass is approximately 50% lower than the deposited mass. This discrepancy may have the same origin as that described in the previous paragraph, namely overestimation of the dilution factor $F_{dilution}$, since the vapor cloud behaves differently from that observed on the glass substrate. It would therefore be possible to reassess the $F_{dilution}$ factor while maintaining mass conservation. The migration of part of the liquid into the substrate could also account for this mass discrepancy.

The evaporation rate kinetics differ for the three tests performed on concrete, as the evolution of the evaporation rate is sensitive to the droplet deposition time for volatile liquids. Droplets deposited very rapidly will exhibit a sharp increase in the evaporation rate.

6.2.4.3 TEP

Figure 69 presents the evaporation rate for the tests carried out on TEP droplets.

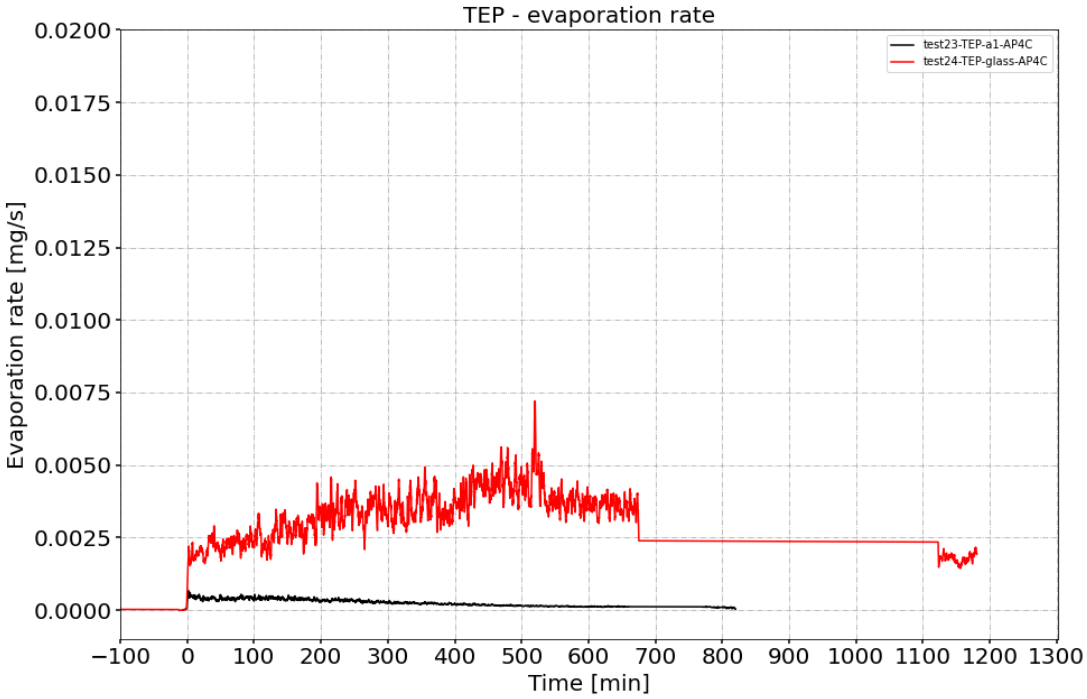


Figure 69: Evaporation rate – TEP droplets

The mass balance obtained by integrating the curves is presented in Table 23.

For both tests, the measured mass is approximately 50% to 100% lower than the deposited mass, as the tests were terminated before complete evaporation of the droplets.

Figure 69 highlights the impact of substrate porosity on evaporation rates, which are lower on porous surfaces because a significant proportion of the liquid contained in the droplet is absorbed by the pores of the substrate and is then re-emitted at a lower rate over a longer period. The test on porous substrate with TEP was interrupted before completion, which means that its extension cannot be verified, but the remaining masses show that the mass evaporated from the non-porous substrate is 222 mg of TEP, whereas that from the porous substrate is only 11 mg of TEP.

The theoretical analysis of the results is carried out in part WE 16 of the project.

7 Conclusion

MODISAFE (Modelling of Sources and Agent Fate) is an international collaborative project dedicated to the study of three technical themes related to the atmospheric dispersion of hazardous substances: the evaporation of pool and droplets from porous and non-porous surfaces, deposition and resuspension phenomena, and the dispersion of buoyant plumes in urban environments.

This document is the report on the campaign of tests on evaporation from pools and droplets on porous and non-porous surfaces.

This campaign consisted of conducting 14 pool evaporation tests and 13 droplet evaporation tests in the Ineris fire galery.

The first step was to measure the vertical wind fluctuation profiles in the fire fire gallery. The various parameters associated with turbulence were determined, namely the mean wind velocity, the main terms of the Reynolds stress tensor, the integral length in the longitudinal axis, the kinetic energy of turbulence and, finally, the friction velocity.

Despite measured fluctuations in wind speed and direction, primarily driven by natural atmospheric variability, these discrepancies were not significant enough to compromise the validity of the evaporation experiments.

. Indeed, the observed fluctuations fall within ranges compatible with the experimental requirements and remain consistent with the uncertainties commonly associated with meteorological measurements in real-world environments.

A comparative analysis of the data obtained from the various measurement devices led to the conclusion that, although some isolated divergences were observed, they do not reflect any major instability in wind conditions over the duration of the experiments. The aerodynamic conditions were therefore regarded as sufficiently homogeneous and representative to allow the experiments to be carried out under controlled conditions.

In this context, the recorded wind parameters were deemed compatible with the objectives of the evaporation tests, whether concerning the study of liquid pools or droplets. The minor disparities observed did not introduce any significant bias in the interpretation of the results, nor did they compromise the reproducibility of the phenomena under investigation. On the contrary, they made it possible to account for a realistic degree of variability, closely reflecting the conditions encountered in real-life scenarios.

7.1 Pool evaporation

For the pool evaporation tests, a reference configuration was defined in advance. This involved 5 L of n-heptane poured onto a glass plate (non-porous substrate) with a rim forming a 1 m² pool. The reference wind velocity at a height of 1 m was 1 m/s. Based on this reference test, four other parameters were tested:

- The volatility of the product (acetone, n-octane and TEP),
- Wind velocity at 2 m/s,
- The nature of the substrate: one dry concrete substrate with a porosity of approximately 9%, another with 12% porosity, and a third with a waterproof coating. The initial saturation level of the substrate with the product was also tested,
- The quantity of product.

The various parameters measured during the tests were the following :

- The temperature of the substrate and the liquid,
- The concentration in the near field of the substrate,
- The concentration in the extraction duct to estimate the evaporation rate,
- The mass of the substrate,
- Ambient conditions (RH, temperature, pressure).

It should be noted that as the tests were not carried out under the same temperature conditions, a correction was applied to the evaporation rate in order to compare results.

The main results that emerged during this campaign are as follows:

- The tests showed relatively consistent results,
- The repeatability of the tests is acceptable,
- The impact of wind velocity was demonstrated by experimental correlations.

7.2 Evaporation of droplets

Several parameters were tested in the droplet evaporation tests:

- Product volatility (n-octane, h-heptane and TEP),
- The nature of the substrate: 1 dry concrete substrate with a porosity of approximately 9% and a non-porous glass substrate.

The following parameters were measured during the tests:

- The temperature of the substrate and the liquid,
- The concentration in the near field of the substrate,
- The mass of the liquid before and after the test (if relevant),
- Ambient conditions (RH, temperature, pressure),

For n-heptane and n-octane, 16x6 droplets were deposited, while for TEP, only 9x6 droplets were deposited.

The main results that emerged during this campaign are as follows:

- The tests showed relatively consistent results,
- The repeatability of the tests is acceptable.
- The impact of substrate porosity was demonstrated by a lower evaporation rate linked to the mechanism of droplet absorption by the pores of the concrete.

The theoretical analysis of the results, whether from pool tests or droplet tests, is carried out in part WP 10/WE16 of the project.

8 References

[1] American Institute of Chemical Engineers – Design Institute for Physical Properties (DIPPR®)

[2] Ineris – Omega 12 – Methods for assessing and preventing accidental risks – Atmospheric dispersion (mechanisms and calculation tools) – 16 March 2021

[3] Ineris – Guide to Good Practice for 3D modelling of atmospheric dispersion scenarios in accident situations – GT 3D dispersion – https://aida.ineris.fr/sites/aida/files/guides/Guide_Bonnes_Pratiques_V2.02_RNT.pdf

[4] Thibauld Pénelon et al, Pool evaporation: Experimental tests at medium-scale with petrol, Journal of Loss Prevention in the Process Industries 65 (2020) 104072

[5] Katja Mader-Arndt et al, Single particle contact versus particle packing behaviour: model-based analysis of chemically modified glass particles Granular Matter - DOI 10.1007/s10035-013-0478-9

[6] Kuldeep Singh et al, Surface roughness characterisation using representative elementary area (REA) analysis, www.nature.com/scientificreports

[7] Zbigniew POKRYSZKA, Arnaud CHARMOILLE, Gaëtan BENTIVEGNA - Development of methods for geochemical monitoring in the gas phase at the surface and in the intermediate cover of geological CO2 storage sites – OGST 2010 No. 65(4)

[8] INERIS study report - Documentation relating to the transfer of know-how concerning the INERIS method for measuring surface gas flux - DRS-06-68890/R01

[9] Alan Robins, Paul Hayden, Emma M.M. Wingstedt, MODITIC wind tunnel experiments – FFI (Norwegian Defence Research Establishment) Report – 13 october 2016.

9 Appendices

List of appendices :

APPENDIX 1 Analysis report on the characteristics of concrete substrates 19 pages 72
APPENDIX 2 Characteristics of glass 3 pages 92
APPENDIX 3 Pool evaporation tests – Characteristics of the paint applied to substrate block a2 1 page 96
APPENDIX 4 : Pool evaporation tests – Temperature changes measured with different thermocouples – 7 pages.....97
APPENDIX 5 : Pool evaporation tests – Temperature change measured with different thermocouples during the first 20 minutes – 7 pages 104
APPENDIX 6 : Pool evaporation tests – Change in concentration measured locally – 7 pages.....111
APPENDIX 7: Pool evaporation tests – Evolution of evaporation rate – 7 pages 118
APPENDIX 8 : Droplet evaporation tests Evolution of evaporation rate – 7 pages.....125

APPENDIX 1

Analysis report on the characteristics of concrete substrates

19 pages

Test report of tests – Characterisation of concrete

1. Purpose and scope

Ce rapport présente la caractérisation de bétons durcis selon les paramètres suivants :

- Énergie de surface (via goniométrie / angle de contact),
- Diamètre de pores (distribution de tailles),
- Rugosité de surface (profilométrie 3D),
- Porosité effective,
- Conductivité thermique,
- Densité (apparente et squelettique).

Les méthodes retenues, l'incertitude de mesure et les résultats normalisés sont détaillés.

2. Samples and packaging

Les échantillons étudiés sont des carottes cylindriques (éprouvettes) prélevées dans des plaques de béton d'une épaisseur de 60 mm. Le béton est armé par un ferraillage interne, ce qui permet de limiter ou d'éviter l'apparition de fissures lors de la manipulation des blocs. Les carottes ont été extraites à l'aide d'une scie cloche, de manière à obtenir des cylindres de 62 mm de diamètre, sans cavité centrale. Ces éprouvettes présentent donc une géométrie homogène et représentative du matériau massif, adaptée aux différents essais de caractérisation.

Avant les essais, toutes les carottes ont été soumises à un séchage contrôlé à 40 °C dans une étuve ventilée pendant 4 jours. L'humidité relative de l'air ambiant du laboratoire (généralement comprise entre 40 et 45%) a été maintenue constante. Les éprouvettes ont ensuite été laissées en stabilisation pendant 3 jours, jusqu'à atteindre une masse stable, définie par une variation relative inférieure à $\triangle m < 0{,}1$ % sur 24 h et 48 h consécutives. À noter qu'aucun ponçage, polissage ou nettoyage par solvants/eau n'a été réalisé avant les mesures. Cette procédure garantit un état hygrométrique reproductible et limite les biais liés à l'humidité résiduelle pour l'ensemble des essais de caractérisation.

3. Test methodologies

3.1. Apparent density

La densité apparente (ou masse volumique apparente) d'un béton durci est le rapport de la masse de l'éprouvette à son volume apparent total (solide + pores ouverts/fermés) :

$$\rho_b = \frac{m}{V}$$

Le volume V est déterminé par pesées hydrostatiques conformément aux pratiques normalisées. Les éprouvettes étant des carottes prélevées in situ, la voie hydrostatique offre une meilleure robustesse que la voie géométrique lorsque les faces ne sont pas parfaitement parallèles/plane-parallèles ou présentent de légers éclats ; elle réduit l'incertitude sur V et améliore la comparabilité entre séries. Sa mise en place revient à considérer :

$$V = \frac{(m_{sss} - m_i)}{\rho_{eau}}$$

où m_{sss} est la masse saturée essuyée, m_i la masse immergée, et ρ_{eau} la masse volumique de l'eau au bain thermostaté (température consignée). On en déduit :

$$\rho_b = \rho_{eau} \cdot \frac{m_d}{m_{SSS} - m_i}$$

En termes opérationnels, chaque éprouvette est (après conditionnement à 40 °C jusqu'à masse stable, cf. précédemment) : (i) saturée, (ii) essuyée puis pesée pour m_{sss}, (iii) pesée immergée pour m_i (élimination préalable des bulles), (iv) séchée et pesée pour m_d. Les formules ci-dessus sont appliquées pour calculer ρ_b selon l'état de référence. Pour chaque état de masse, cinq mesures (répétitions) sont réalisées.

Une vérification a été effectuée par deux re-pesées à +1 h et +2 h dans les mêmes conditions ambiantes, afin de détecter d'éventuelles dérives (évaporation résiduelle, reprise d'humidité, flottabilité/bulles). Aucune dérive n'a pu être constatée.

3.2. Surface roughness by profilometry

La rugosité a été mesurée simplement par profilométrie sur des surfaces telles que prélevées (sans ponçage ni polissage). Pour chaque carotte, des zones représentatives ont été acquises à champ fixe (quelques mm^2) avec un pas latéral micrométrique. Les données ont été mises à plat puis filtrées conformément à l'ISO 25178, avant calcul des paramètres Sa et Sq. Les résultats sont restitués en moyenne ± écart-type (n zones par carotte) afin d'offrir une image fidèle de l'état réel des surfaces pour l'interprétation des mesures (mouillabilité/adhérence, échanges thermiques).

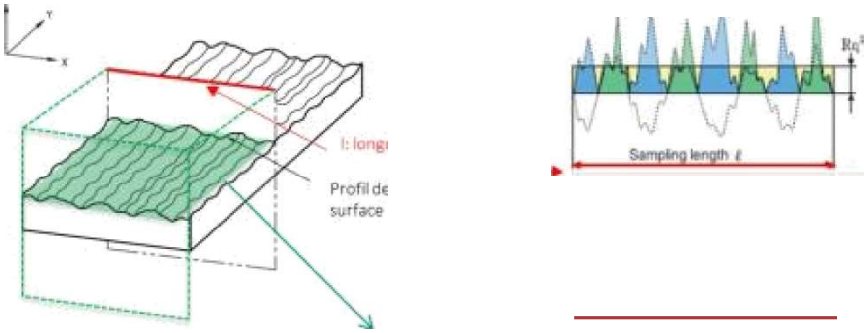


Figure 1. Schematic representation of the characterisation of surface parameters according to a selection (Ra, Rq - standard NF EN ISO 4287) and *following a surface (Sa, Sq - standard NF EN ISO 25178-2).*

3.3. Pore size distribution (pore diameter)

The diameter of pores in concrete varies depending on the types of pores present, which influence its properties, particularly permeability and durability. In particular, we distinguish between

- Air pores or entrained air bubbles, with diameters ranging from 10 µm to 1 mm.
- Capillary pores, which generally have diameters between 0.01 µm and 5 µm. These pores are essential because they have the greatest influence on the permeability of concrete.
- Gel pores, with diameters less than 4 nm (40 Å) containing adsorbed water that is difficult to extract by drying.
- Macropores in the transition zone, with diameters between 01 and 1 µm.
- Effective air pores in air-entrained concrete, with diameters between 0.02 and 0.30 mm (20 to 300 µm), provide protection against freezing.

Reducing the average diameter of capillary pores, particularly by reducing the water/cement ratio, decreases the porosity and permeability of concrete, thereby increasing its durability. The size and distribution of pores therefore play a key role in the behaviour and resistance of concrete to external aggressions.

Depending on the size of the pores, different measurement techniques can be used to determine the distribution of pore diameters. Figure 2 illustrates the two techniques used in this study, namely

- Gas adsorption porosimetry (Nea 77 K, Ar at 87 K, possibly CO at 273 K for ultra-micropores). This technique provides the specific surface area (BET) and size distribution in the micro/mesoporous range (= 0.5—50 nm) via the analysis of adsorption/desorption isotherms.
- Mercury intrusion porosity (MIP). MIP mainly probes pore throats in the network based on Washburn's equation: r = $-2\gamma\cos\theta \; f P$
  (with typically γ(Hg) = 0.485 N-m^{-}* and θ = 140º on cement matrices), which

allows entry radii of the order of a few nanometres to a few hundred micrometres to be achieved depending on the pressure (e.g. = 3—5 nm at -200—400 MPa).

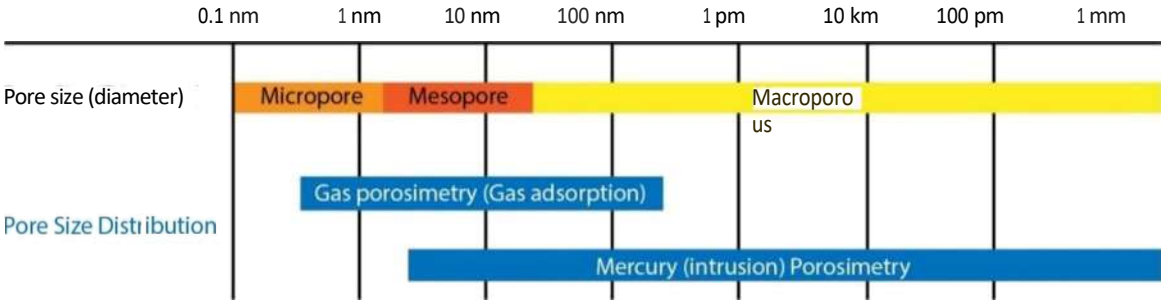


Figure 2. Techniques for measuring pore distribution in concrete (based on the diameters to be characterised

In this study, only one MIP measurement was performed.

3.4. Surface energy by goniometry (contact angle)

Principle: Goniometry is a method for evaluating the surface properties of a material by measuring the contact angle formed by a drop of liquid on its surface (see Appendix). It is based on the equilibrium of surface tensions at the solid/liquid/vapour interfaces and can be used to determine the wettability of a solid and its surface energy.

The contact angle (static or dynamic) is defined as the angle formed at the triple interface between the solid, liquid and vapour. Its measurement is influenced by surface roughness and porosity, which can cause partial absorption of the liquid and alter the shape of the drop (see Appendix).

The characterisation of surface energy properties was carried out according to the acid-base theory proposed by van Oss et al. This approach allows surface energy to be broken down into a dispersive component of the Lifshitz-van der Waals type (γ^{LW}) and a polar acid-base component (γ^{AB}, which is itself divided into acid (γ^{+}) and base (γ^{-}) terms. Determining these components requires measuring the contact angles with at least three liquids of different polarities. Following the recommendations of Della Volpe et al. (2004) and Della Volpe & Siboni (1997, 2000), the chosen triplet systematically includes two polar liquids and one non-polar liquid in order to limit the occurrence of negative values when calculating the components. For this study, the liquids selected are: water, formamide and diodomethane. Their surface energy properties are listed in the table below.

Table 1. Energy properties of liquid surfaces.

Liquids	γ_L (mN/m)	γ_L^{LW} (mN/m)	γ_L^{AB} (mN/m)	γ_L^{+} (mN/m)	γ_L^{-} (mN/m)
Water	72.8	21.8	51.0	25.5	255
Formamide	58.0	39.0	19.0	2.28	396
Diiodomethane	50.8	50.8	0.0	0.0	0

Equipment: Contact angle measurements were performed using an optical goniometer equipped with a microlitre drop deposition system and a high-resolution camera. The device allows drops of a few microlitres (water, formamide, diiodomethane) to be deposited precisely onto the surface of the samples. The evolution of the drop is recorded immediately after deposition and when the drop grows due to the addition of liquid (static and dynamic angles), under controlled lighting, in order to limit the effects of evaporation and absorption by the porous substrate. The contact angles are determined by image analysis, using dedicated software that adjusts the drop profile using the Young-Laplace equation. Figure 3 shows the experimental goniometry device used to measure contact angles, comprising the drop deposition system, the acquisition camera and the associated analysis software.

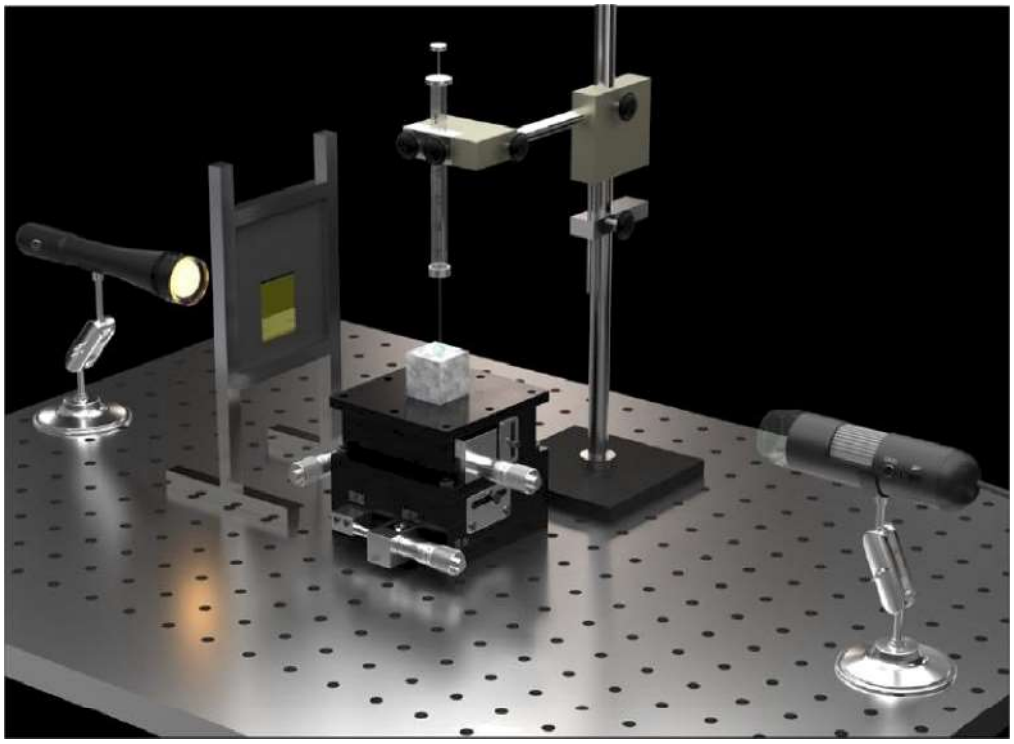


Figure 3. Illustration of a contact angle measurement *device (Kabir, 2023).*

l'fléthodoloeie: The accuracy of contact angle (CA) measurements is influenced not only by the shape and volume of the drops, but also by the fitting algorithm used to determine their profile. The following paragraphs address these two aspects in turn in order to clarify the technical choices and achievements implemented.

In order to exclude the effect of gravity, the diameter of the drop must not exceed the capillary length (λ) of 2.73 mm for deionised water, estimated by the following equation

$$\lambda = \sqrt{\frac{\gamma}{\rho \cdot g}}$$

where ρ is the density of the liquid (997 kg $m^{-3}$for deionised water), g is the acceleration due to gravity (9.81 m/s^2), and γ is the surface tension (= 71.99 mN-m^{-}* for deionised water, see methods section). Thus, the maximum volume of a drop of deionised water (at 23 °C and 50% RH) must not

exceed 10.7 µL for its geometry not to be significantly distorted by its own weight. Conversely, drops smaller than 3 µL should not be analysed as they are easily disturbed by the liquid dispensing system and by the prolonged dissipation of their kinetic energy. Furthermore, sub-microlitre droplets (nano- and picolitres) can evaporate in a matter of seconds (or even milliseconds) and require the use of very fast cameras (100–2000 fps).

As part of this study, the volume of drops used to characterise contact angles was determined on deionised water, and the target value was 4 + 0.5 µL or 10 + 0.5 µL depending on the surfaces and the technical constraints encountered with the surfaces.

In-house software was developed for the accurate estimation of contact angles from images/videos. The processing flow is as follows: (i) import images (raw or video format), (ii) select the ROI around the droplet (with automatic cropping by gradient), (ii) detect the baseline (solid-gas line) by robust regression, (iv) detect the droplet contour by gradient analysis/segmentation, (v) sampling of at least $N > 6$ points in the vicinity of each contact point, with a numerical step $\Delta h < 0.05$, (vi) adjustment of the drop profile using cubic *spline* polynomials and calculation of the tangents at each triple point to obtain θ_{gauche}, $\theta_{straight}$ θ_{mean}, (vi) metric calibration by line and internal reference (fixed diameter of the injection syringe measured separately using a precision tool). The parameters (N, Δh, ROI width, gradient thresholds) were optimised on the basis of representative images in order to stabilise the estimation of tangents to background noise and optical variations. The choice *of* cubic *spline* limits the number of settings and reduces operator influence compared to the DropSnake method (ImageJ plugin), while producing comparable measurements. In practice, the operator indicates the baseline and visually verifies the adjustment the contour ; the remains the processing is automated (pre-/post-processing, angle calculations, export). Validation was conducted on a common set of images analysed: (a) by the in-house software *(*cubic *spline*) and (b) by Images/DropSnake. Comparability was assessed by (1) correlation of measured contact angles, (2) mean bias and standard deviation, (3) paired agreement, and (4) sensitivity to operator settings (inter-/intra-operator repetitions). Both approaches yield consistent results, with the spline being easier to implement (fewer parameters to adjust) and therefore less sensitive to user experience.

ImageJ is a multi-platform, open-source image processing and analysis software developed by the National Institutes of Health, http://imageinih.gov/i|/

3.5. Effective porosity

In this study, we are interested in the effective porosity of different types of concrete, considering the concept of water-accessible porosity. This is the fraction of the test specimen's volume consisting of open, interconnected pores into which water can actually penetrate.

$$\Phi_{eau} = \frac{V_{éprouvette}}{V_{eau\ absorbée}}$$

with $V_{éprouvette}$ and $V_{eau\ absorbée}$, the volumes of the concrete samples and the volume of water absorbed.

For operational purposes, this approach has been translated into a methodology using standard NF P 18-459, which allows Φ_{eau} to be estimated from three measurements: dry mass (m_d), m and submerged mass (m_i) (hydrostatic weighing). The porosity is then expressed as:

$$\Phi_{eau} = \frac{m_{sss} - m_d}{m_{sss} - m_i}$$

The term $m_{sss} - m_i$ corresponds to the mass of displaced water and is equal to $\rho_{eau} \cdot V$ (where ρ_{eau} is the density of water at the test temperature and V is the apparent volume).

The test was conducted in three identical cycles to verify stability/repeatability:

1. Saturation: immersion in water for 48 hours (covered bath, clean water, controlled temperature; degassed bath if possible to limit bubbles).
2. Weighing in saturated condition:
   - remove the test piece, wipe with a lint-free cloth; measure m_{sss} (balance accurate to 0.01 g);
   - weigh immersed to obtain m_i
3. Drying: oven at 40°C for 4 days, then stabilisation at constant mass (criterion: m_dΔm < 01% over 24 h and 48 h) then measure the mass change. The temperature of 40 °C is used to preserve the microstructure and avoid microcracking due to 105 °C.

Note that we performed five weighings per state (repetitions) in order to estimate experimental variability, and we only report Φ_{eau}

3.6. Thermal conductivity λ

Guillaume calculation

4. Results

4.1. Apparent density and effective porosity

La détermination de la densité apparente et la porosité se sont faites sur la base de 5 éprouvettes x 5 pesées (soit 25 valeurs/béton). Les mesures et valeurs estimées sont consignées dans le Tableau 2.

Tableau 2. Bilan par béton : masse « à sec », densité apparente, absorption d'eau A_w et porosité effective ϕ_{eff} (moyenne ± incertitude élargie (95%, $k = t_{0.975,\nu_{eff}}$ (Welch-Satterthwaite)). NB : pt = point de pourcentage.

	Masse à "sec"	Densité apparente	A_w	ϕ_{eff}
	g	kg.m^{-3}		
Béton 1	973,04 ± 11,30	2304,7 ± 3.52	**4,05** ± 0.50%	9.25% (±1.09 pt)
Béton 2	991,51 ± 8,50	2285,2 ± 3.68	**3,90** ± 0.27 per cent	8.78% (±0.60 pt)
Béton 3	988,61 ± 7,39	2340,8 ± 3.41	3.77 ±0.22%	8.76% (±0.54 pt)
Béton 4	953,43 ± 8.89	2178,6 ± 4,01	5.**45** ±0.19%	11.89% (±0.71 pt)
Béton 5	993,64 ± 8,56	2320,6 ± 3.13	**3.76** ±0.24%	8.74% (±0.57 pt)

Pour ce qui est des masses « à sec », les écarts-types agrègent la variabilité inter-éprouvettes (géométrie, teneur en air) et intra-éprouvette (répétabilité de la pesée). Les écarts intra-éprouvette isolés sont généralement très faibles, sauf cas particuliers (ex. éprouvette 4).

Pour ce qui est des densités apparentes, les valeurs sont cohérentes avec un béton courant (plage indicative ≈ 2200 – 2400 kg·m^{-3}), à l'exception du béton 4 qui ressort plus faible ≈ 2182 kg·m^{-3}), ce qui peut traduire une teneur en air plus élevée en cohérence avec sa préparation. Deux re-pesées à +1 h et +2 h ont été effectuées (mêmes conditions ambiantes) pour vérifier l'absence de dérive (évaporation/ré-humidification, flottabilité). Aucune évolution systématique n'a été observée au-delà de la résolution de la balance ; les valeurs retenues pour ρ_b proviennent des séries stabilisées. Les incertitudes ont été calculées *via* la méthode de la propagation d'incertitude (GUM) et la formule suivante :

$$u_c^2(\rho) = \left(\frac{\rho_w}{\Delta} u(m_d)\right)^2 + \left(\frac{m_d}{\Delta} u(\rho_w)\right)^2 + \left(\frac{\rho_w m_d}{\Delta^2} u(\Delta)\right)^2$$

avec $u^2(\Delta) = u^2(m_{SSD}) + u^2(m_i)$.

Pour ce qui est de la porosité effective (accessible à l'eau), on détermine Φ_{eff} à partir des trois pesées : masse sèche m_d, masse saturée surface sèche m_{SSD} et masse immergée m_i (pesée hydrostatique, eau à température contrôlée donnant ρ_w). La porosité effective s'écrit :

$$\Phi_{eff} = \frac{m_{SSD} - m_d}{m_{SSD} - m_i} = \frac{V}{V}$$

avec $m_{SSD} - m_i = \rho_{eau} \cdot V$. L'absorption massique associée est :

$$A_w(\%) = 100\frac{m_{SSD} - m_d}{m_d}$$

et les densités apparentes sont rappelées pour cohérence :

$$\rho_{b,sec} = \rho_w \frac{m_d}{m_{SSD} - m_i}, \qquad \rho_{b,SSD} = \rho_w \frac{m_{SSD}}{m_{SSD} - m_i}.$$

Les quatre bétons présentent des absorptions A_w resserrées autour de 3,8–4,1 %, cohérentes avec des porosités effectives ≈ 8,8–9,3 % au regard des volumes géométriques mesurés. Les écarts inter-bétons restent modestes ; le béton 4, légèrement plus poreux en apparence, est aussi celui dont la densité apparente était la plus basse, ce qui est cohérent. Les incertitudes ont été calculées *via* la méthode de la propagation d'incertitude (GUM) et les formules suivantes :

$u_c^2(A_w) = \left(\frac{100}{m_d} \cdot u(\Delta)\right)^2 + \left(\frac{100 \cdot \Delta}{m_d^2} \cdot u(m_d)\right)^2$ (en considérant Δ et m_d indépendants), et,

$$u_c^2(\Phi) = \left(\frac{1}{\Gamma} u\, m_d\right)^2 + \left(\frac{\Gamma - \Delta}{\Gamma^2} u(m_{SSD})\right)^2 + \left(\frac{\Delta}{\Gamma^2} u(m_i)\right)^2$$

avec $\Phi = \frac{\Delta}{\Gamma}$.

4.2. Pore size distribution

La Figure 4 montre les distributions différentielles de tailles de pores $dP_m/d\log r$ (en cm^3/g) en fonction du rayon des pores r (échelle logarithmique, abscisse en Å). Cette grandeur représente le volume intrudé par unité de décade de rayon ; l'aire sous la courbe est proportionnelle à la porosité intrudable.

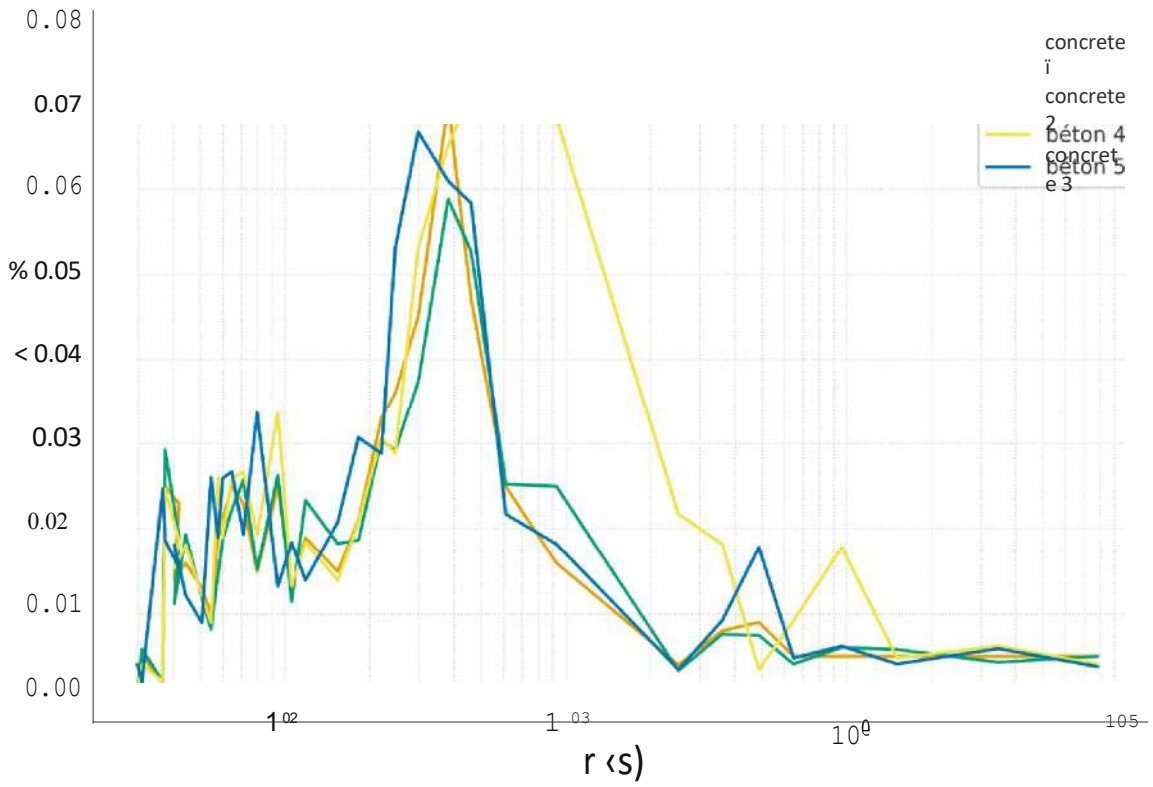


Figure 4. Differential distribution of pore sizes, $dP_m/d\log r$ *(*cm³/g*),* in conjunction *with pore radius*r *(logarithmic scale, Å) for five concretes. Each curve corresponds to a concrete (1 to 5). The area under the curve is proportional to the intrusible porosity* and *the peaks indicate the modal radii of the capillary network.*

The five concretes have a principal mode in the fine capillary range (approximately 30–100 nm). The following observations can be made:

- Concrete 1: maximum around $r \approx 3.8 \times 10^2$ Å (~ 38 nm, amplitude ~0.07 cm³/g per decade), with a shoulder around 3.8×10^2 Å.
- Concrete 2: two marked peaks around 30—46 nm, amplitudes ~0.06 — 0.067 cm³/g.
- Concrete 3: peak centred at 38–46 nm, amplitude ~0.053–0.059.
- Concrete 4: coarser distribution: maximum around 6.1 $\times 10^2$ Å (61 nm, ~0.077), very sustained between 46–93 nm.
- Concrete 5: profile similar to Concrete 2 (dual mode ~30 and 40–46 nm).

Beyond 200 nm, the contributions become weak for all, but it should be noted that

- Concrete 4 retains a significant contribution around 2.5–3.$^{6\times10^3}$ Å, indicating a fraction of more open capillaries.
- Concretes 2 and 5 show a small bulge towards = 0.5 µm, greater than that of concretes 1 and 3.

The increasing order of capillary coarsening (relative importance of radii >40–60 nm) is Concrete 4 > Concrete 2 = Concrete 5 > Concrete 3 = Concrete 1.

This hierarchy is consistent with the other measured parameters: Concrete 4, which had the lowest apparent density and one of the highest effective porosities, shows the highest amplitude in the 60–100 nm range and a more pronounced tail, signatures of a more connected and potentially more permeable capillary network.

Concretes 2 and 5 are bimodal (peaks ~ 30 nm then ~ 40–46 nm), which may reflect a more spread-out capillary distribution (formulation/curing effect).

Concretions 1 and 3 remain finer, with maxima around 38–46 nm and weak contributions beyond 0.2 µm, suggesting a less coarse capillary network.

4.3. Surface roughness

Roughness was characterised by profilometry and summarised using the following parameters: arithmetic roughness (S_a) and mean square roughness (S_q). Values are reported as the mean + standard deviation for three areas per concrete.

Table 3. Roughness parameters: arithmetic roughness S_a and *mean square roughness* S_q *(in nm).*

	Arithmetic roughness S_a (nm)	average quadratic roughness S_q s (nm)
Concrete 1	5394 + 827	7043 + 766
Concrete 2	6076 + 489	7745 + 495
Concrete 3	5735 + 745	7498 + 576
Concrete 4	4774 + 258	6021 + 428
Concrete 5	5967 + 678	7658 + 502

4.4. Surface energies.

Wettability measured by goniometry depends on the actual texture of surfaces. When the geometric assumptions are met (droplets small enough to neglect gravity and ellipticity, base well contained within a locally homogeneous area), roughness corrections can be handled within the framework proposed by Marmur (2003), based on the generalised Cassie-Baxter formulation. In this framework, the apparent contact angle $\theta_{apparent}$ of a drop on a rough/composite surface is related to the intrinsic Young's angle $\theta_{intrinsèque}$ (same chemistry, smooth surface) by:

$$\cos\theta_{apparent} = r_f \cdot f \cdot \cos\theta_{intrinsèque} + f - 1$$

where:

- r_f is the roughness factor of the wet solid fraction (ratio of actual area to projected area projected onto the areas actually in liquid-solid contact);
- f is the projected solid fraction actually in contact with the liquid (the complement $1 - f$ representing the "air" fraction under the droplet);
- $\theta_{intrinsèque}$ is the intrinsic angle on a chemically identical smooth surface.

Roughness measurements are used to construct a digital surface faithful to the topography, from which we deduce:

- the local roughness factor $r_f(h)$ (actual area of wet areas / projected area),
- the projected solid fraction $f(h)$ (projected area of wet areas / total projected area), depending on a parameter h of liquid penetration into crevices. The

couple $(r_f(h), f(h))$ used in the generalised Cassie–Baxter equation is evaluated at the equilibrium state $h = h_{eq}$ by minimising the Gibbs free energy of the system at the interfaces.

A simple and operational energy function (per unit of projected area A_{proj}) is:

$$\mathcal{G}(h) = \gamma_{LV}\frac{S_{LV}(h)}{A_{proj}} + (\gamma_{SL} - \gamma_{SV})\frac{S_{SL}(h)}{A_{proj}}$$

WHERE γ_{LV} γ_{SL} γ_{SV} are the liquid-vapour, solid-liquid, and solid-vapour interfacial tensions; $S_{LV}(h)$ and $S_{SL}(h)$ are the interfacial areas derived from the numerical surface and the penetration level h. The state of equilibrium is defined by

$$\left.\frac{d\mathcal{G}}{dh}\right|_{h=h_{eq}} = 0, \qquad \left.\frac{d^2\mathcal{G}}{dh^2}\right|_{h=h_{eq}} > 0,$$

which gives h_{eq}, then $r_f = r_f(h_{eq})$ and f = f(h_{eq}). Substituting into the previous equation gives the correction that relates θ*apparent* and θintrinsic. The restitution figure (Figure 5, plot of apparent cosθ as a function of intrinsic cosθ) highlights the deviation due to texture and, conversely, allows θintrinsic to be identified from the corrected apparent measurements. In the case of the concretes analysed here, the deviation is very small.

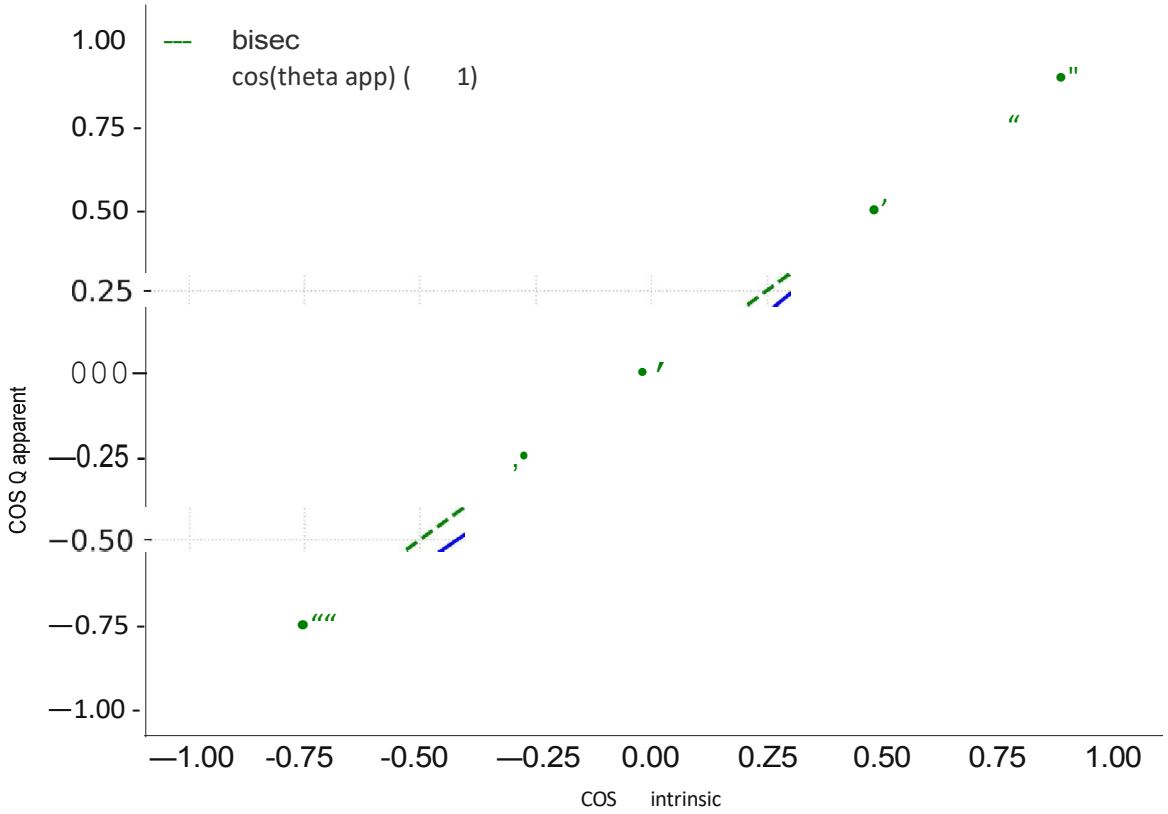


Figure 5. Illustration of a plot of $\cos\theta_{apparent}$ versus $\cos\theta_{intrinsic}$ for the aperture al considering water as the probe liquid.

Table 4. Measurement *of corrected contact angles for the three probe liquids.*

	Diiodomethane	Formamide	Water
Concrete 1	23 + 3	19 ± 2	11 ± 1
Concrete 2	21 + 2	18 ± 3	11 ± 2
Concrete 3	21 + 3	19 ± 1	10 ± 1
Concrete 4	19 + 4	15 ± 2	11 ± 2
Concrete 5	22 + 4	15 ± 4	11 ± 2

According to the van Oss—Chaudhury—Good (vOCG) theory and the contact angle values in Table 3, it is possible to estimate the dispersive components γ^{LW} , , acidic γ^{+}, basic γ^{-}, acidic—base $\gamma^{AB} = 2\sqrt{\gamma^{+}\gamma^{-}}$, and total γ_S at the interface. For information purposes, the associated uncertainties

The surface energy components were evaluated using Monte Carlo simulation (10^5 draws), jointly propagating uncertainties on contact angles and liquid constants (normal, independent laws) and reporting the median as the estimator with a 95% coverage interval ($k \approx 2$), in accordance with the GUM.

Table 5. Estimation of the surface energy components for the different concretes.

	γ_S^{LW} $(mN \cdot m^{-1})$	γ_S^{+} $(mN \cdot m^{-1})$	γ_S^{-} $(mN \cdot m^{-1})$	γ_S^{AB} $(mN \cdot m^{-1})$	γ_S $(mN \cdot m^{-1})$
Concrete 1	46.84 + 5.23	012 + 01	57.88 + 3.87	5.3 + 0.54	5214 + 7.34
Concrete 2	47.48 + 4.23	011 + 0.07	57.43 + 5.43	5.07 + 0.1	52.55 + 5.41
Concrete 3	47.48 + 3.33	0.09 + 0.03	58.4 + 5.81	4.49 + 0.74	51.97 + 7
Concrete 4	48.07 + 5.43	0.5 + 0.04	56s 3 + 51	5.72 + 0.48	53.79 + 8.3
Concrete 5	4717 + 4.64	0.2 + 01	56.04 + 5.97	6.7 + 0.64	53.87 + 5.34

The total surface energies range from 52,*et* 54,mNm^{-1}, dominated by a component dispersive (-47—48$mN \cdot m^{-1}$) and a more moderate acid-base component (-4.5—6.7$mN \cdot m^{-1}$). All surfaces are strongly basic ($\gamma^{-} \gg \gamma^{+}$), in accordance with the chemistry of cement hydrates . The classification γ_S is B5 1 B4 > B2 1 B1 > B3, with B5 standing out due to its stronger polar interaction.

4.5. Summary table

To conclude the characterisation, Table 6 summarises the key indicators for each concrete: bulk density, surface roughness (ISO 25178 parameters:S_a ,S_q), and surface energies obtained using the van Oss—Chaudhury—Good model based on contact angles (water, formamide, diiodomethane). The uncertainties of the energies were evaluated by Monte Carlo simulation (joint propagation of angles and liquid constants) and the densities are accompanied by their expanded uncertainty (k=2).

Overall, the five concretes exhibit high total energies (~52 – 54 mN·m^{-1}) dominated by the dispersive component γ_S^{LW} component (~ 47 – 48$mN \cdot m^{-1}$), with a moderate acid-base component (~4.5—6.7$mN \cdot m^{-1}$), reflecting very basic surfaces ($\gamma^{-} \gg \gamma^{+}$) — consistent with the low angles measured. In terms of texture, Concrete 2 is the roughest (S_a ,S_q higher), Concrete 4 the smoothest (and also the lowest in apparent density). We therefore expect, on

hydrophilic surfaces, lower apparent angles and more pronounced hysteresis for the roughest concretes, while the smoothest concrete exhibits more stable angles. Finally, Concrete 5 is distinguished by the strongest polar component (γ_S^{AB}), indicating a more pronounced interaction more pronounced interaction with polar liquids.

Table 6. Summary by concrete type: apparent density, roughness S_a / S_q , and surface *energies (γ_S^{LW}, γ_S^{AB}, γ_S). The values are provided as means ± SD (or 95% CI where specified).*

Béton	Densité apparente ($kg \cdot m^{-3}$)	S_a (nm)	S_q (nm)	γ_S^{LW} ($mN \cdot m^{-1}$)	γ_S^{AB} ($mN \cdot m^{-1}$)	γ_S ($mN \cdot m^{-1}$)
1	2304.7 + 3.52	5394 + 827	7043 + 766	46.84 + 5.23	5.30 + 0.54	52.14 + 7.34
2	2285.2 + 3.68	6076 + 489	7745 + 495	47.48 + 4.23	5.07 + 0.10	52.55 + 5.41
3	2340.8 + 3.41	5735 + 745	7,498 + 576	47.48 + 3.33	4.49 + 0.74	51.97 + 7.10
4	2181.6 + 3.59	4774 + 258	6021 + 428	48.07 + 5.43	5.72 + 0.48	53.79 + 8.30
5	2320.6 + 3.13	5,967 + 678	7658 + 502	47.17 + 4.64	6.70 + 0.64	53.87 + 5.34

Appendix A - Wettability

Wetting of perfect surfaces

The surface free energies of solids cannot be measured directly. Various independent approaches can be used to estimate them, including wettability measurements. These involve placing a drop of liquid with known surface tension on a solid. Due to specific interactions occurring at the interface between the solid, the liquid and its vapour, the drop adopts a spatial configuration which, in thermodynamic equilibrium, corresponds to the minimum energy of the system. Measurements taken for different liquids can then be used to determine the surface energy components of the solid.

To address the case of partial wetting, in 1805 Young considered a system consisting of a flat, non-deformable, smooth, chemically homogeneous solid substrate partially wetted by a liquid. He proposed a vector representation of the forces acting on the shape of the drop (Figure 6).

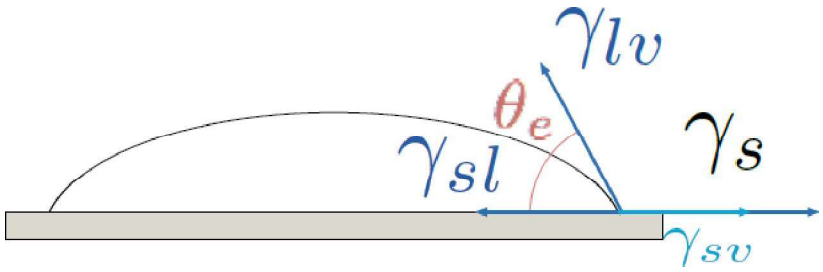


Figure 6. Diagram of a water droplet partially wetting a solid surface. The contact angle

Considering the energy associated with the system shown in Figure 6 for an infinitesimal displacement of the contact line, Young's work led him to establish that, at thermodynamic equilibrium, surface tensions are linked by the following relationship:

$$\gamma_{SV} = \gamma_{SL} + \gamma_{LV} \cos\theta$$

where γ_{LV} γ_{SV} γ_{SV} are respectively the surface tensions at the liquid-vapor, solid-vapor, and solid-liquid interfaces.

The above equation therefore establishes a link between the surface energies of the solid surfaces studied γ_{SV}), the energy properties of the liquid γ_{LV}) used for measurement, and the surface energies resulting from the liquid-solid surface interaction. This unique link for any liquid-surface pair is fully quantified by the value of the angle μ, which is the subject of wettability measurements.

Determining the surface energies of perfect surfaces

En définitive, l'équation d'Young contient les paramètres γ_{LV} et $\cos\theta$ expérimentalement déterminés, et les relie à l'énergie de surface de la phase solide recherchée γ_{SV}. Une inconnue demeure toutefois : l'énergie interfaciale solide-liquide γ_{SL}.

Afin d'évaluer la composante γ_{SV} via l'équation d'Young, diverses théories permettent de décrire γ_{SL} telle une fonction de γ_{SV} et des interactions spécifiques entre le solide et le liquide [Sharma and Rao, 2002]. Les premières modélisations de γ_{SL} proposées et présentées dans la littérature consistent à exprimer γ_{SL}. en termes d'énergies de surface solide et liquide par le biais d'une équation d'état [Kwok and Neumann, 2000]. Une deuxième approche approxime empiriquement l'énergie de surface solide en introduisant le concept d'angle critique, correspondantà la tension de surface qui sépare les liquides à mouillabilité totale et partielle sur le solide considéré [Fox and Zisman, 1952]. Enfin, la dernière méthode la théorie Acide-Base) conduit pour sa part à décomposer l'énergie de surface totale afin d'écrire l'énergie interfaciale solide-liquide γ_{SL}.) en termes d'énergies de surface solide et liquide [Owens and Wendt, 1969, Van Oss et al., 1986, Fowkes, 1987].

Seule cette approche est ici développée dans la mesure où elle tente d'expliquer l'origine des énergies de surfaces au travers des interactions de van der Waals et acide-base de Lewis.

La théorie Acide-Base Le modèle dit « théorie Acide-Base » est issu des travaux initiés par Fowkes [1987]. Il avançe que les interactions physiques entre corps en contact résultent de la combinaison de contributions de nature diverses, tel que cela a été évoqué précédemment. Durant les décennies qui suivent, Van Oss, Chaudhury et Good VCG) complétèrent cette approche pour finalement considérer que :

$$\gamma_{LV}(1+\cos\theta) = 2\left(\sqrt{\gamma_{SV}^{LW}\gamma_{LV}^{LW}} + \sqrt{\gamma_{SV}^{+}\gamma_{LV}^{-}} + \sqrt{\gamma_{SV}^{-}\gamma_{LV}^{+}}\right)$$

où pour un couple {liquide - surface} sont considérés :

- θ, l'angle de contact de la goutte déposée sur la surface ;
- γ_{LV}^{LW}, γ_{LV}^{-}, γ_{LV}^{+} : les composantes énergétiques du liquide utilisé ;
- γ_{SV}^{LW}, γ_{SV}^{-}, γ_{SV}^{+} : les composantes énergétiques du solide à caractériser.

Dans la mesure où les études de mouillabilité ont pour objectif d'évaluer l'énergie de surface solide, l'équation précédente mène à penser que la détermination des angles de contact associée à trois liquides différent est suffisante pour calculer γ_{SV}.

Judicieusement choisis, les liquides communément considérés sont 2 liquides polaires et 1 liquide apolaire.

Methods for measuring wettability

Pour les échantillons solides, deux types de mesure d'angles de contact peuvent être effectués soit en mode statique, soit en mode dynamique.

En mode statique, le profil d'une goutte au repos déposée sur un substrat est étudié à

using an acquisition camera and image processing software. The angle measured is simply that of the drop placed on the surface and is the angle value most often used in the literature.

In dynamic mode, the focus is on the phenomenon known as contact angle hysteresis. Due to roughness and/or heterogeneities, this hysteresis corresponds experimentally to the difference observed between the apparent contact angle measured and that which would have been measured on the corresponding ideal surface. Thus, to limit the dispersion associated with static angle measurements, the advance angle is generally used for sufficiently smooth and homogeneous surfaces [Neumann et al., 1974]. The angle of advance µa corresponds to the contact angle measured when the triple line starts to move (Figure 1.4). It is obtained by adding liquid to a drop previously formed on a surface or by tilting the substrate on which the drop is deposited, then noting the angle at which the triple line starts to move.

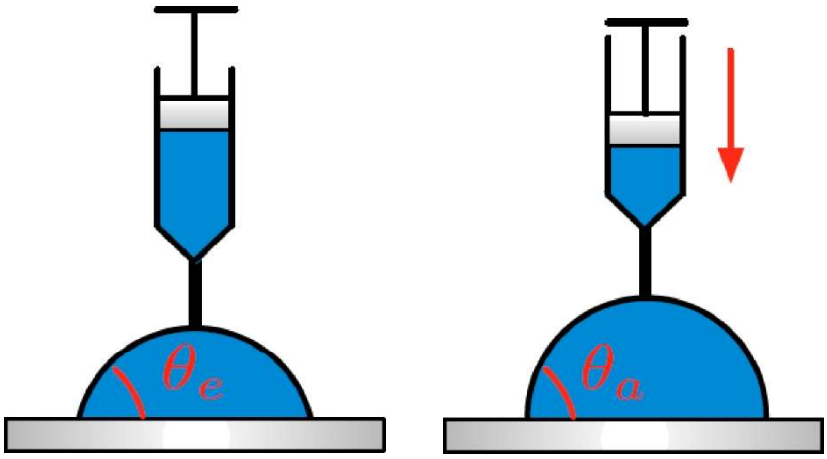


Figure 7. Illustration of a measurement of the angle of advance of a liquid on a surface.

Wetting of textured surfaces

As Johnson and Dettre observed, water droplets placed on a rough hydrophobic substrate can behave very differently depending on the surface roughness [Dettre and Johnson, 1964]. This observation, subsequently confirmed by other more modern experiments, raises the question of surface roughness and its consideration in surface wettability models remains essential. Two possible wetting situations, known as Wenzel and Cassie-Baxter (Figure 1.5), are highlighted.

The Wenzel model The first to examine the dependence of the contact angle
With roughness, Wenzel seeks to define the apparent contact angleθ^*on a rough surface
rough surface as a function of the $_{\text{apparent}}$contact angle$\theta_{eq}$and the surface roughness r [Wenzel, 1936]. This
dimensionless term r is defined as the ratio of the effective surface area (taking into account surface roughness) to the corresponding geometric plane surface area, and is in fact a number greater than or equal to 1.

Assuming Young's law is locally verified, Wenzel's model establishes that

$$\cos\theta^{*}=r\cdot co\ s\ \theta_{eq}$$

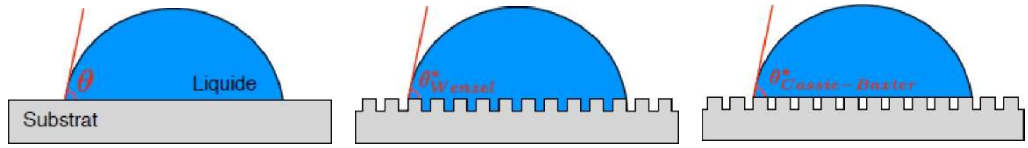
The Cassie-Baxter model In 1944, Cassie and Baxter introduced a concept known as "air pockets" to describe the wettability of porous surfaces, whereby the crevices in the substrate trap small pockets of air between the liquid and the substrate [Cassie and Baxter, 1944]. Cassie generalised this description in 1948, extending his analysis to chemically heterogeneous surfaces. His reasoning, based on an energy description similar to that of Wenzel, allows us to consider a drop resting on a smooth surface composed of n types of materials randomly distributed on the flat substrate. Each material is characterised by its own coefficients °i,sI and °i,sv, as well as by the fraction fi of the substrate surface with$f_1+\cdots+f_n=1$.

The formulation showing the apparent Cassie-Baxter contact angle is

then amounts to averaging the cosines of the angles on each of the n surfaces, weighting each term by the corresponding surface fractions

$$\cos\theta^{*}=\sum_{i=1}^{n} f_i\cos\theta_{eq,i}$$

where i indexes the surfaces considered for measuring contact angles.



(a) Wetting of an ideal surface Nb) Wenzel state bc) **Cassie state**

Figure 8. Presentation of the three possible wetting states of a surface: partial wetting of an ideal surface *a), wetting by a liquid conforming to the solid* surface *b)* and *wetting by a liquid resting on the peaks of the asperities c).*

Reconciling the Wenzel and Cassie-Baxter models The need to control dynamic wetting processes has led to the development of more precise underlying wetting models. However, proposing a formulation to describe the equilibrium state of a drop placed on a hydrophobic surface proves to be a difficult problem. This is evidenced by the plethora of (often erroneous) rewritings and reinterpretations of the Wenzel and Cassie-Baxter equations [Milne and Amirfazli, 2012]. Among the established results, various studies highlight the study of variations in the Gibbs energy function [Wolansky and Marmur, 1998, Brandon et al., 2003, Marmur, 2003, Marmur and Bittoun, 2009]. By assuming a large drop deposited in front of the wavelength of the crevices or chemical heterogeneities, the approximation remains valid and puts the Wenzel and Cassie-Baxter equations into perspective within a well-defined mathematical and thermodynamic framework.

The necessary conditions for transition between regimes with homogeneous or heterogeneous wettability are then derived from the determination of the local extrema of the Gibbs function with respect to the apparent contact angle μ? and the fraction of wet solid, f. For cases of

partial wetting, the conclusions of the study of variations in a formulation of the Cassie-Baxter relationship:

$$\cos\theta^{*} = r_f \cdot f \cdot \cos\theta + f - 1$$

Bibliography

ABD Cassie and S Baxter. Wettability of porous surfaces. Transactions of the Faraday Society, 1944.

C Della Volpe and S Siboni. Some reflections on acid—base solid surface free energy theories. Journal of Colloid and Interface Science, 1997.

C Della Volpe and S Siboni. Acid—base surface free energies of solids and the definition of scales in the Good—van Oss—Chaudhury theory. Journal of Adhesion Science and ... , 2000.

C Della Volpe, D Maniglio, M Brugnara, and S Siboni. The solid surface free energy calculation: I. In defence of the multicomponent approach. Journal of Colloid and ... , 2004.

Marmur, A. 2003). Wetting on hydrophobic rough surfaces: to be heterogeneous or not to be*. *Langmuir,* 1920), 8343-8348.

Abraham Marmur and Eyal Bittoun. When Wenzel and Cassie are right: reconciling local and global considerations. Langmuir, 253):1277—1281, 2009.

A W Neumann, R J Good, C j Hope, and M Sejpal. An equation-of-state approach to determine surface tensions of low-energy solids from contact angles. Journal of Colloid and Interface Science, 492):291—304, November 1974.

D K Owens and R C Wendt. Estimation of the surface free energy of polymers. Journal of Applied Polymer Science, 1969.

L H Sharpe and H Schonhorn. Surface Energetics, Adhesion, and Adhesive joints. In pubs.acs.org, pages 189—201. AMERICAN CHEMICAL SOCIETY, WASHINGTON, D.C., January 1964.

C J Van Oss, R J Good, and M K Chaudhury. The role of van der Waals forces and hydrogen bonds in “hydrophobic interactions” between biopolymers and low energy surfaces. Journal of Colloid and Interface Science, 1112):378—390, June 1986.

Gershon Wolansky and Abraham Marmur. The Actual Contact Angle on a Heterogeneous Rough Surface in Three Dimensions. Langmuir, 1418):5292—5297, September 1998.

APPENDIX 2

Characteristics of glass

3 pages

6

Calculated by: JUSTINE JEAN | Calculated on: 01/12/2025 | Product catalogue: France | Standards: EN410:2011

Type of glazing



Glass

- PLANICLEAR (6mm) - Annealed

Simulated performance data

Light factors	**CIE015:2018**
Light transmission (LT)	90
External reflection (RLe)	8
Internal reflection (RLi)	8
Energy factors	**EN410:2011**
Energy transmission (ET)	85
UV (Tuv)	67
External energy reflection (Ree)	8
Internal energy reflection (Rei)	8
Absorption A1 (AE1)	7
Solar factors	**EN410:2011**
Solar factors (g)	0.87
Shading coefficient (SC)	1.0
Thermal transmittance	**EN673:2011**
Relative to vertical	0
Ug	5.7 W/(m2.K)
Acoustics	**EN 12758**

Acoustic values according to standard EN 12758 from a notified body

Rw (C;Ctr)	32 (-1; -2) dB
Ra	31 dB
Ra,tr	30 dB
STC (ASTM E413)	0
OITC (ASTM E1332)	0
Colour rendering	**CIE015:2018**
Light Transmission (Ra)	99.1
External reflection (Ra)	98.4
Safety glass	**EN12600**
Impact resistance	NPD
Burglar resistance	**EN356**
Burglary resistance	NPD

Manufacturing dimensions

Nominal thickness	6.0 mm
Weight	15 kg/m²

Durability

Carbon footprint

The value is calculated based on the simulated composition in accordance with European standard EN 15804+A1/CN (2019)

Global Warming Potential (GWP) – A1-A3 (kg CO_2 eq./m²)	**EN 15804+A1/CN (2019)** 14.3

Verified Results EN 410 EN 673 TÜVRheinland CERTIFIED www.tuv.com ID 0000036859

Calumen® calculates the photometric characteristics and thermal transmittance of glazing using calculation algorithms that comply with the following standards: European standards EN 410 and EN 673, international standard ISO9050, Japanese standard JIS R 3106/3107, and Korean standard KS L 2514/2525. Calumen®'s calculation and functional output rules for standards EN 410 and EN 673 have been validated by TÜV Rheinland (report 11923R-11-33705). The technical performance obtained in accordance with these standards is provided for information purposes only and is subject to change. Only the values included in the performance declaration and available on the Saint-Gobain Glass CE marking website are official. Sound reduction indices are measured in accordance with EN ISO 10140 and EN 12758 standards. The calculated indices are provided for information purposes only. The accuracy of the Rw index is within a range of +/-2dB. The calculations of glass thicknesses are in accordance with the description in DTU39-P4 version 2012.

PRODUCT DESCRIPTION

Clear glass by Vitro Architectural Glass is a soda-lime float glass product with a slightly green inherent color that deepens as thickness increases. Its relatively high visible light transmittance (89% at 6mm) and its greenish edge are two characteristics. Clear glass mechanical and physical properties are similar to other soda-lime float glass products.

APPROXIMATE WEIGHTS

Per m^2		Per ft^2	
thickness	**weight**	**thickness**	**weight**
2.5 mm	6.9	3/32	1.3 lbs
3.0 mm	8.2 kg	1/8	1.5 lbs
4.0 mm	9.9 kg	5/32	2.0 lbs
5.0 mm	11.9 kg	3/16	2.4 lbs
6.0 mm	14.2 kg	1/4	2.9 lbs
8.0 mm	19.8 kg	5/16	4.0 lbs
10.0 mm	23.8 kg	3/8	4.9 lbs
12.0 mm	31.8 kg	1/2	6.4 llbs
16.0 mm	41.0 kg	5/8	8.0 ilbs
19.0 mm	50.9 kg	3/4	10.0 lbs

COLOR

	6.0mm
Transmitted Color: D65, 10° L*	95.4
a*	-1.8
b*	0.1
Hue Angle (°)	176
Dominant wavelength: C, 2°	496 nm

CHEMICAL COMPOSITION

SiO_2	73%
Na_2O	14%
CaO	9%
MgO and Trace elements	4%

MECHANICAL PROPERTIES

Knoop Hardness Number (indentation hardness) indenter load--500 gm	470 kgf/mm^2	
Poisson's Ratio	0.22	
Modulus of Elasticity (Young's)	73.1 GPa	10,600,000 psi
Tensile Strength (Determined as Modulus of Rupture, ultimate)	41.4 MPa	6,000 psi
Density at 21°C (70°F)	2.51 g/cm^3	157 lb/ft^3

THERMAL PROPERTIES

Hemispherical Emissivity at -18 to 66 °C (0 to 150°F)) glass	0.84	
Expansion Coefficient (linear) 20 to 300°C (68 to 572°F)	$8.6*10^{-6}$/ °C	$4.8*10^{-6}$/ °F
Specific heat at 0 to 100°C (32 to 212°F)	858 J/kg-K	0.205 Btu/lb-°F
Thermal Conductivity (k) at 50°C (122°F)	0.937 W/m-K	0.542 Btu/hr-ft-°F
Softening Point	723°C	1333°F
Annealing Point	544°C	1011°F
Strain Point	504°C	939°F

SUSTAINABILITY

To provide architects with the assurance and documentation they need to meet and verify their sustainability goals, Vitro Architectural Glass participates in a range of programs and initiatives. Resources available include, but are not limited to:

- Type III Environmental Product Declarations
- *Cradle to Cradle Certifiied*™ Bronze with associated Gold Material Health Certificate
- *LEED*® and Living Building Challenge documentation
- Material Ingredient Disclosure and Safety Data Sheets
- Annual Corporate Sustainability Report

Further information is available through VitroGlazings.com or by calling 855-887-6457 (VTRO GLS)

SOLAR PERFORMANCE VALUES [1]

Glass Thickness		Transmittance				Reflectance	
inches	**mm**	**Ultra-violet (%)**	**Visible (%)**	**Infrared (%)**	**Total Solar (%)**	**Visible (%)**	**Total Solar (%)**
1/8	3.0	73	90	78	83	9	8
5/32	4.0	71	90	75	81	9	7
3/16	5.0	69	89	72	79	9	7
1/4	6.0	66	89	69	77	8	8
5/16	8.0	61	88	62	72	8	7
3/8	10.0	58	87	56	69	8	7
1/2	12.0	53	85	48	64	8	6
5/8	16.0	48	84	41	59	8	6
3/4	19.0	46	83	36	55	8	6

[1] Figures may vary due to manufacturing tolerances. All tabulated solar performance data are based on the methodology prescribed in ISO 9050, 2003 except Infrared, which is based on the solar irradiance data prescribed by ISO 9050, 2003 from 780 to2500 nm. Slight changes in transmitted optical properties may occur on exposure to sunlight.

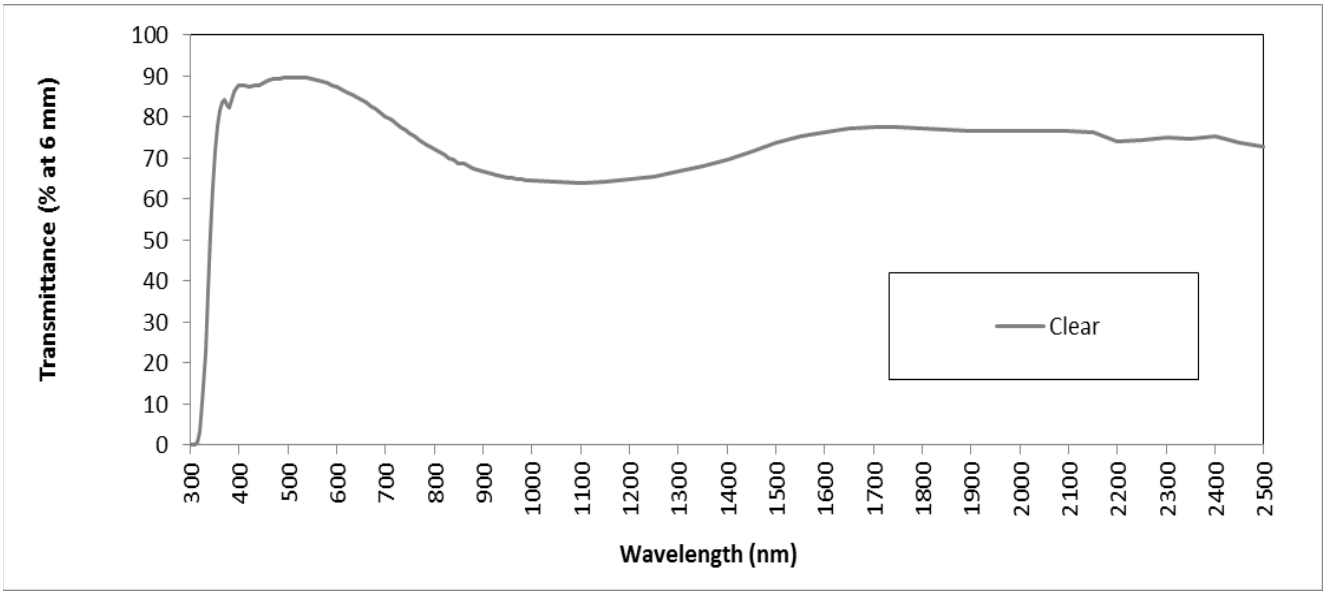
Vitro Architectural Glass
Glass Technology Center
400 Guys Run Rd.Pittsburgh, PA 15024

VitroGlazings.com
archservices@vitroglazings.com

1.855.887.6457 / 1.855.VTRO.GLS

Transmittance (% at 6 mm/0.223")

Wavelength (nm)	Clear Glass %T	Wavelength (nm)	Clear Glass %T	Wavelength (nm)	Clear Glass %T	Wavelength (nm)	Clear Glass %T	Wavelength (nm)	Clear Glass %T
300	0.0	430	87.7	660	83.5	890	67.1	1600	76.5
305	0.0	440	87.8	670	82.8	900	66.8	1650	77.2
310	0.1	450	88.3	680	81.9	910	66.4	1700	77.5
315	0.7	460	89.0	690	81.2	920	66.1	1750	77.5
320	3.5	470	89.3	700	80.2	930	65.8	1800	77.2
325	10.7	480	89.4	710	79.4	940	65.6	1850	76.9
330	22.8	490	89.6	720	78.6	950	65.4	1900	76.7
335	37.5	500	89.7	730	77.7	960	65.1	1950	76.7
340	51.5	510	89.8	740	77.0	970	65.0	2000	76.6
345	63.2	520	89.8	750	76.2	980	64.8	2050	76.7
350	71.8	530	89.7	760	75.2	990	64.6	2100	76.8
355	77.8	540	89.5	770	74.4	1000	64.5	2150	76.4
360	81.7	550	89.3	780	73.6	1050	64.1	2200	74.0
365	83.8	560	89.0	790	72.9	1100	64.1	2250	74.3
370	84.4	570	88.7	800	72.2	1150	64.3	2300	75.2
375	83.0	580	88.3	810	71.5	1200	64.8	2350	74.9
380	82.4	590	87.9	820	70.9	1250	65.6	2400	75.2
385	84.2	600	87.3	830	70.1	1300	66.8	2450	73.8
390	86.2	610	86.8	840	69.7	1350	68.2	2500	72.7
395	87.2	620	86.2	850	68.8	1400	69.7		
400	87.7	630	85.5	860	68.6	1450	71.7		
410	87.7	640	84.9	870	68.0	1500	73.7		
420	87.6	650	84.2	880	67.5	1550	75.3		



ADDITIONAL INFORMATION/DOCUMENTS

The following documents can be referenced for additional information regarding Clear glass;

Clear Performance Data, Vitro Float Glass Warranty, Vitro Float Glass SDS, C2C Material Health Certificate, Vitro Float Glass EPD

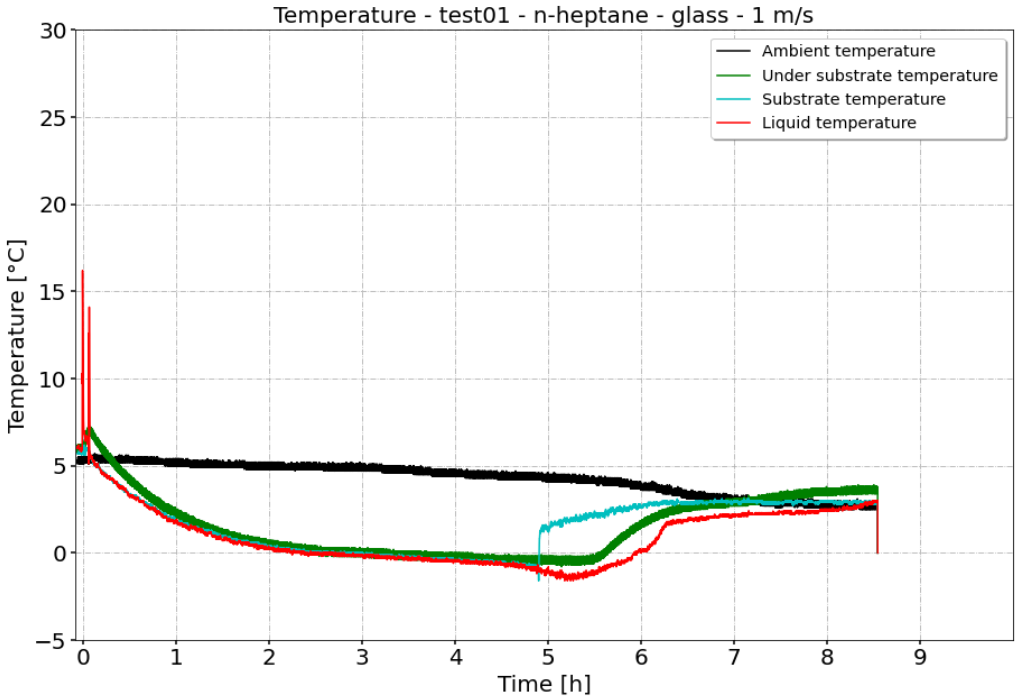
APPENDIX 3

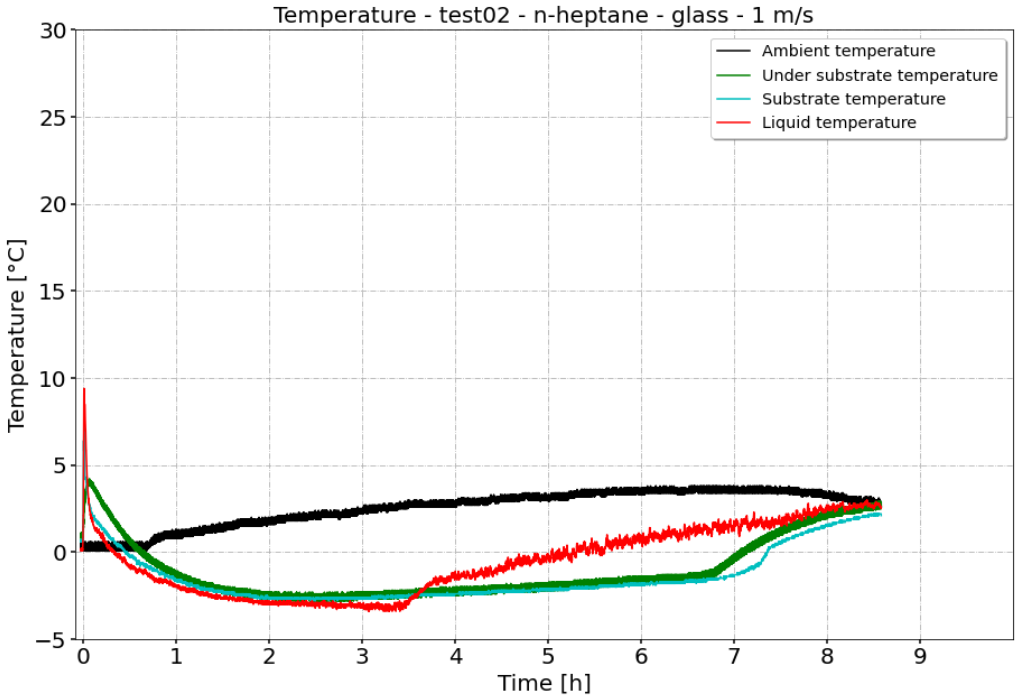
Pool evaporation tests – Characteristics of the paint applied to substrate block a2

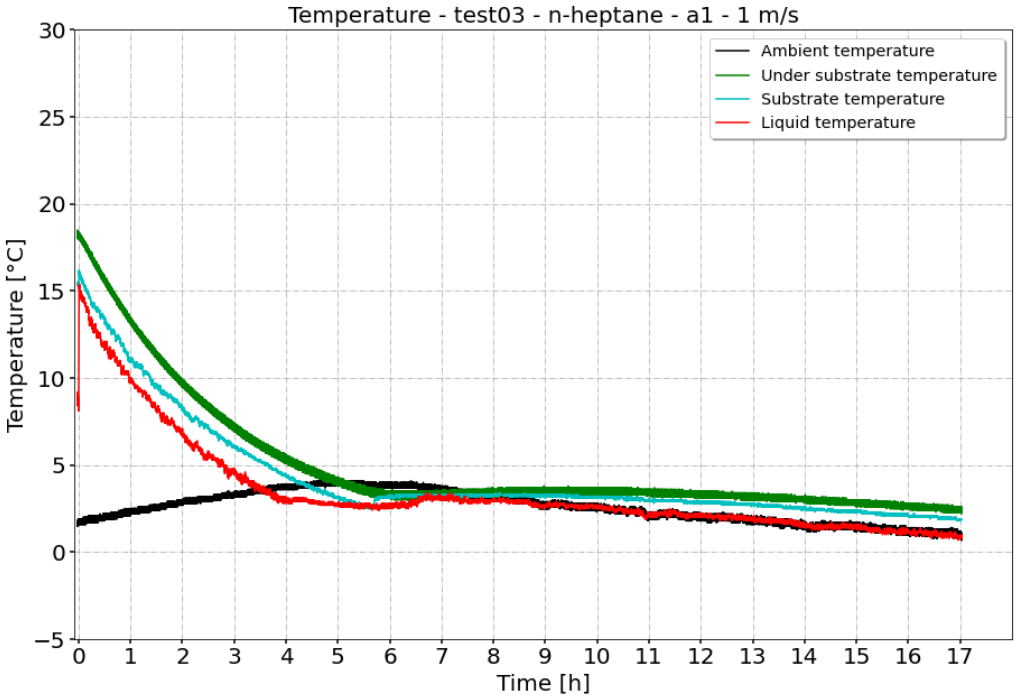
1 page

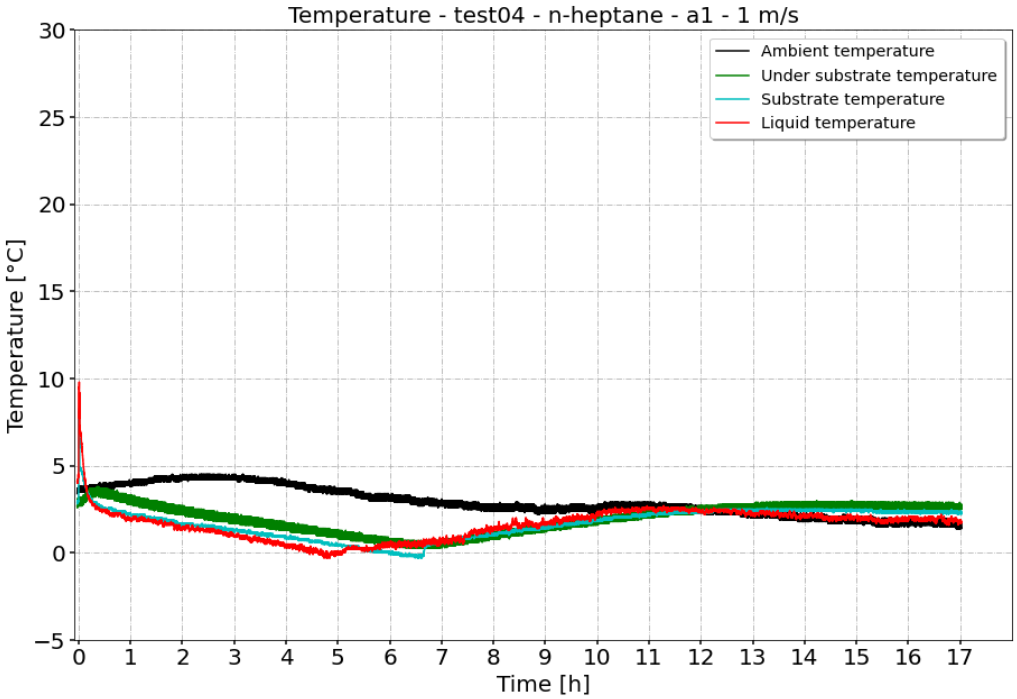
Product type	**Epoxy/polyamide**
Density at 20°C (kg/L)	1.40 – 1.65
Viscosity at 20°C	75 – 85 KU (Stormer)

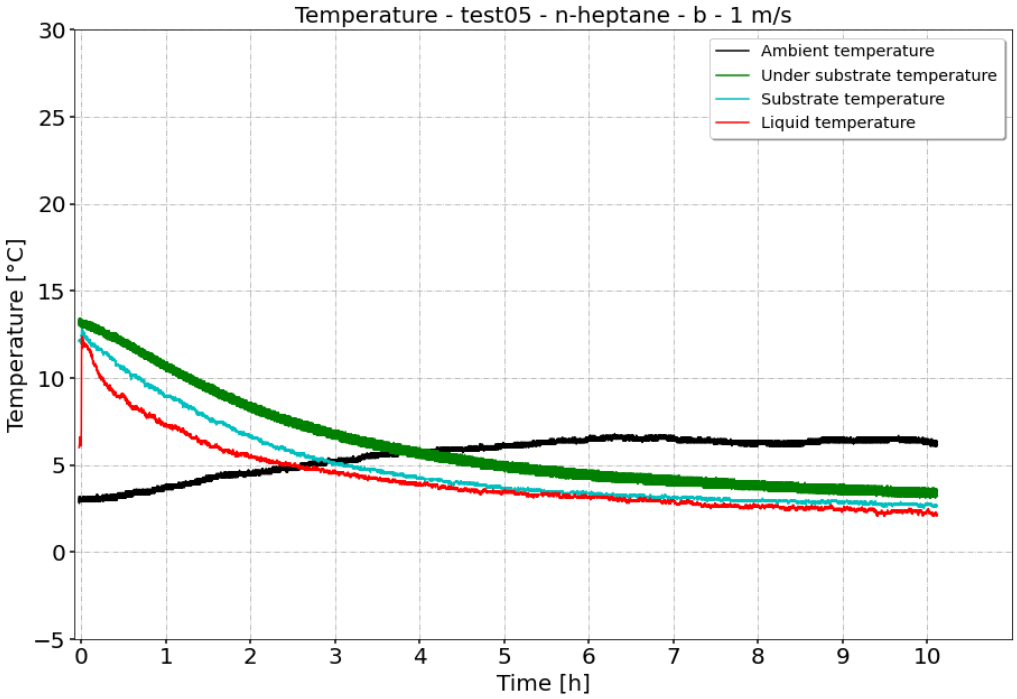
APPENDIX 4 : Pool evaporation tests – Temperature changes measured with different thermocouples – 7 pages

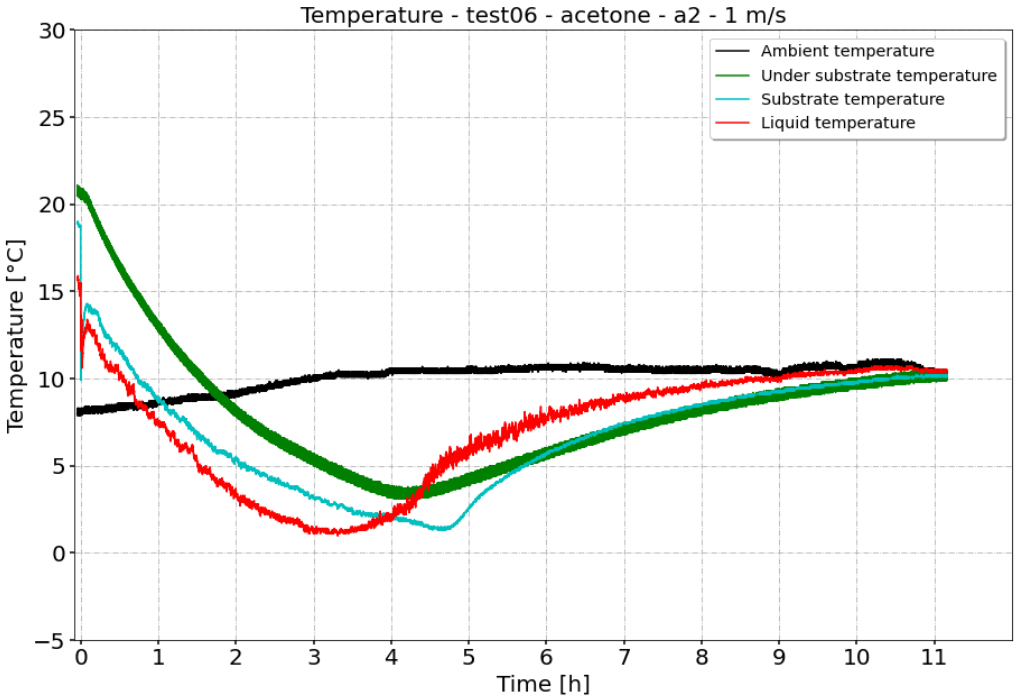


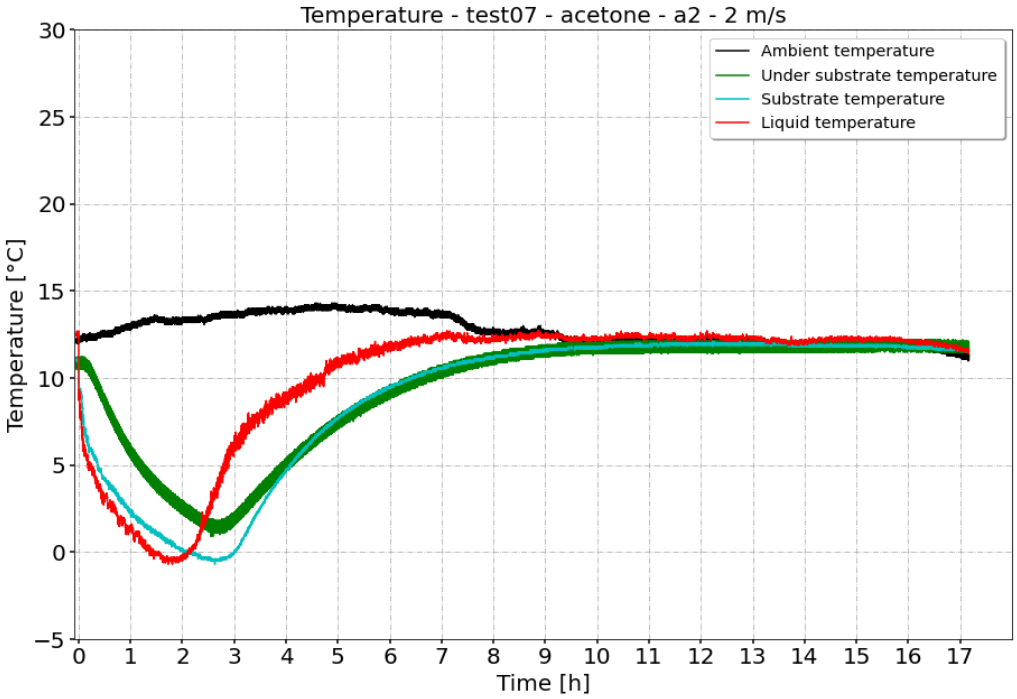


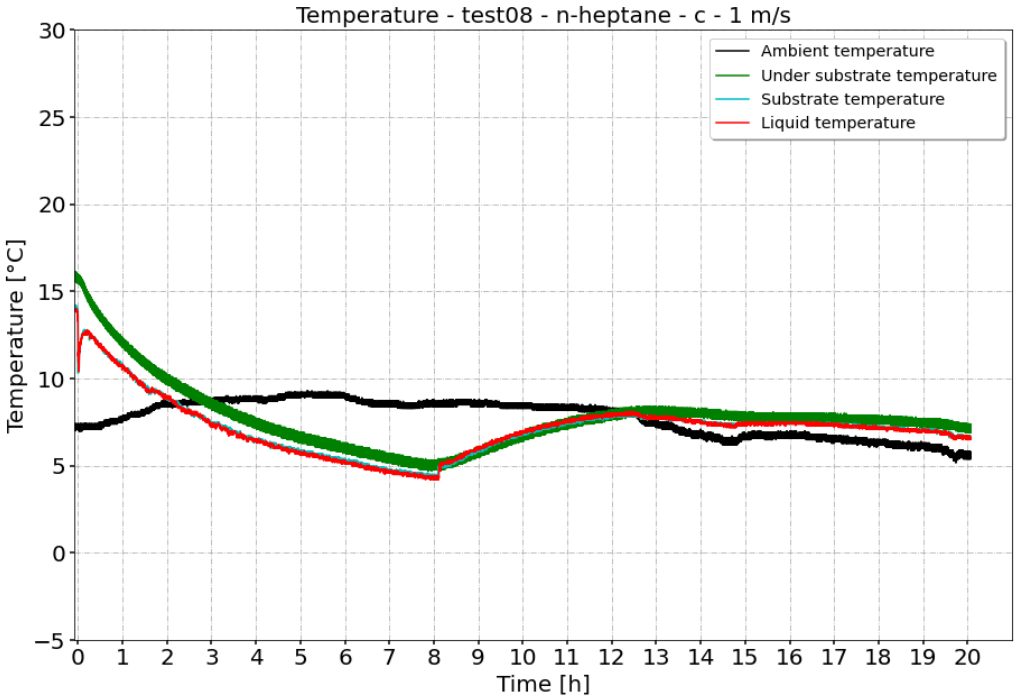

Temperature - test03 - n-heptane - a1 - 1 m/s
Ambient temperature
Under substrate temperature
Substrate temperature
Liquid temperature
Temperature [°C]
Time [h]

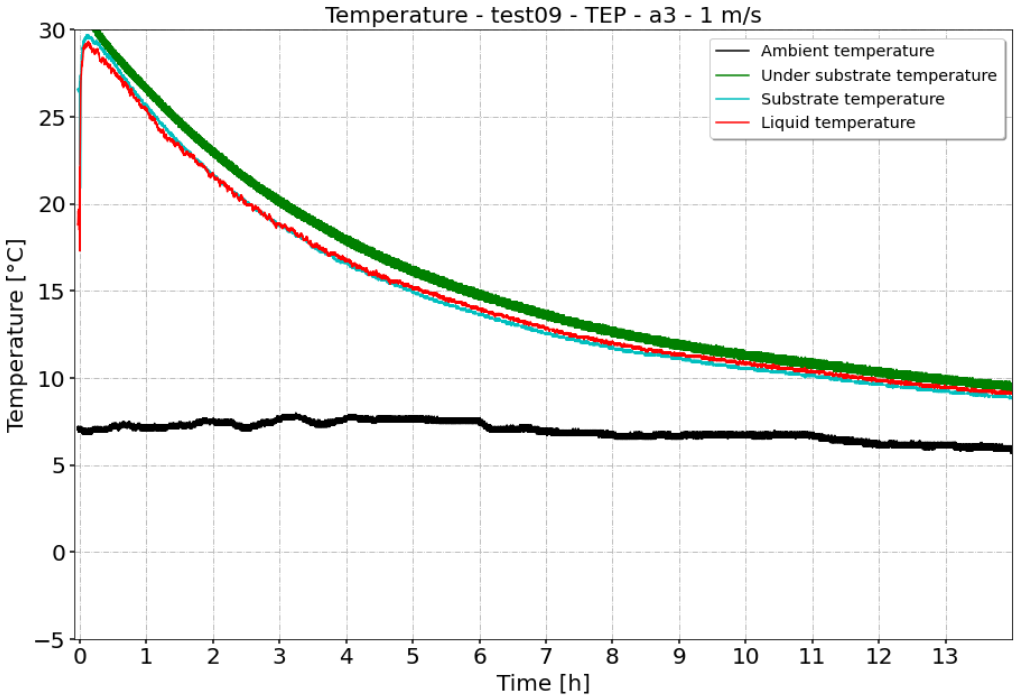

Temperature - test04 - n-heptane - a1 - 1 m/s
Ambient temperature
Under substrate temperature
Substrate temperature
Liquid temperature
Temperature [°C]
Time [h]

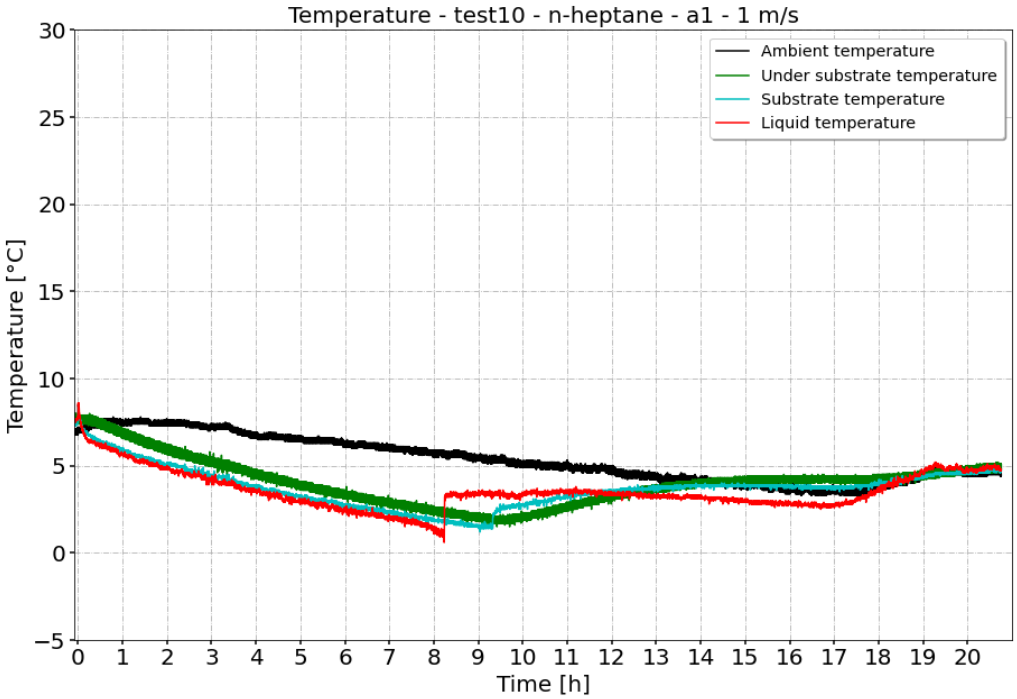

Temperature - test05 - n-heptane - b - 1 m/s
Ambient temperature
Under substrate temperature
Substrate temperature
Liquid temperature
Temperature [°C]
Time [h]

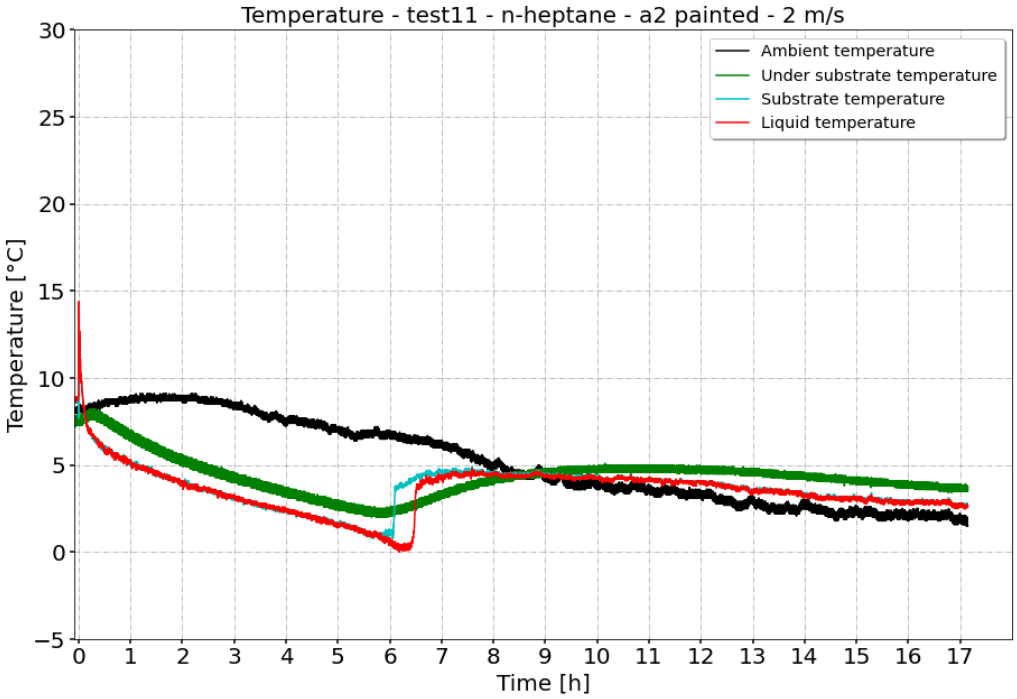

Temperature - test06 - acetone - a2 - 1 m/s
Ambient temperature
Under substrate temperature
Substrate temperature
Liquid temperature
Temperature [°C]
Time [h]

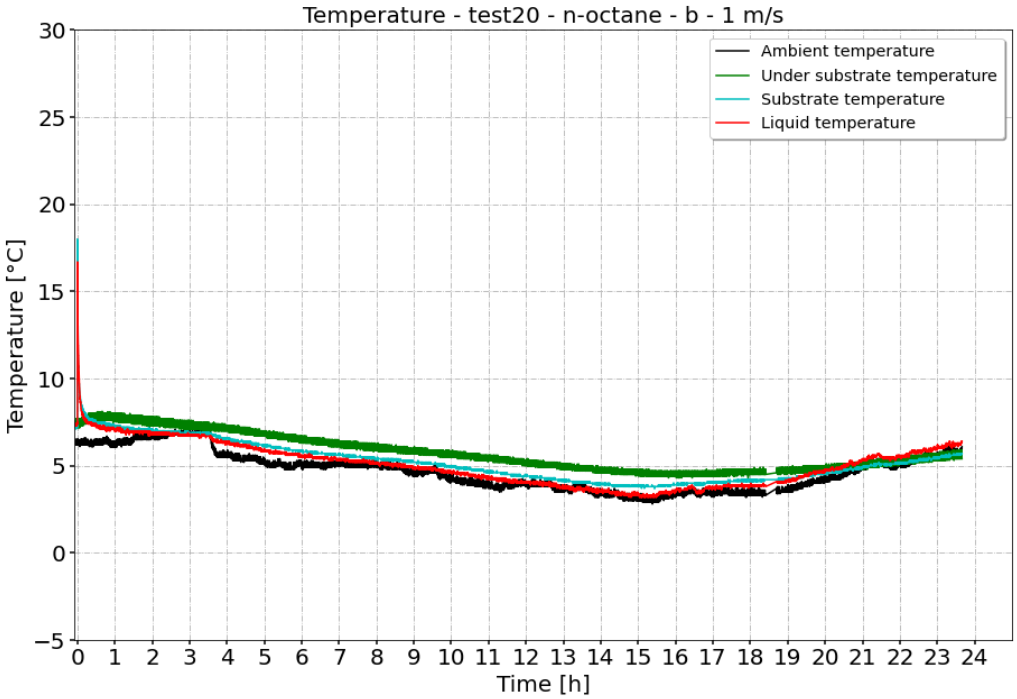

Temperature - test07 - acetone - a2 - 2 m/s
Ambient temperature
Under substrate temperature
Substrate temperature
Liquid temperature
Temperature [°C]
Time [h]

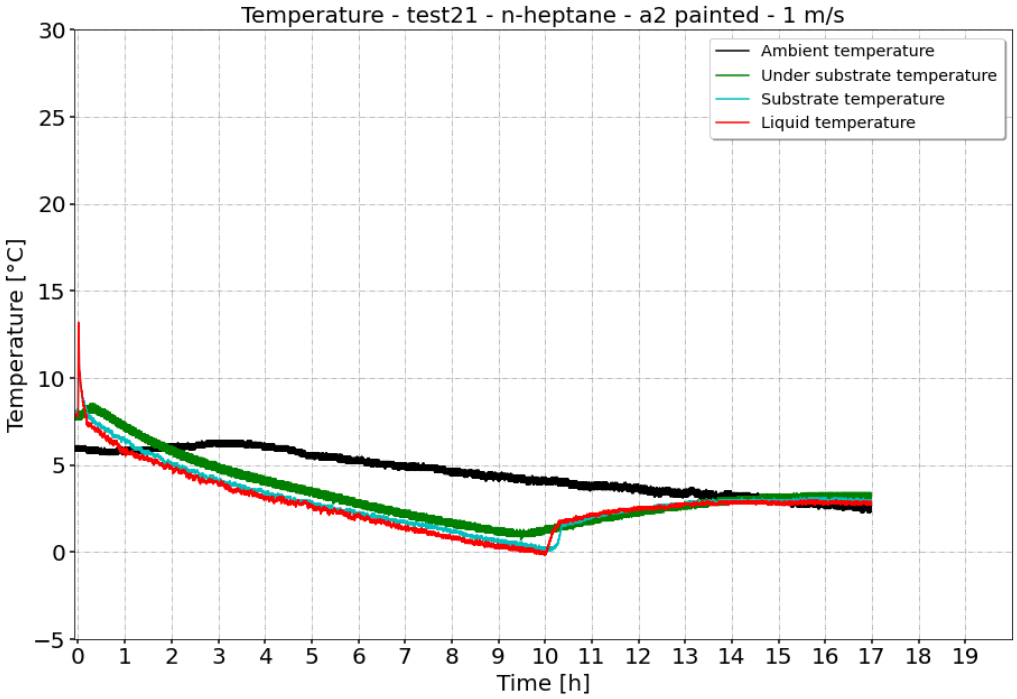

Temperature - test08 - n-heptane - c - 1 m/s
Ambient temperature
Under substrate temperature
Substrate temperature
Liquid temperature
Temperature [°C]
Time [h]

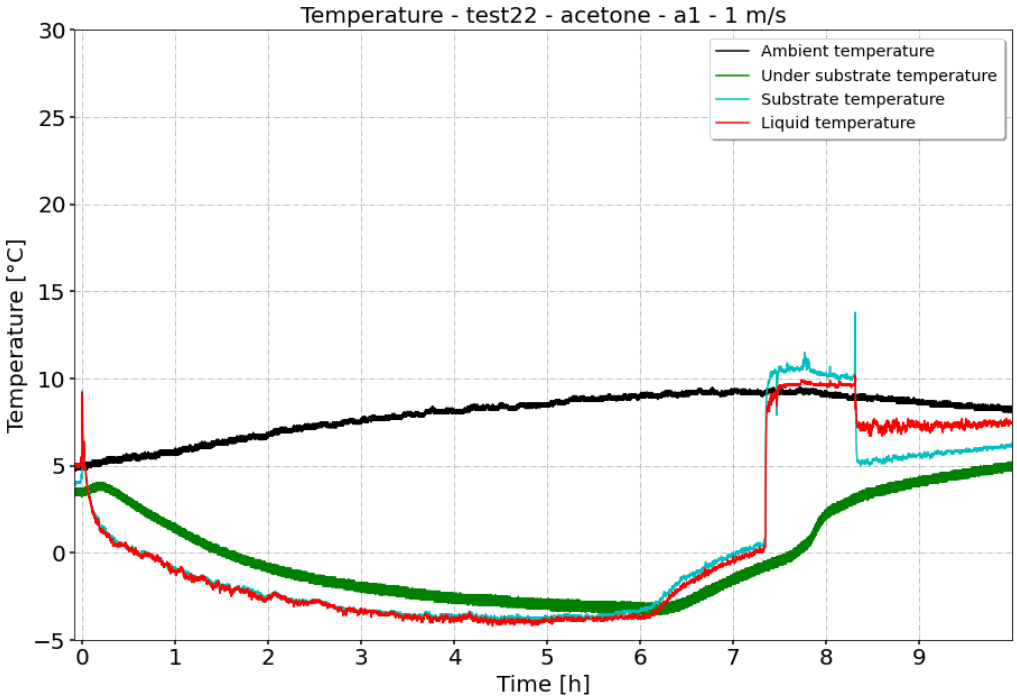

Temperature - test09 - TEP - a3 - 1 m/s
Ambient temperature
Under substrate temperature
Substrate temperature
Liquid temperature
Temperature [°C]
Time [h]


Temperature - test10 - n-heptane - a1 - 1 m/s
Ambient temperature
Under substrate temperature
Substrate temperature
Liquid temperature
Temperature [°C]
Time [h]

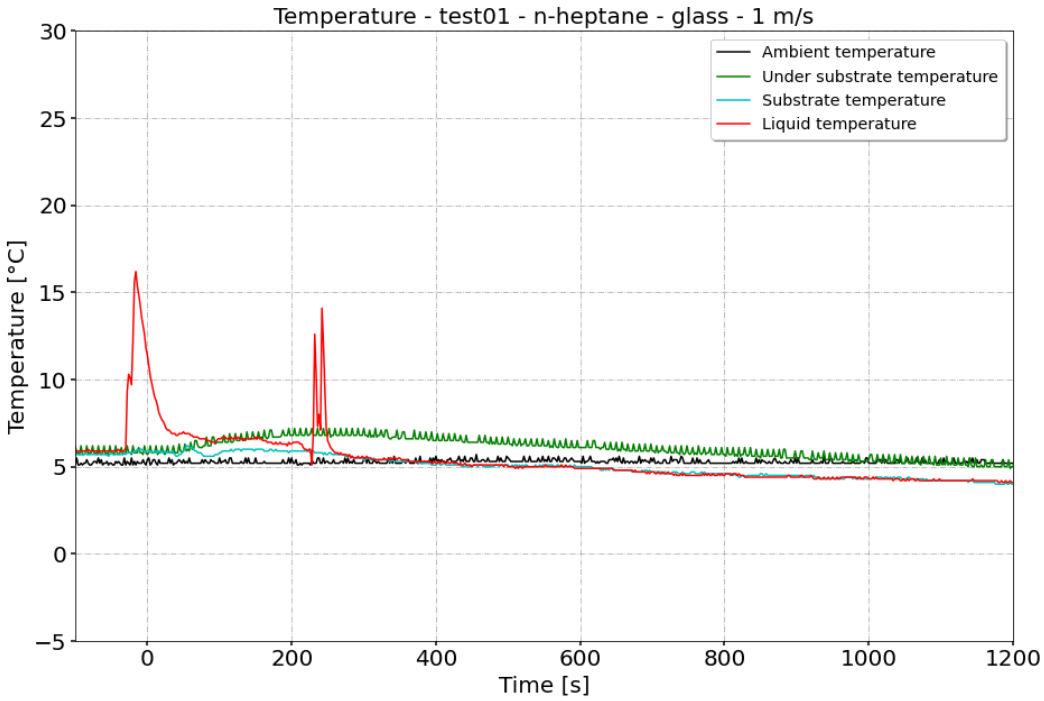

Temperature - test11 - n-heptane - a2 painted - 2 m/s
Ambient temperature
Under substrate temperature
Substrate temperature
Liquid temperature
Temperature [°C]
Time [h]

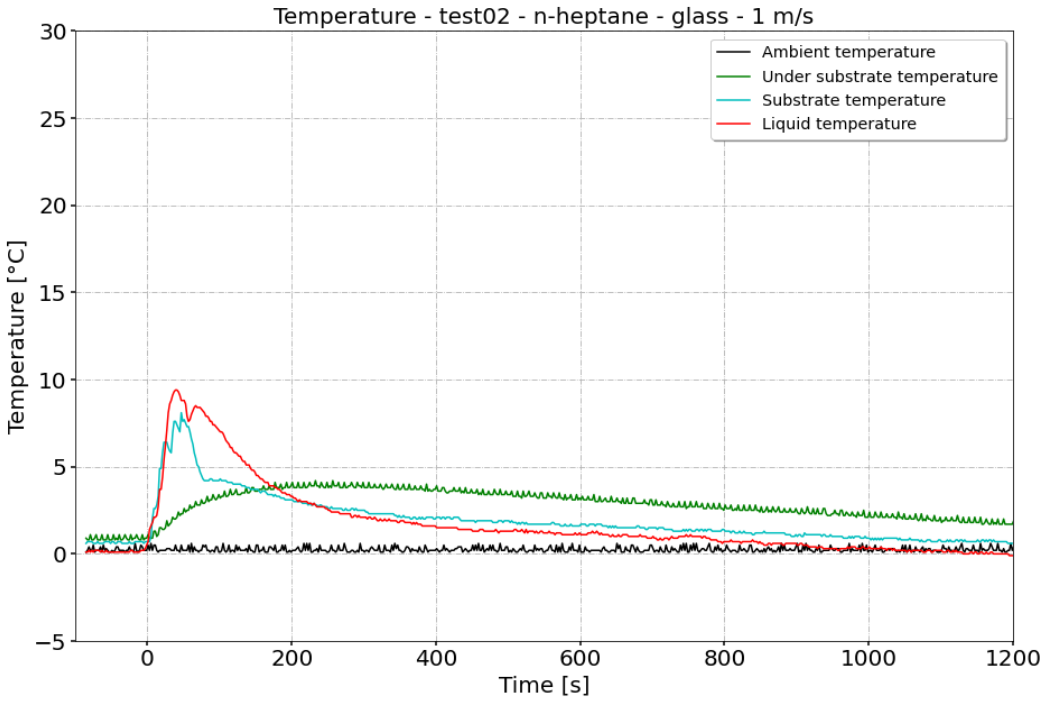

Temperature - test20 - n-octane - b - 1 m/s
Ambient temperature
Under substrate temperature
Substrate temperature
Liquid temperature
Temperature [°C]
Time [h]

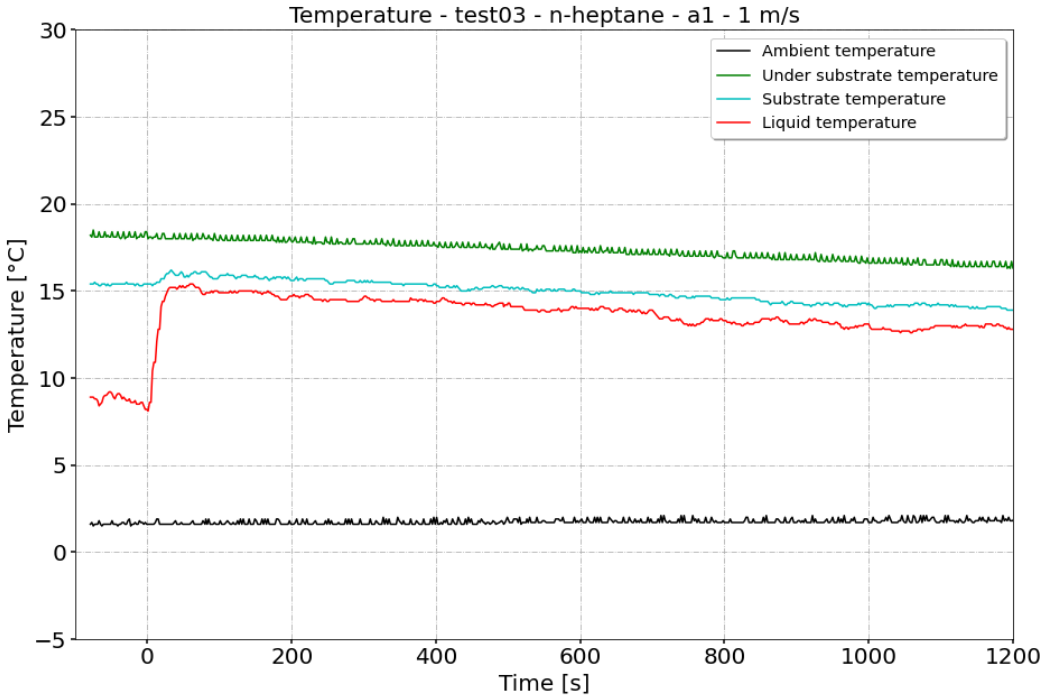

Temperature - test21 - n-heptane - a2 painted - 1 m/s
Ambient temperature
Under substrate temperature
Substrate temperature
Liquid temperature
Temperature [°C]
Time [h]

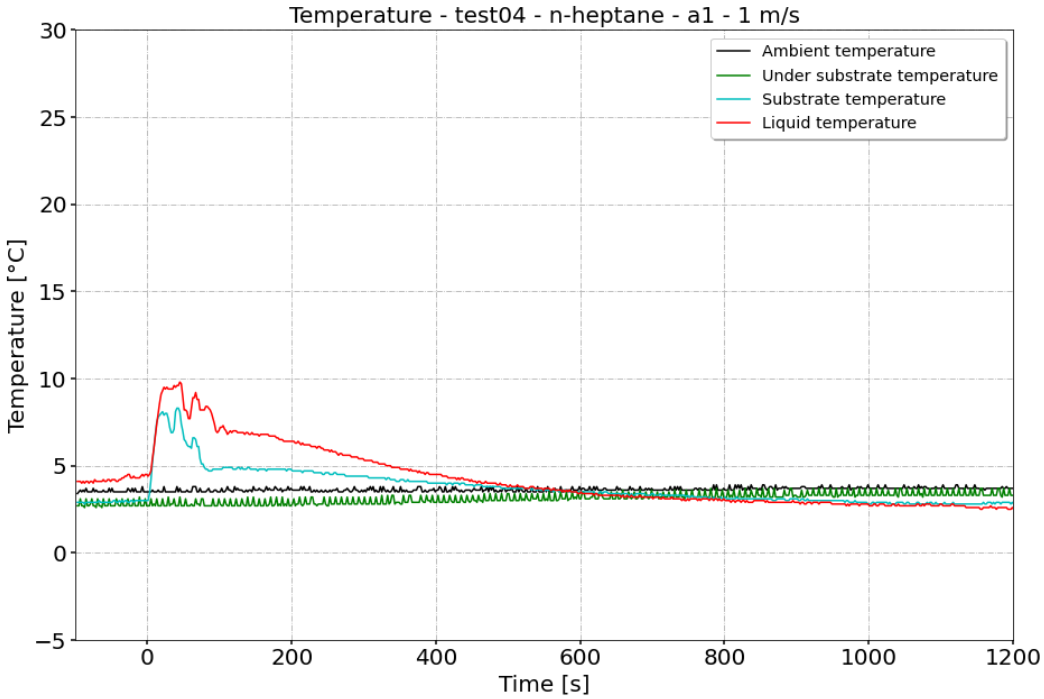

Temperature - test22 - acetone - a1 - 1 m/s
Ambient temperature
Under substrate temperature
Substrate temperature
Liquid temperature
Temperature [°C]
Time [h]

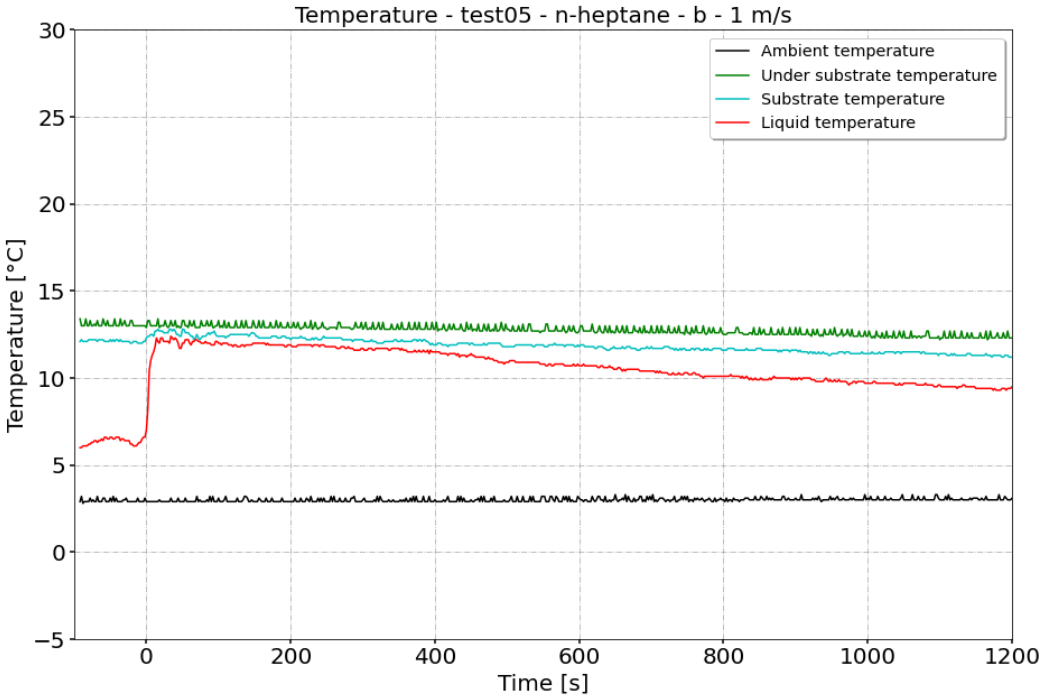
APPENDIX 5 : Pool evaporation tests – Temperature change measured with different thermocouples during the first 20 minutes – 7 pages

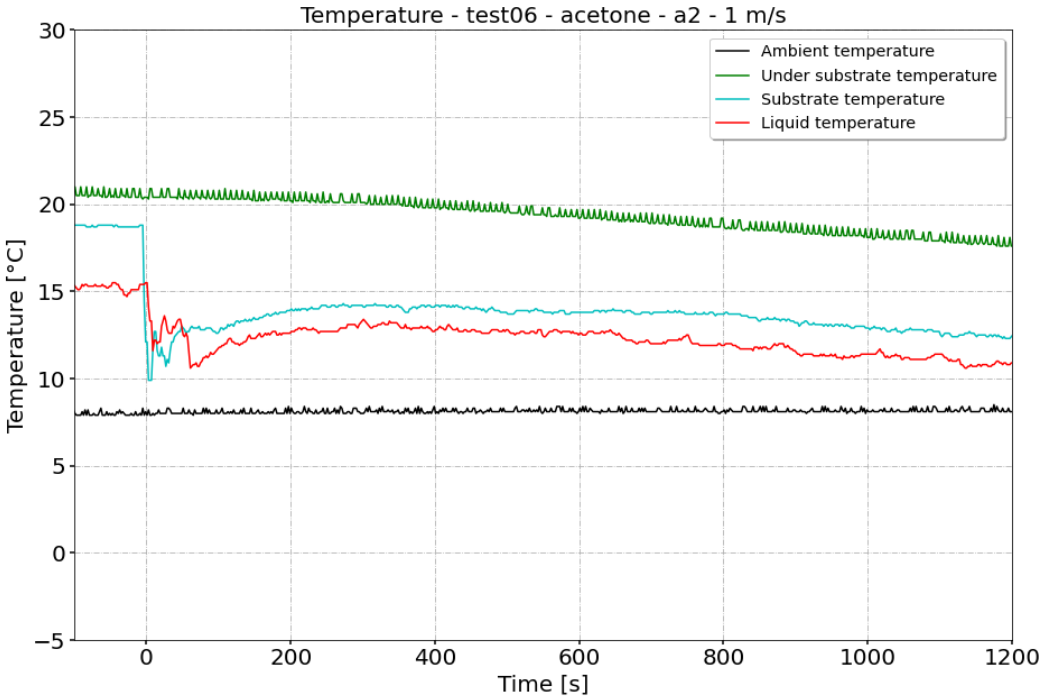


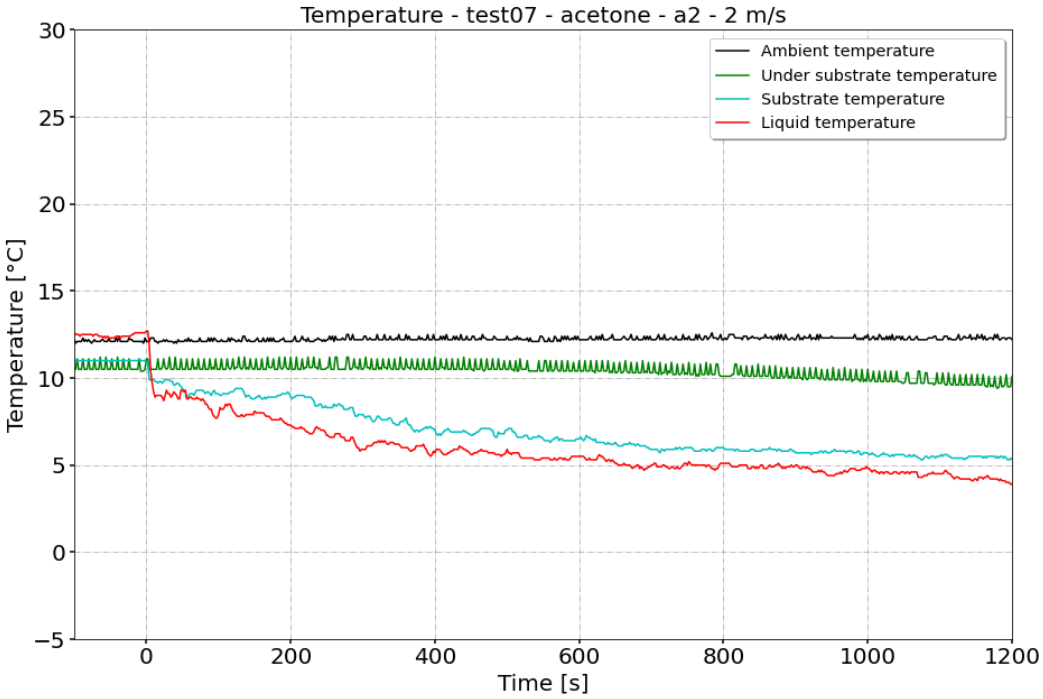


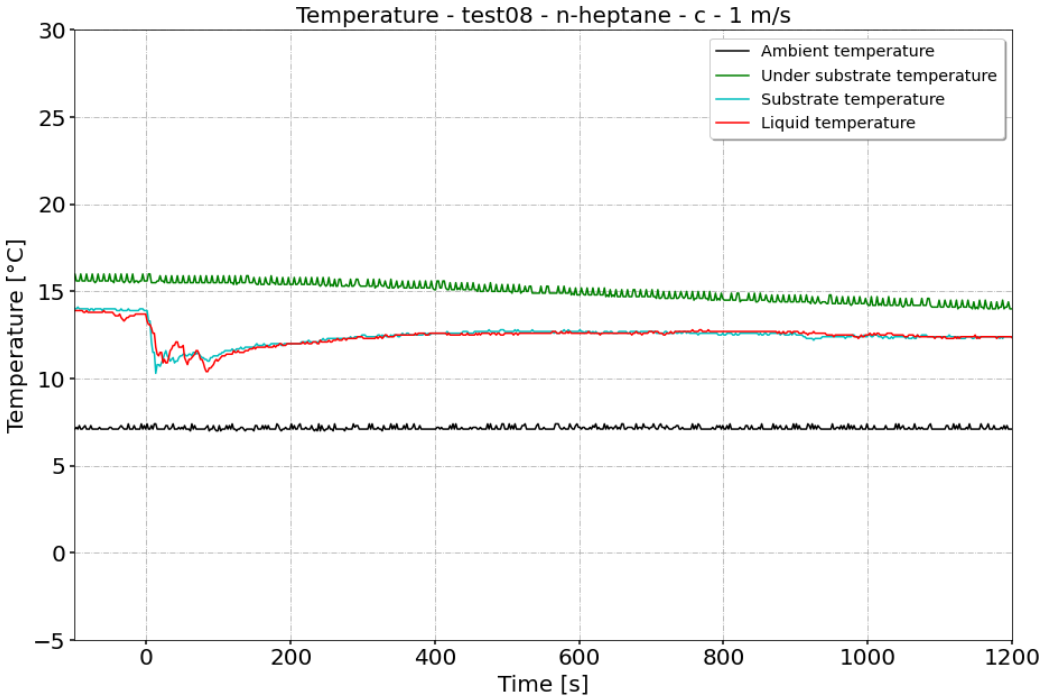

Temperature - test03 - n-heptane - a1 - 1 m/s
Ambient temperature
Under substrate temperature
Substrate temperature
Liquid temperature
Temperature [°C]
Time [s]
30
25
20
15
10
5
0
−5
0
200
400
600
800
1000
1200

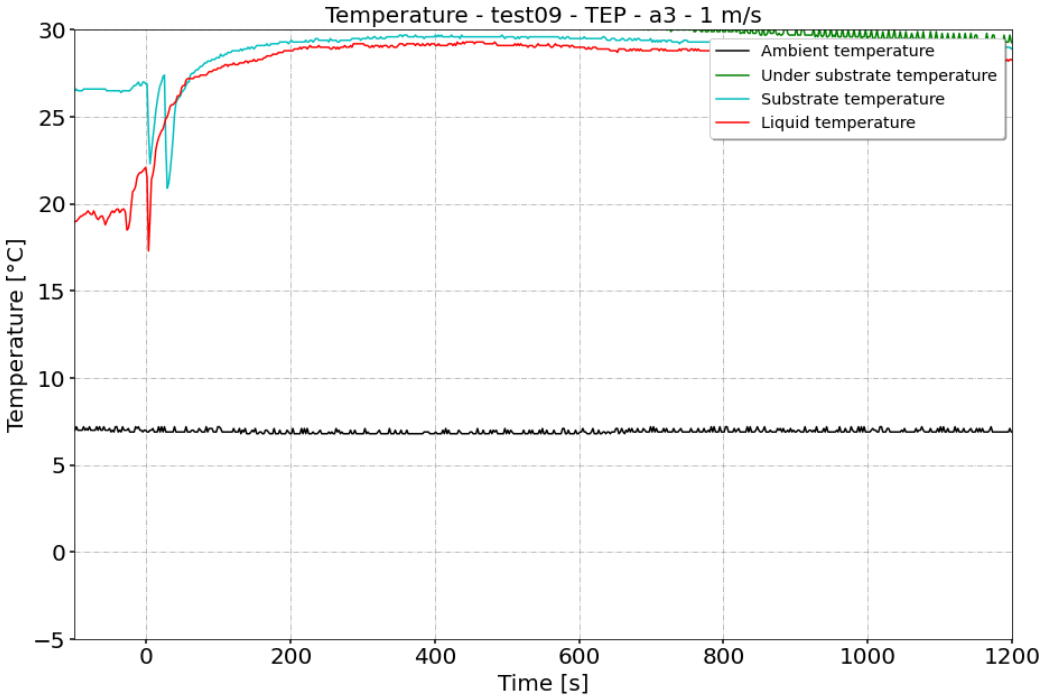

Temperature - test04 - n-heptane - a1 - 1 m/s
Ambient temperature
Under substrate temperature
Substrate temperature
Liquid temperature
Temperature [°C]
Time [s]
30
25
20
15
10
5
0
−5
0
200
400
600
800
1000
1200

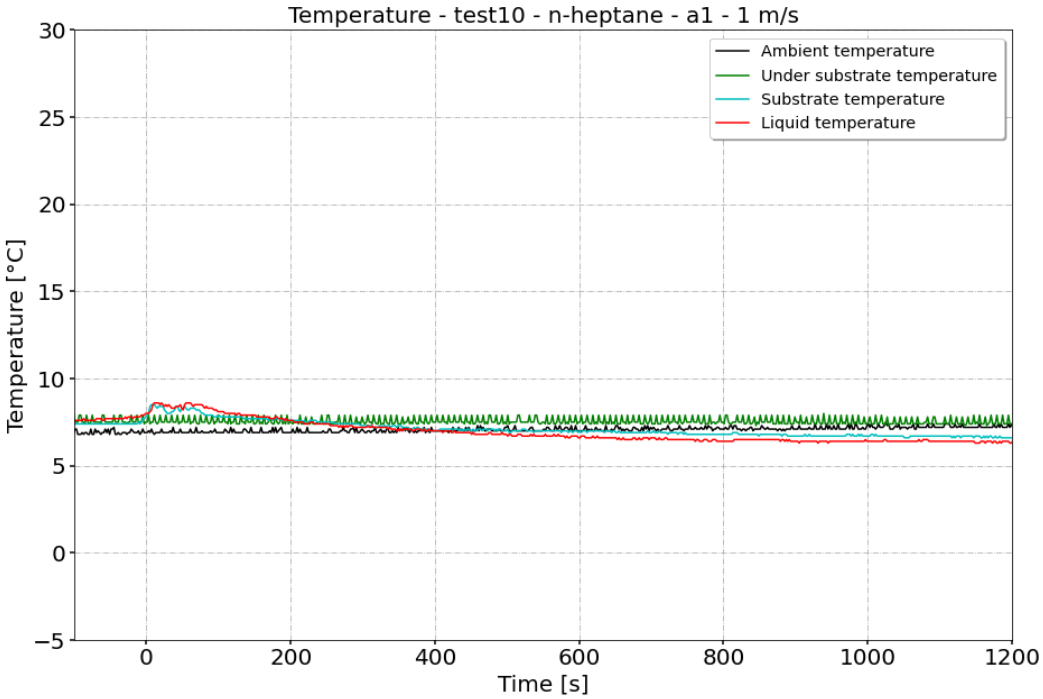

Temperature - test05 - n-heptane - b - 1 m/s
Ambient temperature
Under substrate temperature
Substrate temperature
Liquid temperature
Temperature [°C]
Time [s]
30
25
20
15
10
5
0
−5
0
200
400
600
800
1000
1200

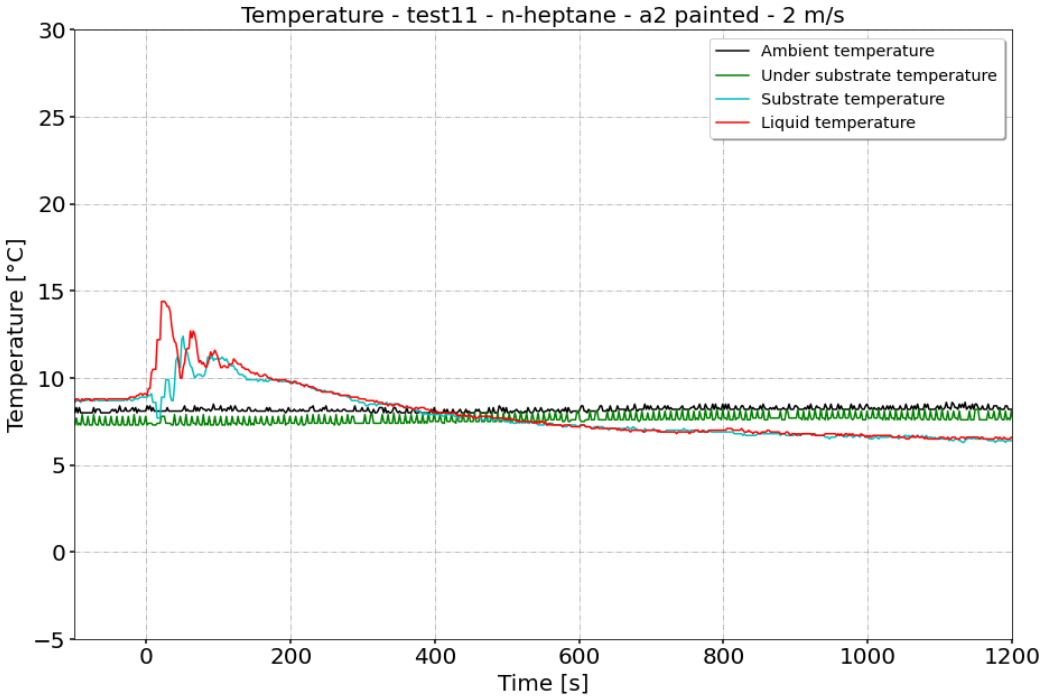

Temperature - test06 - acetone - a2 - 1 m/s
Ambient temperature
Under substrate temperature
Substrate temperature
Liquid temperature
Temperature [°C]
Time [s]
30
25
20
15
10
5
0
−5
0
200
400
600
800
1000
1200

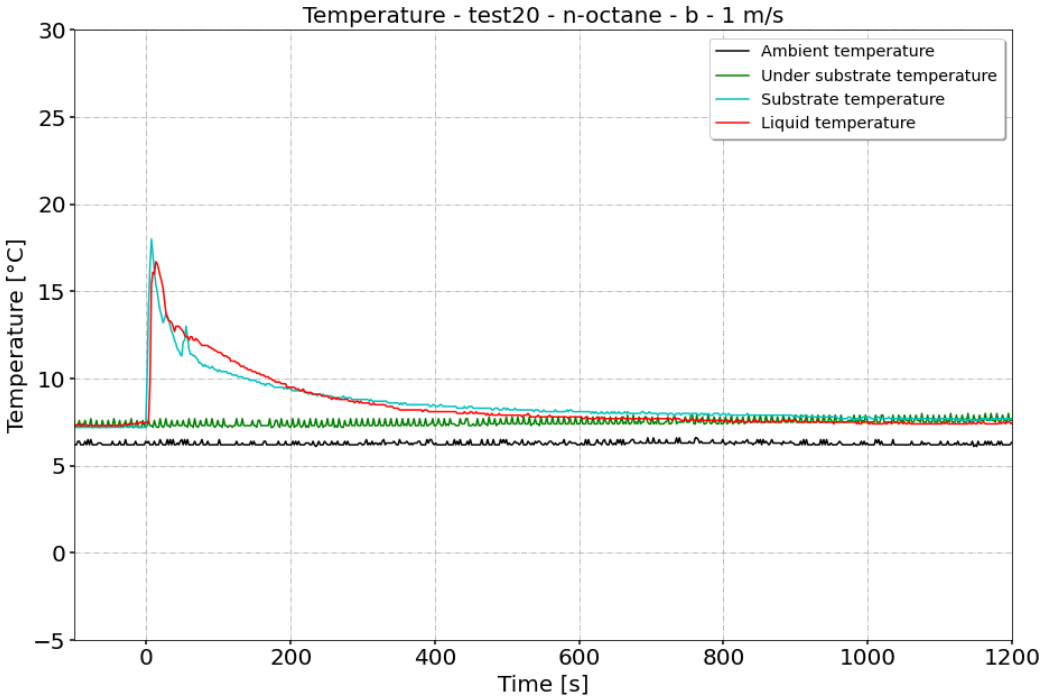

Temperature - test07 - acetone - a2 - 2 m/s
Ambient temperature
Under substrate temperature
Substrate temperature
Liquid temperature
Temperature [°C]
Time [s]
30
25
20
15
10
5
0
−5
0
200
400
600
800
1000
1200

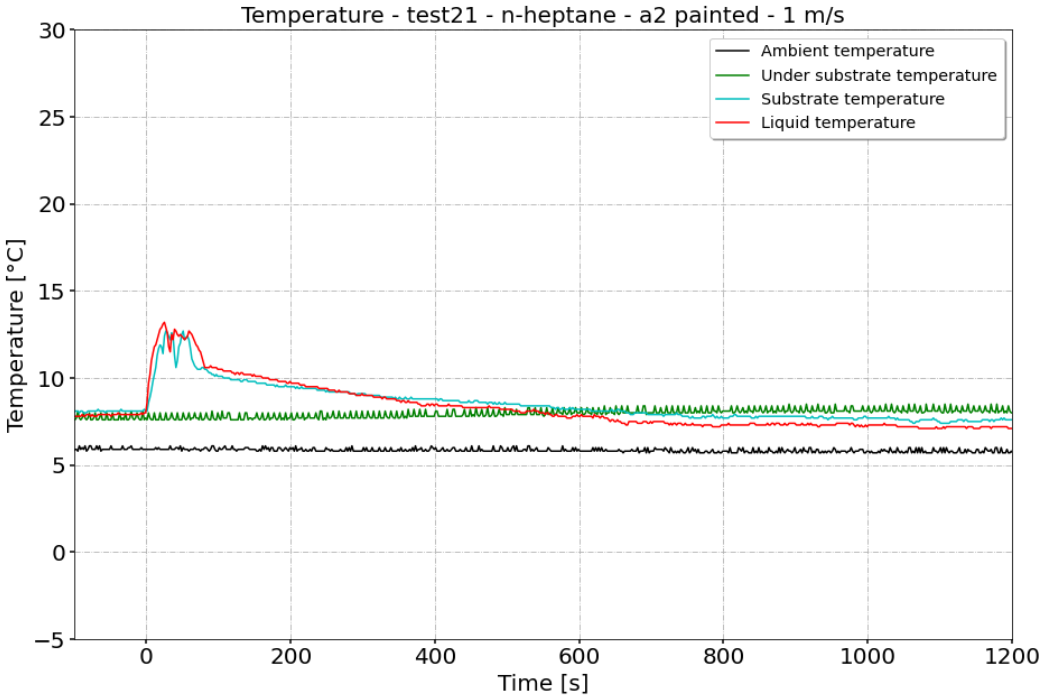

Temperature - test08 - n-heptane - c - 1 m/s
Ambient temperature
Under substrate temperature
Substrate temperature
Liquid temperature
Temperature [°C]
Time [s]
30
25
20
15
10
5
0
−5
0
200
400
600
800
1000
1200

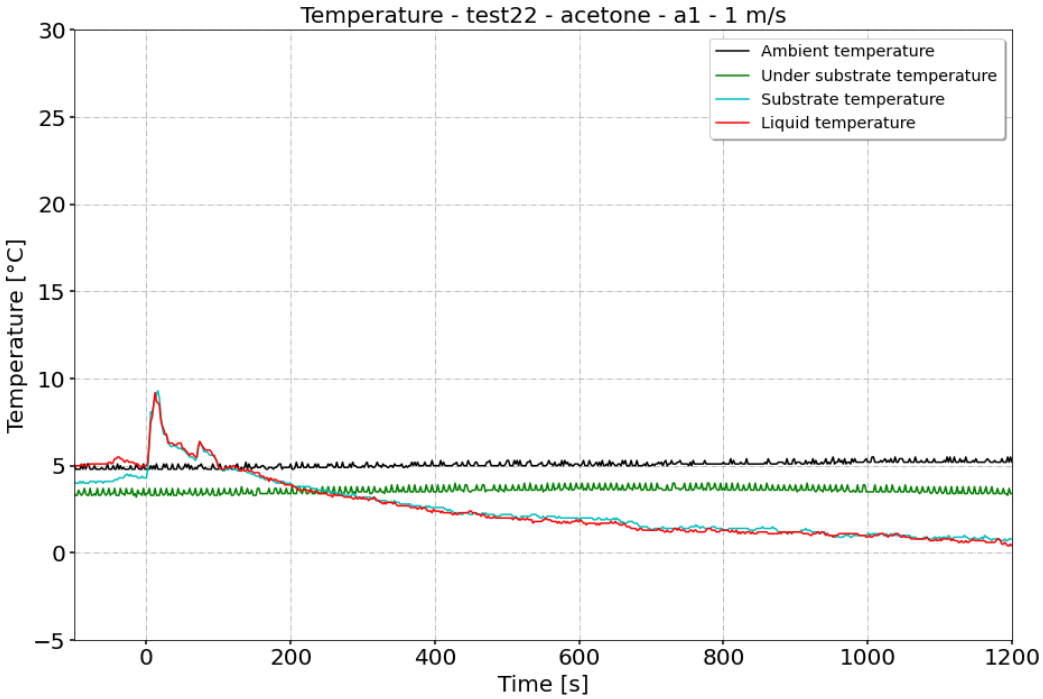

Temperature - test09 - TEP - a3 - 1 m/s
Ambient temperature
Under substrate temperature
Substrate temperature
Liquid temperature
Temperature [°C]
Time [s]
30
25
20
15
10
5
0
−5
0
200
400
600
800
1000
1200


Temperature - test10 - n-heptane - a1 - 1 m/s
Ambient temperature
Under substrate temperature
Substrate temperature
Liquid temperature
Temperature [°C]
Time [s]
30
25
20
15
10
5
0
−5
0
200
400
600
800
1000
1200

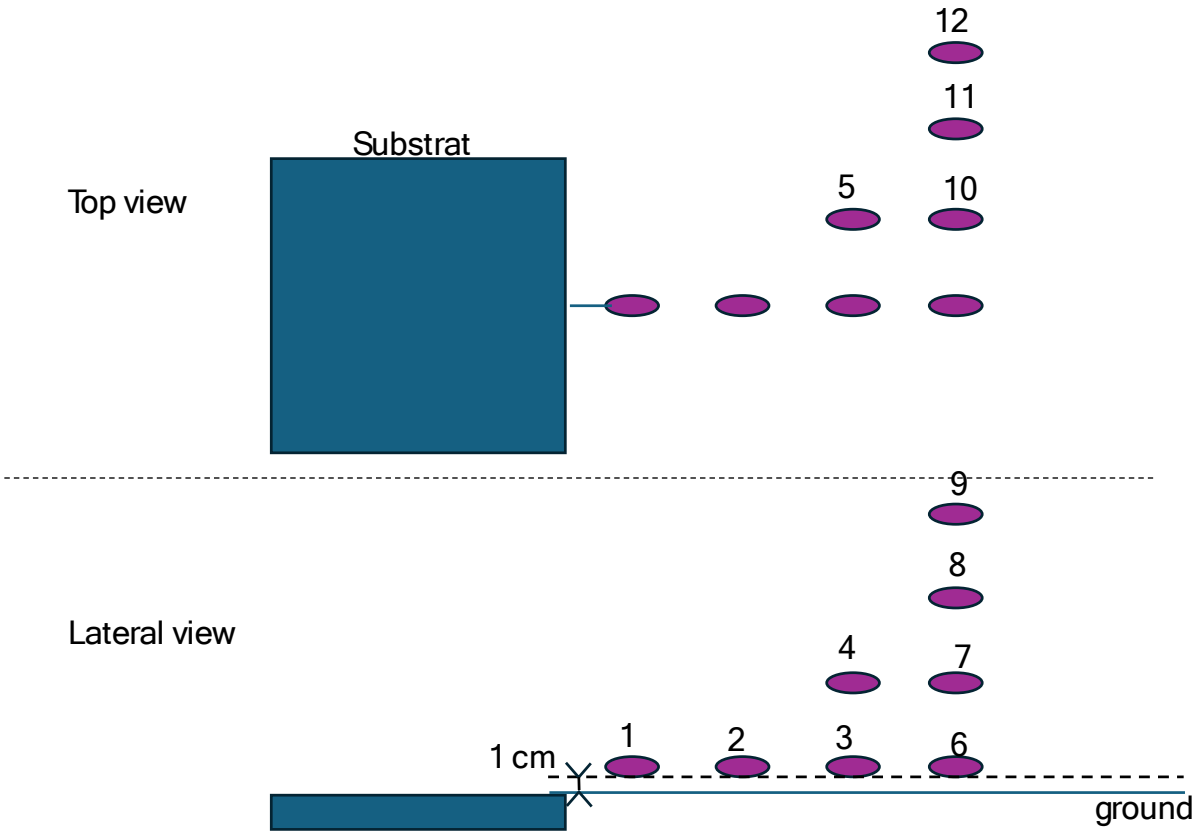

Temperature - test11 - n-heptane - a2 painted - 2 m/s
Ambient temperature
Under substrate temperature
Substrate temperature
Liquid temperature
Temperature [°C]
Time [s]
30
25
20
15
10
5
0
−5
0
200
400
600
800
1000
1200

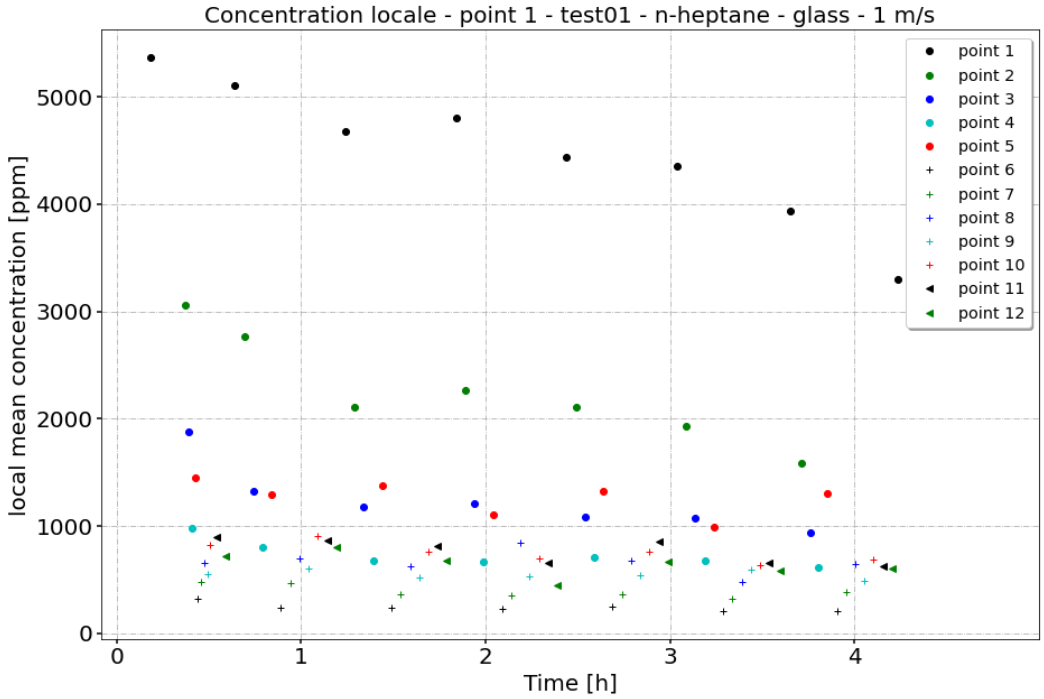

Temperature - test20 - n-octane - b - 1 m/s
Ambient temperature
Under substrate temperature
Substrate temperature
Liquid temperature
Temperature [°C]
Time [s]
30
25
20
15
10
5
0
−5
0
200
400
600
800
1000
1200

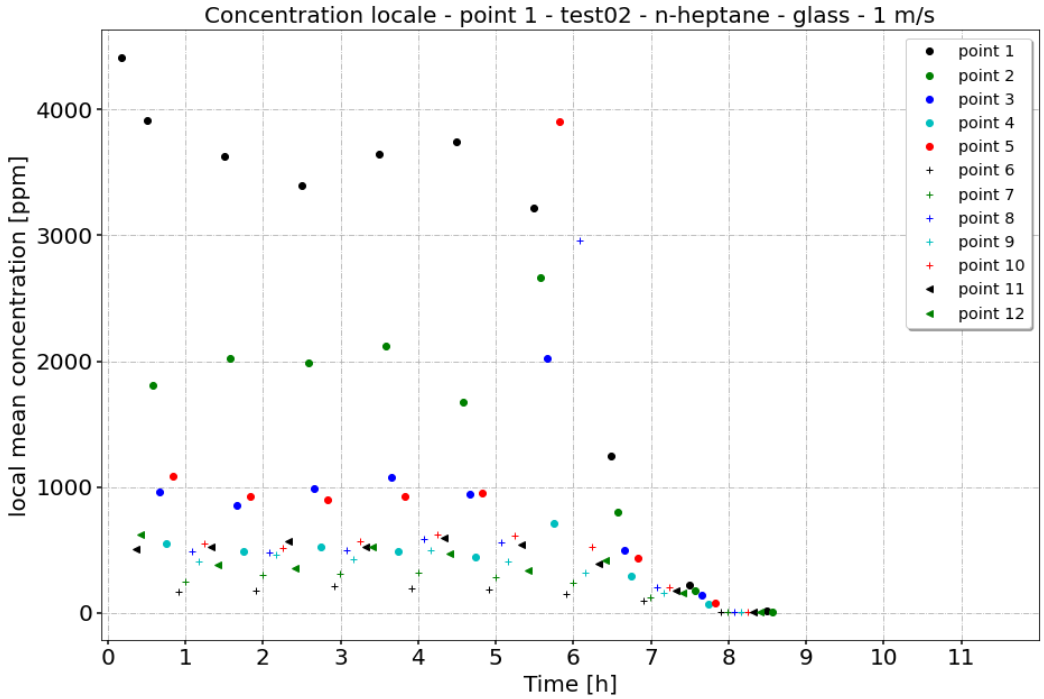

Temperature - test21 - n-heptane - a2 painted - 1 m/s
Ambient temperature
Under substrate temperature
Substrate temperature
Liquid temperature
Temperature [°C]
Time [s]
30
25
20
15
10
5
0
−5
0
200
400
600
800
1000
1200

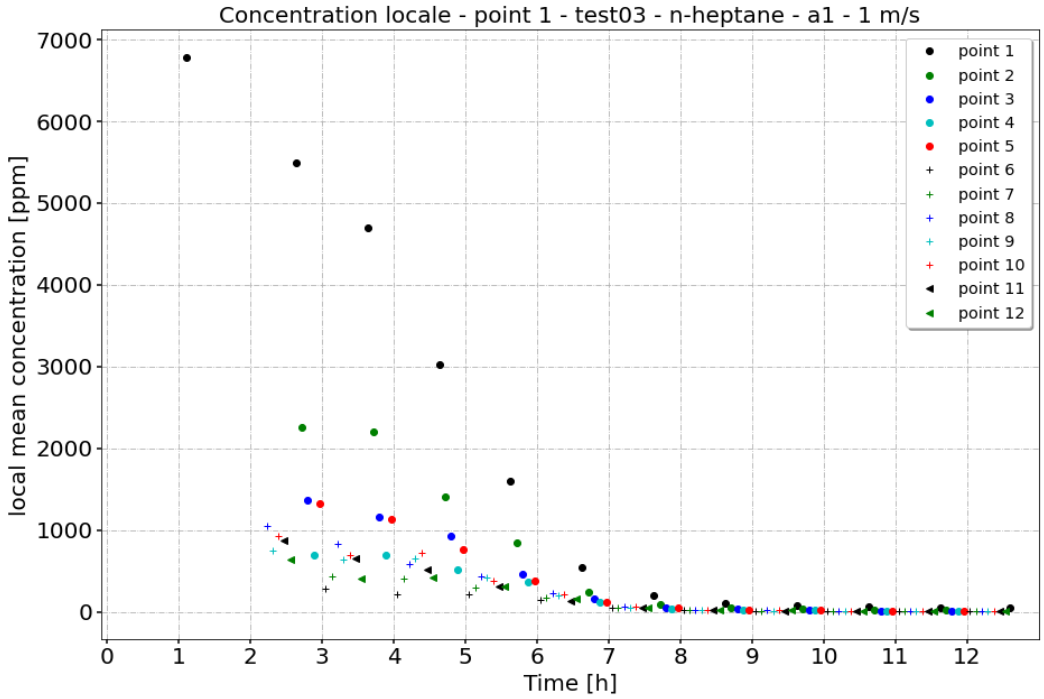

Temperature - test22 - acetone - a1 - 1 m/s
Ambient temperature
Under substrate temperature
Substrate temperature
Liquid temperature
Temperature [°C]
Time [s]
30
25
20
15
10
5
0
−5
0
200
400
600
800
1000
1200

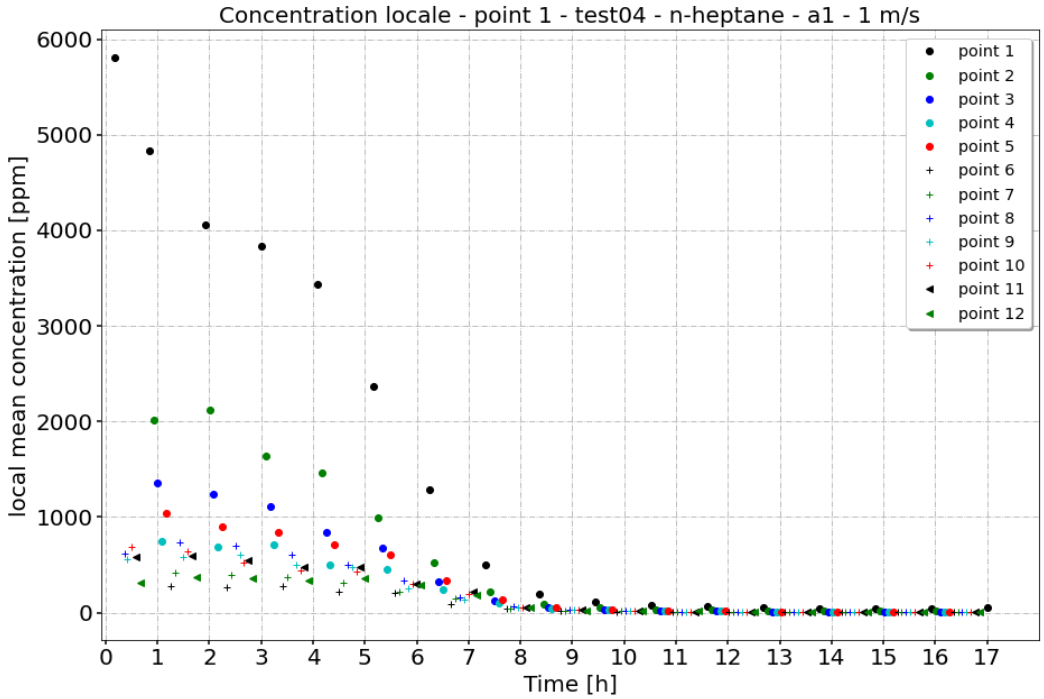
APPENDIX 6 : Pool evaporation tests – Change in concentration measured locally – 7 pages

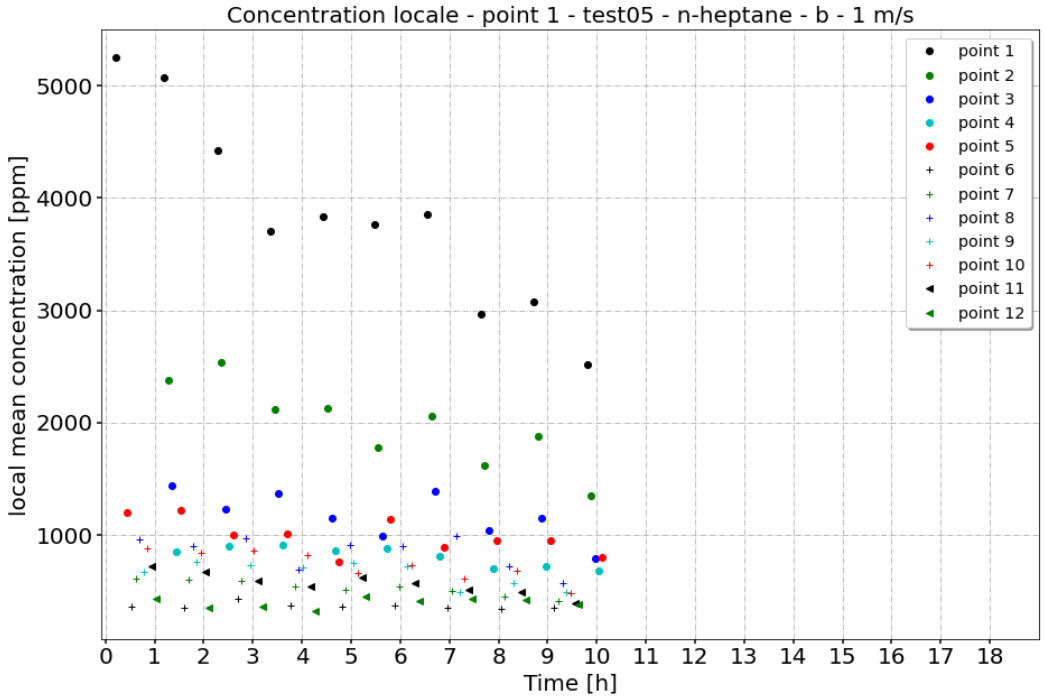


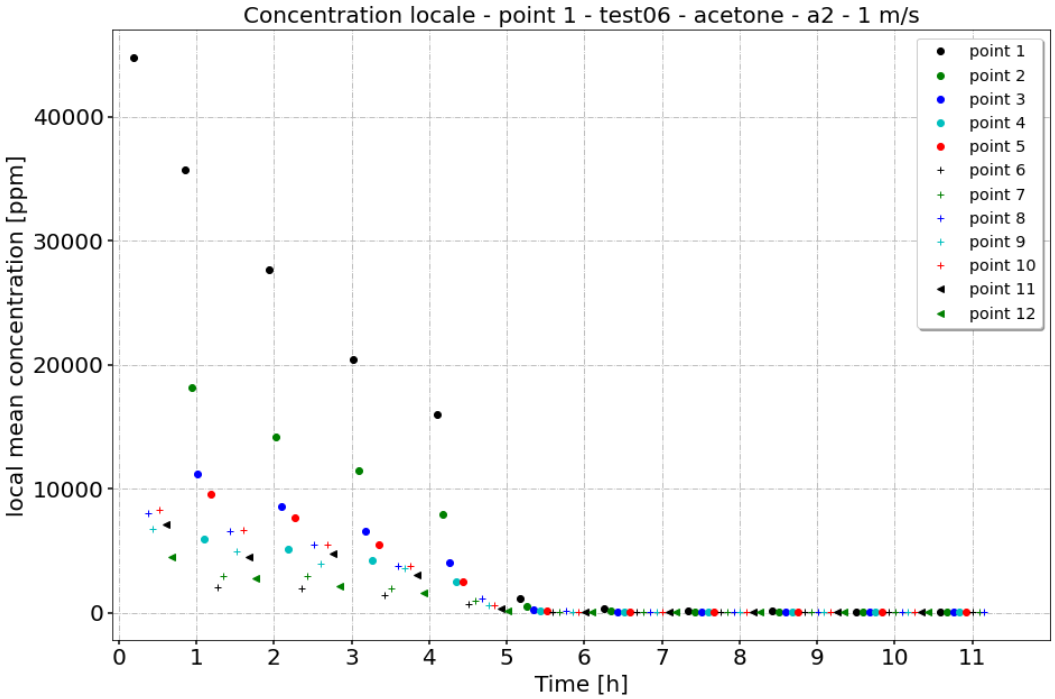

Concentration locale - point 1 - test01 - n-heptane - glass - 1 m/s
local mean concentration [ppm]
Time [h]
point 1
point 2
point 3
point 4
point 5
point 6
point 7
point 8
point 9
point 10
point 11
point 12

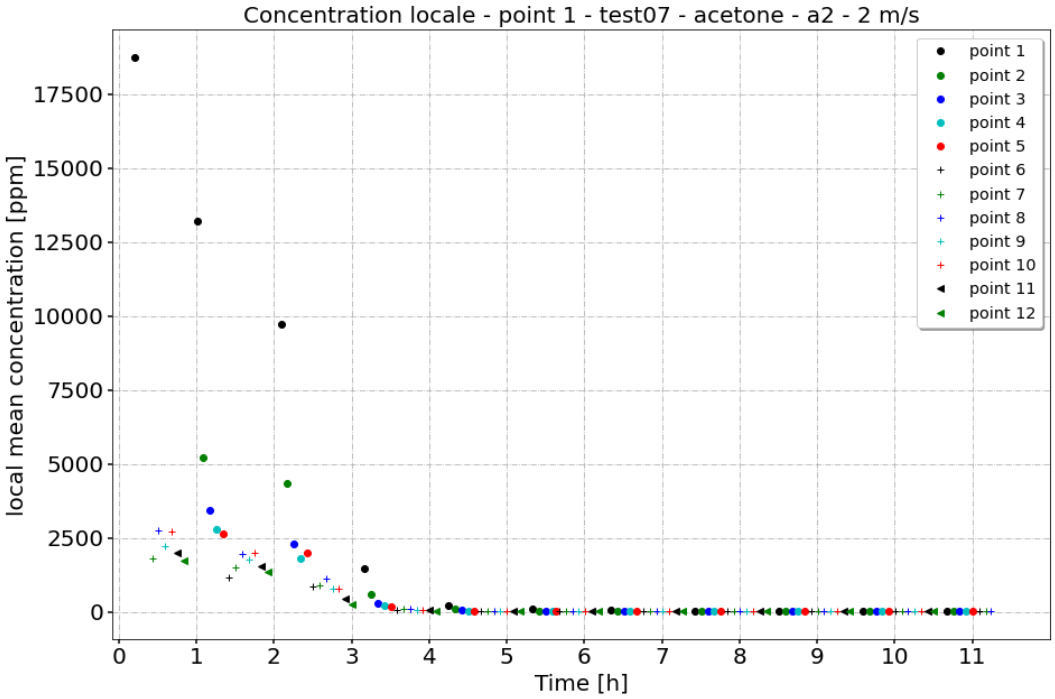

Concentration locale - point 1 - test02 - n-heptane - glass - 1 m/s
local mean concentration [ppm]
Time [h]
point 1
point 2
point 3
point 4
point 5
point 6
point 7
point 8
point 9
point 10
point 11
point 12

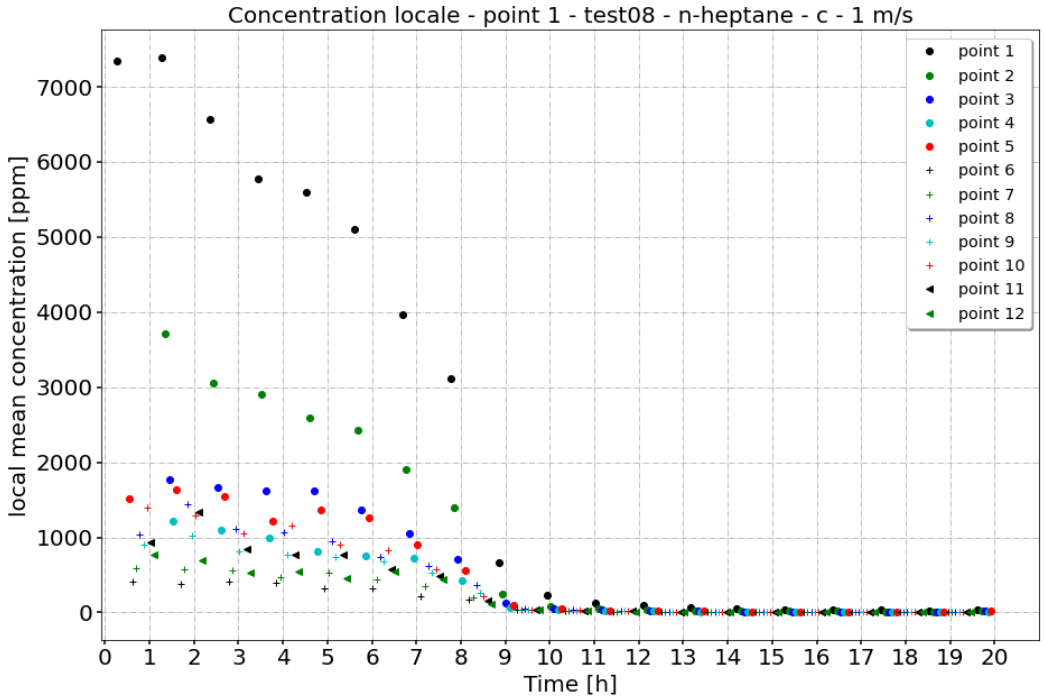

Concentration locale - point 1 - test03 - n-heptane - a1 - 1 m/s
local mean concentration [ppm]
Time [h]
point 1
point 2
point 3
point 4
point 5
point 6
point 7
point 8
point 9
point 10
point 11
point 12

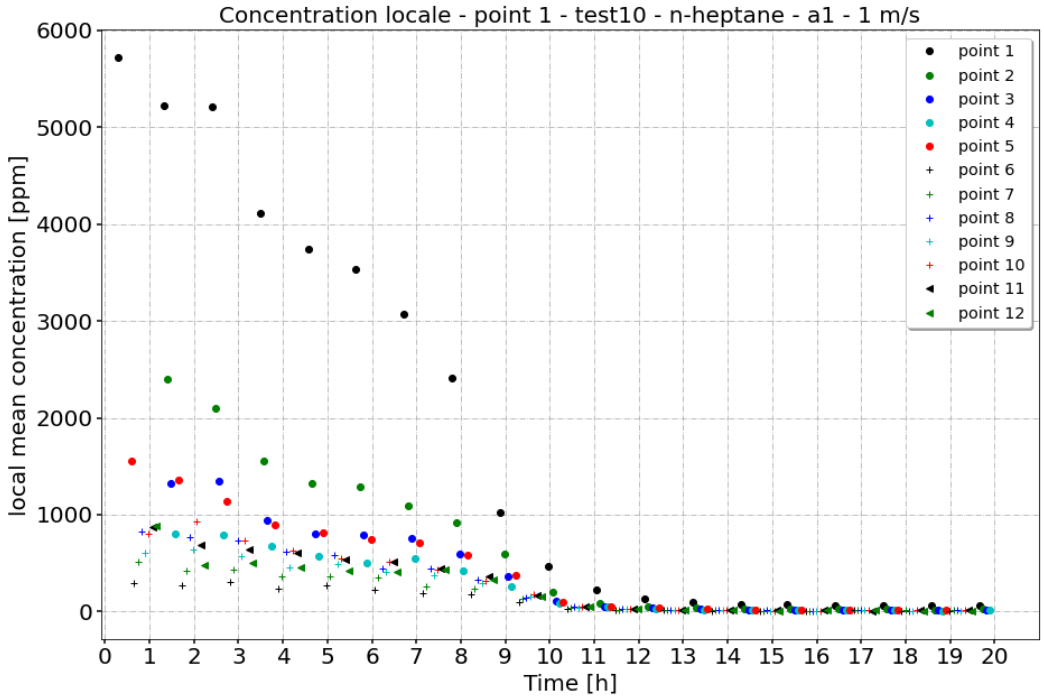

Concentration locale - point 1 - test04 - n-heptane - a1 - 1 m/s
local mean concentration [ppm]
Time [h]
point 1
point 2
point 3
point 4
point 5
point 6
point 7
point 8
point 9
point 10
point 11
point 12

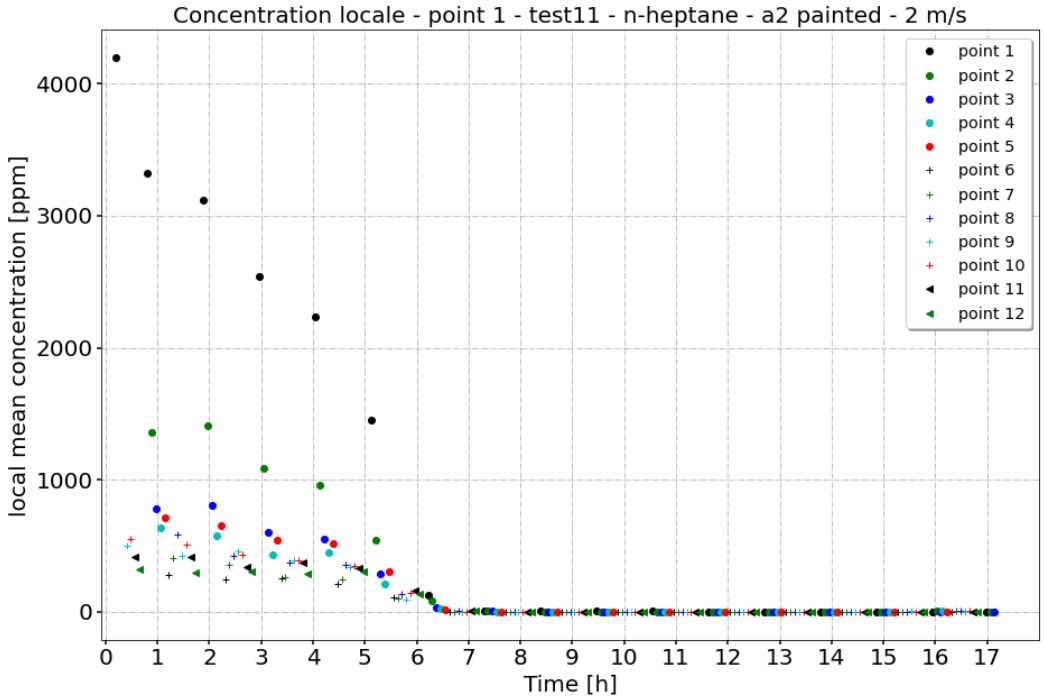

Concentration locale - point 1 - test05 - n-heptane - b - 1 m/s
local mean concentration [ppm]
Time [h]
point 1
point 2
point 3
point 4
point 5
point 6
point 7
point 8
point 9
point 10
point 11
point 12

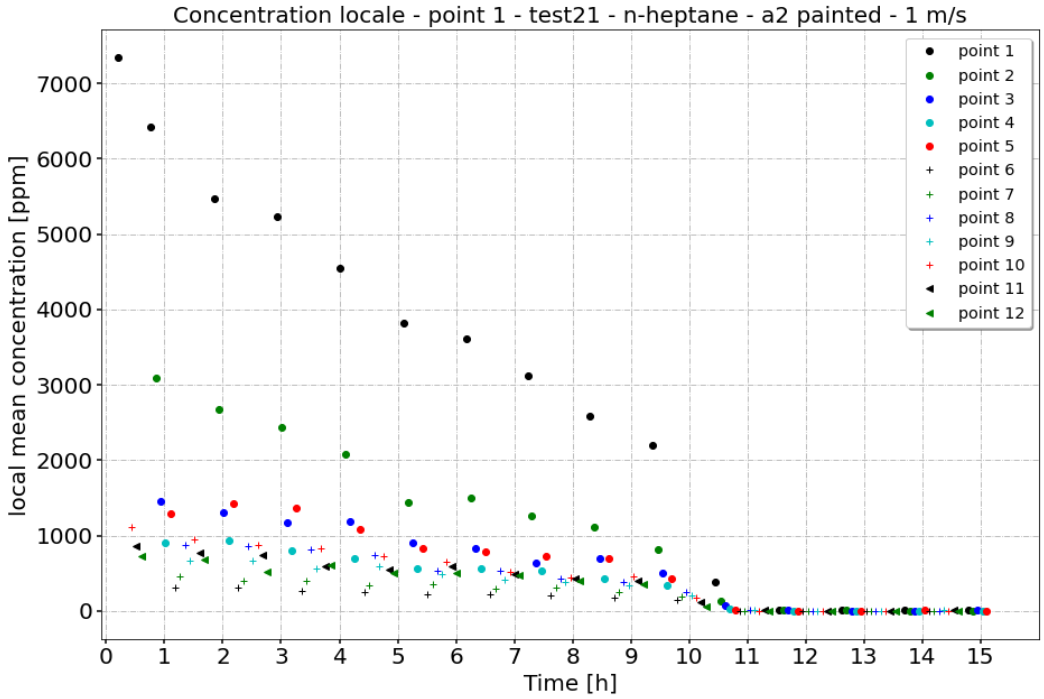

Concentration locale - point 1 - test06 - acetone - a2 - 1 m/s
local mean concentration [ppm]
Time [h]
point 1
point 2
point 3
point 4
point 5
point 6
point 7
point 8
point 9
point 10
point 11
point 12

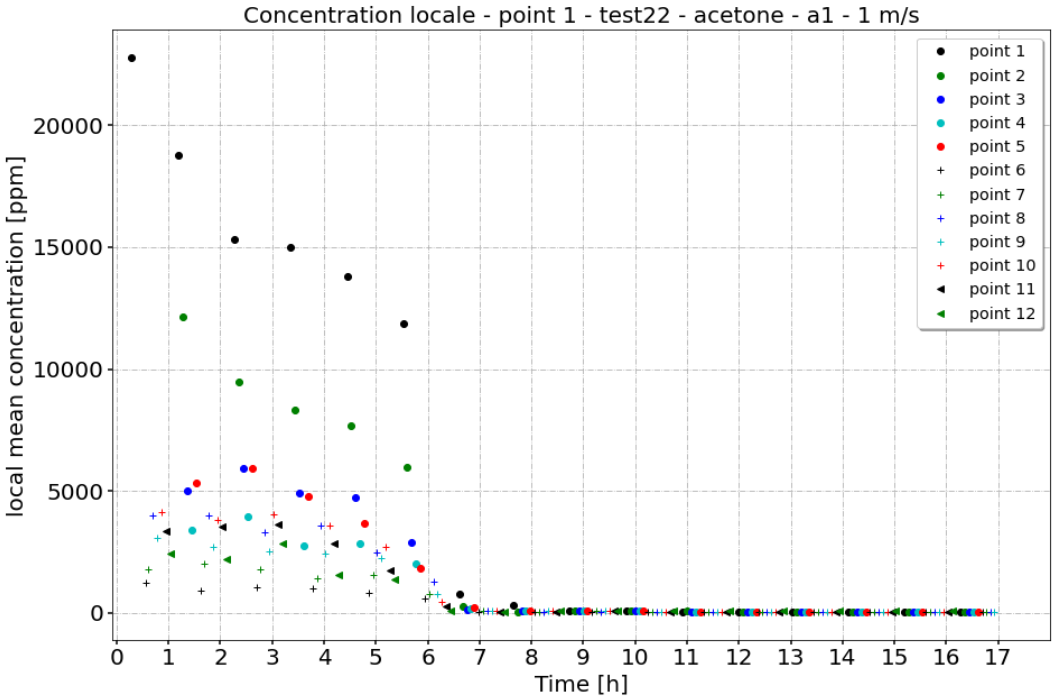

Concentration locale - point 1 - test07 - acetone - a2 - 2 m/s
local mean concentration [ppm]
Time [h]
point 1
point 2
point 3
point 4
point 5
point 6
point 7
point 8
point 9
point 10
point 11
point 12


Concentration locale - point 1 - test08 - n-heptane - c - 1 m/s
local mean concentration [ppm]
Time [h]
point 1
point 2
point 3
point 4
point 5
point 6
point 7
point 8
point 9
point 10
point 11
point 12

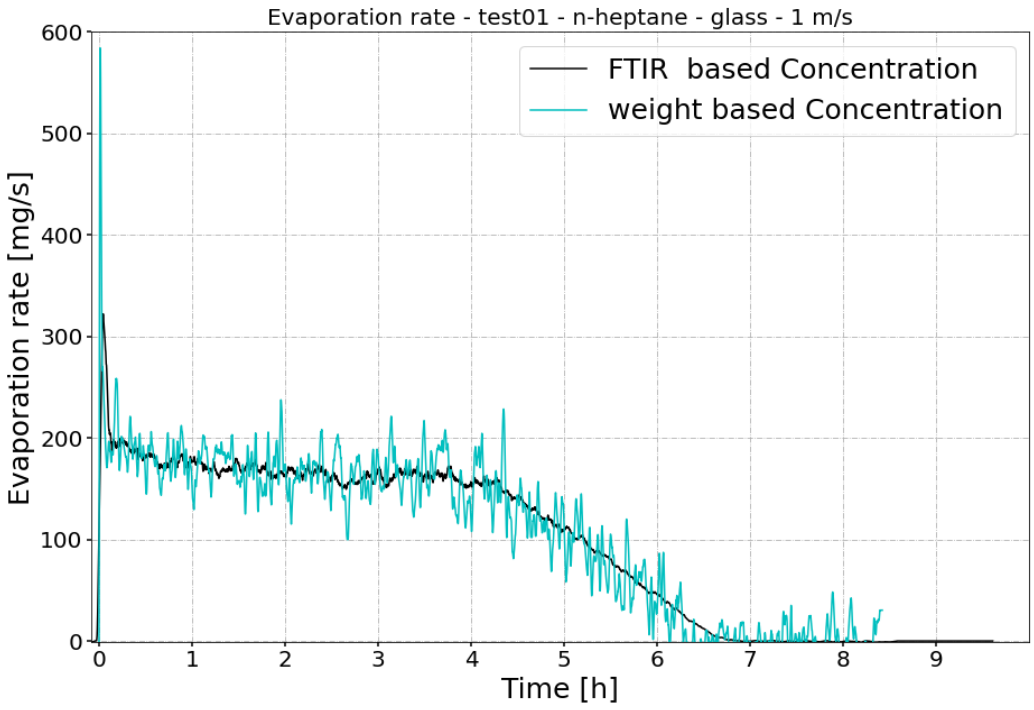

Concentration locale - point 1 - test10 - n-heptane - a1 - 1 m/s
local mean concentration [ppm]
Time [h]
point 1
point 2
point 3
point 4
point 5
point 6
point 7
point 8
point 9
point 10
point 11
point 12

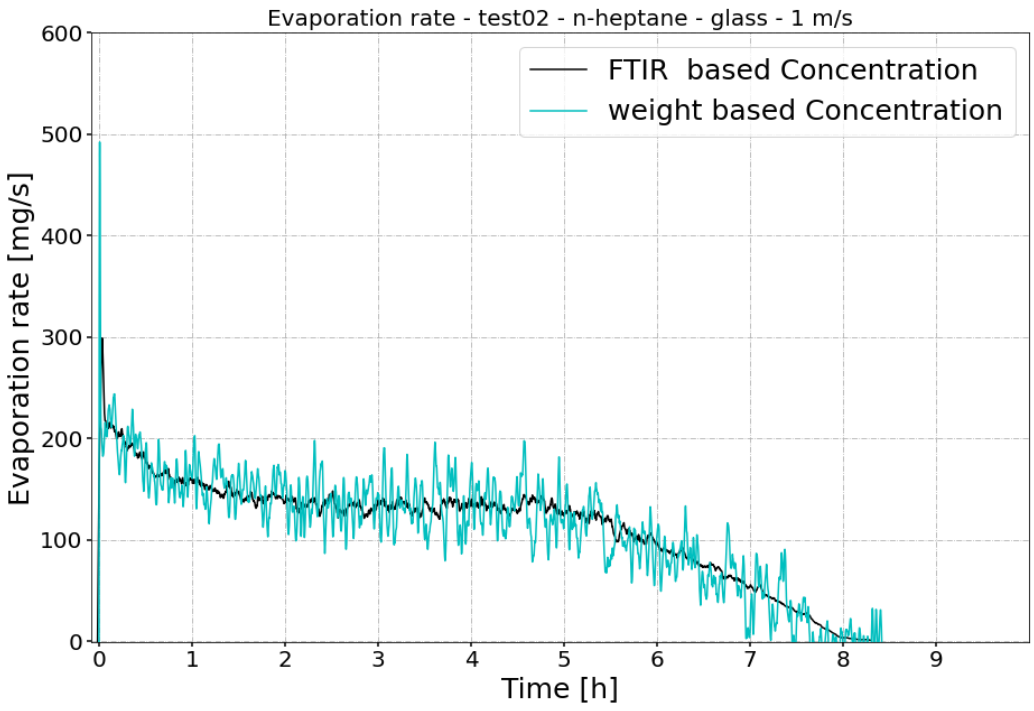

Concentration locale - point 1 - test11 - n-heptane - a2 painted - 2 m/s
local mean concentration [ppm]
Time [h]
point 1
point 2
point 3
point 4
point 5
point 6
point 7
point 8
point 9
point 10
point 11
point 12

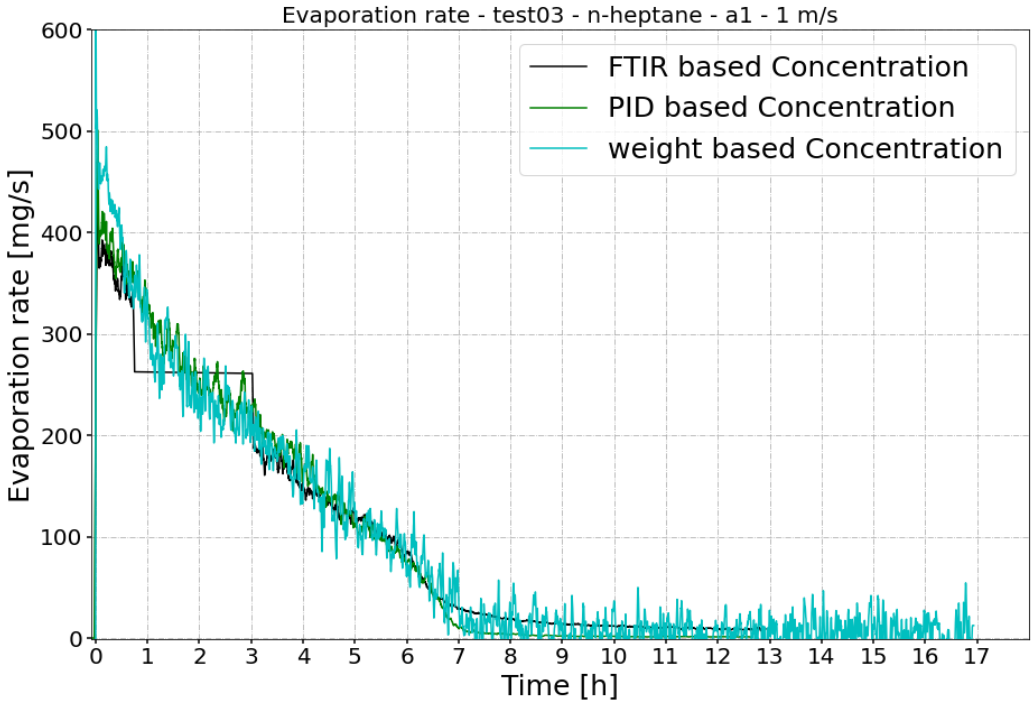

Concentration locale - point 1 - test21 - n-heptane - a2 painted - 1 m/s
local mean concentration [ppm]
Time [h]
point 1
point 2
point 3
point 4
point 5
point 6
point 7
point 8
point 9
point 10
point 11
point 12

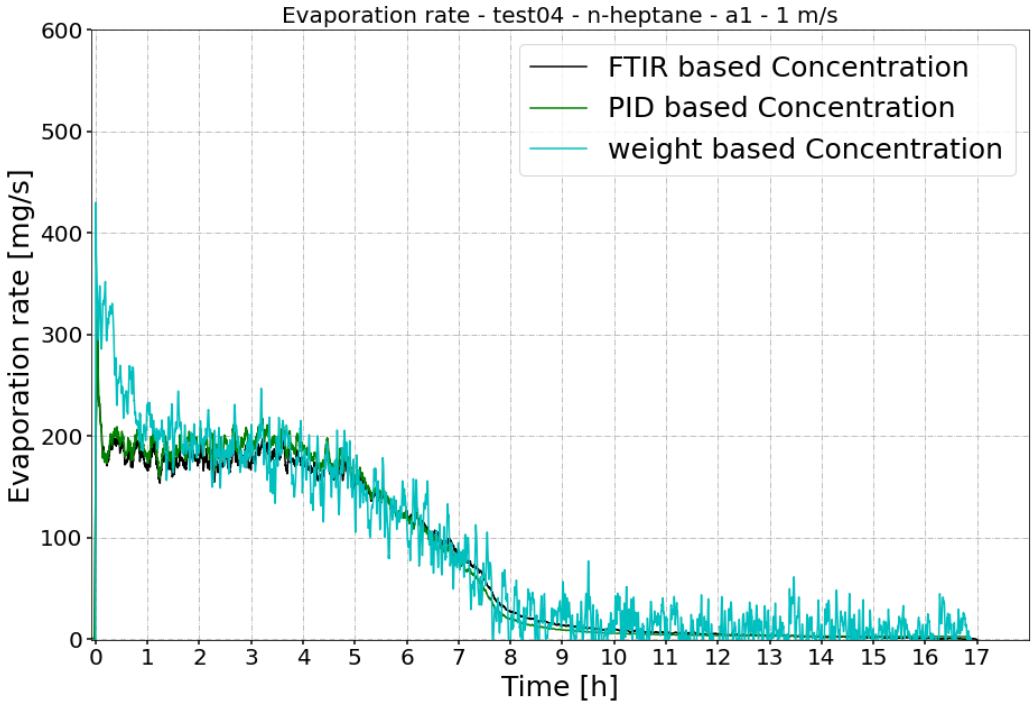

Concentration locale - point 1 - test22 - acetone - a1 - 1 m/s
local mean concentration [ppm]
Time [h]
point 1
point 2
point 3
point 4
point 5
point 6
point 7
point 8
point 9
point 10
point 11
point 12

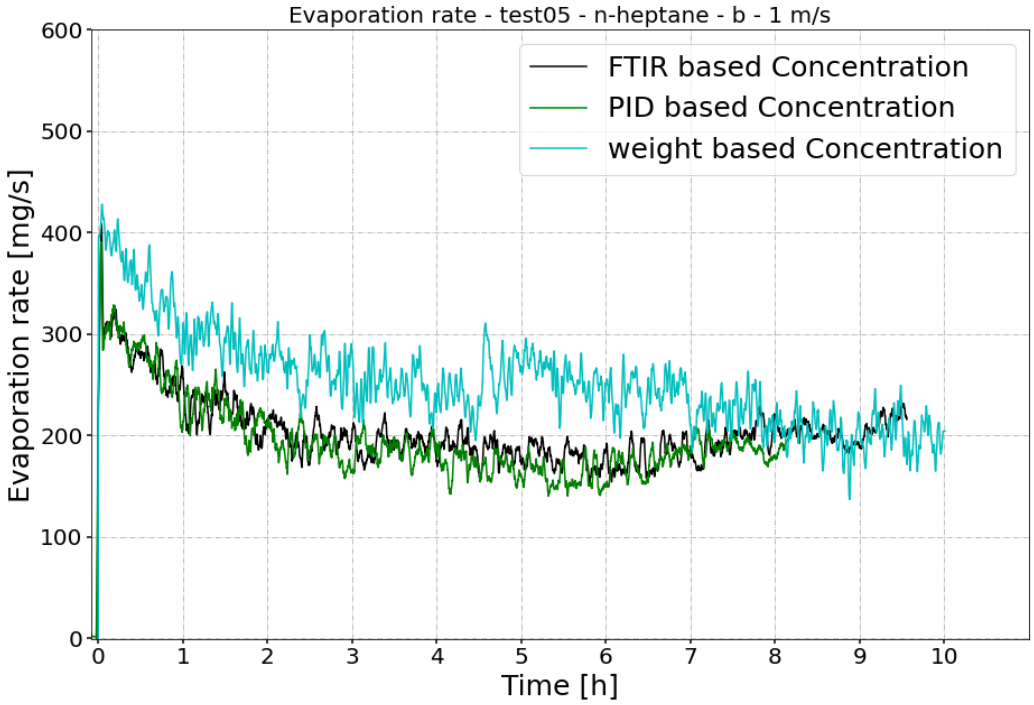
APPENDIX 7: Pool evaporation tests – Evolution of evaporation rate – 7 pages

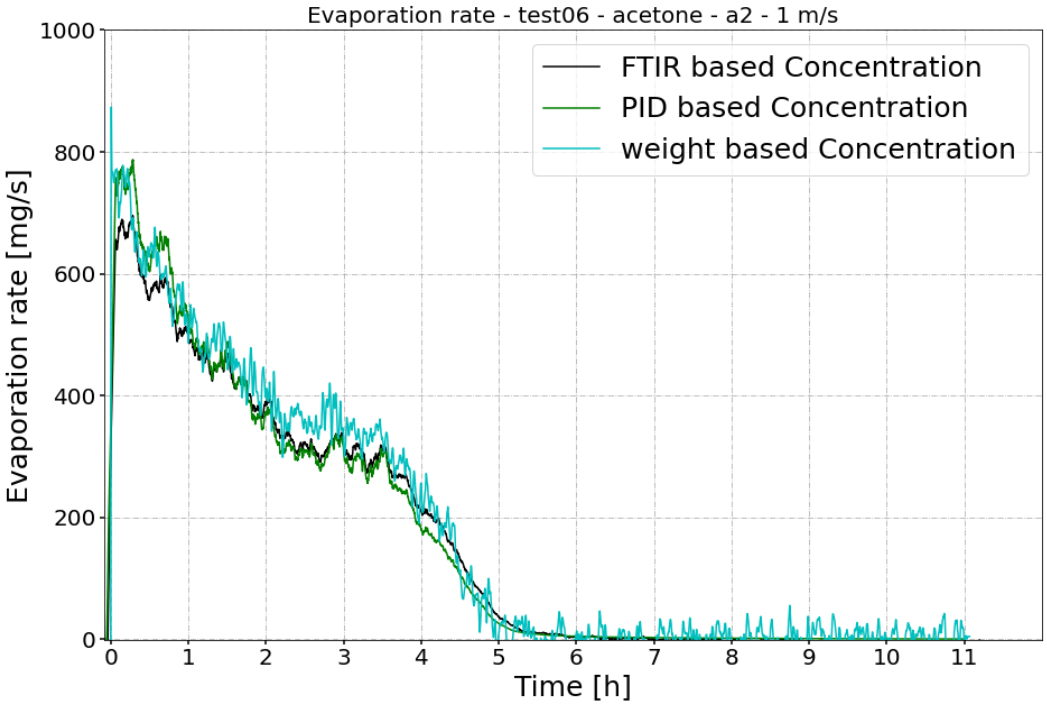


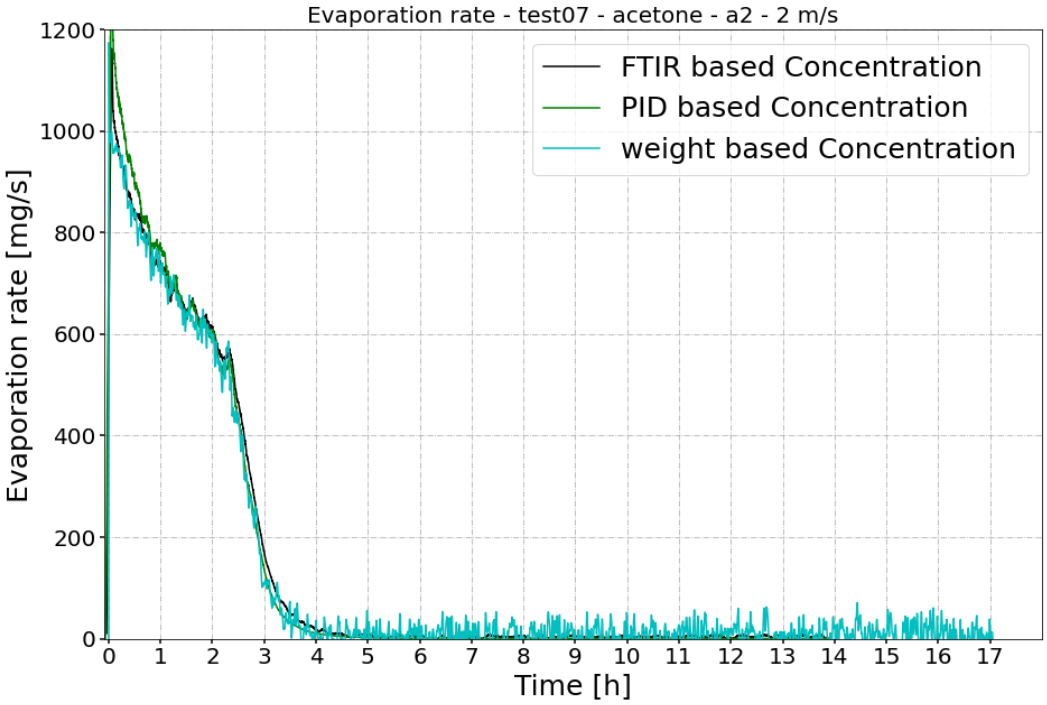


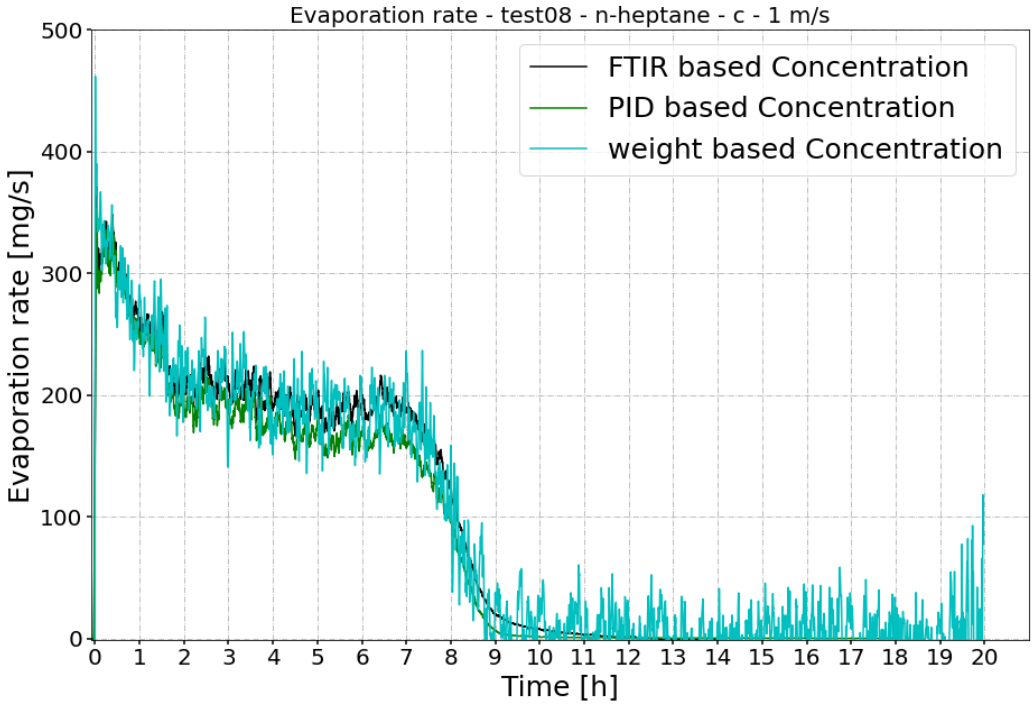

Evaporation rate - test03 - n-heptane - a1 - 1 m/s
FTIR based Concentration
PID based Concentration
weight based Concentration
Evaporation rate [mg/s]
Time [h]

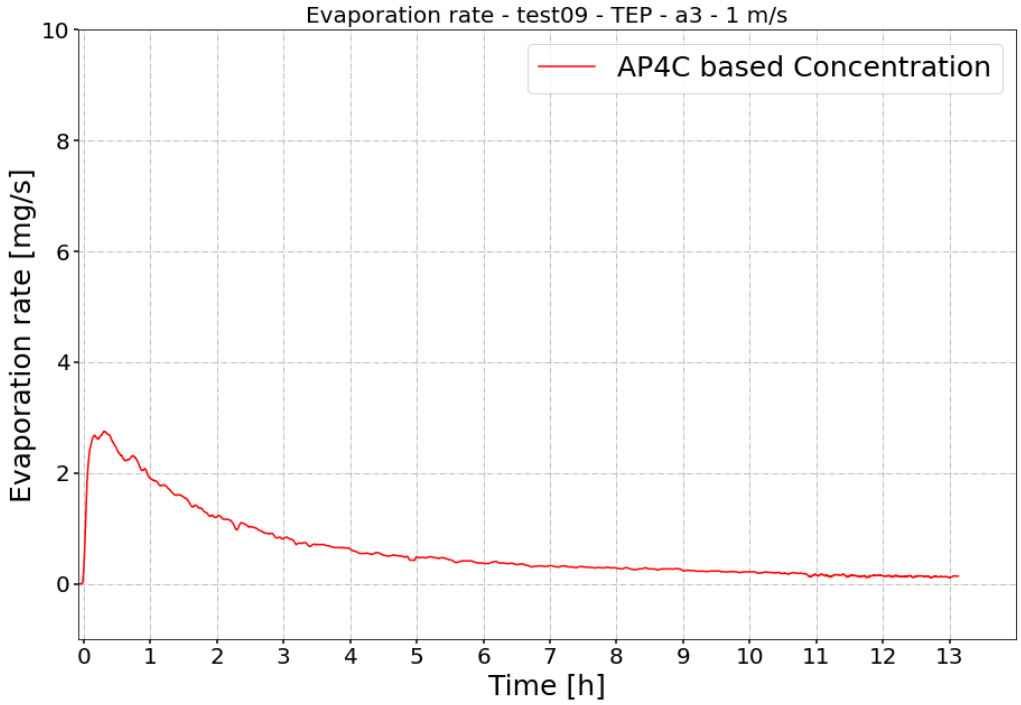

Evaporation rate - test04 - n-heptane - a1 - 1 m/s
FTIR based Concentration
PID based Concentration
weight based Concentration
Evaporation rate [mg/s]
Time [h]

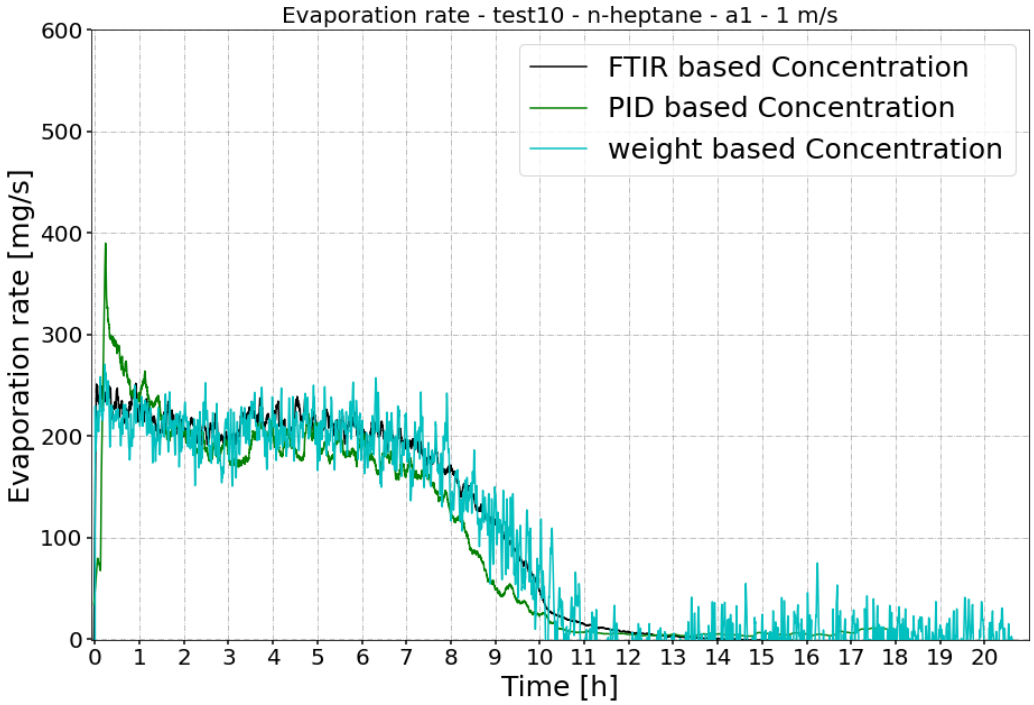

Evaporation rate - test05 - n-heptane - b - 1 m/s
FTIR based Concentration
PID based Concentration
weight based Concentration
Evaporation rate [mg/s]
Time [h]
0
100
200
300
400
500
600
0
1
2
3
4
5
6
7
8
9
10

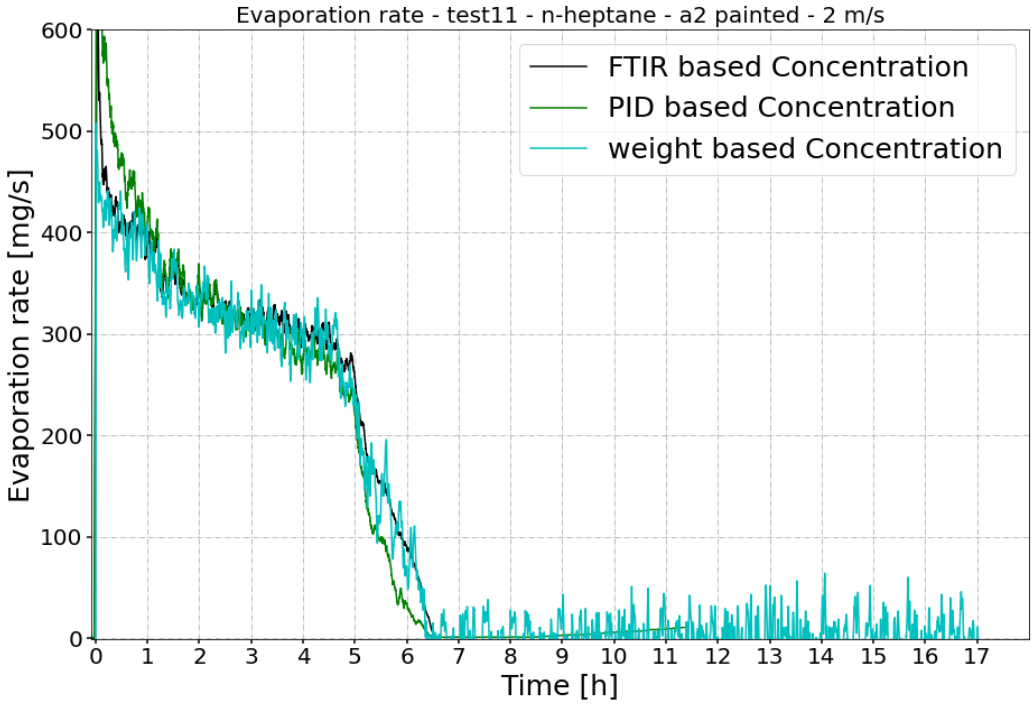

Evaporation rate - test06 - acetone - a2 - 1 m/s
FTIR based Concentration
PID based Concentration
weight based Concentration
Evaporation rate [mg/s]
Time [h]
0
200
400
600
800
1000
0
1
2
3
4
5
6
7
8
9
10
11

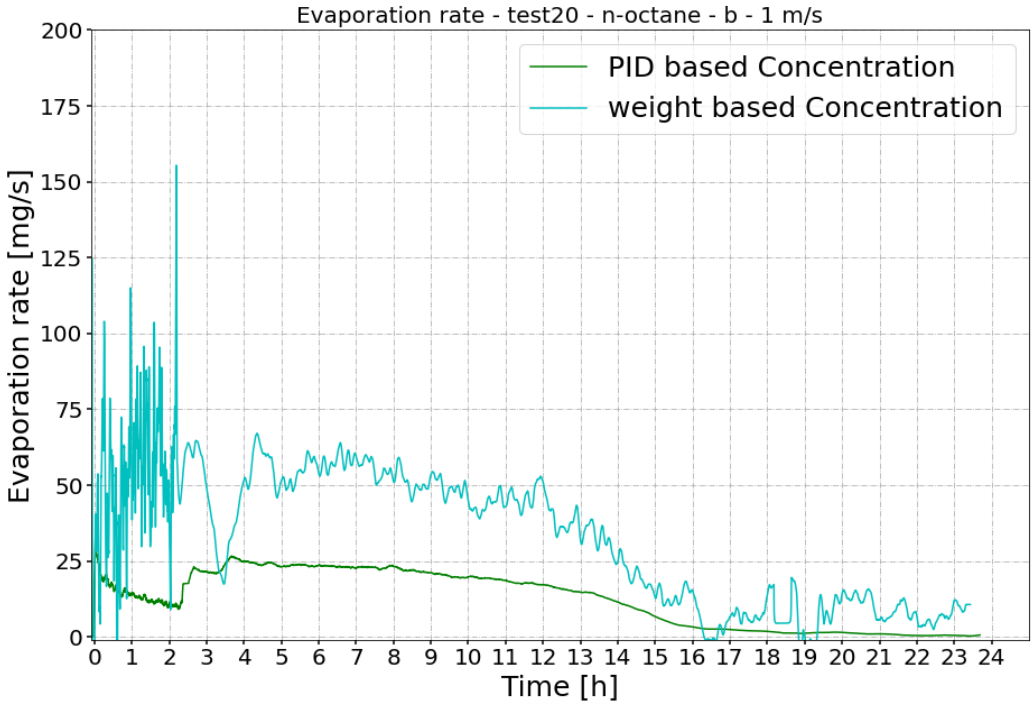

Evaporation rate - test07 - acetone - a2 - 2 m/s
FTIR based Concentration
PID based Concentration
weight based Concentration
Evaporation rate [mg/s]
Time [h]
0
200
400
600
800
1000
1200
0 1 2 3 4 5 6 7 8 9 10 11 12 13 14 15 16 17

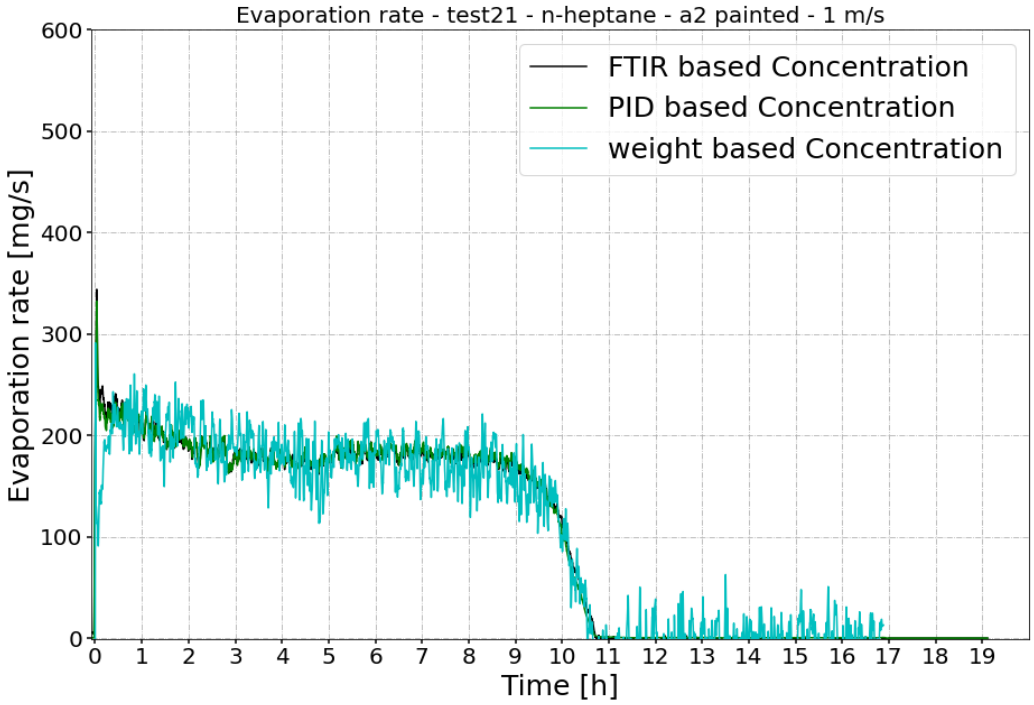

Evaporation rate - test08 - n-heptane - c - 1 m/s
FTIR based Concentration
PID based Concentration
weight based Concentration
Evaporation rate [mg/s]
Time [h]
0
100
200
300
400
500
0 1 2 3 4 5 6 7 8 9 10 11 12 13 14 15 16 17 18 19 20

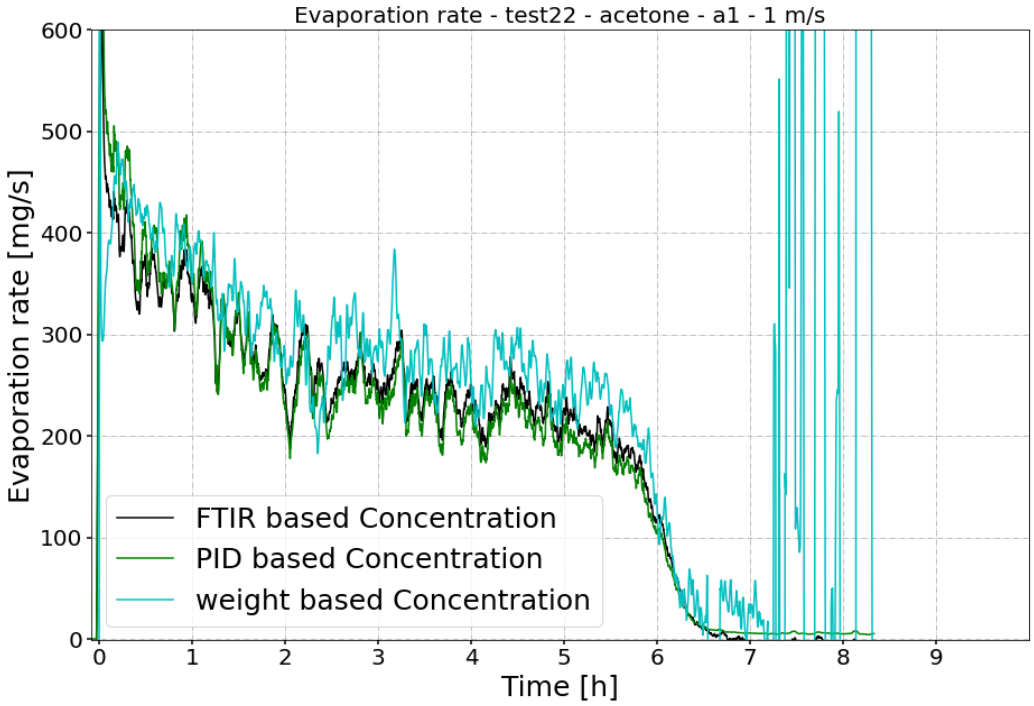

Evaporation rate - test09 - TEP - a3 - 1 m/s
AP4C based Concentration
Evaporation rate [mg/s]
Time [h]


Evaporation rate - test10 - n-heptane - a1 - 1 m/s
FTIR based Concentration
PID based Concentration
weight based Concentration
Evaporation rate [mg/s]
Time [h]

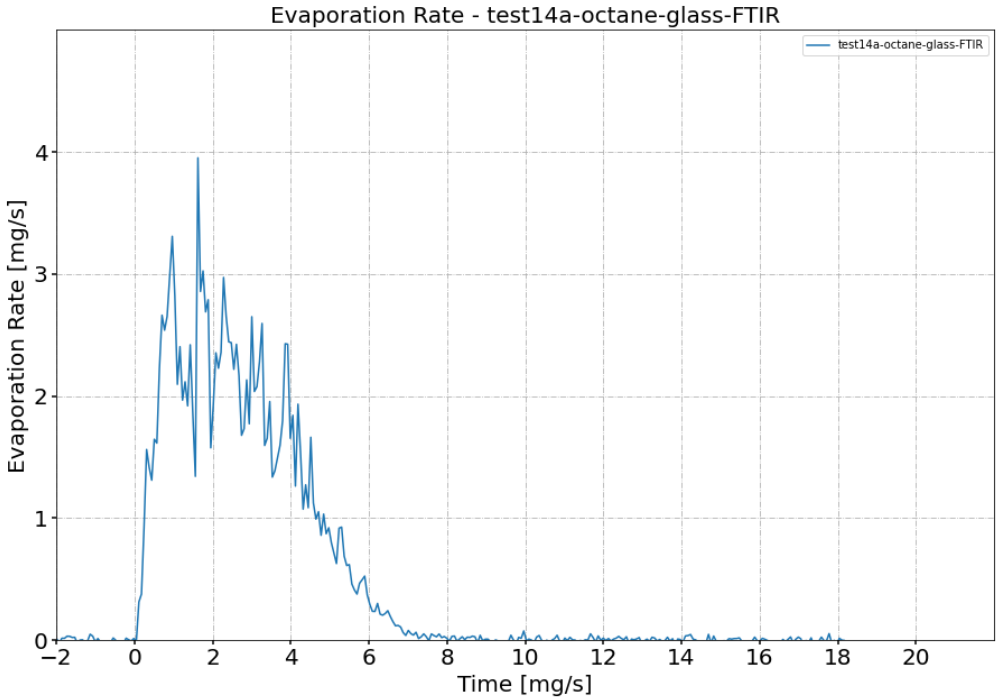

Evaporation rate - test11 - n-heptane - a2 painted - 2 m/s
FTIR based Concentration
PID based Concentration
weight based Concentration
Evaporation rate [mg/s]
Time [h]

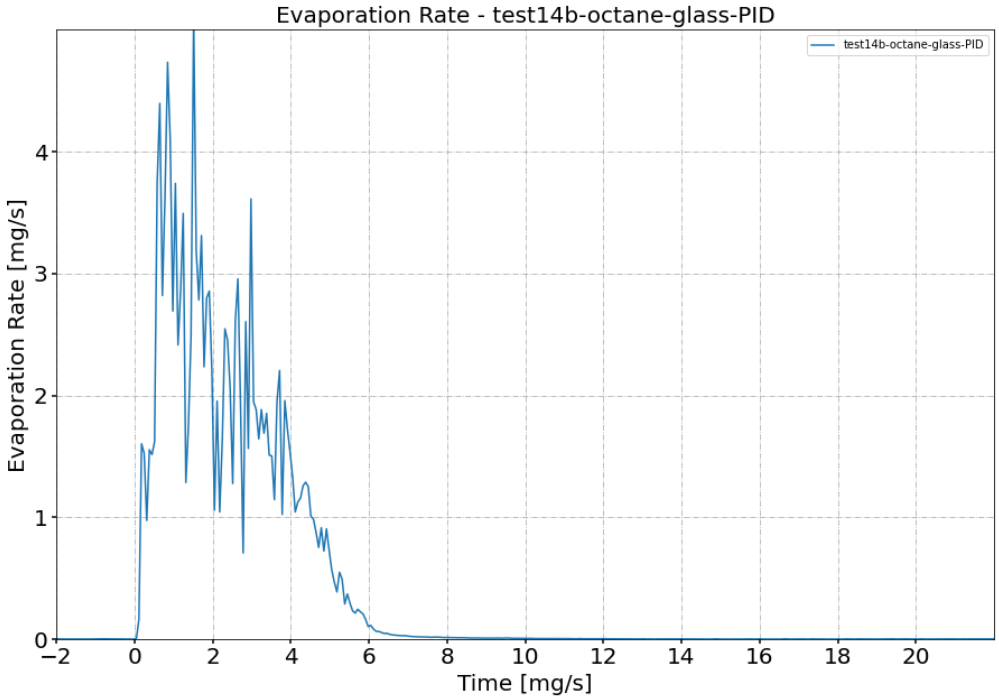

Evaporation rate - test20 - n-octane - b - 1 m/s
PID based Concentration
weight based Concentration
Evaporation rate [mg/s]
Time [h]

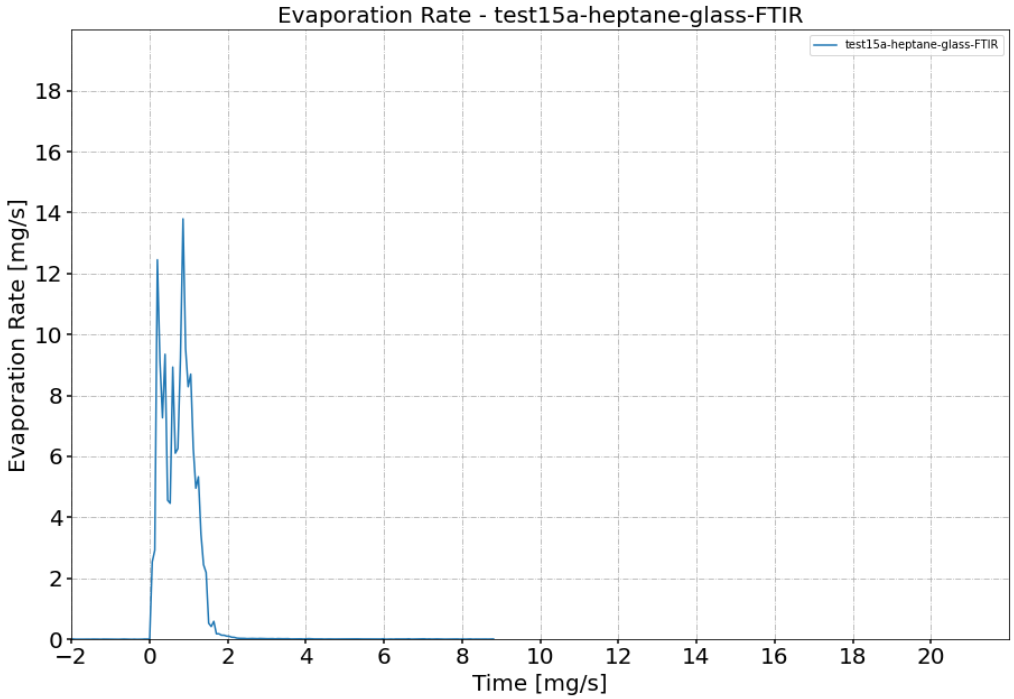

Evaporation rate - test21 - n-heptane - a2 painted - 1 m/s
FTIR based Concentration
PID based Concentration
weight based Concentration
Evaporation rate [mg/s]
Time [h]

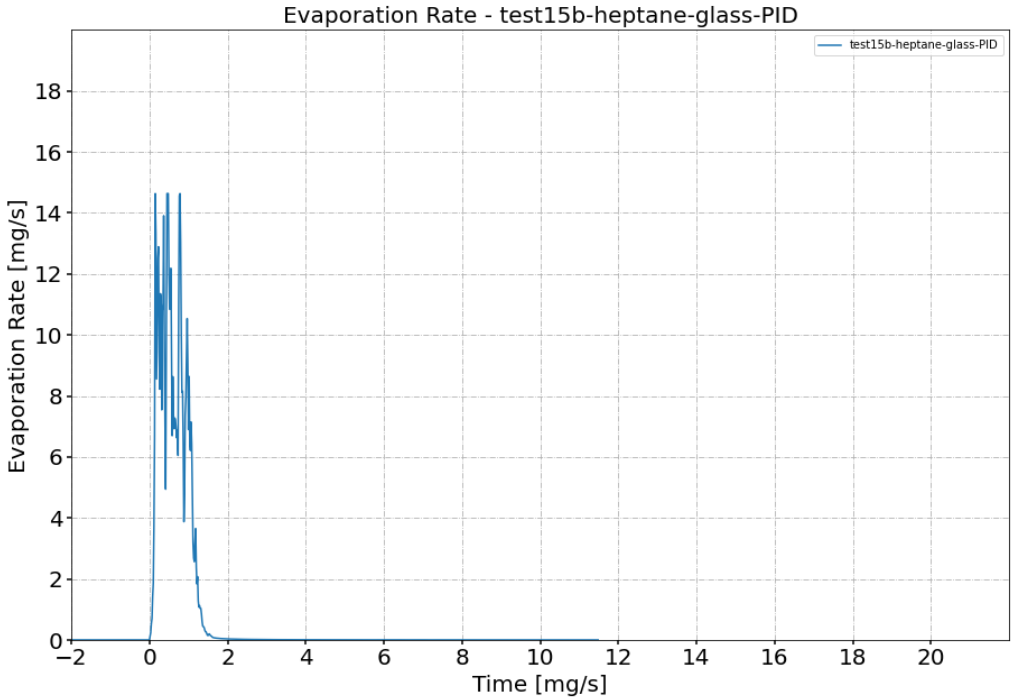

Evaporation rate - test22 - acetone - a1 - 1 m/s
FTIR based Concentration
PID based Concentration
weight based Concentration
Evaporation rate [mg/s]
Time [h]

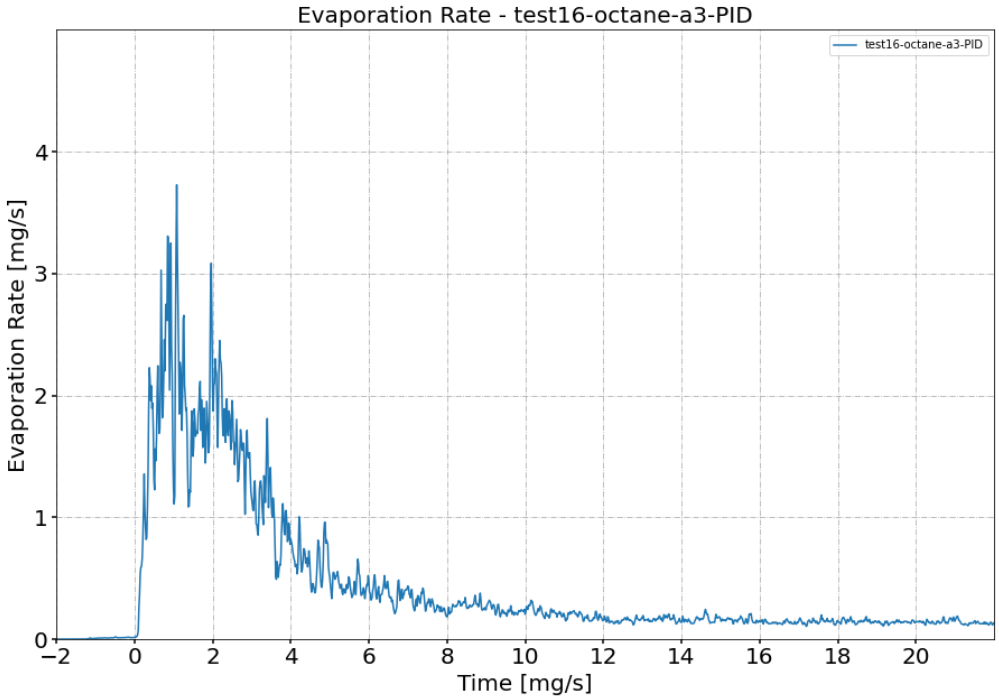
APPENDIX 8 : Droplet evaporation tests
Evolution of evaporation rate – 7 pages

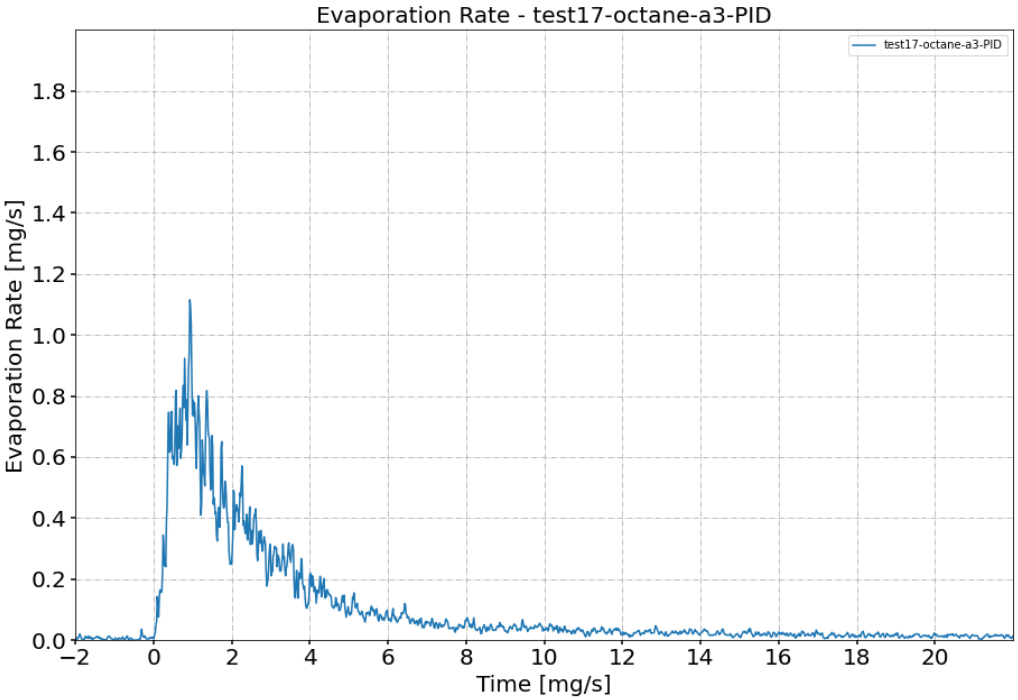


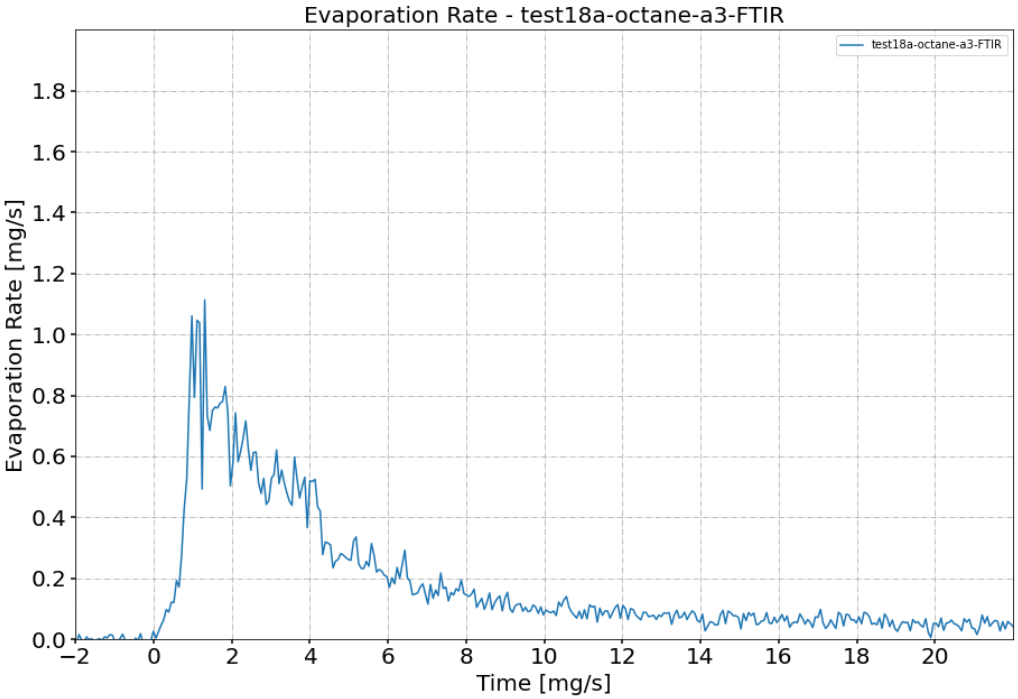


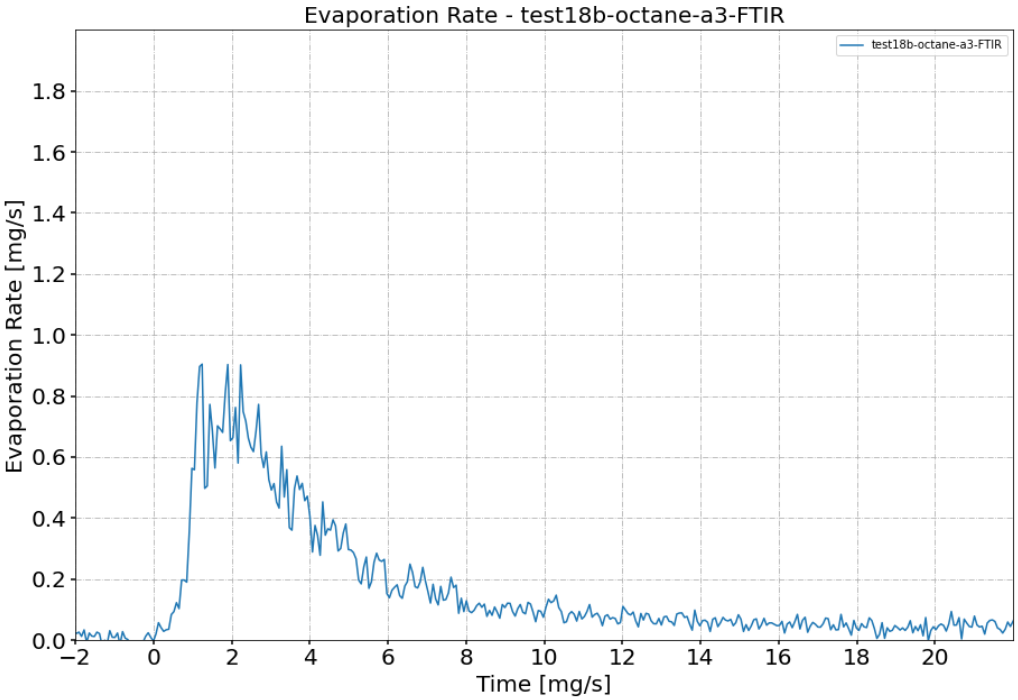

Evaporation Rate - test15a-heptane-glass-FTIR
test15a-heptane-glass-FTIR
Evaporation Rate [mg/s]
Time [mg/s]
0
2
4
6
8
10
12
14
16
18
−2
0
2
4
6
8
10
12
14
16
18
20

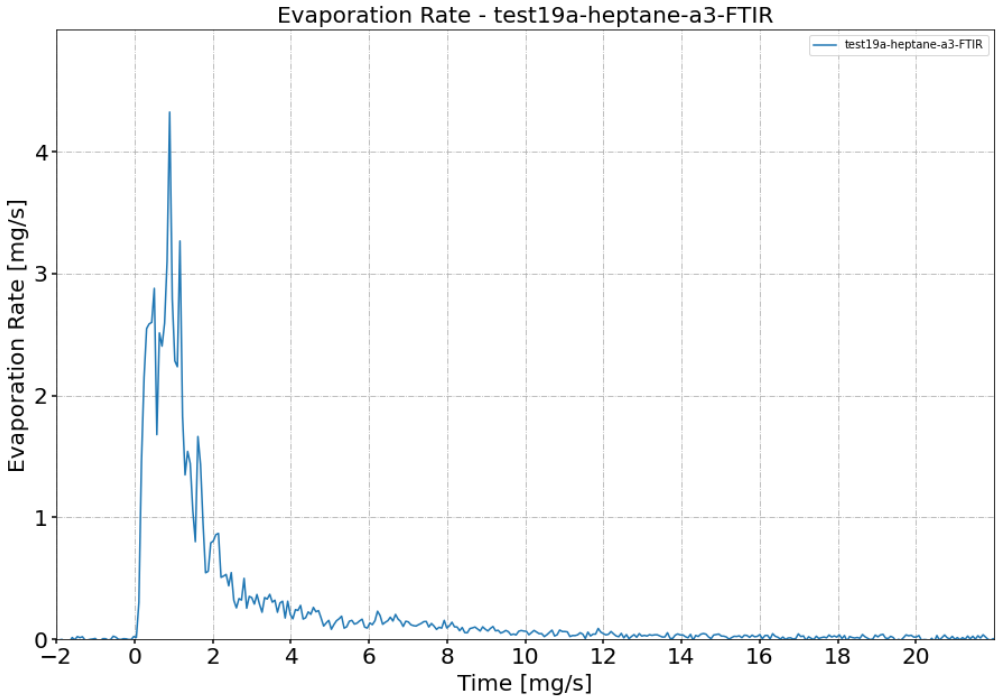

Evaporation Rate - test15b-heptane-glass-PID
test15b-heptane-glass-PID
Evaporation Rate [mg/s]
Time [mg/s]
0
2
4
6
8
10
12
14
16
18
−2
0
2
4
6
8
10
12
14
16
18
20

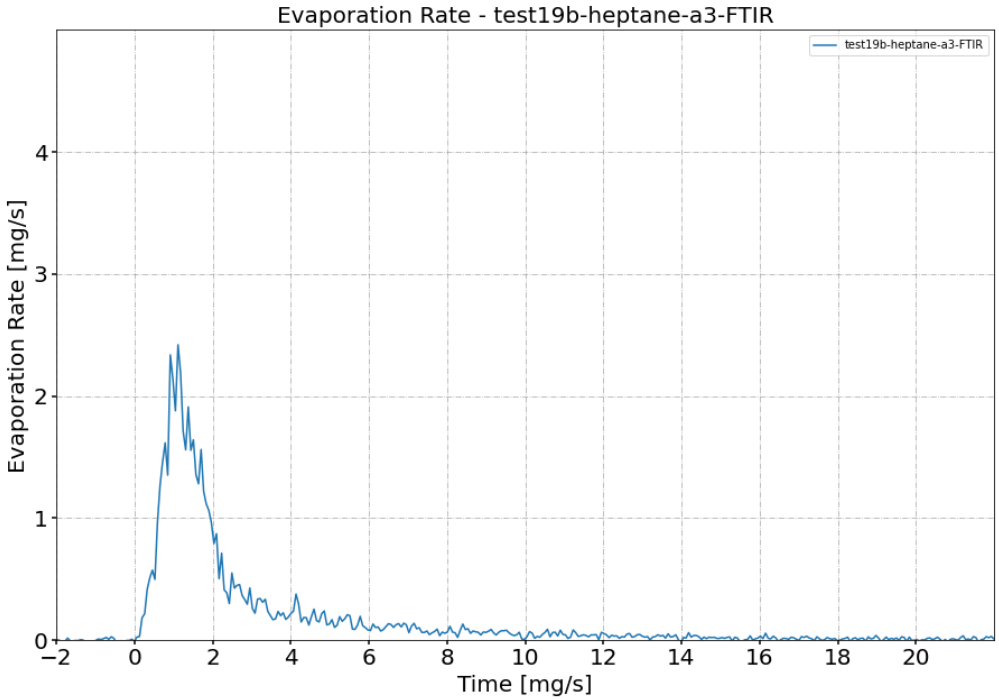

Evaporation Rate - test16-octane-a3-PID
test16-octane-a3-PID
Evaporation Rate [mg/s]
Time [mg/s]
0
1
2
3
4
−2
0
2
4
6
8
10
12
14
16
18
20

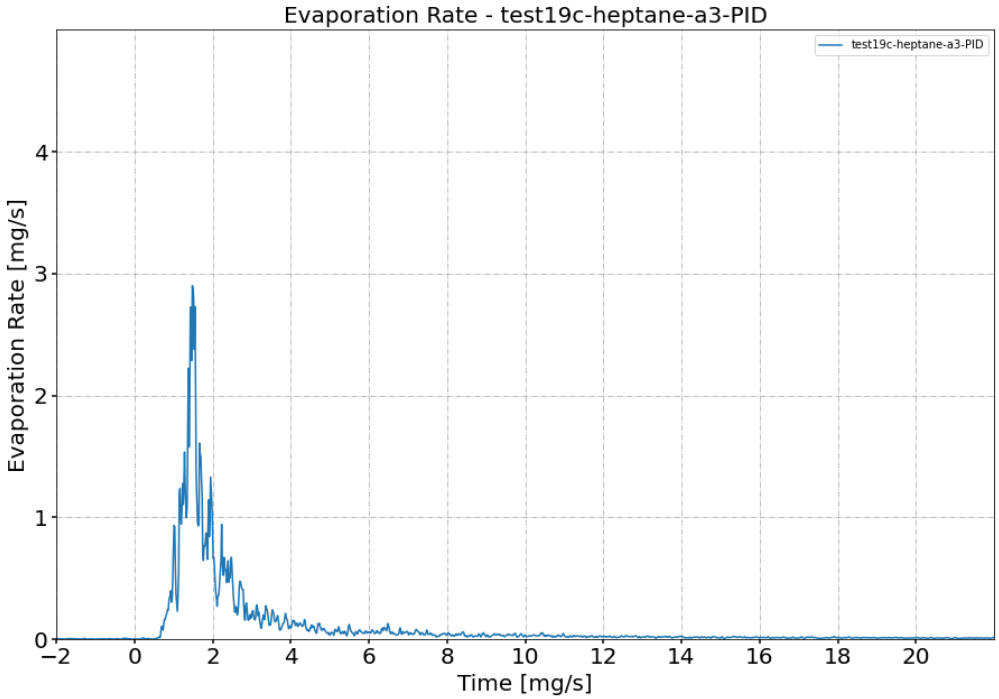

Evaporation Rate - test17-octane-a3-PID
test17-octane-a3-PID
Evaporation Rate [mg/s]
Time [mg/s]
0.0
0.2
0.4
0.6
0.8
1.0
1.2
1.4
1.6
1.8
−2
0
2
4
6
8
10
12
14
16
18
20

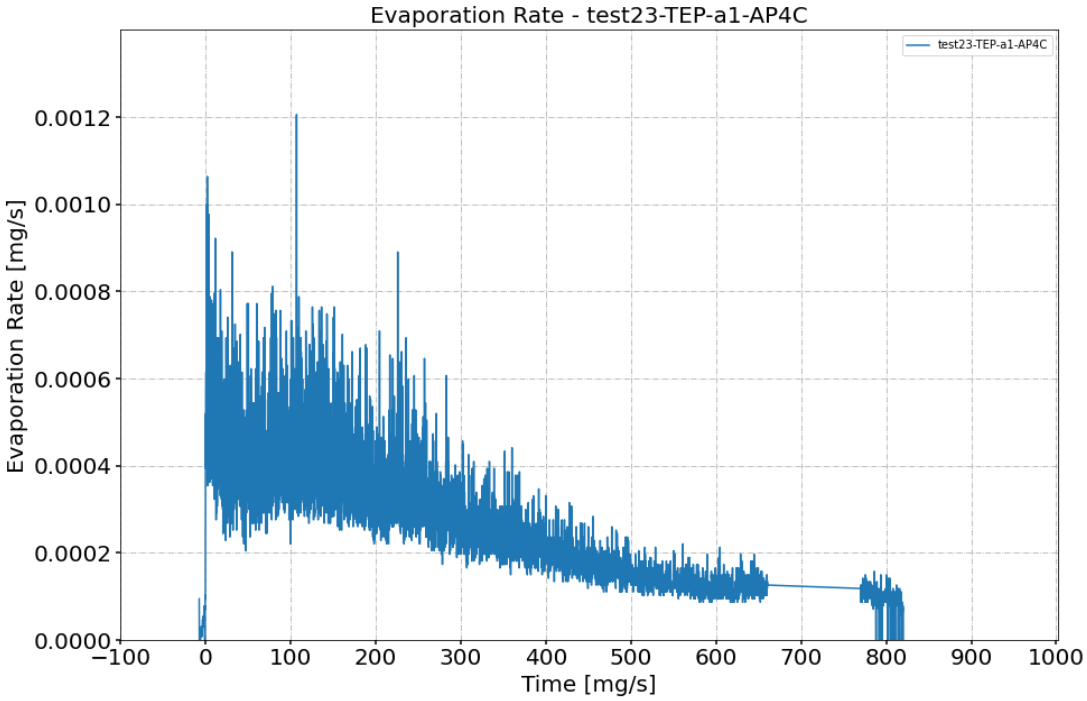

Evaporation Rate - test18a-octane-a3-FTIR
test18a-octane-a3-FTIR
Evaporation Rate [mg/s]
Time [mg/s]
0.0
0.2
0.4
0.6
0.8
1.0
1.2
1.4
1.6
1.8
−2
0
2
4
6
8
10
12
14
16
18
20

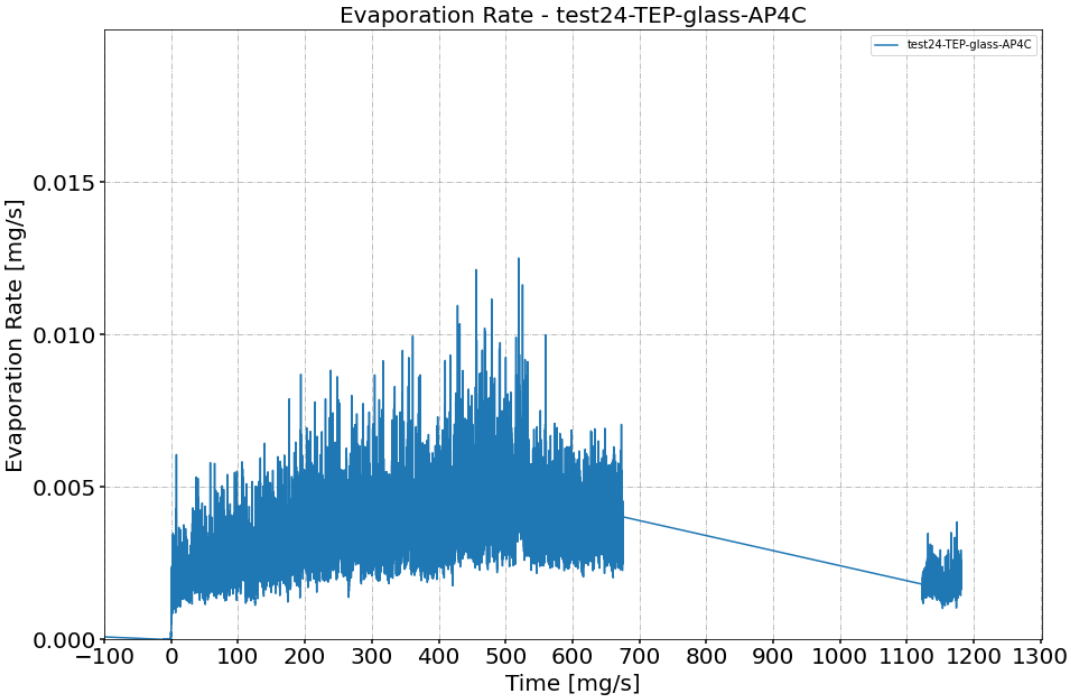

Evaporation Rate - test18b-octane-a3-FTIR
test18b-octane-a3-FTIR
Evaporation Rate [mg/s]
Time [mg/s]
0.0
0.2
0.4
0.6
0.8
1.0
1.2
1.4
1.6
1.8
−2
0
2
4
6
8
10
12
14
16
18
20


Evaporation Rate - test19a-heptane-a3-FTIR
test19a-heptane-a3-FTIR
Evaporation Rate [mg/s]
Time [mg/s]
0
1
2
3
4
−2
0
2
4
6
8
10
12
14
16
18
20


Evaporation Rate - test19b-heptane-a3-FTIR
test19b-heptane-a3-FTIR
Evaporation Rate [mg/s]
Time [mg/s]
0
1
2
3
4
−2
0
2
4
6
8
10
12
14
16
18
20


Evaporation Rate - test19c-heptane-a3-PID
test19c-heptane-a3-PID
Evaporation Rate [mg/s]
Time [mg/s]
0
1
2
3
4
−2
0
2
4
6
8
10
12
14
16
18
20


Evaporation Rate - test23-TEP-a1-AP4C
test23-TEP-a1-AP4C
Evaporation Rate [mg/s]
Time [mg/s]
0.0000
0.0002
0.0004
0.0006
0.0008
0.0010
0.0012
−100
0
100
200
300
400
500
600
700
800
900
1000


Evaporation Rate - test24-TEP-glass-AP4C
test24-TEP-glass-AP4C
Evaporation Rate [mg/s]
0.015
0.010
0.005
0.000
−100
0
100
200
300
400
500
600
700
800
900
1000
1100
1200
1300
Time [mg/s]

National Institute for Industrial Environment and Risks
Alata Technology Park • PO Box 2 • F-60550 Verneuil-en-Halatte
03 44 55 66 77 • ineris@ineris.fr • www.ineris.fr

